MONTE CARLO AND MEAN FIELD STUDIES OF POLYMERS IN SOLUTION

MARC PÉPIN

Monte Carlo and Mean Field Studies of Polymers in Solution

by

© Marc Pépin

M.Sc. (Queen's University, Kingston, Canada) 1992
B.Sc.H. (Queen's University, Kingston, Canada) 1990

A thesis submitted to the
School of Graduate Studies
in partial fulfilment of the
requirements for the degree of
Doctor of Philosophy

Department of Physics and Physical Oceanography
Memorial University of Newfoundland

(September, 1999)

St. John's Newfoundland

Abstract

This thesis presents a comprehensive study of the structure and physical properties of polymers in solution. The focus is on Monte Carlo (MC) simulations. The results are compared with mean field theoretical predictions and used to study the limitations of the mean field theories.

Four distinct systems are investigated. The first one consists of A-b-B diblock copolymer "crew-cut" micelles in A solvent. The relatively long B block is incompatible with the solvent and forms the core of the micelles, and the relatively short A block forms a thin corona. Results from simulations for the size of the core as a function of the molecular weight of the B block are compared with simple mean field theories in the literature and extensions in this thesis. They support the argument that the weaker dependence observed in recent experiments is a non-equilibrium effect.

When a small amount of B homopolymer is added to the block copolymer solution, it can be solubilized within the micelle cores and swell the micelles, or separate into a macrophase with the copolymers at the homopolymer-solvent interface and/or in micelles. Results from Monte Carlo simulations show a threshold volume fraction of homopolymer below which the homopolymer is solubilized within the micelle cores and above which macrophase separation occurs. These results are in qualitative agreement with previous experiments and a simple mean field theory.

In the third system, one end of each polymer is end-tethered to a surface and the

remaining section of the polymer stretches into good solvent forming an end-tethered layer. The fourth system includes free polymer in solution. The focus of this work is on system regimes which correspond to those studied in most experiments. In both systems, the results of the MC simulations agree well with those of the numerical self-consistent field (NSCF) calculations for surface concentrations above a threshold. A scaling analysis of the layer thickness shows that the systems are not in the limit of high molecular weight and highly stretched chains. Furthermore, in systems with relatively high molecular weight free polymers, the degree of penetration of the free polymer into the end-tethered layer is greater than predicted by asymptotic SCF theories, although still less than observed in recent experiments.

To my grandmother Florette

and to my parents.

Contents

List of Tables

List of Figures

Acknowledgements

I would like to take this opportunity to thank all those who have made contributions to this dissertation.

I wish to thank my thesis supervisor, Dr. Mark D. Whitmore, for sharing his knowledge and expertise. His constant support has made this work possible. I also thank him for his interest and efforts in my career as a teacher and physicist.

I thank Dr. John Whitehead and Dr. John de Bruyn for acting as members of my Supervisory Committee and for their guidance throughout the program.

I am very grateful to Dr. Gary Slater for sharing his time and expertise and to Dr. Michael S. Kent for insightful discussions.

I gratefully acknowledge the financial assistance by the School of Graduate Studies and Department of Physics Physical Oceanography and in the form of graduate fellowships.

I also wish to acknowledge research assistance from Canada's C3.ca program. In particular, I wish to thank the following members of C3.ca for their generosity in supplying computing resources and expertise: Memorial University of Newfoundland, University of Alberta, University of Calgary and Université de Montréal.

I would like to thank all my friends and colleagues in St. John's. My friends have made this special time in St. John's a wonderful experience. I thank Dr. Allan B. MacIsaac for his help in getting started on my research. Special thanks to Dr. Roman Baranowski for his constant help during my studies and for allowing me to

use his code for some of my calculations. I also thank Martin Kenward for running simulations and helping with the code.

I would like to thank my dear love Ranya for always reminding me that there is much more to life than a Ph.D. thesis.

Finally, special thanks to my parents and family, who have always been there for me. Their love and encouragement are greatly appreciated.

Chapter 1

Introduction

1.1 Polymers in Solution – General Remarks

In recent years polymers have gained remarkable popularity in diverse fields of study. The interest in polymers is attributed to the wide range of possible morphologies formed by polymers which can be tailored for specific applications. The variety and complexity of the various polymer systems have generated extensive experimental and theoretical studies.

One aspect of polymers which contributes to an extensive number of applications is the variety of morphologies and properties arising from polymer blends and polymers in solvent. For example, a combination of polymers consisting of a hard but brittle polymer and a soft but malleable polymer can result in a product which is hard but not brittle and can be used in numerous commercial applications. In general, different species of polymers are immiscible, and for example, diblock copolymers might be used as compatibilizers to improve the miscibility between two polymer-

s and change the morphology and properties of the system. Various morphologies produced from combinations of polymers can include spheres, cylinders and layers. These nano-structures can be useful in applications such as lithography [3]. Polymers are also found in composite materials, adhesives and coatings. Recent interests have been in the use of polymers as coatings in the manufacture of medical devices such as bioimplants where the polymer surfaces form strong repulsive layers which can act as lubricants when in contact with other biomatter. The tailoring of the morphologies and the ability to form protective coatings can also be useful in developing efficient drug delivery systems. In order to understand the mechanisms responsible for the morphology and properties of polymer systems, an understanding of their thermodynamic properties is required.

Polymers are molecules composed of repeating chemical units, known as *monomers*. The repeat units are bonded together to form various architectures. The simplest architecture is the linear homopolymer, in which identical monomers are joined in a single chain. The number of monomers that make up a polymer is referred to as the degree of polymerization, Z, and in general is relatively high ($10^2 - 10^5$). Other structures include branched polymers, which can be used to form star and comb-like structures. Copolymers contain two or more types of monomers. In particular, *diblock copolymers* consist of a block of monomers A (e.g. polystyrene) of degree of polymerization Z_{CA} and a block of monomers B (e.g. polybutadiene) of degree of polymerization Z_{CB}. They are chemically bonded together to form a molecule with

$Z_C = Z_{CA} + Z_{CB}$.

When polymers are immersed in solvent the behavior is largely dependent on the interactions between the solvent and polymer. The quality of the solvents is described by three categories: good, poor and Θ solvent. A polymer of infinite molecular weight will dissolve in a good solvent and not in a poor solvent. The Θ solvent represents the cross-over between good and poor solvent. The radius of gyration R_g of a polymer also depends on the quality of the solvent and scales approximately as

$$R_g \propto \begin{cases} Z^{3/5} & \text{for good solvent} \\ Z^{1/2} & \text{for } \Theta \text{ solvent or bulk polymer} \\ Z^{1/3} & \text{for poor solvent [4].} \end{cases} \tag{1.1}$$

The exponent (1/2) for Θ solvent or bulk polymer corresponds to a random walk of unperturbed "ideal" chains. In good solvent, the solvent therefore swells the chains.

When small amounts of *A-b-B* diblock copolymer, typically 2% volume fraction, are immersed in a selective solvent which is poor for the *B* block and good for the *A* block, microdomains with sizes of order $20 - 50$ nm can form. These microdomains are referred to as micelles. The *B* blocks form the core of the micelles and the *A* blocks form a corona. Of interest is the size of the core and corona as functions of the degree of polymerization and solvent quality with respect to both blocks of the copolymer. Generally, copolymers with relatively short core blocks form micelles with small cores and relatively thick coronas but recent interest has been in the study of so-called "crew-cut" micelles with large cores and thin coronas which consist of

copolymer with relatively long core-forming blocks. This system is the first of four systems investigated in this thesis.

When a small amount of low molecular weight *B* homopolymer is added to a system of *A*-*b*-*B* diblock copolymer micelles, the homopolymer can either be solubilized within the micelle cores resulting in a microphase, or phase separate with the copolymers at the homopolymer-solvent interface and/or in micelles. In the microphase, the homopolymer swells the micelles. The effect of the copolymer at the interface between the homopolymer and solvent is to reduce the interfacial tension. Of interest is the interplay between the micro and macrophases, which is dependent on the molecular weights and volume fractions of the *B* homopolymer and *B* copolymer, and the solvent quality and selectivity. This constitutes the second system investigated in this thesis.

In many cases, polymers at surfaces and interfaces can be used to produce desired effects in polymer systems. For example, in a polymer/solvent system, when one end of each polymer is end-tethered to a surface, the properties and the structure of the polymer layer will depend on the polymer used and the surface density of the polymer. As the surface density increases, the polymers become strongly stretched away from the surface and a polymer "brush" is formed. The thickness of the end-tethered layer is dependent on the surface density and the degree of polymerization of the polymer. In the study of this third system, the focus is on the structure and behavior of the end-tethered layer in good solvent.

The end-tethered layers can be used to alter surface properties and provide protective coatings but they can also be used in other applications. In some cases, when a thin film of liquid (~ 300 nm) is applied uniformly to a surface, the film often dewets the surface. The presence of an end-tethered layer in conjunction with small amounts of free homopolymer in solution tends to stabilize the films for extended periods of time. A threshold amount of free polymer is required to stabilize the films [5,6]. End-tethered or free polymer alone does not stabilize the films and it is believed [5,6] that the coupling between the end-tethered and free polymers along with the overlap of the free polymers strongly affect the stability of the film. A study of thin films and the interactions between the end-tethered layer and free polymer make-up the fourth system studied in this dissertation.

All four systems are directly related to experiments and have important applications. The microphase behavior found in micelle and swollen micelle systems is very useful in materials science, oil recovery and drug delivery. End-tethered layers can be useful in the stabilization of colloids [7,8], adhesion [9] and lubrication, and biophysics. Applications for uniform thin films are found in several technological fields, as in lithography in the microelectronics industry. A theoretical study of the properties of these systems which can be compared with existing experimental data is therefore very important. In addition, we compare different theoretical models at studying these systems and quantify the range of applicabilty of each approach used in this study and how they compare to experiments. Different models are discussed

in the following section.

1.2 Theoretical Models

The four polymer systems discussed above have been studied extensively in experiments. Several theoretical methods have been developed to study these systems. This section provides a brief description of the theoretical models along with the advantages and disadvantages of each approach. Details and references are given in later sections.

The models can be categorized as shown in Figure 1.1. In general, the analyt-

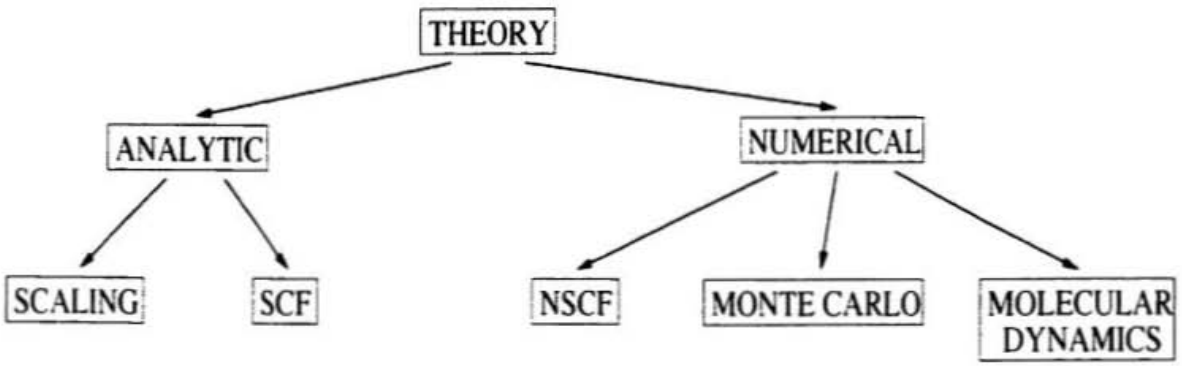

Figure 1.1: Breakdown of various theoretical methods.

ical models provide global information in terms of scaling laws with respect to the physical characteristics of the systems and may provide detailed information about the properties of the systems in limiting cases only. On the other hand, the numerical techniques can provide more detailed information about the physical properties

including scaling laws at the expense of more extensive computational demands, but they are not restricted to limiting cases.

The analytical models can be subdivided into two categories: Scaling [10] and mean field theories. The scaling theories are based on scaling arguments and provide a good starting point for the study of end-tethered polymers [11, 12] and thin films [13]. They are limited in their range of applicability due to assumptions about the structure of the systems and in general do not provide details about the structure of the systems. Analytical mean field theories have been successful in the study of end-tethered layers [14, 15] and thin films [16, 17]. The theories were developed in terms of an analytical self-consistent field (SCF) theory. The model is based on an analogy drawn by Semenov [18]. The analogy stems from the correspondence between the configuration of a weakly stretched or unstretched chain and the possible trajectories of a quantum-mechanical particle. On the other hand, the configuration of the completely stretched chain is reminiscent of the trajectory of a classical particle. In the case of end-tethered layers with chains of degree of polymerization Z, when the density of chains is high enough so that they are considerably stretched the layer thickness h scales as $h \sim Z$. In this regime the chains are highly stretched compared to the end-to-end distance R of an unperturbed chain. For the unperturbed chains, $R \sim Z^{1/2}$ and they therefore fluctuate about some path. In the asymptotic limit of infinite molecular weight ($Z \to \infty$) and for highly stretched chains, the analytical SCF model uses the most probable path. This approximation is strictly valid in the

limit of infinite molecular weight where the chains are highly stretched. This imposes a limit on the range on surface densities of end-tethered polymer to which this SCF theory applies. Nonetheless, this analytical formalism provided scaling laws and more detailed information on the structural properties of the systems.

With the advent of high performance computing, numerical techniques have become increasingly important because of their capability to simulate systems comprised of a large number of interacting macromolecules and solvent molecules. These large systems are therefore suitable for description in the language of statistical physics. In general, the description of the system proceeds in three steps:

1. Modeling and determination of the energy of the various microscopic configurations of the system. The modeled configurations must be compatible with the macroscopic state.

2. Determination of the partition function $\boldsymbol{Z}$.

3. Evaluation of the Helmholtz free energy

$$\mathcal{F} = -k_B T \ln \boldsymbol{Z} \, . \tag{1.2}$$

Most relevant physical quantities can be determined from the free energy expression in Equation (1.2). The approach to evaluating the free energy is not unique and the way the particular approach addresses points (1) and (2) can be used to classify the model. The numerical models of interest in this thesis can be divided into three categories: mean field theory, Monte Carlo (MC) simulations and molecular dynamics

(MD). The polymers can be modeled by discrete units or as continuous space curves. The mean field theories, in the context of this study, constitute a combination of mean field theories and numerical self-consistent field (NSCF) theories. A simple mean field approach is used for micelles [19–31] and swollen micelles [32]. These models usually consist of calculating a free energy from various contributions which depend on the structure of the polymer system. The contributions are determined from Flory type mean field expressions [33]. The free energy is then minimized with respect to the variables which characterize the system. These theories once again offer a global description of the physical properties of systems, including polymers with realistic degrees of polymerization, but require *a priori* assumptions about the structure of the system.

A single chain mean field theory (SCMF) was developed by Carignano and Szleifer [34] and applied to end-tethered layers [34–38] and thin films [39]. The theory involves evaluating an expression for the Helmholtz free energy involving the probability distribution function of chain conformations. To obtain this function, the free energy is minimized and the resulting expression is a function of the chain conformations only. The finite set of single chain conformations is generated using a lattice model or rotational isomeric state (RIS) model (off-lattice model).

The NSCF theories have been very successful in the study of end-tethered polymers [40–46], thin films [17, 47], micelles [48–51] and swollen micelles [52–54] with the advantage of supplying a more detailed structure of the physical systems, but they

are also limited in their range of applicability. The calculations become more computationally intensive than the simple mean field theories but nonetheless systems with realistic degrees of polymerization are modeled.

In these models, fluctuations about the equilibrium conformation of the chains are included. Therefore, for end-tethered systems, the restriction to strongly stretched, high molecular weight polymers does not apply. On the other hand, both the NSCF and the analytical SCF approaches assume laterally homogeneous systems and contact interactions between components. Hence, the density fluctuations parallel to the end-tethering surface which occur at low concentrations are ignored.

In the NSCF models, the polymer configurations are modeled by trajectories in continuous space, as in this thesis, or by walks on a lattice. Scheutjens and Fleer applied a lattice model to systems of end-tethered homopolymers [41–44], copolymer adsorbed at an interface [55–57] and thin films [17, 47]. The polymer chains are described as walks on a lattice. Each effective monomer experiences an inhomogeneous field which is an averaged quantity modeled from nearest neighbor pair interactions and surface-monomer interactions. The surface interactions are limited to lattice sites directly in contact with the surface. The mean field therefore depends on the local concentrations of polymer which, in turn, are determined from the mean field. The problem is solved self-consistently. The NSCF approach is effective for treating finite molecular weight corrections but is restricted by the mean field approximation.

Molecular Dynamics (MD) methods have been used extensively to study polymers.

In principle, the MD method implies solving the classical Newtonian equation of motion and does not require the approximation of a mean field. When treating macromolecules with a fully atomistic model, problems arise in the length scales involved. For a simple flexible chain there is structure on scales from that of a single chemical bond ($\approx$ 0.1 nm) to the coil radius ($\approx$ 10 nm). Additional length scales occur due to structure in the system such as micelle formation. As a result, large systems with many polymers are required for modeling real systems. The problem with the feasibility of the simulations is even greater when the time scales involved are considered. In polymers, motions occur on many different time scales. For example, vibrations on the length scale of the C-C bond may occur on time scales of order of 10^{-13} s or less whereas transitions from *trans* to *gauche* states or vice-versa occur over 10^{-11} s. In micelle systems the time scale involved in the exchange of polymers between micelles can be as high as 10^{2} s or more. This effect causes serious problems in atomistic models.

An alternative to MD is the Monte Carlo approach, in which the macromolecules are modeled as coarse-grained polymers on a lattice. This method offers several advantages in terms of computational efficiency and feasibility. In this type of simulation each "effective bond" corresponds to several chemical bonds along the chain of the polymer. The length scale of the "effective bond" is that of the persistence length rather than the chemical bond. By eliminating the structure at short length scales, the small time scale motions are effectively eliminated. The lattice structure also al-

lows for efficient algorithms. This model can be used to study the systems of interest in this thesis but the number of the effective monomers per chain is still restricted to 200 or fewer. Another drawback to this model is the loss of the structure at short length scales which results in a loss of information in terms of the dynamics involved at all time and length scales.

Other coarse-grained models such as the bond-fluctuation model have also been successful in the study of large systems. In the bond-fluctuation model the chemical structure can be kept by indirectly choosing appropriate distributions of the length of the effective bonds and/or the distribution of the angle between subsequent effective bonds. These models have been successful in the study of end-tethered polymers [58] but this approach is still restricted to simulations of relatively few, low molecular weight polymers.

There have been recent advances in MC simulation techniques. Doruker and Mattice [59] have performed simulations of polyethylene (PE) thin films in an attempt to bridge the gap between the comparatively small systems in fully atomistic models and the MC simulations for coarse-grained structureless polymers. MC simulations were done on a high coordination lattice which reflects the structure of PE. The MC simulations were performed after the PE chains were mapped onto the coarse-grained lattice. Throughout a simulation it is feasible to reverse map the snap shots back to the atomistic model allowing the study of large bulk systems while keeping atomistic features of the polymer chains.

Each method described above has its advantages and shortcomings. The mean field theories can treat systems with realistic degrees of polymerization at relatively low computational cost, but they are restricted in their range of applicability due to the neglect of fluctuation effects and/or requirement of *a priori* knowledge about the structure of the system. The MC approach incorporates fluctuation effects, but is restricted to relatively low molecular weight polymers. In this thesis, the emphasis is on the use of Monte Carlo simulations as a complement to mean field theories. Monte Carlo simulations are used to study the limitations of the mean field theories and the mechanisms involved with polymers in solution. The following subsections discuss how these models have been used to study each of the four systems. Each subsection also discusses how MC simulations, in conjunction with existing models or other models developed in this thesis, will be used to gain a further understanding of the mechanisms responsible for the structure and properties of these systems.

1.3 Crew-cut Micelles

Block copolymers have been used in a wide variety of applications, and their effect on the behavior of solutions and blends is important. The systems of interest have low concentrations of *A*-*b*-*B* block copolymer. The immiscibility between the *B* block of the copolymer and the matrix (solvent or homopolymer) in conjunction with a relatively low entropic penalty in localizing the polymers results in the formation of micelles. The *B* blocks form the cores of the micelles, and the *A* blocks form coronas as

shown in Figure 1.2. If the overall copolymer concentration is low enough, the micelles

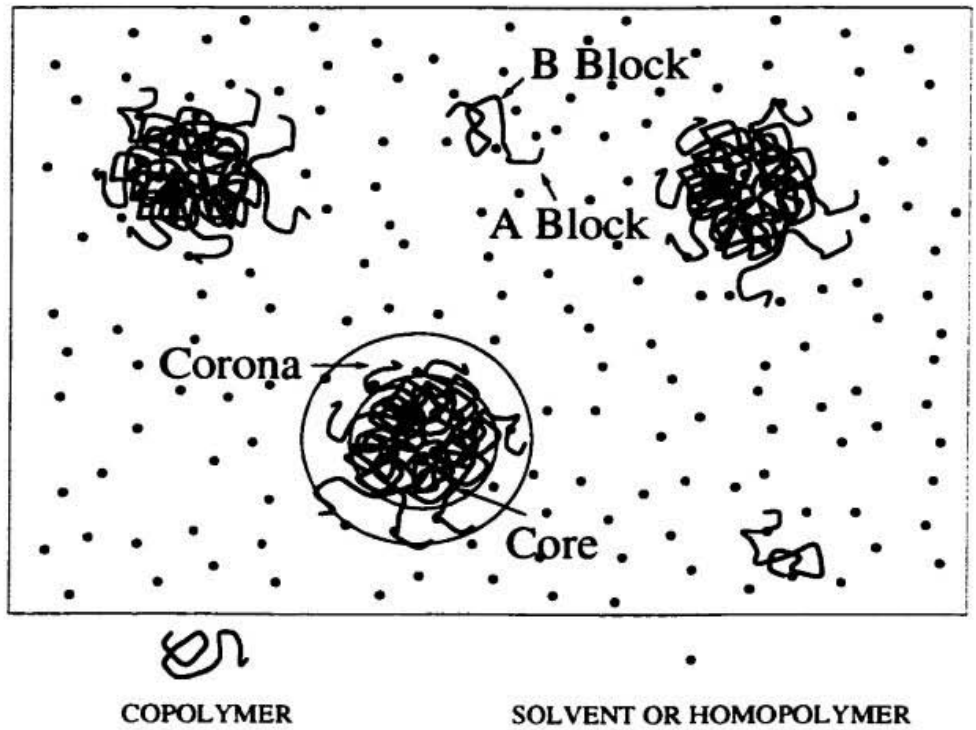

Figure 1.2: Schematic picture of block copolymer micelles.

are randomly distributed in solution. Theoretical and experimental interest has been focused on the study of micelles for which the B block of the copolymer is short compared to the A block. Hence, the micelles have a relatively small core compared to the size of the corona. Recently, there has been interest in the experimental study [1,60] of so called "crew-cut" micelles, for which the B block is longer than the A-block. The crew-cut micelles therefore have relatively large cores compared to the thickness of the corona.

Of particular interest in all these systems is the critical micelle concentration

(CMC) and the size of the micelles as a function of the degrees of polymerization of A and B blocks, Z_{CA} and Z_{CB}, respectively. To obtain the radius of the core and the thickness of the corona a simple mean field theory, which is outlined in Chapter 3, has been used. In this theory, it is assumed that the core and corona regions have uniform density profiles, and the total free energy is calculated from a total of six contributions. In a strongly segregated system, the size of the micelles is mainly controlled by the interplay between the interfacial tension at the core-corona interface and the elastic energy associated with stretching of the core-forming block of the copolymer. The interfacial tension tends to increase the size of the micelle by reducing the *total* interfacial area which results in fewer but larger micelles. On the other hand, as the size increases, the B block of the copolymer must stretch to the center of the micelle. The penalty in free energy associated with stretching the B block tends to keep the micelles small. Simple mean field theory predicts that the radius of the core of the micelle, l_B, scales as

$$l_B \propto Z_{CB}^{\alpha}, \quad \alpha \gtrsim 2/3 \,. \tag{1.3}$$

The analytical expression for l_B in Equation (1.3) does not show a dependence on the length of the corona block Z_{CA} but a numerical analysis within the same model shows a weak, inverse dependence on the A block. Other mean field theories predict similar scaling laws and in all cases $\alpha \geq 0.6$.

The scaling laws obtained are in agreement with many experiments on micelles with relatively short core-forming blocks. However, recent experiments [1] on crew-

cut micelles resulted in a different scaling relation with $l_B \propto Z_{CB}^{0.4} Z_{CA}^{-0.15}$. In this case, the scaling exponent of the Z_{CB} term was much lower than that predicted by simple mean field theory. The authors noted that these systems were not at equilibrium and that the discrepancy in the scaling exponents might be a non-equilibrium effect. In those experiments, the polymers were dissolved in a solvent which is good for both components of copolymers. The solution was then dialyzed against water, which is a poor solvent for one of the blocks, for a period of time. As the solvent quality for the core block decreased, micelles formed. When the solvent quality was decreased further, the copolymers were trapped in the micelles which results in non-equilibrium structures. The measured sizes of the cores may therefore reflect equilibrium conditions at the point where the copolymers began to be trapped in the micelles.

Simple mean field theory [21] suggests that the solvent quality at which the micelles become non-equilibrium structures strongly depends on the degree of polymerization of the core block. In the study of crew-cut micelles presented here, the non-equilibrium effects are simulated in our MC simulations by identifying the conditions where the copolymers begin to be trapped in the micelles. The MC simulations are then used to investigate scaling relations and compare with mean field results. Furthermore, the MC simulations are used to probe the structure of the micelles and investigate the assumptions of the mean field approach.

1.4 Swollen Micelles

Normally, a binary blend of A and B homopolymers macrophase separates because of the repulsive effective interactions as discussed in the previous section. The phase separated blend consists of domains of the minority component dispersed in the majority one. The sizes of the domains depend on the processing history, but typically are on the order of microns or larger. When small amounts of A-b-B block copolymer are added to the A/B blend, the copolymers can act as surfactant to disperse the minority component into smaller domains.

The next system of interest in this thesis is the A-b-$B/A/B$ ternary blend, with only a few percent of both copolymer and B homopolymer, in a host of A homopolymer or solvent. In this system, one can imagine a number of possibilities, including a single macrophase populated by micelles swollen by homopolymer and whose sizes are of the order of molecular dimensions; or macrophase separation (see Figure 1.3). Of particular interest is the interplay between microphase and macrophase separation and the micelle sizes and number density.

A previous mean field and experimental study by Whitmore and Smith [32] has been done to study block copolymer micelles swollen by added homopolymer. The theory predicts that, for relatively low molecular weight homopolymer, there exists a threshold volume fraction of homopolymer below which the homopolymer will be solubilized within the micelle cores and above which it macrophase separates. The theoretical results were in qualitative agreement with experiments where PEO

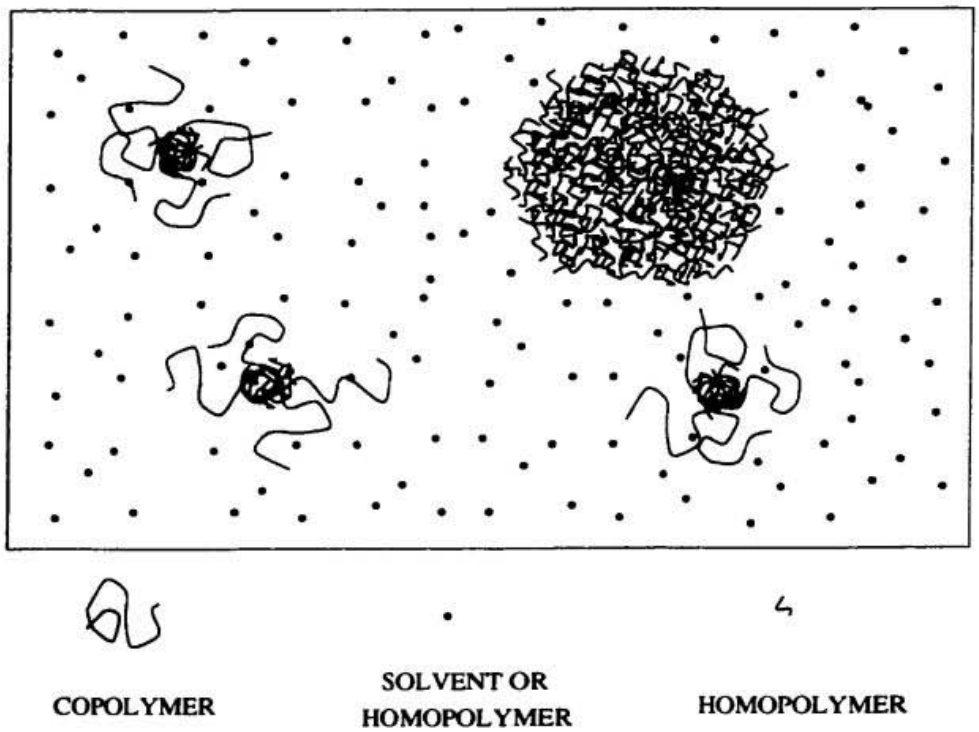

Figure 1.3: Schematic picture of micelles swollen by homopolymer and macrophase separated homopolymer.

homopolymer was added to a mixture consisting of polystyrene-*block*-poly(ethylene oxide) (PS-*b*-PEO) block copolymers in PS polymer hosts. Transmission electron micrographs (TEM) showed micelle cores ranging in diameter from 20 to 40 nm without added PEO homopolymer and from 20 to 60 nm with a relatively small volume fraction of PEO homopolymer. With a volume fraction of homopolymer well above the predicted threshold, domains ranging up to 400 nm were observed.

Although the mean field approach was successful in predicting the solubility limits in such systems some questions arise about some of the mean field approximations. The solubilization limits are calculated on the basis of a simple expression for the free

energy. In the case of swollen micelles in the strong segregation limit, the density profiles of the copolymer and homopolymer within each micelle are assumed to be uniform, with a sharp core-corona interface and all micelles having the same size. These assumptions about the structure of the micelles can be investigated with the use of MC simulations.

In the study of swollen micelles, we perform MC simulations of block copolymers in solvent with added homopolymer which is compatible with the core-forming block of the micelle. In these simulations the micelles self-assemble and no *a priori* assumptions about their structure or size distribution are required. We investigate the structure of the micelles swollen by the homopolymer and the solubilization limits predicted by mean field theory. We revisit the phase behavior reported in the mean field calculations by investigating the threshold volume fractions of homopolymer and its dependence on the relative degrees of polymerization of the copolymer and the added homopolymer.

1.5 End-tethered Layers

There is considerable interest in the theoretical and experimental study of "end-tethered" polymer chains at surfaces. Typical systems with one end of each polymer end-tethered to a surface and the polymer chains forming a layer in solvent are frequently referred to as polymer brushes. As discussed in Section 1.2, several theoretical [12–14, 40, 46, 58, 61–65] studies have been done to investigate the properties of

the end-tethered layers. As well, numerous experiments [57, 66–72] were performed to study end-tethered layers.

A system is characterized by the molecular weight M and the polymer surface density. The average area per molecule is denoted by Σ and the average number of chains per unit area by $\sigma = 1/\Sigma$. The surface density can also be characterized by the reduced surface coverage which is defined as

$$\sigma^* = \pi R_g^2/\Sigma = \sigma \pi R_g^2 \,, \tag{1.4}$$

where R_g is the free polymer radius of gyration. The behavior of the system depends on the reduced surface coverage. To illustrate this we consider the two limits as shown in Figure 1.4. For $\sigma^* \ll 1$ the average distance d between polymer chains is greater than R_g and the polymers are isolated from each other. The layer is laterally inhomogeneous and its thickness, h, is independent of the surface concentration and given by

$$h \propto Z^{\nu} \sigma^0 \tag{1.5}$$

where Z is the degree of polymerization of the dangling block and $\nu \simeq 3/5$ in good solvent. This is called the *mushroom* regime. In the limit $\sigma^* \gg 1$, the average distance between polymer end-tethering points is much smaller than R_g. In this limit the dangling chains are stretched into the solvent and the layer is laterally homogeneous except at the surface and the tip. This is often referred to as the *brush* regime.

Analytical theories have been developed for highly stretched brushes. Alexander and de Gennes (AdG) [12, 13] used the concept of "blobs" along with scaling argu-

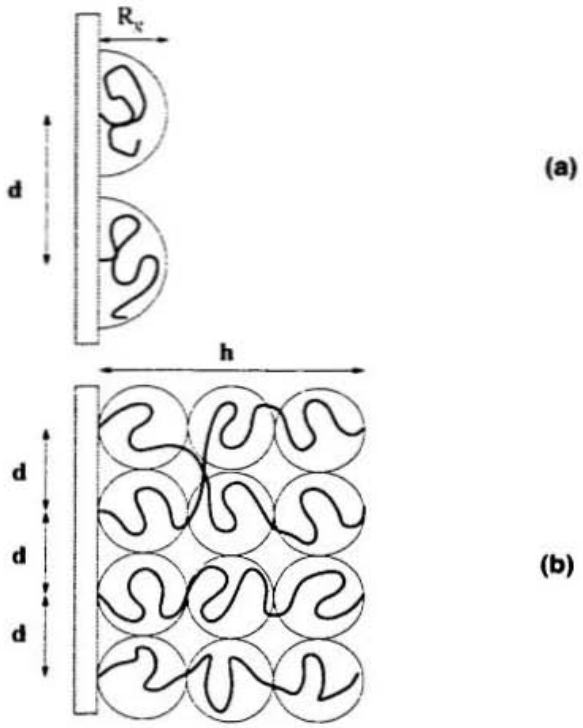

Figure 1.4: Polymer chains end-tethered by one end to a surface: a) $\sigma^* \ll 1$ and b) $\sigma^* \gg 1$. The layer thickness is h. The average distance between polymer chains is d.

ments to obtain the layer height. Milner, Witten and Cates (MWC) [14] developed an analytic self-consistent field (SCF) theory of the end-tethered layer. Both the SCF and scaling theories predicted that, in the *asymptotic* brush limit of large Z and at high surface coverage, the layer height scales as

$$h \propto Z\sigma^{1/3}. \tag{1.6}$$

The scaling and analytical SCF theories have been successful in describing highly stretched end-tethered polymers. On the other hand, Kent *et al.* [69] remark that, in all cases except studies by Auroy *et al.* [66, 67] where the layers are formed from semi-dilute and concentrated solutions, the reduced surface coverage is limited to

$\sigma^* \lesssim 15$. As a result, the experiments may not fall in the asymptotic limit. Results from the experiments were corroborated with numerical self-consistent field (NSCF) studies of Baranowski and Whitmore [46]. The experimental and theoretical results imply that these systems do not correspond to the asymptotic limit for this usual range of $\sigma^* \lesssim 15$.

In the present study, the primary interests are in detailed comparisons among analytic SCF theories, NSCF calculations, MC simulations and experimental results. The experiments imply that the polymers are not as highly stretched as assumed in the asymptotic theories and that NSCF calculations may be more appropriate. The NSCF calculations do not incorporate density fluctuations or lateral inhomogeneities which must occur at the tip of the layer for all σ^*, and throughout the layer for low σ^*. MC simulations are therefore performed in conjunction with NSCF calculations to quantify a range of reduced surface concentrations were the NSCF approach is valid.

1.6 Thin Films

As discussed in the previous Section, there is considerable interest in the theoretical and experimental study of polymers at surfaces. Polymers at surfaces can alter the surface properties by changing the interfacial tension, and sometimes the systems can be tailored to obtain desired results. In the case of uniform thin films of liquid ($\sim$ 300 nm thick) the films will tend to dewet over a period of time. When the

liquid is dominated by van der Waals interactions there are two important parameters: (1) the Hamaker constant, A, which describes long range interactions and to a first approximation is controlled by the polarizability of the three phases, and (2) the spreading coefficient, S, which is a measure of short range surface interactions. The free energy, U, per unit area of a liquid film of thickness h_0 due to the van der Waals interactions is [73]

$$U(h_0) = -\frac{A}{12\pi h_0^2}. \tag{1.7}$$

When A is positive, the van der Waals interactions tend to thin the film. The spreading coefficient is defined as

$$S = \gamma_{sv} - (\gamma_{sl} + \gamma_{lv}) \tag{1.8}$$

where γ_{sv}, γ_{sl} and γ_{lv} are the solid-vapor, solid-liquid and liquid-vapor surface tensions, respectively. If S is negative the liquid does not wet the surface. The case where A is positive and S is negative is classified as *partial wetting*. In this case the films are unstable. Holes begin to form due to thermal fluctuations and the films eventually break up into droplets [5].

In thin films applications it is generally preferred that the films be stable against dewetting in order to keep the films at a uniform thickness. The presence of end-tethered or free polymer can strongly alter the properties of the system. It has been remarked in experimental studies [5], that an end-tethered layer or free polymer alone cannot be used to stabilize the films and a combination of both is required to make the films stable for extended periods of time. Furthermore, there is a minimum bulk

volume fraction of free polymer required. The threshold concentration is approximately five times the overlap concentration of the free polymer which, in turn, is dependent on the degree of polymerization of the free polymer. These experiments suggest that the key elements in understanding the stabilization of these systems are: (1) the coupling between the free and end-tethered polymers as a function of the degree of polymerization of the polymers, the grafting density and the volume fraction of free polymer, and (2) the effect of the overlap concentration.

Scaling [13] and analytical SCF [16, 17, 74] theories have been developed for the study of thin films. The analyses were restricted to $Z_F \lesssim Z_A$ where Z_F and Z_A are the degrees of polymerization of the free and end-tethered chains, respectively. In the case where $Z_F > Z_A$, the partial penetration of long free chains was assumed negligible [29]. For $Z_F \lesssim Z_A$, three major regimes were identified. In the first regime, the surface coverage is high, the end-tethered polymers are highly stretched, the penetration of free chains is negligible and the layer height is not affected by the free polymer. In the second regime, the overall volume fraction of free chains is large enough so that the end-tethered layer is affected by the presence of the free chains but the surface coverage is high enough to prevent penetration of free chains in the end-tethered layer. In the third regime, the surface coverage is low enough to allow the free chains to completely envelop the end-tethered layer.

Penetration of relatively high molecular weight free homopolymer in the end-tethered layer has been observed in recent experiments [2] at commonly observed

end-tethering densities ($\sigma^* \lesssim 15$). This observation suggests that corrections to the asymptotic brush limit may be important and that the penetration of the free chains should be investigated for end-tethering densities which are more closely related to experiment. A NSCF approach is appropriate to deal with finite molecular weight corrections expected for this range of reduced surface concentrations except that, again, lateral inhomogeneities in the planes parallel to the end-tethering surface at low concentrations impose a restriction on the applicability of the NSCF approach. In this thesis, a Monte Carlo study is done in order to obtain a range of reduced surface concentrations over which the NSCF approach is valid. The volume fraction profiles, layer heights and interpenetration of chains at the interface are investigated, and a comparison with NSCF theory for various molecular weights and surface coverages is done to quantify the range of applicability of the NSCF theory. The NSCF approach is also used to make direct comparisons with the experimental work of Kent *et al.*, and with power laws predicted by scaling and SCF theories for the degree of penetration of the end-tethered and free chains. In particular, the height of the end-tethered layer and the overlap between the free and end-tethered polymers are investigated for the three major regimes predicted by scaling and SCF theories.

Chapter 2

Monte Carlo Simulations

2.1 Introductory Remarks

The general formalism for Monte Carlo simulations is reviewed in this section, and the simulations specific to polymer/solvent systems will be discussed in the following sections.

In statistical physics, a problem of interest is the calculation of thermal averages in the canonical ensemble. They are given by

$$< A >_T = \frac{1}{\mathcal{Z}} \int d\{x\} A(\{x\}) \exp[-\beta \mathcal{H}(\{x\})] \tag{2.1}$$

where $\{x\}$ is a vector describing a state in phase space, $A(\{x\})$ is a local operator, $\mathcal{H}(\{x\})$ is the Hamiltonian, $\beta = 1/k_B T$ where k_B is Boltzmann's constant, and $\mathcal{Z}$ is given by

$$\mathcal{Z} = \int d\{x\} \exp[-\beta \mathcal{H}(\{x\})]. \tag{2.2}$$

If one or more of the x's in $\{x\}$ is discrete, the integration in Equation (2.1) is replaced

by the appropriate sum.

In practice. it is not always possible to evaluate thermal averages by the means shown in Equation (2.1). An alternative is to evaluate them numerically by means of Monte Carlo simulations. In the MC simulations a finite subset of phase space is sampled. and the appropriate averages are then evaluated. There are two major methods of sampling. The first method is called "simple sampling" in which case. M states are sampled with equal probability ($P = 1/M$). The averages are then calculated with the appropriate statistical weight $P_{eq}\{x\}$ where

$$P_{eq}\{x\} = \frac{1}{\mathcal{Z}} \exp[-\beta \mathcal{H}(\{x\})]. \tag{2.3}$$

This is called the normalized Boltzmann factor. This method can be very inefficient if most of the states do not contribute significantly to the integrand in Equation (2.1). A more efficient technique is called "importance sampling". In this approach. the states are chosen with a statistical weight proportional to the normalized Boltzmann factor so that most of the states that are sampled from the finite phase space are those which contribute significantly to the integrand in Equation (2.1). Thermal averages are then approximated by

$$< A >_T \approx \frac{1}{M} \sum_{\nu=1}^{M} A(\{x\}_\nu) \tag{2.4}$$

where M is the number of states sampled. The accuracy of the result depends on the number of points sampled and also on the finite size of the system. The accuracy can be increased by sampling more points and increasing the size of the system. Limited

computing resources may not allow calculations on systems which are large enough to eliminate the finite size effects: in this case the results can be extrapolated by means of finite size scaling techniques [75, 76].

Metropolis *et al.* [77] advanced the concept of importance sampling and suggested that a set of states $\{x\}_\nu$ can be generated by choosing states by means of a trajectory in phase space rather than choosing states independently of each other. The result is a Markov process where a state $\{x\}_{\nu+1}$ is constructed from the previous state $\{x\}_\nu$ via a suitable transition probability $W(\{x\}_\nu \to \{x\}_{\nu+1})$. A restriction on the transition probability W must be imposed such that in the limit $M \to \infty$ the probability distribution function of the states generated by the process tends towards the equilibrium distribution function defined in Equation (2.3). To achieve this condition the principle of detailed balance is imposed with

$$P_{eq}(\{x\}_\nu)W(\{x\}_\nu \to \{x\}_{\nu'}) = P_{eq}(\{x\}_{\nu'})W(\{x\}_{\nu'} \to \{x\}_\nu) \tag{2.5}$$

where any state $\{x\}_{\nu'}$ is obtained from any other state $\{x\}_\nu$ by a finite series of steps in phase space. Although the principle of detailed balance does not uniquely specify $W(\{x\}_\nu \to \{x\}_{\nu'})$ a suitable condition which satisfies Equation (2.5) is

$$W(\{x\}_\nu \to \{x\}_{\nu'}) = \begin{cases} 1 & \text{if } \Delta\mathcal{H} \geq 0 \\ \exp(-\beta\Delta\mathcal{H}) & \text{if } \Delta\mathcal{H} < 0 \end{cases} \tag{2.6}$$

where $\Delta\mathcal{H} = \mathcal{H}(\{x\}_{\nu'}) - \mathcal{H}(\{x\}_\nu)$. Having defined a transition probability, a general algorithm for Monte Carlo simulations can be constructed as follows:

1. Choose a new state $\{x\}_{\nu+1}$ from the state $\{x\}_\nu$.

2. Calculate the change in energy, $\Delta\mathcal{H}$, in the transition from the state $\{x\}_\nu$ to the state $\{x\}_{\nu+1}$.

3. Generate a random number r such that $r \epsilon [0, 1)$.

4. If $r \leq W(\{x\}_\nu \rightarrow \{x\}_{\nu'})$ then the new state is accepted; otherwise it is rejected and the old state is counted anew. This step is known as the *Metropolis* rule.

5. Repeat steps 1 to 4 many times.

The method used to generate new states depends on the model being used, and for the work here, the method is described for polymer/solvent systems in the following sections. We also define time in MC simulations in units of the number of attempts at generating new states.

The Markov process provides a means of generating new states efficiently, but the states can be correlated. In general $\{x\}_\nu$ and $\{x\}_{\nu+1}$ are highly correlated and n MC steps are required before the two states $\{x\}_\nu$ and $\{x\}_{\nu+n}$ are no longer correlated. In order to generate M uncorrelated states, a time nM is required. In practice, the initial state of a system may be far from equilibrium and a number, n_0, of MC steps are required before a system reaches an equilibrium state. Therefore, n_0 MC steps are required before generated states can be used in statistical averaging. In principle all subsequent states can be used for statistical averaging. However in practice, for computational efficiency, there are δt MC steps in between states which are used in the statistical averages. For computational efficiency an appropriate choice of n_0, n

and δt is required but in general, n_0, n and δt are not known *a priori*. This problem is resolved by monitoring various relaxation functions which determine the appropriate time scales. We define the normalized relaxation function of a quantity A as

$$o_A(t) = \frac{< A(0)A(t) > - < A >^2}{< A^2 > - < A >^2}. \tag{2.7}$$

The relaxation time associated with the quantity A is defined as

$$\tau_A = \int_0^\infty o_A(t)dt. \tag{2.8}$$

Several relaxation times can be calculated corresponding to various properties, and the maximum relaxation time (τ_{max}) determines the minimum number of MC steps n between uncorrelated states. Generally $n_0 \approx 20\tau_{max}$ is a sufficient number of MC iterations for equilibrium statistics. The calculation of the relaxation times also provides a means of calculating the statistical error in the averaged quantities. The expectation value of the square of the statistical error is given by [78]

$$< (\delta A)^2 >= \frac{1}{M}[< A^2 > - < A >^2](1 + 2\frac{\tau_A}{\delta t}). \tag{2.9}$$

The correction term $2\tau_A/\delta t$ accounts for correlations between states. If $\delta t \gg \tau_A$, then the correction term is negligible and the standard formula in the square of the statistical error for uncorrelated states is recovered. In the opposite case where $\delta t \ll \tau_A$, we find

$$< (\delta A)^2 >\approx \frac{2\tau_A}{M\delta t}[< A^2 > - < A >^2] = 2\frac{\tau_A}{\tau_{obs}}[< A^2 > - < A >^2] \tag{2.10}$$

where $\tau_{obs} = M\delta t$. Both limits indicate that the important criterion in minimizing the statistical error is $\tau_{obs} \gg \tau_{max}$, where τ_{obs} is the observation time.

The techniques described above provide a general algorithm for MC simulations in the canonical ensemble and a means of determining the time required to reach equilibrium (n_0) and the appropriate duration of the simulation (τ_{obs}). The more specific MC algorithm for polymer/solvent systems is described in the following sections.

2.2 Monte Carlo Simulations of Polymers

In this section, the Monte Carlo simulations of polymer/solvent systems are discussed. The formalism and general approach presented here are applied to all four polymeric systems, with slight variations from one system to another. A general description of the simulations is therefore given here and specific details concerning individual systems will be discussed in the following chapters. More specific details of the simulations are also given in Appendix A.

In this thesis, the polymers are represented on a three dimensional lattice. Each effective monomer of the polymer chains occupies a lattice site of a simple cubic lattice and the empty sites correspond to solvent (S). The systems have volume $V = L_x \times L_y \times L_z$ where L_i is the length of the system in the direction i. In general, periodic boundary conditions are applied in all directions except for cases where confined geometries are required. The linear dimensions are chosen to accommodate all the polymers with the condition that the size of the system is large enough so

that finite size effects are negligible. In all systems, $L_i > Z_j$ where $i = x, y, z$ and Z_j corresponds to the polymer with the largest number of effective monomers in the system, and usually $L_i \gg Z_j$. The polymer/solvent systems may contain A-b-B copolymer (C) with the A and B blocks denoted by CA and CB, respectively. Free homopolymer in solution, denoted by HB or F, and end-tethered homopolymer (A) can also be present in the systems. The combination of types of polymers is dependent on the system studied.

Each effective monomer is subject to an excluded volume interaction where only one effective monomer is allowed to occupy a lattice site. Generally, the energies E_{ij} , with $(i, j = A, B, F, S)$, are associated with nearest neighbor contacts for each species in the system. The reduced interaction energies are given by $\epsilon_{ij} = E_{ij}/k_BT$, where k_B is Boltzmann's constant and T is the temperature.

The general algorithm described in Section 2.1 is used to generate new states with new configurations being generated via a combination of four types of motions: reptation, kink-jump (including end-flip), crankshaft and Brownian motion [79–82]. They are illustrated in Figure 2.1. In Figure 2.1(a) the polymer moves via reptation: One of the end monomers jumps to a nearest neighbor site and each remaining effective monomer jumps to the site occupied by its preceding neighbor along the chain. In Figure 2.1(b), one of the effective monomers from within the polymer moves to another site by a flip of the two bonds connecting the effective monomer. The bond of an end monomer can also flip to change the position of the effective end monomer. In

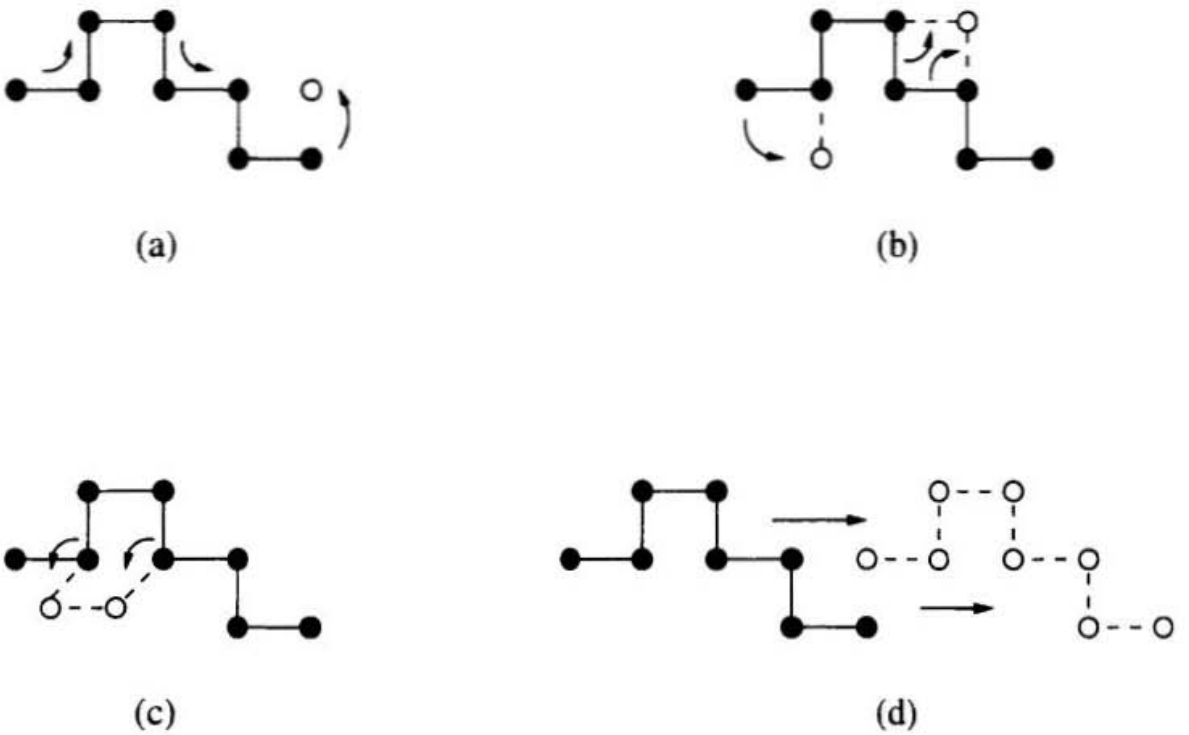

Figure 2.1: Various elementary MC moves: (a) reptation. (b) kink-jump (including end-flip). (c) crankshaft and (d) Brownian motion.

crankshaft motion, as shown in Figure 2.1(c). two nearest neighbor effective monomers along the polymer chain move such that the two bonds connecting them to the rest of the polymer. rotate through an angle of $\pm 90°$. Figure 2.1(d) shows Brownian motion. by which the entire polymer is translated. The polymer is allowed to translate a distance which is larger than one lattice spacing but limited by a sphere centered about one of the effective monomers.

At the beginning of each simulation. the interaction energies ϵ_{ij} are set to zero and the simulation is run for a period of 10.000 N-bead cycles where one N-bead cycle corresponds to N Monte Carlo attempts with N being the total number of effective

monomers in the system ($N = \sum_{i=1}^{P} Z_i N_i$). The summation is over all species of polymers in the system. Z_i is the number of repeat units of the polymers of type i and N_i is the number of polymers of species i in the system.

In order to evaluate the relaxation time of the systems, τ_{max}, several relaxation times are calculated for the different types of polymers in the system. At each interaction energy ϵ_{ij}, the system is then allowed to reach equilibrium by iterating for a period of 20−100 system relaxation times. At this point all calculated quantities have reached a limit and the system is assumed to be at equilibrium. Ensemble averages are taken over a minimum period of 40−200 relaxation times. If required, once the ensemble averages are done the interaction energies are increased in small increments. This process is repeated until the maximum interaction energies of interest are reached or the relaxation times no longer permit the simulation to progress. The times required for equilibrium and ensemble averages vary and will be discussed in further detail in the following chapters. In Section 2.2.1, the calculation of relaxation times for systems with free polymers in solution is described, and Section 2.2.2 gives a description of simulations with end-tethered polymers.

2.2.1 Free Polymers

In MC simulations with free polymers, local conformations of the chains must be allowed to relax. Also, the polymers must move around in the lattice and interact with other polymers. In order to determine the relevant time scales of the system,

relaxation times are extracted from the relaxation functions defined in Equation (2.7). In practice, different times scales are determined from various autocorrelation times which are extracted from autocorrelation functions. We define an end-to-end vector autocorrelation function by

$$C_X(t) = \frac{< \vec{X}(t) \cdot \vec{X}(0) > - < \vec{X}(t) > \cdot < \vec{X}(0) >}{< \vec{X}(0)^2 > - < \vec{X}(0) >^2} . \tag{2.11}$$

where $\vec{X}$ corresponds to the polymer end-to-end vectors $\vec{R}_C$, $\vec{R}_{CB}$, $\vec{R}_{CA}$ and $\vec{R}_{HB}$, of the copolymer, B block, A block and B homopolymer, respectively. The symbols $< ... >$ refer to an average over time and polymers.

In systems with free polymers, aggregates may form and it is important to allow time for the polymers to escape and migrate from one aggregate to another. We define an "aggregate" as having 2 or more polymers which are in contact with each other. We specify "small aggregates" as having 2 or more, but less than 10, polymers. "Micelles" have 10 or more polymers and a size of the order of the molecular dimensions whereas "large aggregates" are defined as macro structures with a large number (typically more than 100) of polymers. Reasons for these choices will be clear in Chapters 4 and 5. To monitor relevant times scales associated with the polymers in aggregates we have defined chain extraction and chain exchange autocorrelation functions for the copolymer and the homopolymer which are given by [83]

$$C_f(t) = \frac{< f(t)f(0) >}{< f(0)^2 >} . \tag{2.12}$$

For the chain extraction autocorrelation function, $f(t) = 1$ if the polymer was origi-

nally in an aggregate at time $t = 0$ and has not escaped the aggregate at time t, and zero otherwise. For the exchange autocorrelation function, $f(t) = 1$ if the polymer was originally in an aggregate at time $t = 0$ and has not migrated to another aggregate at time t, and zero otherwise. The polymers can exchange between aggregates via single chain or multiple chain exchange. Multiple chain exchange occurs when the aggregates split to form smaller aggregates, or different aggregates merge to form larger aggregates. For example, when one micelle breaks into two smaller micelles, one of the two micelles is identified as the original micelle by comparing the center of mass (CM) of each micelle with the CM of the original micelle. The micelle with the CM which is farther from the CM of the original micelle is identified as the new micelle and all its polymers have exchanged. The converse applies for two micelles that merge.

We also define weighted chain extraction and exchange autocorrelation functions where

$$C_g(t) = \frac{< g(t)g(0) >}{< g(0)^2 >} . \tag{2.13}$$

In this case a greater weight is given to polymers in larger aggregates. For the weighted chain extraction autocorrelation function, if a polymer was originally in an aggregate with N_M polymers at time $t = 0$ and has not escaped at time t, then $g(t) = N_M$; $g(t) = 0$ otherwise. Similarly, for the weighted chain exchange autocorrelation function, $g(t) = N_M$ corresponds to the case where the polymer was originally in an aggregate at time $t = 0$ and has not migrated to another aggregate at time t, and

$g(t) = 0$ otherwise.

Each autocorrelation function is monitored and, in practice, the autocorrelation times τ_i are evaluated using [62]

$$\tau_i = \frac{\int_0^{t_i} C_i(t)dt}{1 - C_i(t_i)}. \tag{2.14}$$

where t_i is defined such that $C_i(t_i) = 1/e$ (*i.e.* $t_i \simeq \tau_i$) and $i = s, f$.

Heterogeneity in these systems can affect the autocorrelation functions defined above. In addition, there can be at least two mechanisms for each autocorrelation function. For example, Haliloğlu *et al.* [84] have suggested that there are mainly two types of mechanisms for the exchange dynamics of copolymers in micelles. The first mechanism was referred to as insertion/expulsion (I/E) by which single chains escape micelles and move to other micelles. The second mechanism, which is referred to as merger/splitting (M/S), occurs when the copolymers exchange when micelle cores come into contact (merger) or when a micelle core splits to form more than one micelle (splitting). Our calculation of the autocorrelation functions does not discriminate between different mechanisms, but incorporates them by averaging over all polymers in the system. This implies that the functions can be expressed as a sum of exponentials or stretched exponentials [85–87].

It is also important to allow time for the polymers to move throughout the system. The motion of the copolymers and B homopolymers is monitored by calculating diffusion constants D_C and D_{HB}, respectively. The diffusion constants are approximated

by

$$D_j = \frac{< d_j^2(t) >}{6t} \ . \tag{2.15}$$

where $\vec{d}_j(t) = \vec{r}_j(t) - \vec{r}_j(0)$ is the displacement at time t of the center of mass of a polymer of type j (copolymer $j = C$ or homopolymer $j = HB$) from its initial position. The time, t, at which the diffusion constant is evaluated corresponds to approximately twice the maximum autocorrelation time defined by Equation (2.14) for all the quantities defined previously. A relevant time scale associated with the time required for a free polymer to travel the average distance between nearest neighbor free polymers $\bar{r}_j$ in the system is defined by

$$\tau_{D_j} = \frac{\bar{r}_j^2}{6D} \ . \tag{2.16}$$

with

$$\bar{r}_j = \left(\frac{6V}{\pi N_j} \right)^{\frac{1}{3}} \ . \tag{2.17}$$

The relaxation time of the system is taken as the maximum of all calculated times.

2.2.2 End-tethered Polymers

In this section, the procedure for performing Monte Carlo simulations with end-tethered polymers is described. The simulations are once again performed on a cubic lattice, but impermeable walls are placed at $z = 1$ and $z = L_z$. These systems must be treated differently due to the constraints in the geometry of the system and the mobility of the end-tethered polymers.

For this type of simulations we define the following autocorrelation functions [58, 62]:

$$C_Y(t) = \frac{< Y(t)Y(0) > - < Y(t) >< Y(0) >}{< Y(0)^2 > - < Y(0) >^2} , \tag{2.18}$$

where the variable Y correspond to the quantities R_z, R_g, $R_{g\perp}$ and R_{gz}. The z-component of the end-to-end vector is R_z and the radius of gyration is denoted by R_g. The quantities $R_{g\perp}$ and R_{gz} are related to the radius of gyration with respect to the directions perpendicular and parallel to the normal to the surface, respectively. They are defined as

$$R_{g\perp}^2 = \frac{1}{Z}\sum_{i=1}^{Z}\{(x_i - x_{c.m.})^2 + (y_i - y_{c.m.})^2\} . \tag{2.19}$$

$$R_{gz}^2 = \frac{1}{Z}\sum_{i=1}^{Z}(z_i - z_{c.m.})^2 \tag{2.20}$$

and

$$R_g^2 = R_{g\perp}^2 + R_{gz}^2 . \tag{2.21}$$

The autocorrelation times are calculated from Equation (2.14). Simulations with end-tethered polymers may also contain free polymers F in the system as in the case of thin films. A diffusion constant D_F and its associated time τ_{D_F} are therefore calculated with

$$D_F = \frac{< d_F^2(t) >}{4t} , \tag{2.22}$$

where $\vec{d}_F(t)$ is the displacement, at time t, of the center of mass of a free polymer from its initial position calculated from the x and y components only. The time τ_{D_F}

is given by

$$\tau_{D_F} = \frac{\overline{r}_F^2}{4D_F} \,. \tag{2.23}$$

where $\overline{r}_F^2$ is given by Equation (2.17).

The end-to-end vector autocorrelation function described by Equation (2.11) is applied to the free polymers. Once again the relaxation time of the system is taken as the maximum of all defined time scales.

Chapter 3

Mean Field Theory

3.1 Introductory Remarks

In this chapter the mean field theories used to study the polymers in solution are discussed. In the case of crew-cut micelles, simple mean field theory is used to study the characteristics of the micelles. For the swollen micelle case, the simple mean field theory of micelles, which has been extended to the case of swollen micelles elsewhere [32], is reviewed. For the end-tethered layers and thin films, the NSCF formalism of Whitmore *et al.* [46, 88, 89] is discussed and applied to these systems.

3.2 Micelles

3.2.1 General Case

In the study of crew-cut micelles, the systems consist of copolymer in a host which can be homopolymer or solvent. In this thesis the host is solvent, but the theory is

developed for both homopolymer and solvent. The host is denoted by S and the only differences in the expressions arise in the degree of polymerization of the host which is $Z_S = 1$ for solvent and, generally, $Z_S \gg 1$ for a homopolymer host. The simple mean field theory of micelles involves calculating contributions to the free energy and minimizing the free energy with respect to the characteristic structure of the micelles and the system in general.

In this theory, the micelles are modeled as shown in Figure 3.1. Region (1) consists of the core of the micelle which is comprised of the B block of the copolymer and some solvent. Region (2) is the corona of the micelle and is composed of the A block of the copolymer and the solvent. The volume fraction profiles throughout the core and corona are assumed to be uniform. Region (3) consists mainly of the solvent with small amounts of A-b-B diblock copolymers. The radius of the core is denoted by l_B, and l_A describes the thickness of the corona. The overall volume fractions of copolymer and solvent are denoted by ϕ_C^0 and ϕ_S^0, respectively.

The overall volume fraction for each component of copolymer is given by

$$\phi_{c\kappa}^0 = f_\kappa \phi_C^0, \tag{3.1}$$

for $\kappa = A, B$, where f_κ is given by

$$f_\kappa = \frac{Z_{c\kappa}\rho_{0C}}{Z_C \rho_{0\kappa}}, \tag{3.2}$$

with ρ_{0C} and $\rho_{0\kappa}$ defined as the density of pure copolymer and pure component κ, respectively. The overall volume fraction of copolymer can be expressed in terms of

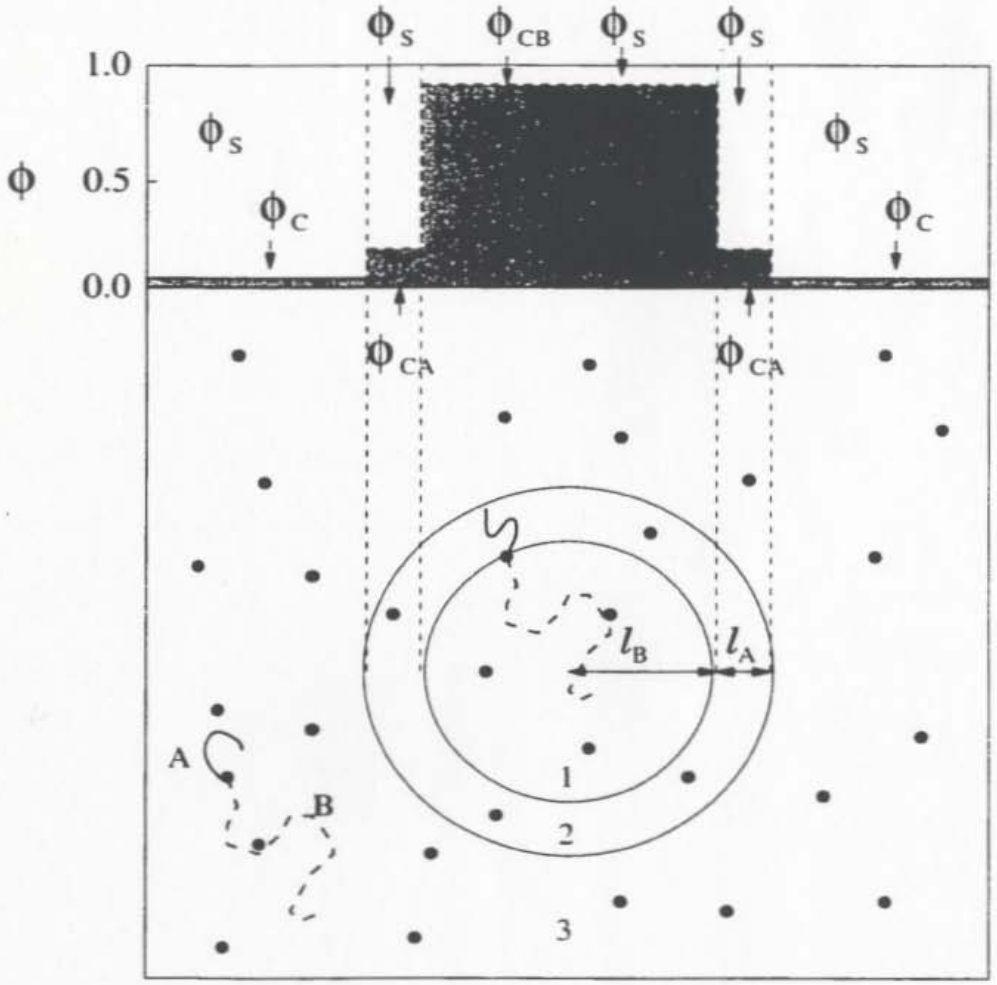

Figure 3.1: Structure of the crew-cut micelles. Region (1) is the core of the micelle and contains the B block and some solvent. Region (2) consists of the corona with the presence of the A block and solvent and Region (3) is mainly comprised of solvent with small amounts of copolymer in solution.

the overall volume fractions of the A and B blocks as $\phi_C^0 = \phi_{CA}^0 + \phi_{CB}^0$, and from Equations (3.1) and (3.2) the density of pure copolymer is given by

$$\rho_{0C} = Z_C \left\{ \frac{Z_{CA}}{\rho_{0A}} + \frac{Z_{CB}}{\rho_{0B}} \right\}^{-1} . \tag{3.3}$$

The incompressibility condition holds in the three separate regions with

$$\begin{aligned} o_{CB}^{(1)} + o_S^{(1)} &= 1. \\ o_{CA}^{(2)} + o_S^{(2)} &= 1. \\ o_C^{(3)} + o_S^{(3)} &= 1. \end{aligned} \tag{3.4}$$

where $o_\kappa^{(i)}$ is the local volume fraction of component κ in region i.

The free energy of the system with micelles (G_M) is calculated with respect to the free energy in a homogeneous system (G_H) where all the polymers are in solution. The free energy per unit volume is given in units of $k_B T \rho_0$ where ρ_0 is the reference density. The free energy per unit volume is then given by

$$\Delta g = \frac{G_M - G_H}{k_B T \rho_0 V} \tag{3.5}$$

where V is the total volume.

The free energy, which has been calculated previously [21,22], is approximated by the sum of six terms. These contributions are an enthalpic contribution, two terms from the entropy of mixing of the solvent and the localization of the A-b-B block copolymer joints at the core-corona interface, a contribution from the stretching of the copolymers in micelles, one due to the translational entropy of the micelles, and one from the interfacial tension arising from the core-corona interface.

The largest contribution to the free energy is the change in interaction energy due to the reduced number of energetically unfavorable contacts in the micellar phase. It

is given by

$$
\begin{aligned}
g_{int} &= -\chi_{AB} f_A f_B (\phi_C^0)^2 [1 - (F_3^C)^2 / G_3^V] \\
&\quad -\chi_{AS} f_A \phi_C^0 \phi_S^0 [1 - F_2^S F_M^C / G_2^V - F_3^S F_3^C / G_3^V] \\
&\quad -\chi_{BS} f_B \phi_C^0 \phi_S^0 [1 - F_1^S F_M^C / G_1^V - F_3^S F_3^C / G_3^V].
\end{aligned} \tag{3.6}
$$

where χ_{kl} is the Flory interaction parameter between two species k and l. F_M^C is the fraction of copolymer in micelles. $F_3^C = 1 - F_M^C$. F_i^S is the fraction of solvent molecules present in region i and G_i^V is the fraction of the total volume occupied by region i. It is given by

$$
\begin{aligned}
G_1^V &= (l_B/R)^3. \\
G_2^V &= ((l_A + l_B)/R)^3 - G_1^V. \\
G_3^V &= 1 - (G_1^V + G_2^V).
\end{aligned} \tag{3.7}
$$

where R is the radius of a sphere which, on average, contains one micelle. There is an interfacial tension denoted by γ at the core-corona boundary. The corresponding contribution to the free energy is given by

$$
g_I = \frac{\gamma}{\rho_0 k_B T} \frac{3 l_B^2}{R^3} . \tag{3.8}
$$

The expression for γ has been derived earlier [20] and is given in Appendix B. The expression for γ derived in Appendix B assumes linear density profiles of the polymer at the interface. We also derived an analytical expression for γ using parabolic density profiles, but the differences in results obtained using the two expressions are less than

1%. For convenience, we therefore use the more simple expression derived for linear density profiles.

In the micellar phase the solvent molecules are partially excluded from regions (1) and (2). Also, the copolymer molecules which are in micelles are assumed to have joints localized at the core-corona interface. The remaining copolymers in solution are confined to region (3). The free energy contributions are therefore given by

$$g_S = \frac{\rho_{0S}}{\rho_0}\frac{\phi_S^0}{Z_S}\{F_1^S \ln(F_1^S/G_1^V) + F_2^S \ln(F_2^S/G_2^V) + F_3^S \ln(F_3^S/G_3^V)\} \tag{3.9}$$

and

$$g_J = \frac{\rho_{0C}}{\rho_0}\frac{\phi_C^0}{Z_C}\left\{F_M^C \ln\left(\frac{F_M^C R^3}{3l_B^2 d}\right) + F_3^C \ln\left(F_3^c/G_3^V\right)\right\} \tag{3.10}$$

for the solvent and copolymer, respectively.

The block copolymers in the micelles are stretched. This results in a reduction in the entropy. This contribution to the free energy is called the elastic free energy and is given by the Flory expression

$$g_{el} = \frac{\rho_{0C}}{\rho_0}\frac{\phi_C^0}{Z_C}\frac{F_M^C}{2}\left\{\alpha_B^2 + \frac{2}{\alpha_B} + \alpha_A^2 + \frac{2}{\alpha_A} - 6\right\}. \tag{3.11}$$

where

$$\alpha_A = (3/Z_{CA})^{1/2} l_A/b_A \tag{3.12}$$

and

$$\alpha_B = (3/Z_{CB})^{1/2} l_B/b_B \tag{3.13}$$

are the stretching of blocks A and B respectively. When $\alpha_i = 1$, the polymer corresponds to an unstretched Gaussian chain as discussed in Chapter 1.

The final contribution to the free energy comes from the translational entropy of the micelles, which is given by

$$g_{tr} = \frac{\rho_{0C}}{\rho_0}\frac{o_C^0}{N_M Z_C} F_M^C \{\ln(G_1^V + G_2^V) + G_3^V/(G_1^V + G_2^V)\ln G_3^V\}. \qquad (3.14)$$

where N_M is the number of copolymer molecules per micelle. This term is small and does not affect the structure of the micelles.

In earlier work [21,22], these expressions were combined to give Δg as a function of four independent parameters which were calculated by minimizing the free energy with respect to them. However, there were no conditions imposed on the chemical potentials in each region. In this thesis, we extend the model to impose the additional constraint of equal chemical potential of the solvent in regions (1) and (3). In the mean field theory, the solvent chemical potential in region i is given by [90]

$$\mu_S^{(i)} = \mu_{0S} + 1 - o_S^{(i)} + \log(o_S^{(i)}) - \frac{1}{2}\sum_{j,j'} \chi_{jj'} o_j^{(i)} o_{j'}^{(i)}. \qquad (3.15)$$

where μ_{0S} is the chemical potential of pure solvent. Requiring $\mu_S^{(1)} = \mu_S^{(3)}$ reduces the number of independent parameters to three, which can be chosen to be l_B, G_2^V and F_M^C. These three independent variables are determined from the minimization of the free energy subject to the constraint of equal chemical potentials in regions (1) and (3). This minimization is done numerically.

3.2.2 Strong Segregation limit

In strongly segregated systems with highly selective solvent, an approximate solution for l_B can be obtained analytically. For simplicity we consider the case that $b_A = b_B = b$ and $\rho_{0A} = \rho_{0B}$, which results in $f_\kappa = Z_{C\kappa}/Z_C$. We set the Flory interaction parameters to be $\chi = \chi_{AB} = \chi_{BS}$, and make the solvent the same species as the A block of copolymer, so that $\chi_{AS} = 0$ and $\rho_{0S} = \rho_{0A}$. To a good approximation, the solvent is excluded from the cores for strongly segregated systems and we may set $o_{CB}^{(1)} = 1$ and $F_1^S = 0$. The incompressibility condition in Equation (3.4) then gives $G_1^V = f_B F_M^C \phi_C^0$. The interaction energy term is then

$$\begin{aligned} g_{int} &= -\chi \frac{Z_{CB}}{Z_C} F_M^C \phi_C^0 \left\{ 1 - \frac{Z_{CB}}{Z_C} \left(1 - \frac{(F_3^C)^2}{G_3^V} \right) \frac{\phi_C^0}{F_M^C} \right\} \\ &\simeq -\chi (Z_{CB}/Z_C) F_M^C \phi_C^0. \end{aligned} \tag{3.16}$$

The interfacial tension term in Appendix B is derived for an interface of a ternary mixture of A and B homopolymer and solvent. For this specific system we assumed that $o_{CB}^{(1)} \simeq 1$ and the interfacial tension γ in Equation (B.14), derived in Appendix B, gives

$$\gamma' = \frac{\gamma}{\rho_0 k_B T} = \gamma_0' \sqrt{\frac{1}{2}(2 - o_S^{(2)})(1 - 2\phi_S^{(2)}(\ln 2)/\chi)} \tag{3.17}$$

where γ_0' is the interfacial tension for an A-B homopolymer-homopolymer interface and is given in Equation (B.15). When the matrix is A homopolymer the interface consists of two homopolymers, $\phi_S^{(2)} \to 0$ in Equation (3.17) and $\gamma' \to \gamma_0'$, as expected [91]. In the derivation of the approximate analytical expressions for l_B and the

critical micelle concentration, we make use of the expression given in Equation (3.17) for the interfacial tension and assume that $\phi_S^{(2)}$ in the corona is independent of Z_{CB}.

Similarly, the width of the interface derived in Equation (B.12) of Appendix B reduces to

$$d = d_0 \sqrt{\frac{2 - \phi_S^{(2)}}{2(1 - 2\phi_S^{(2)}(\ln 2)/\chi)}} \tag{3.18}$$

where d_0 is the width of an A-B homopolymer-homopolymer interface and is given in Equation (B.13). The contribution from the interfacial tension to the free energy in Equation (3.8) is then

$$g_I = 3\frac{Z_{CB}}{Z_C}\phi_C^0 \frac{\gamma'}{l_B}. \tag{3.19}$$

The term arising from the localization of the copolymer joints to the interface is approximated by neglecting the $F_3^C \ln F_3^C$ term, which results in

$$g_J \simeq \frac{\phi_C^0 F_M^C}{Z_C} \ln\left(\frac{Z_C}{3Z_{CB}\phi_C^0}\frac{l_B}{d}\right). \tag{3.20}$$

In previous derivations [21] of l_B, the matrix was a higher molecular weight homopolymer and the term arising from the localization of the matrix components was neglected. In the case of solvent as the host, we keep this term and the approximation gives

$$g_S \simeq \frac{\phi_C^0 F_M^C}{Z_C}\frac{Z_{CB}}{Z_S}. \tag{3.21}$$

The contribution to the free energy from the translational entropy term is negligible and the change in free energy can be approximated as

$$\Delta g \simeq \frac{\phi_C^0 F_M^C}{Z_C}\left\{-\chi Z_{CB} + 3Z_{CB}\frac{\gamma'}{l_B} + \ln\left(\frac{Z_C}{3Z_{CB}\phi_C^0}\frac{l_B}{d}\right)\right. \tag{3.22}$$

$$+\frac{Z_{CB}}{Z_S}+\frac{1}{2}\left(\alpha_B^2+\frac{2}{\alpha_B}+\alpha_A^2+\frac{2}{\alpha_A}-6\right)\Bigg\}.$$

To obtain the radius of the core l_B the expression in Equation (3.22) is minimized with respect to l_B resulting in

$$l_B \simeq (\gamma')^{1/3}(bZ_{CB})^{2/3}\left\{1+O(1/Z_{CB}^{1/3})\right\}. \tag{3.23}$$

The radius l_B therefore scales as $Z_{CB}^{2/3}$ as long as $\phi_S^{(2)}$ is independent of Z_{CB}, which is nearly the case, and is determined from the competition between the interfacial tension and the free energy associated with the stretching of the core block. Substituting l_B into Equation (3.22) and setting $\Delta g = 0$ gives an approximate expression for the critical micelle concentration:

$$\begin{aligned}\phi_c^{crit} \simeq \tfrac{1}{3}\tfrac{Z_C}{Z_{CB}^{1/3}}\left(\tfrac{\gamma'}{b}\right)^{1/3}\tfrac{b}{d}\ \exp\Bigg\{&\left(\frac{1}{Z_S}-\chi\right)Z_{CB}+3\left(\frac{\gamma'}{b}\right)^{2/3}Z_{CB}^{1/3}\\ &+\frac{1}{2}\left(3\left(\frac{\gamma'}{b}\right)^{2/3}Z_{CB}^{1/3}+\frac{2}{\sqrt{3}}\left(\frac{b}{\gamma'}\right)^{1/3}\frac{1}{Z_{CB}^{1/6}}-3\right)\\ &+\frac{1}{2}\left(\alpha_A^2+\frac{2}{\alpha_A}-3\right)\Bigg\}.\end{aligned} \tag{3.24}$$

This analytical expression can be used to obtain qualitative features of the micelle systems. For a high molecular weight homopolymer host with $Z_{CB} \ll Z_S$, the theory predicts that micelles can form for $\chi > 0$ whereas for a solvent host with $Z_{CB} \gg Z_S$, the expression in Equation (3.24) predicts micelles for $\chi > 1$. This is an approximate result and the CMC is affected by other terms, but the essential features remain. In either case, the CMC is driven by the product of the Flory parameter χ and the degree of polymerization of the B block Z_{CB}.

For the special case of high molecular weight homopolymer with $Z_S \gg Z_{CB}$, $\gamma' \to \gamma'_0$ and $d \to d_0$ in Equations (3.17) and (3.18), respectively, and the expression for the critical micelle concentration in Equation (3.24) simplifies to

$$\begin{aligned} \phi_c^{crit} \simeq 0.30 \frac{\chi Z_C}{(\chi Z_{CB})^{1/3}} \exp\Big\{ & -\chi Z_{CB} + 1.65(\chi Z_{CB})^{1/3} \\ & + \frac{1}{2}\left(1.65(\chi Z_{CB})^{1/3} + \frac{1.56}{(\chi Z_{CB})^{1/6}} - 3\right) \\ & + \frac{1}{2}\left(\alpha_A^2 + \frac{2}{\alpha_A} - 3\right)\Big\} \ . \end{aligned} \tag{3.25}$$

3.3 Swollen Micelles

The simple mean field theory of swollen micelles has been developed earlier [32] and is reviewed in this section to gain some insights about the physics involved in the interplay between the macrophases and microphase. This theory is an extension of the simple mean field theory [21] developed for A-b-B diblock copolymer in A homopolymer or solvent as discussed in the previous section. However, small amounts of B homopolymer are now added to the binary system. There is only one effective Flory interaction parameter χ with $\chi = \chi_{AB} = \chi_{BS}$ and $\chi_{AS} = 0$. For simplicity also, the densities are taken to be $\rho_0 = \rho_{0A} = \rho_{0B} = \rho_{0S}$. For these systems $\phi^0_{CB} \simeq 0.02$ and the total volume fraction of B polymer is $\phi^0_B = \phi^0_{CB} + \phi^0_{HB}$.

Experimentally, these systems are generally strongly segregated and the homopolymers are highly incompatible. Therefore, the model neglects any B homopolymer dispersed in the A homopolymer matrix. Instead, it assumes that a certain fraction,

f, of the B homopolymer is solubilized within the micelle cores, and the remaining fraction, $1 - f$, forms a separate macrophase. The theory is formulated by calculating the free energy of the system as a function of f. The equilibrium fraction f is determined by minimizing the free energy. The matrix component is assumed to be expelled from the core. The fraction of the volume of the entire system which consists of micelle cores is therefore

$$o_{core} = o^0_{CB} + f o^0_{HB} \tag{3.26}$$

and the volume fraction occupied by the separate B homopolymer phase is $(1-f)o^0_{HB}$.

Another restriction is imposed on the degree of polymerization of the B homopolymer such that $Z_{HB} \lesssim Z_{CB}$. In this case, the entropic effects result in solubilized homopolymer being distributed throughout the cores. This is corroborated by experiment [92-95] and theory [96, 97]. In the model, the volume fraction profiles of all components are assumed to be uniform in the core and corona. The B block of copolymer must therefore stretch to the center of the micelles to prevent the homopolymer from accumulating at the center of the micelles. Otherwise, the copolymers would relax, the homopolymers would accumulate at the center of the micelles, and the aggregates would grow without penalty. This would correspond to one of the suggested macrophase-separated systems. The point at which the entropic penalty due to stretching the B block of the copolymer is too large to keep the volume fraction profiles constant provides the basis for a model where two limits are considered: swollen micelles with uniform cores, and macrophase separated B homopolymer.

To obtain an expression for the free energy, we begin with the free energy of a binary system containing A-b-B diblock copolymer in an A matrix, and discuss the effect of including a third component, consisting of B homopolymer, in the system. The expressions simplify because of the assumed limits $F_M^C \to 1$ and $F_1^S \to 0$. The contribution due to the interaction energy in Equation (3.6) reduces to

$$g_{int} \simeq -\chi o_{CB}^0 (o_{CA}^0 + o_S^0) \tag{3.27}$$

which, physically, reflects the absence of A-B or S-B contacts in the segregated system. Contributions from the interfacial tension, localization of the copolymer joints and the elastic free energy are given by Equations (3.19), (3.20) and (3.11), respectively, noting that $o_{CB}^0 = o_C^0 Z_{CB}/Z_C$ in this case. The contribution due to the solvent entropy is obtained from Equation (3.9) assuming that $F_1^S \simeq 0$:

$$g_S \simeq \frac{\rho_{0S}}{\rho_0}\frac{o_S^0}{Z_S}\{F_2^S \ln(F_2^S/G_2^V) + F_3^S \ln(F_3^S/G_3^V)\}. \tag{3.28}$$

The term arising from the translational entropy of the micelle in Equation (3.14) is neglected and the free energy of the binary system is

$$\begin{aligned} \Delta g \simeq\ & -\chi o_{CB}^0 (o_{CA}^0 + o_S^0) + 3 o_{CB}^0 \frac{\gamma'}{l_B} + \frac{o_C^0}{Z_C} \ln\left(\frac{l_B}{3d}\frac{1}{o_{CB}^0}\right) \\ & + \frac{1}{2}\frac{o_C^0}{Z_C}\left(\alpha_B^2 + \frac{2}{\alpha_B} + \alpha_A^2 + \frac{2}{\alpha_A} - 6\right) \\ & + \frac{o_S^0}{Z_S}\left[F_2^S \ln\left(\frac{F_2^S}{G_2^V}\right) + F_3^S \ln\left(\frac{F_3^S}{G_3^V}\right)\right]. \end{aligned} \tag{3.29}$$

Equation (3.29) is an approximate expression for a binary system. Now we obtain an approximate expression for the free energy for systems with added B homopolymer.

The first term in Equation (3.29) is a contribution from the interaction energy. Since we assume that there is no mixing of the B homopolymer in the A matrix this term is independent of f. The contributions from the interfacial tension and localization of the copolymer joints corresponding to the second and third terms in Equation (3.29), respectively, depend on the volume fraction of the cores. Contributions from these two terms can therefore be obtained by replacing o^0_{CB} with o_{core}. In the term in Equation (3.29) involving the solvent entropy of mixing, any effect of the core swelling on the volume of the corona is neglected, and we assume that this contribution is independent of f. In ternary mixtures an entropy of mixing term arises due to the added B homopolymer. If $f = 0$ the system is macrophase separated and the added homopolymer occupies a volume fraction o^0_{HB}. On the other hand, when $f = 1$, the homopolymer can occupy a larger volume fraction $o^0_B = o^0_{HB} + o^0_{CB}$. For the general case, the fraction f of B homopolymer is localized to the volume fraction o_{core} and the remaining fraction, $1 - f$, to the volume fraction $(1 - f)o^0_{HB}$. The free energy contribution can therefore be written as

$$g_{HB} = \frac{o^0_{HB}}{Z_{HB}} \left[f \ln \left(\frac{o^0_B}{o_{core}} \right) + (1 - f) \ln \left(\frac{o^0_B}{(1 - f)o^0_{HB}} \right) \right]. \tag{3.30}$$

The remaining term is due to the stretching of the core and corona blocks. As noted earlier, the change in the corona upon swelling the core of the micelles is neglected and therefore only the stretching term corresponding to the core block remains.

The new expression for the change in free energy is now available from the corrections to Equation (3.29) and the new term in Equation (3.30). It is however

convenient to define the free energy as

$$\begin{aligned}\Delta\tilde{g} &\equiv \Delta g(f) - \Delta g(f=0) \qquad (3.31)\\ &= 3\gamma'\left(\frac{\phi_{core}}{l'_B} - \frac{\phi^0_{CB}}{l_B}\right) + \left\{\frac{\phi^0_{CB}}{Z_{CB}}\left[\ln\left(\frac{l'_B}{\phi_{core}}\frac{\phi^0_{CB}}{l_B}\right)\right.\right.\\ &\quad \left. + \frac{1}{2}\left((\alpha'_B)^2 + \frac{2}{\alpha'_B} - \alpha_B^2 - \frac{2}{\alpha_B}\right)\right]\\ &\quad \left. + \frac{\phi^0_{HB}}{Z_{HB}}\left[f\ln\left(\frac{\phi^0_{HB}}{\phi_{core}}\right) - (1-f)\ln(1-f)\right]\right\}.\end{aligned}$$

where l'_B and α'_B correspond to the radius of the core and the stretching of the core block, respectively, when the B homopolymer is present. To obtain properties of the ternary system, $\Delta\tilde{g}$ is minimized with respect to l'_B and f. The minimization with respect to l'_B, assuming that the core block of the copolymer is strongly stretched with $\alpha_B \gg 1$, yields

$$l'_B \simeq \left(\frac{\phi_{core}}{\phi^0_{CB}}\right)^{1/3} l_B. \qquad (3.32)$$

The radius of the swollen micelles therefore depends on the fraction f of added homopolymer solubilized in the micelle core. Also, the total number of micelles divided by the total volume is

$$n_M = \frac{3}{4\pi(l'_B)^3}\phi_{core}\,. \qquad (3.33)$$

Substituting the expression for l'_B from Equation (3.32) into Equation (3.33) yields the result that the number of micelles is independent of the amount of added homopolymer or the fraction f. To calculate f, we need to substitute the expression for l'_B from Equation (3.32) into $\Delta\tilde{g}$ which yields

$$\Delta\tilde{g} = \frac{\phi^0_{CB}}{Z_{CB}}\left\{3(\gamma')^{2/3} Z_{CB}^{1/3}\left[\left(\frac{\phi_{core}}{\phi^0_{CB}}\right)^{2/3} - 1\right] + \frac{2}{3}\ln\left(\frac{\phi^0_{CB}}{\phi_{core}}\right)\right. \qquad (3.34)$$

$$+\frac{(\alpha_B)^2}{2}\left[\left(\frac{\sigma_{core}}{\sigma^0_{CB}}\right)^{2/3}-1\right]+\frac{1}{\alpha_B}\left[\left(\frac{\sigma^0_{CB}}{\sigma_{core}}\right)^{1/3}-1\right]$$
$$+\frac{Z_{CB}}{Z_{HB}}\frac{\sigma^0_{HB}}{\sigma^0_{CB}}\left[f\ln\left(\frac{\sigma^0_{HB}}{\sigma_{core}}\right)-(1-f)\ln(1-f)\right]\Bigg\}\ .$$

Since we have assumed that the corona region is unaffected by the swelling in the strong segregation limit, we can approximate the interfacial tension in Equation (3.17) as $\gamma' = C^{1/2}\gamma'_0$. The quantity C corresponds to the argument under the square root sign in Equation (3.17) and is taken to be constant. The free energy in Equation (3.34) therefore reduces to

$$\Delta\tilde{g} = \frac{\sigma^0_{CB}}{Z_{CB}}\left\{\left(\frac{9C\chi Z_{CB}}{2}\right)^{1/3}\left[\left(\frac{\sigma_{core}}{\sigma^0_{CB}}\right)^{2/3}-1\right]+\frac{2}{3}\ln\left(\frac{\sigma^0_{CB}}{\sigma_{core}}\right)\right. \tag{3.35}$$
$$+\frac{(\alpha_B)^2}{2}\left[\left(\frac{\sigma_{core}}{\sigma^0_{CB}}\right)^{2/3}-1\right]+\frac{1}{\alpha_B}\left[\left(\frac{\sigma^0_{CB}}{\sigma_{core}}\right)^{1/3}-1\right]$$
$$+\frac{Z_{CB}}{Z_{HB}}\frac{\sigma^0_{HB}}{\sigma^0_{CB}}\left[f\ln\left(\frac{\sigma^0_{HB}}{\sigma_{core}}\right)-(1-f)\ln(1-f)\right]\Bigg\}\ .$$

This free energy is a function of the four variables χZ_{CB}, Z_{HB}/Z_{CB}, $\sigma^0_{HB}/\sigma^0_{CB}$ and f. The first three variables specify the system and f is determined from the minimization of the free energy, which is done numerically. Whitmore and Smith [32] report that the numerical solution always gives $f = 0$ or $f = 1$. This can be explained as follows. At low concentrations of B homopolymer, all the homopolymer is solubilized within the micelle core. Although there is a small increase in the stretching of the core block, this effect is offset by entropic effects where the volume of the micelle cores is larger than that of the separate HB phase. There is therefore a larger entropic penalty in localizing the added homopolymer to a separate HB phase. As the

volume fraction of added homopolymer increases, the contributions to the free energy due to the stretching of the core block and the interfacial tension also increase until a certain threshold volume fraction is reached. Above this threshold the homopolymer is expelled from the micelles into a separate HB phase. If only a small fraction of the homopolymer were to be expelled, the change in the stretching and interfacial energies would be small and a large entropic penalty would occur in localizing the homopolymer to the correspondingly small fraction of the total volume. Instead, all the homopolymer is expelled, maximizing the entropy and minimizing the stretching free energy. We therefore define the largest value of ϕ^0_{HB} for which $f = 1$ as ϕ^{max}_{HB}. From the functional form of Equation (3.35) we find

$$\phi^{max}_{HB} \propto \phi^0_{CB}. \tag{3.36}$$

The proportionality constant is R^{max} and, from Equation (3.35), R^{max} is a function of χZ_{CB} and the relative degrees of polymerization Z_{HB}/Z_{CB}.

For purposes of illustration we approximate the expression for $\Delta\tilde{g}$ in Equation (3.35) by assuming $\phi^{max}_{HB}/\phi^0_{CB} \gg 1$, which is not unreasonable as long as $Z_{HB}/Z_{CB} \ll 1$, and obtain an analytical expression for $\phi^{max}_{HB}/\phi^0_{CB}$. Therefore, assuming that $Z_{HB}/Z_{CB} \ll 1$, Equation (3.35) can be rewritten as

$$\Delta\tilde{g} \simeq \frac{\phi^0_{CB}}{Z_{CB}} \left\{ \Gamma(\chi Z_{CB})^{1/3} \left(\frac{\phi^{max}_{HB}}{\phi^0_{CB}} \right)^{2/3} - \frac{2}{3} \ln \left(\frac{\phi^{max}_{HB}}{\phi^0_{CB}} \right) - \frac{Z_{CB}}{Z_{HB}} \right\}, \tag{3.37}$$

where Γ is a numerical factor. An approximate expression is obtained by setting

$\Delta\tilde{g} = 0$. Then, if $\ln(\phi_{HB}^{max}/\phi_{CB}^{0}) \ll Z_{CB}/Z_{HB}$, the analytical solution is

$$\frac{\phi_{HB}^{max}}{\phi_{CB}^{0}} \propto (\chi Z_{CB})^{-1/2} \left(\frac{Z_{HB}}{Z_{CB}}\right)^{-3/2}. \tag{3.38}$$

The results from Equations (3.37) and (3.38) are strictly valid for the case where $Z_{HB}/Z_{CB} \ll 1$ but they nonetheless highlight the essential features. The expression for $\Delta\tilde{g}$ in Equation (3.37) clearly shows that the relative threshold $\phi_{HB}^{max}/\phi_{CB}^{0}$ is dependent on χZ_{CB} and Z_{HB}/Z_{CB}. The χZ_{CB} term arises from a balance between the stretching energy and the interfacial tension and suggests that the ratio $\phi_{HB}^{max}/\phi_{CB}^{0}$ decreases with increasing Z_{CB} and/or a decrease in temperature. The Z_{HB}/Z_{CB} term is due to entropic effects in localizing the added homopolymer. When Z_{HB} decreases relative to Z_{CB}, the entropic penalty in localizing the added homopolymer to a smaller region outside the micelles cores increases. This results in an increase in the threshold volume fraction of added homopolymer. These qualitative results obtained from Equation (3.38) are consistent with the numerical calculations.

3.4 Numerical Self-consistent Field Theory

In this section the NSCF formalism of end-tethered polymers and thin films is presented. The general formalism presented here is based on the SCF theory of Edwards and Dolan [98-100], Helfand and coworkers [101-103], Hong and Noolandi [90, 104, 105], Ohta and Kawasaki [106], Whitmore and Noolandi [88, 89], Banaszak [107], and Baranowski and Whitmore [108, 109]. In this study, the formalism as

published by Baranowski and Whitmore [108, 109] is reviewed with some modifications to extend the application to thin films. It reduces to end-tethered layers by simply excluding the free polymer in solution.

In the statistical mechanical description of the polymer systems, three steps are followed as described in Section 1.2. In the first step, the polymers are represented by linear flexible chains with interactions between segments. The interactions are divided into two categories: those which are limited to a few segments along the chain and are referred to as "short range interactions", and the "long range", effective monomer-monomer interactions between segments which are far apart along the chain [33, 110, 111], or segments on two different chains, or solvent-monomer interactions.

In macroscopic systems there exist some physical quantities which obey universal laws. A microscopic model of a system should therefore be able to reproduce such universal descriptions. One simple quantity for which many microscopic models can reproduce the same universal scaling law is the root-mean-squared (*rms*) end-to-end distance

$$< \boldsymbol{R}^2 >= b^2 Z \tag{3.39}$$

where b is an effective bond length which depends on the local structure and is referred to as the statistical segment length. A simple but powerful model which satisfies this criterion is the Gaussian chain model, in which an equivalent chain of n segments with segment length Δs is chosen such that the contour length remains constant: $n\Delta s = bZ$. For the Gaussian chain, every bond has a Gaussian distribution of bond

vectors

$$\iota(\boldsymbol{r}) = \left(\frac{3}{2\pi b\Delta s}\right)^{3/2} \exp\left(-\frac{3\boldsymbol{r}^2}{2b\Delta s}\right) . \tag{3.40}$$

The mean square bond length is therefore

$$< \boldsymbol{r}^2 >= b^2 \tag{3.41}$$

where $\boldsymbol{r}$ is a bond vector. The Gaussian distribution function in Equation (3.40) can be used to calculate the probability that a chain with Z segments will follow a particular spatial conformation. $\Psi(\boldsymbol{r}_0, \boldsymbol{r}_1, \ldots, \boldsymbol{r}_{Z-1}) \equiv \Psi_Z(\{\boldsymbol{r}_\tau\})$. The probability $\Psi_Z(\{\boldsymbol{r}_\tau\})$ can be written as

$$\Psi_Z(\{\boldsymbol{r}_\tau\}) = \prod_{k=0}^{Z-1} \iota(\boldsymbol{r}_{k+1} - \boldsymbol{r}_k) . \tag{3.42}$$

where $\boldsymbol{r}_k$ is the position of monomer k and $\boldsymbol{r}_{k+1} - \boldsymbol{r}_k$ is the k^{th} bond vector. The end-to-end distance squared is then

$$< R^2 >= \int d\boldsymbol{R} R^2 \Psi(\{\boldsymbol{r}_\tau\}) = n(b\Delta s) = b^2 Z \tag{3.43}$$

which defines the equivalent Gaussian chain, where $\boldsymbol{R}$ is the end-to-end vector of the chain.

For convenience, the probability that a chain with segments indexed from 0 to n starts at $\boldsymbol{r}_0$ and ends at $\boldsymbol{r}_n$ is defined by integrating over all possible conformations with fixed $\boldsymbol{r}_0$ and $\boldsymbol{r}_n$. The result is the chain "propagator". For the equivalent Gaussian chain it is given by

$$Q(\boldsymbol{r}_n, n|\boldsymbol{r}_0, 0) \equiv \int \Psi_n(\{\boldsymbol{r}'_\tau\})\delta(\boldsymbol{r}'_0 - \boldsymbol{r}_0)\delta(\boldsymbol{r}'_n - \boldsymbol{r}_n) \prod_{k=0}^{n} d\boldsymbol{r}'_k \tag{3.44}$$

$$= \left(\frac{3}{2\pi b\Delta s}\right)^{3n/2} \int \exp\left[-\frac{3}{2b}\sum_{k=0}^{n}\frac{(\boldsymbol{r}'_{k+1}-\boldsymbol{r}'_k)^2}{\Delta s}\right]\delta(\boldsymbol{r}'_0-\boldsymbol{r}_0)\delta(\boldsymbol{r}'_n-\boldsymbol{r}_n)\prod_{k=0}^{n}d\boldsymbol{r}'_k \ .$$

In the continuous limit of $n \to \infty$ and $\Delta s \to 0$ the *Wiener Measure* [112] is defined:

$$P[\boldsymbol{r}(\cdot)] \propto \exp\left[-\frac{3}{2b^2}\int_0^Z d\tau \left|\frac{d\boldsymbol{r}(\tau)}{d\tau}\right|^2\right] \ . \tag{3.45}$$

and the polymer is modeled as a continuous space curve $\boldsymbol{r}(\tau)$ with τ varying from 0 to Z. The resulting propagator is

$$Q(\boldsymbol{r}_Z, Z|\boldsymbol{r}_0, 0) = \int \mathcal{D}\boldsymbol{r}(\cdot)\,\delta(\boldsymbol{r}(0)-\boldsymbol{r}_0)\delta(\boldsymbol{r}(Z)-\boldsymbol{r}_Z)P[\boldsymbol{r}(\cdot)] \ . \tag{3.46}$$

This function satisfies the ordinary diffusion equation

$$\frac{b^2}{6}\boldsymbol{\nabla}^2\boldsymbol{Q}(\boldsymbol{r},\tau|\boldsymbol{r}',0) = \frac{\partial}{\partial\tau}\boldsymbol{Q}(\boldsymbol{r},\tau|\boldsymbol{r}',0) \tag{3.47}$$

with the initial conditions

$$\boldsymbol{Q}(\boldsymbol{r},0|\boldsymbol{r}',0) = \delta(\boldsymbol{r}-\boldsymbol{r}') \ . \tag{3.48}$$

The polymer chains are therefore modeled as continuous space curves described by the propagator $\boldsymbol{Q}(\boldsymbol{r},\tau|\boldsymbol{r}',0)$, which turns out to be equivalent to the Green's function for the diffusion equation (Equation (3.47)).

The second step in the description consists of calculating the partition function. It is evaluated with the use of the propagator defined in Equation (3.46) in the presence of long and short range interactions. The system consists of $\tilde{N}_A$ end-tethered polymers, $\tilde{N}_F$ free polymers and $\tilde{N}_S$ solvent molecules. The end-tethered polymers are characterized by the degree of polymerization Z_A, the statistical segment length

b_A and the density of pure material ρ_{0A}. Similarly, the free polymers are characterized by Z_F, b_F and ρ_{0F}, and the density of pure solvent is ρ_{0S}. The number of monomers of type κ is therefore $N_\kappa = \tilde{N}_\kappa Z_\kappa$.

In the experiments we are concerned with in this thesis, there is no attraction to any surface except that the end of the tethered block is confined to an interface at the surface. In fact, there is a large energy penalty associated with any monomer extending beyond any surface, so the surfaces can be modeled as impermeable walls. In the experiments of Kent *et al.* [2, 68, 69, 113], the B block of the copolymer is strongly adsorbed to the air-solvent interface and so the A block is end-tethered. Other types of arrangements include B-block adsorption to a solid surface, or, with the possibility of having a B block consisting of one monomer which is an end-functional group that binds tightly to the surface, end-grafted homopolymer. In all these cases, the dangling chains can be modeled as homopolymers with a large energy barrier that confines one end of each polymer to an interface of width a, next to an impermeable wall. In the formalism presented here, two impermeable walls are placed at $z = 0$ and $z = L$. The interface at which the polymers are end-tethered is at $z = 0$. The volume of the system is $\Omega = \mathcal{A}L$ where $\mathcal{A}$ is the area of the interface and $L \gg b_\kappa Z_\kappa$, where $\kappa = A, F$. In the formalism developed in this study it is assumed that there is no volume change upon mixing. This is also known as the incompressibility condition

and is equivalent to requiring that the volume fractions adding up to unity everywhere

$$\sum_{\kappa} \frac{< \hat{\rho}_{\kappa}(\boldsymbol{r}) >}{\rho_{0\kappa}} = 1 \ . \tag{3.49}$$

where $\hat{\rho}_{\kappa}(\boldsymbol{r})$ is the local density of species κ for a given configuration, and $< \ldots >$ denotes the ensemble average.

With the polymer chains modeled as continuous space curves and subject to long and short range interactions in an incompressible system, the partition function can be written as a series of functional integrals over all possible chain configurations and locations of solvent molecules:

$$\begin{aligned} \boldsymbol{Z} \ = \ & \left(\prod_{\kappa=A,F,S} \frac{\mathcal{Z}_{\kappa}^{\hat{N}_{\kappa}}}{\hat{N}_{\kappa}!} \right) \int \left(\prod_{i=1}^{\hat{N}_S} d\boldsymbol{r}_{Si} \right) \times \\ & \int \prod_{j}^{\hat{N}_A} \mathcal{D}\boldsymbol{r}_{Aj}(\cdot) P[\boldsymbol{r}_{Aj}(\cdot)] \ \times \\ & \int \prod_{j}^{\hat{N}_F} \mathcal{D}\boldsymbol{r}_{Fj}(\cdot) P[\boldsymbol{r}_{Fj}(\cdot)] \ \times \\ & \prod_{\boldsymbol{r}} \delta \left(1 - \sum_{\kappa=A,F,S} \frac{\hat{\rho}_{\kappa}(\boldsymbol{r})}{\rho_{0\kappa}} \right) \times \\ & \exp \left[-\beta \hat{V}' \right] \ . \end{aligned} \tag{3.50}$$

The kinetic energy contribution due to the solvent molecules and the polymer chains is $\mathcal{Z}_{\kappa}$. $P[\boldsymbol{r}_{\kappa j}(\cdot)]$ is the Wiener measure and $\mathcal{D}\boldsymbol{r}_{\kappa j}(\cdot)$ denotes the integration over configurations of the j^{th} chain of type κ. The incompressibility condition is applied via the Dirac delta function $\delta \left(1 - \sum \frac{\hat{\rho}_{\kappa}(\boldsymbol{r})}{\rho_{0\kappa}} \right)$. The potential $\hat{V}'$ includes interactions between all components in the system, contributions from the impermeable walls and

contributions from the confinement of one end of the end-tethered polymers. The potential $\hat{\Gamma}'$ can therefore be written as

$$\hat{\Gamma}' = \hat{\Gamma} + \hat{\Gamma}'' \tag{3.51}$$

where $\hat{\Gamma}$ includes the interactions between components and $\hat{\Gamma}''$ consists of all remaining terms.

Since the potential term $\hat{\Gamma}'$ includes interactions between components and interactions of each component with an external potential, it is therefore a function of the microscopic densities which are modeled as

$$\hat{\rho}_S(\boldsymbol{r}) = \sum_{i=1}^{\hat{N}_S} \delta(\boldsymbol{r} - \boldsymbol{r}_{Si}) \tag{3.52}$$

$$\hat{\rho}_\kappa(\boldsymbol{r}) = \sum_{j=1}^{\hat{N}_\kappa} \int_0^{Z_\kappa} d\tau\ \delta(\boldsymbol{r} - \boldsymbol{r}_{\kappa j}(\tau))\ . \tag{3.53}$$

where $\boldsymbol{r}_{\kappa j}(\tau)$ describes the position of monomer τ of type κ of the j^{th} chain.

In general the interactions between all molecules in the system are not pairwise additive. However, for most theoretical models involving Gaussian chains the binary interactions are assumed to be sufficient to describe real polymers in solution [110]. The potential can therefore be written in terms of two-body interactions

$$\beta\hat{\Gamma} \equiv \beta\hat{H} = \frac{1}{2} \sum_{\kappa\kappa'=A,F,S} \int d\boldsymbol{r} \int d\boldsymbol{r}'\, \hat{\rho}_\kappa(\boldsymbol{r}) W_{\kappa\kappa'}(\boldsymbol{r} - \boldsymbol{r}') \hat{\rho}_{\kappa'}(\boldsymbol{r}') \tag{3.54}$$

where $W_{\kappa\kappa'}(\boldsymbol{r} - \boldsymbol{r}')$ is the potential acting on a particle κ at position $\boldsymbol{r}$ due to another particle κ' at $\boldsymbol{r}'$. The interactions due to the external potential can be written as

$$\beta\hat{\Gamma}'' \equiv \beta\hat{H}'' = \sum_{\kappa=A,F,S} \int d\boldsymbol{r} \hat{\rho}_\kappa(\boldsymbol{r}) W''_\kappa(\boldsymbol{r}) \tag{3.55}$$

with the external potential $W_\kappa'''(\boldsymbol{r})$ acting on a particle κ at $\boldsymbol{r}$. From Equation (3.51), (3.54) and (3.55) we can define

$$\beta\hat{U}'' = \hat{W}'' \equiv \hat{W}' + \hat{W}''' . \tag{3.56}$$

The microscopic particle densities in Equations (3.52) and (3.53) are expressed in terms of individual solvent molecules and chain segments. We perform a change of variables via the introduction of a Dirac delta function where

$$\prod_{\boldsymbol{r}} \delta\left(1 - \sum_{\kappa=A,F,S} \frac{\hat{\rho}_\kappa(\boldsymbol{r})}{\rho_{0\kappa}}\right) \exp\left[-\hat{W}''\right] = \tag{3.57}$$
$$\int \left\{ \prod_{\kappa=A,F,S} \mathcal{D}\rho_\kappa(\cdot)\delta\left[\rho_\kappa(\cdot) - \hat{\rho}_\kappa(\cdot)\right] \right\} \prod_{\boldsymbol{r}} \delta\left(1 - \sum_{\kappa=A,F,S} \frac{\rho_\kappa(\boldsymbol{r})}{\rho_{0\kappa}}\right) \exp\left[-W''(\{\rho_\kappa(\cdot)\})\right] .$$

The function $W''(\{\rho_\kappa(\cdot)\})$ represents the two-body interactions and the interactions with the external potential but evaluated for continuous $\{\rho_\kappa(\cdot)\}$. The Fourier transform of each Dirac delta function

$$\delta\left[\rho_\kappa(\cdot) - \hat{\rho}_\kappa(\cdot)\right] = \mathcal{N}_1 \int \mathcal{D}\omega_\kappa'(\cdot) \exp\left[\int d\boldsymbol{r}\omega_\kappa'(\boldsymbol{r})[\rho_\kappa(\boldsymbol{r}) - \hat{\rho}_\kappa(\boldsymbol{r})]\right] . \tag{3.58}$$

and

$$\prod_{\boldsymbol{r}} \delta\left(1 - \sum_{\kappa} \frac{\rho_\kappa(\boldsymbol{r})}{\rho_{0\kappa}}\right) = \mathcal{N}_2 \int \mathcal{D}\eta(\cdot) \exp\left[\int d\boldsymbol{r}\eta(\boldsymbol{r}) \left(1 - \sum_{\kappa} \frac{\rho_\kappa(\boldsymbol{r})}{\rho_{0\kappa}}\right)\right] \tag{3.59}$$

is introduced, where the limits of integration for the fields $\omega_\kappa'(\cdot)$ and $\eta(\cdot)$ are $\pm i\infty$, and $\mathcal{N}_1$ and $\mathcal{N}_2$ are normalization factors.

The partition function can then be expressed in terms of continuous functions which lead to

$$\boldsymbol{Z} = \left(\prod_{\kappa=A,F,S} \frac{\mathcal{Z}_\kappa^{\hat{N}_\kappa}}{\hat{N}_\kappa!}\right) \times \int \left[\prod_{\kappa=A,F,S} \mathcal{D}\rho_\kappa(\cdot)\mathcal{D}\omega_\kappa'(\cdot)\right] \mathcal{D}\eta(\cdot) \times$$

$$\left(\prod_{\kappa=A,F,S} \mathcal{Q}_\kappa^{\hat{N}_\kappa}\right) \times \exp\left[\int d\boldsymbol{r}\ \eta(\boldsymbol{r})\left(1 - \sum_{k=A,F,S} \frac{\rho_k(\boldsymbol{r})}{\rho_{0k}}\right)\right] \times \tag{3.60}$$
$$\exp\left[\sum_{k=A,F,S} \int d\boldsymbol{r}\ \omega'_\kappa(\boldsymbol{r})\rho_k(\boldsymbol{r})\right] \times \exp\left[-H''[\{\rho_k(\cdot)\}]\right] .$$

where, for solvent

$$\mathcal{Q}_S = \int d\boldsymbol{r}\ \exp[-\omega'_S(\boldsymbol{r})] . \tag{3.61}$$

and for the end-tethered and free polymers

$$\mathcal{Q}_\kappa = \int \mathcal{D}\boldsymbol{r}_\kappa(\cdot) P[\boldsymbol{r}_\kappa(\cdot)] \times \exp\left[-\int_0^{Z_\kappa} d\tau\ \omega'_\kappa[\boldsymbol{r}_\kappa(\tau)]\right] . \tag{3.62}$$

It is convenient to introduce the propagators

$$\begin{aligned} \boldsymbol{Q}_\kappa(\boldsymbol{r}, \tau|\boldsymbol{r}', 0) \ &= \ \int \mathcal{D}\boldsymbol{r}_\kappa(\cdot)\delta[\boldsymbol{r}_\kappa(\tau) - \boldsymbol{r}]\delta[\boldsymbol{r}_\kappa(0) - \boldsymbol{r}'] \times \\ &\exp\left\{-\int_0^\tau d\tau' \left(\frac{3}{2b_\kappa^2}\left|\frac{d\boldsymbol{r}(\tau')}{d\tau'}\right|^2 + \omega'_\kappa[\boldsymbol{r}_\kappa(\tau')]\right)\right\} . \end{aligned} \tag{3.63}$$

and it can be shown that the propagators satisfy the modified diffusion equation

$$\left[\frac{b_\kappa^2}{6}\boldsymbol{\nabla}^2 - \omega'_\kappa(\boldsymbol{r})\right] \boldsymbol{Q}_\kappa(\boldsymbol{r}, \tau|\boldsymbol{r}', 0) = \frac{\partial}{\partial\tau}\boldsymbol{Q}_\kappa(\boldsymbol{r}, \tau|\boldsymbol{r}', 0) . \tag{3.64}$$

with the initial condition given by Equation (3.48).

The field ω'_κ includes contributions from the external field which restrict the polymer or solvent to the region between the two impermeable surfaces. The contributions also restrict one end of each end-tethered polymer to the interface. The result is $\boldsymbol{Q}_\kappa(\boldsymbol{r}, \tau|\boldsymbol{r}', \tau') = 0$ if either $\boldsymbol{r}$ or $\boldsymbol{r}'$ lies outside the region defined by the two impermeable walls. In addition, for the end-tethered polymers, $\boldsymbol{Q}_A(\boldsymbol{r}, \tau|\boldsymbol{r}', 0) = 0$ if $\boldsymbol{r}'$ does not lie in the interface. There is an alternative approach to solving the modified diffusion

equation (Equation (3.64)) subject to the external potential field. It involves solving the diffusion equation while neglecting contributions from the external potential in ω'_κ and directly applying the appropriate initial and boundary conditions. We define ω_κ such that $\omega'_\kappa \to \omega_\kappa$ when there is no external potential. Therefore in Equation (3.64), $\omega'_\kappa \to \omega_\kappa$, but now the initial condition in Equation (3.48) applies to those regions defined by the impermeable walls and the interface. Effectively, the external potentials are taken into account by applying the appropriate initial and boundary conditions. As a result, the partition function can be evaluated by considering the interactions between the components only. We set $\omega'_\kappa \to \omega_\kappa$ in Equations (3.60)-(3.64) and, for convenience, we do not rewrite these equations. Instead from now on we refer to the potential fields as having contributions from interactions between the components only.

In this approach the tethered end is subject to a different initial condition than that at a free end. We therefore define the propagator $\tilde{\boldsymbol{Q}}_A(\boldsymbol{r}, \tau|\boldsymbol{r}', 0)$ which also satisfies the modified diffusion equation but has the additional constraint that one end is confined to the interface. From Equation (3.63), the integrals $\mathcal{Q}_\kappa$ in Equation (3.62) can therefore be written as

$$\mathcal{Q}_F = \int d\boldsymbol{r}\, d\boldsymbol{r}'\, \boldsymbol{Q}_F(\boldsymbol{r}, Z_F|\boldsymbol{r}', 0) \tag{3.65}$$

and

$$\mathcal{Q}_A = \int d\boldsymbol{r}\, d\boldsymbol{r}'\, \tilde{\boldsymbol{Q}}_A(\boldsymbol{r}, Z_A|\boldsymbol{r}', 0)\ . \tag{3.66}$$

for the free and end-tethered polymers, respectively.

With the use of the Stirling approximation the partition function can be written as

$$\boldsymbol{Z} = \mathcal{N} \int \prod_{\kappa=A,F,S} \mathcal{D}\rho_\kappa(\cdot)\mathcal{D}\omega_\kappa(\cdot)\mathcal{D}\eta(\cdot) \exp\left[-\mathcal{F}_T[\{\rho_\kappa(\cdot)\}, \{\omega_\kappa(\cdot)\}, \eta(\cdot)]\right] . \quad (3.67)$$

where $\mathcal{N}$ is a normalization factor and $\mathcal{F}_T[\{\rho_\kappa(\cdot)\}, \{\omega_\kappa(\cdot)\}, \eta(\cdot)]$ is the free energy functional given by

$$\mathcal{F}_T[\{\rho_\kappa(\cdot)\}, \{\omega_\kappa(\cdot)\}, \eta(\cdot)] = F[\{\rho_\kappa(\cdot)\}, \{\omega_\kappa(\cdot)\}] + G[\{\rho_\kappa(\cdot)\}, \eta(\cdot)] . \quad (3.68)$$

with

$$F[\{\rho_\kappa(\cdot)\}, \{\omega_\kappa(\cdot)\}] = \left[W[\{\rho_\kappa(\cdot)\}] - \sum_{\kappa=A,F,S} \int d\boldsymbol{r}\, \omega_\kappa(\boldsymbol{r})\rho_\kappa(\boldsymbol{r})\right] + \sum_{\kappa=A,F,S} \tilde{N}_\kappa \left\{ \ln \frac{\tilde{N}_\kappa}{\mathcal{Z}_\kappa \mathcal{Q}_\kappa} - 1 \right\} \quad (3.69)$$

$$G[\{\rho_\kappa(\cdot)\}, \eta(\cdot)] = \int d\boldsymbol{r}\, \eta(\boldsymbol{r}) \left[\sum_{\kappa=A,F,S} \frac{\rho_\kappa(\boldsymbol{r})}{\rho_{0\kappa}} - 1 \right] . \quad (3.70)$$

With this description of the partition function, physical quantities can be calculated. One relevant quantity is the average density distribution of each component which is expressed as

$$\begin{aligned} \langle \hat{\rho}_\kappa(\boldsymbol{r}) \rangle = \frac{1}{\boldsymbol{Z}} \left(\prod_{\kappa'=A,F,S} \frac{\mathcal{Z}_{\kappa'}^{\tilde{N}_{\kappa'}}}{\tilde{N}_{\kappa'}!} \right) \int \left(\prod_{i=1}^{\tilde{N}_S} d\boldsymbol{r}_{Si} \right) \times \\ \int \prod_{j}^{\tilde{N}_\kappa} \mathcal{D}\boldsymbol{r}_{\kappa j}(\cdot) P[\boldsymbol{r}_{\kappa j}(\cdot)] \times \\ \hat{\rho}_\kappa(\boldsymbol{r}) \times \\ \prod_{\boldsymbol{r}} \delta \left(1 - \sum_{\kappa'=A,F,S} \frac{\hat{\rho}_{\kappa'}(\boldsymbol{r})}{\rho_{0\kappa'}} \right) \times \\ \exp\left[-\beta \hat{\Gamma}' \right] . \end{aligned} \quad (3.71)$$

Performing the same transformations of variables for this expression as were done for the partition function, it can be shown [107] that, for solvent, the density is

$$\langle \hat{\rho}_S(\boldsymbol{r}) \rangle = \frac{\mathcal{N}}{\boldsymbol{Z}} \int \left[\prod_{\kappa=A,F,S} \mathcal{D}\rho_\kappa(\cdot)\mathcal{D}\omega_\kappa(\cdot) \right] \mathcal{D}\eta(\cdot) \frac{\tilde{N}_S}{\mathcal{Q}_S} \frac{\delta \mathcal{Q}_S}{\delta \omega_S(\boldsymbol{r})} \exp\left[-\mathcal{F}_\mathcal{T}[\{\rho_\kappa(\cdot)\}, \{\omega_\kappa(\cdot)\}, \eta(\cdot)]\right] . \tag{3.72}$$

and for each type of polymer ($\kappa = A, F$)

$$\langle \hat{\rho}_\kappa(\boldsymbol{r}) \rangle = \frac{\mathcal{N}}{\boldsymbol{Z}} \int \left[\prod_{\kappa'=A,F,S} \mathcal{D}\rho_{\kappa'}(\cdot)\mathcal{D}\omega_{\kappa'}(\cdot) \right] \mathcal{D}\eta(\cdot) \frac{\tilde{N}_\kappa}{\mathcal{Q}_\kappa} \frac{\delta \mathcal{Q}_\kappa}{\delta \omega_\kappa(\boldsymbol{r})} \exp\left[-\mathcal{F}_\mathcal{T}[\{\rho_{\kappa'}(\cdot)\}, \{\omega_{\kappa'}(\cdot)\}, \eta(\cdot)]\right] . \tag{3.73}$$

3.4.1 Mean Field Approximation

In this section the problem of calculating the free energy and the spatial density distributions is addressed. The solution involves evaluating the functional integrals in Equations (3.67), (3.72), and (3.73) by the saddle point technique [114, 115]. In this approximation, the free energy, partition function and density distributions reduce to

$$\mathcal{F}_\mathcal{T} \rightarrow \mathcal{F}_\mathcal{T}[\{\rho_\kappa^0(\cdot)\}, \{\omega_\kappa^0(\cdot)\}, \eta^0(\cdot)] \tag{3.74}$$

$$\boldsymbol{Z} \rightarrow \boldsymbol{Z^0} \propto \exp\{-\mathcal{F}_\mathcal{T}[\{\rho_\kappa^0(\cdot)\}, \{\omega_\kappa^0(\cdot)\}, \eta^0(\cdot)]\} \tag{3.75}$$

$$\langle \hat{\rho}_\kappa(\boldsymbol{r}) \rangle \rightarrow -\frac{\tilde{N}_\kappa}{\mathcal{Q}_\kappa} \frac{\delta \mathcal{Q}_\kappa}{\delta \omega_\kappa(\boldsymbol{r})}\bigg|_0 \qquad \kappa = A, F, S . \tag{3.76}$$

where the superscript 0 denotes the saddle point values of the fields. The saddle point technique involves minimizing $\mathcal{F}_\mathcal{T}$ with respect to each of $\rho_\kappa(\boldsymbol{r}), \omega_\kappa(\boldsymbol{r})$ and $\eta(\boldsymbol{r})$ subject to the constraint of conservation of particle number for each component in

the system.

$$\int d\boldsymbol{r}\langle\hat{\rho}_\kappa(\boldsymbol{r})\rangle = N_\kappa \quad \kappa = A.F.S\ . \tag{3.77}$$

where $\tilde{N}_S = N_S$ for solvent, and $N_\kappa = \tilde{N}_\kappa Z_\kappa$ for $\kappa = A.F.$ The only part of $\mathcal{F}_T$ which depends on the field $\eta(\boldsymbol{r})$ is G, and this minimization gives

$$\sum_{\kappa=A.F.S} \frac{\rho_\kappa^0(\boldsymbol{r})}{\rho_{0\kappa}} = 1\ . \tag{3.78}$$

Hence

$$G = 0\ . \tag{3.79}$$

so that

$$\mathcal{F}_T^0 = F^0\ . \tag{3.80}$$

Minimization with respect to the field $\omega_\kappa(\boldsymbol{r})$ yields

$$\rho_\kappa^0(\boldsymbol{r}) + \frac{\tilde{N}_\kappa}{\mathcal{Q}_\kappa}\frac{\delta\mathcal{Q}_\kappa}{\delta\omega_\kappa(\boldsymbol{r})}\bigg|_0 = 0\ . \tag{3.81}$$

Equations (3.76) and (3.81) imply that the saddle point values of $\rho_\kappa^0(\boldsymbol{r})$, which are what can be calculated, are equal to the equilibrium density distributions $\langle\hat{\rho}_k(\boldsymbol{r})\rangle$ in this approximation. The constraint in Equation (3.77) can therefore be written as

$$\int d\boldsymbol{r}\rho_\kappa^0(\boldsymbol{r}) = N_\kappa \quad \kappa = A.F.S\ . \tag{3.82}$$

Minimization gives a set of equations for every component, connecting the interaction energy, densities and self-consistent potentials given in Equation (3.81) and

$$\frac{\delta\Pi^*}{\delta\rho_\kappa(\boldsymbol{r})} - \omega_\kappa(\boldsymbol{r}) + \frac{\eta(\boldsymbol{r})}{\rho_{0\kappa}} - \lambda_\kappa = 0\ . \tag{3.83}$$

where λ_κ are the Lagrange multipliers associated with Equation (3.82). The superscripts can now be dropped, but all quantities are intended to refer to the saddle point. Equations (3.61) and (3.81) yield

$$\rho_S(\boldsymbol{r}) = \frac{\tilde{N}_S}{\mathcal{Q}_S} \exp[-\omega_S(\boldsymbol{r})] \,. \tag{3.84}$$

Expressions for the densities of each type of polymer are obtained from the functional derivatives $\frac{\delta \mathcal{Q}_s}{\delta \omega_\kappa(\boldsymbol{r})}$. Following the derivation presented in Ref. [107], it can be shown that

$$\rho_F(\boldsymbol{r}) = \frac{\tilde{N}_F}{\mathcal{Q}_F} \int_0^{Z_F} d\tau \left\{ \int d\boldsymbol{r}'\, d\boldsymbol{r}'' \boldsymbol{Q}_F(\boldsymbol{r}, \tau | \boldsymbol{r}', 0)\, \boldsymbol{Q}_F(\boldsymbol{r}'', (Z_F - \tau) | \boldsymbol{r}, \tau) \right\} \tag{3.85}$$

and

$$\rho_A(\boldsymbol{r}) = \frac{\tilde{N}_A}{\mathcal{Q}_A} \int_0^{Z_A} d\tau \left\{ \int d\boldsymbol{r}'\, d\boldsymbol{r}'' \tilde{\boldsymbol{Q}}_A(\boldsymbol{r}, \tau | \boldsymbol{r}', 0)\, \boldsymbol{Q}_A(\boldsymbol{r}'', (Z_A - \tau) | \boldsymbol{r}, \tau) \right\} \,. \tag{3.86}$$

The potential energy defined in Equation (3.54) is very general but in practice it is useful to express it in terms of Flory interaction parameters [33] and the volume fractions of the components. A symmetric form of the potential energy [90] is therefore introduced where

$$U_{\kappa\kappa'}(\boldsymbol{r}) = W_{\kappa\kappa'}(\boldsymbol{r}) - \frac{1}{2} \left(W_{\kappa\kappa'}(\boldsymbol{r}) \rho_{0\kappa}^2 + W_{\kappa\kappa'}(\boldsymbol{r}) \rho_{0\kappa'}^2 \right) \,. \tag{3.87}$$

Equation (3.54) can be written as

$$\begin{aligned} W &= \frac{1}{2} \sum_{\kappa = A,F,S} W_{\kappa\kappa} \rho_{0\kappa} N_\kappa + \\ &\quad \frac{1}{2} \sum_{\kappa\kappa'} \int d\boldsymbol{r}\, d\boldsymbol{r}' \rho_\kappa(\boldsymbol{r}) U_{\kappa\kappa'}(\boldsymbol{r} - \boldsymbol{r}') \rho_{\kappa'}(\boldsymbol{r}') \,. \end{aligned} \tag{3.88}$$

where

$$W_{\kappa\kappa'} = \int d\boldsymbol{r} W_{\kappa\kappa'}(\boldsymbol{r}) \tag{3.89}$$

and is a measure of the overall strength of each interaction. The contributions to W that depend on $\rho_\kappa(\boldsymbol{r})$ enter only via $U_{\kappa\kappa'}$, not $W_{\kappa\kappa'}$. Performing a gradient expansion [90] where $U_{\kappa\kappa'}(\boldsymbol{r}-\boldsymbol{r}')$ is assumed to be short ranged, the potential can be written as

$$\begin{aligned} W &= \frac{1}{2}\sum_{\kappa=A,F,S} W_{\kappa\kappa}\rho_{0\kappa}N_\kappa + \\ &\frac{1}{2}\rho_{ref}\sum_{\kappa\kappa'}\chi_{\kappa\kappa'}\int d\boldsymbol{r}\left(\phi_\kappa(\boldsymbol{r})\phi_{\kappa'}(\boldsymbol{r}) - \frac{\sigma^2}{6}\nabla\phi_\kappa(\boldsymbol{r})\nabla\phi_{\kappa'}(\boldsymbol{r})\right) . \end{aligned} \tag{3.90}$$

where the Flory parameters [33] are defined as [107]

$$\chi_{\kappa\kappa'} = \frac{\rho_{0\kappa}\rho_{0\kappa'}}{\rho_{ref}}U_{\kappa\kappa'} \tag{3.91}$$

and

$$U_{\kappa\kappa'} = \int d\boldsymbol{r} U_{\kappa\kappa'}(\boldsymbol{r}), \tag{3.92}$$

$$\sigma^2 = \frac{\int d\boldsymbol{r}|\boldsymbol{r}|^2 U_{\kappa\kappa'}(\boldsymbol{r})}{U_{kk'}} . \tag{3.93}$$

The reference density used to define the Flory interaction parameters is usually taken to be the density of pure solvent present in the system, ρ_{0S}. The parameter σ is a measure of the effective range of the interaction and, for these calculations, is taken to be $\sigma^2 = 0$. The local volume fraction $\phi_\kappa(\boldsymbol{r})$ is defined as

$$\phi_\kappa(\boldsymbol{r}) \equiv \frac{\rho_\kappa(\boldsymbol{r})}{\rho_{0\kappa}} . \tag{3.94}$$

The self-consistent potentials can be evaluated through Equation (3.83), using the expression for the potential energy in Equation (3.90). The result is

$$\omega_\kappa(\boldsymbol{r}) = \frac{\eta(\boldsymbol{r})}{\rho_{0\kappa}} + \frac{\rho_{0S}}{\rho_{0\kappa}} \sum_{\kappa'} \chi_{\kappa\kappa'} o_{\kappa'}(\boldsymbol{r}) - \lambda_\kappa \ . \tag{3.95}$$

The field $\eta(\boldsymbol{r})$ can be eliminated using Equations (3.84) and (3.95), and each λ_κ is chosen so that $\omega_\kappa(\boldsymbol{r}) = 0$ if $o_\kappa(\boldsymbol{r}) = \bar{o}_\kappa$ where the $\bar{o}_\kappa$'s correspond to average volume fractions. By requiring that $\omega_S(\boldsymbol{r}) = 0$ for $o_S(\boldsymbol{r}) = \bar{o}_S$, Equation (3.84) yields

$$\omega_S(\boldsymbol{r}) = \ln\left(\frac{\bar{o}_S}{o_S(\boldsymbol{r})}\right) \tag{3.96}$$

Because of the incompressibility assumption in Equation (3.78), the density distribution of the solvent can be obtained from the distributions of both polymers from

$$o_S(\boldsymbol{r}) = 1 - o_A(\boldsymbol{r}) - o_B(\boldsymbol{r}) \ . \tag{3.97}$$

Using Equations (3.95) and (3.96) the potentials are therefore given by

$$\omega_\kappa(\boldsymbol{r}) = \frac{\rho_{0S}}{\rho_{0\kappa}} \left\{ \ln\left(\frac{\bar{o}_S}{o_S(\boldsymbol{r})}\right) + \sum_{\kappa'=A,F,S} (\chi_{\kappa\kappa'} - \chi_{S\kappa'})(o_{\kappa'}(\boldsymbol{r}) - \bar{o}_{\kappa'}) \right\} \tag{3.98}$$

where $\kappa = A, F$.

Finally the free energy in the mean field approximation can be written as

$$\begin{aligned} F[\{\rho_\kappa(\cdot)\}, \{\omega_\kappa(\cdot)\}] \ = \ & W[\{\rho_\kappa(\cdot)\}] - \sum_{\kappa=A,F,S} \int d\boldsymbol{r} \ \omega_\kappa(\boldsymbol{r}) \rho_\kappa(\boldsymbol{r}) + \\ & \sum_{\kappa=A,F,S} \bar{N}_\kappa \left\{ \ln \frac{\bar{N}_\kappa}{\mathcal{Z}_\kappa Q_\kappa} - 1 \right\} \ . \end{aligned} \tag{3.99}$$

where $W[\{\rho_\kappa(\cdot)\}]$ is given by Equation (3.90).

3.4.2 Summary – Self-consistent Mean Field Theory

To summarize, the theoretical approach presented above is based on the following assumptions:

- Polymer chains in bulk are described by continuous Gaussian random walks [110–112].
- Incompressibility is assumed, which is equivalent to assuming no volume change on mixing [90]. The local volume fractions of all components therefore sum locally to unity everywhere.
- Effective interactions between the components are two-body and are expressed in terms of Flory parameters [33] and local volume fractions of the components.
- A Mean field approximation is used which means that the density fluctuations about the most probable distribution are neglected.

These general assumptions result in equations for the density profiles of every component present in the system and a free energy expression written in terms of the densities, interaction parameters and effective fields.

The density profiles for both kinds of polymers are calculated using Equations (3.85) and (3.86), and the density distribution of solvent is determined using Equation (3.97). To obtain the density distributions of polymers, one has to solve the modified diffusion equation (Equation (3.64)) for the propagators $\boldsymbol{Q}_{\kappa}(\boldsymbol{r}, \tau | \boldsymbol{r}', 0)$ which

are subject to geometry-dependent boundary conditions. The potentials $\omega_\kappa(\boldsymbol{r})$ which modify the diffusion equation include enthalpic interactions between the molecules. The potentials are therefore written in terms of Flory parameters, and terms arising from the condition that there is no volume change upon mixing.

The problem has to be solved self-consistently. To solve the diffusion equations, potentials are needed which depend on the densities, and the densities are determined from solutions of the diffusion equations.

3.4.3 Problems in One Dimension

In this thesis, a further, lateral averaging approximation is used in the study of end-tethered polymers and thin films, which implies that the volume fraction profiles are homogeneous in the planes parallel to the surfaces. The problem therefore reduces to one dimension, and $\rho_\kappa(\boldsymbol{r}) \rightarrow \rho_\kappa(z)$ and $\omega_\kappa(\boldsymbol{r}) \rightarrow \omega_\kappa(z)$. It is useful to introduce integral representations of the propagators given by

$$q_\kappa(\boldsymbol{r}, \tau) = q_\kappa(z, \tau) = \int d\boldsymbol{r}' \, \boldsymbol{Q}_\kappa(\boldsymbol{r}, \tau | \boldsymbol{r}', 0) \tag{3.100}$$

and

$$\tilde{q}_A(\boldsymbol{r}, \tau) = \tilde{q}_A(z, \tau) = \int d\boldsymbol{r}' \, \tilde{\boldsymbol{Q}}_A(\boldsymbol{r}, \tau | \boldsymbol{r}', 0) \, . \tag{3.101}$$

Expressions for the densities follow and Equations (3.85) and (3.86) reduce to

$$\rho_F(z) = \frac{\tilde{N}_F}{\mathcal{Q}_F} \int_0^{Z_F} d\tau \; q_F(z, \tau) \; q_F(z, Z_F - \tau) \tag{3.102}$$

and

$$\rho_A(z) = \frac{\tilde{N}_A}{\mathcal{Q}_A} \int_0^{Z_A} d\tau\, \tilde{q}_A(z,\tau)\, q_A(z, Z_A - \tau)\,. \tag{3.103}$$

respectively. The propagator $q_\kappa(z,\tau)$, where $\kappa = A, F$, is proportional to the probability that a chain of type κ and of length τ ends at z given that it starts somewhere in the system. The $\tilde{q}_A(z,\tau)$ is proportional to the probability that an end-tethered chain of length τ ends at z given that it starts in the interface. The expressions for $\mathcal{Q}_F$ and $\mathcal{Q}_A$ in Equations (3.65) and (3.66) can also be rewritten in terms of the surface area $\mathcal{A}$ as

$$\mathcal{Q}_\kappa = \mathcal{A}\, \mathcal{Q}'_\kappa\,. \tag{3.104}$$

where, from Equations (3.65), (3.66), (3.100) and (3.101),

$$\mathcal{Q}'_F = \int dz\, q_F(z, Z_F) \tag{3.105}$$

and

$$\mathcal{Q}'_A = \int dz\, \tilde{q}_A(z, Z_A)\,. \tag{3.106}$$

The density of free polymer in Equation (3.102) can be rewritten in terms of the overall volume fraction $\bar{\phi}_F = \tilde{N}_F Z_F/(\rho_{0F}\mathcal{A}L)$ of free polymer with

$$\rho_F(z) = \frac{\rho_{0F}\bar{\phi}_F L}{Z_F \mathcal{Q}'_F} \int_0^{Z_F} d\tau\, q_F(z,\tau)\, q_F(z, Z_F - \tau)\,. \tag{3.107}$$

Similarly, the density of end-tethered polymer in Equation (3.103) can be expressed in term of the surface coverage $\sigma = \tilde{N}_A/\mathcal{A}$, and with Equation (3.106) the density is

$$\rho_A(z) = \frac{\sigma}{\mathcal{Q}'_A} \int_0^{Z_A} d\tau\, \tilde{q}_A(z,\tau)\, q_A(z, Z_A - \tau)\,. \tag{3.108}$$

The propagators $q_F(z,\tau)$, $q_A(z,\tau)$ and $\tilde{q}_A(z,\tau)$ have been constructed from $\boldsymbol{Q}_F$, $\boldsymbol{Q}_A$ and $\tilde{\boldsymbol{Q}}_A$, respectively. In addition $\boldsymbol{Q}_F$, $\boldsymbol{Q}_A$ and $\tilde{\boldsymbol{Q}}_A$ satisfy the modified diffusion equation. Equation (3.47), and can be used to show that q_F, q_A and $\tilde{q}_A$ also satisfy the modified diffusion equation

$$\left[-\frac{b_\kappa^2}{6}\frac{\partial^2}{\partial z^2}+\omega_\kappa(z)\right]q_\kappa(z,\tau)=-\frac{\partial}{\partial\tau}q_\kappa(z,\tau), \tag{3.109}$$

where b_κ is the statistical segment length.

The propagators must satisfy appropriate boundary conditions. At the end-tethering surface, we set $o_\kappa(z)=0$. As a consequence the first boundary condition is

$$q_\kappa(0,\tau)=0\,. \tag{3.110}$$

An impermeable wall is placed at $z=L$, which implies

$$q_\kappa(L,\tau)=0 \tag{3.111}$$

for $q_\kappa = q_F, q_A, \tilde{q}_A$. One end of the each end-tethered polymer is confined to the interface of thickness a. The propagator $\tilde{q}_A$ therefore satisfies the initial condition

$$\tilde{q}_A(z,0)=\theta(z)\theta(a-z). \tag{3.112}$$

The free end is simply restricted to the region $0<z<L$, so q_A obeys

$$q_A(z,0)=\theta(z)\theta(L-z). \tag{3.113}$$

Similarly, the ends of free polymer are also restricted to the region $0<z<L$ and

results in the initial condition

$$q_F(z,0) = \theta(z)\theta(L - z). \tag{3.114}$$

The formalism described in this section will be used in Chapters 6 and 7. Further details of the NSCF calculations are given in those chapters and details of the numerical solutions are given in a previous study [109].

Chapter 4

Crew-cut Micelles

4.1 Introduction and Review

Diblock copolymer micelles have been studied extensively both theoretically and experimentally. Most of the studies have been focused on systems of micelles with relatively short core blocks and long corona blocks. The result is a micelle structure with a small core and a thick corona. In the limit of strong segregation between the core block and the solvent, it is generally understood that the size of the micelle is controlled by the interplay between the interfacial tension and the free energy associated with stretching the core block. Consequently the radius of the micelle core scales as $l_B \propto Z_{CB}^{\alpha}$ where $\alpha \simeq 2/3$. This scaling relation has been consistent with experiment [116], and the above physical mechanism is believed to be correct. However, recent experimental studies of crew-cut micelles in water suggest otherwise and so further investigation on micelles with relatively long core forming blocks is warranted.

Of particular interest in all these systems is the sizes of the micelle core and corona as functions of the degrees of polymerization of the A and B blocks. Z_{CA} and Z_{CB}, respectively. de Gennes [117] found that the radius of the micelle cores scaled as Z_{CB}^{α} where $\alpha = 2/3$. Leibler *et al.* [19] extended the work of de Gennes for systems of A-*b*-B diblock copolymer micelles by minimizing the total free energy of the system. A scaling expression was obtained for fixed composition of copolymer ($Z_{CB}/Z_{CA} = K$ where K is a constant). The core radius of the micelles again scaled as Z_{CB}^{α} with $\alpha = 2/3$. Noolandi and Hong [118] have performed mean field calculations on diblock copolymer micelles in selective solvent with fixed Z_{CB}/Z_{CA} and obtained a scaling relation for the core radius l_B with $l_B \propto Z_{CB}^{\alpha}$ where $\alpha = 0.64$. The radius $l = l_B + l_A$ of the entire micelle was found to scale as $l \propto Z_C^{\gamma}$ and $\gamma = 0.68$. Whitmore and Noolandi [21] extended the work of Hong and Noolandi. Varying Z_{CA} and Z_{CB} independently, their results for the radius of the core gave $l_B \propto Z_{CB}^{\alpha} Z_{CA}^{\beta}$, with $0.67 \leq \alpha \leq 0.76$ and $-0.1 \leq \beta \leq 0$. For the thickness of the corona they found $l_A \propto Z_{CA}^{\nu}$ with $0.5 \leq \nu \leq 0.86$. Nagarajan and Ganesh [24] performed a similar calculation but with polydisperse systems of micelles. They obtained similar results with $l_B \propto Z_{CB}^{\alpha} Z_{CA}^{\beta}$ with $0.70 \leq \alpha \leq 0.73$ and $-0.17 \leq \beta \leq -0.08$, and $l_A \propto Z_{CB}^{\mu} Z_{CA}^{\nu}$ with $0.06 \leq \mu \leq 0.07$ and $0.68 \leq \nu \leq 0.74$.

All these theories assumed a constant volume fraction profile of all constituents in the micelle core and corona. Halperin [25] noted that micelles are structurally similar to colloidal particles coated by grafted chains and to star polymers. Therefore,

he performed a scaling analysis of the micelle structure by adapting the theory of Daoud and Cotton [26] for star polymers. He considered the two limiting cases of $Z_{CA} \gg Z_{CB}$ and $Z_{CA} \ll Z_{CB}$. The first case corresponds to micelles with relatively short core blocks and the scaling relation obtained gives $l_B \propto Z_{CB}^{\alpha}$ with $\alpha = 3/5$ and $l \propto Z_{CB}^{\alpha} Z_{CA}^{\beta}$ with $\alpha = 4/25$ and $\beta = 3/5$. The second limiting case corresponds to crew-cut micelles and $l \approx l_B \propto Z_{CB}^{\alpha}$ where $\alpha = 2/3$. These results are summarized in Table 4.1. Experiments on the structure of polystyrene-*block*-poly(ethylene oxide) (PS-*b*-PEO) block copolymer micelles in cyclopentane and deuterated cyclohexane were also done by Gast *et al.* [119]. They concluded that the star-like model was best suited for describing density profiles in micelles with moderate aggregation numbers and long corona blocks.

NSCF lattice calculations [48,49,51] have been done to obtain the volume fraction profiles in the core and corona. MD [122] and MC simulations have also been used to study micelles. In particular, Mattice *et al.* [83,84,123-131] have done extensive MC studies of diblock copolymer micelles on a cubic lattice but scaling relations were not investigated in these studies.

Generally, the predicted scaling relations have been in good agreement with experiments. Whitmore and Noolandi [21] made a direct comparison with the small angle neutron scattering (SANS) experiments of Selb *et al.* [116] on poly(styrene-*b*-butadiene) diblock copolymers in polybutadiene. The experimental results showed micelles with a narrow size distribution, and the micelle core radii scaled as $Z_{CB}^{\alpha} Z_{CA}^{\beta}$

	$l_B \propto Z_{CB}^{\alpha} Z_{CA}^{\beta}$		$l_A \propto Z_{CB}^{\mu} Z_{CA}^{\nu}$	
Authors	α	β	μ	ν
†de Gennes [117]	2/3			
†Leibler *et al.* [19]	2/3			
†Hong *et al.* [118]	0.64			
†Whitmore *et al.* [21]	0.67-0.76	-(0-0.1)	0	0.5-0.86
†Nagarajan *et al.* [24]	0.70-0.73	-(0.08-0.17)	0.06-0.07	0.68-0.74
†Halperin [25] $Z_{CB} \ll Z_{CA}$	3/5			
†Halperin [25] $Z_{CB} \gg Z_{CA}$	2/3			
‡Selb *et al.* [116]	0.75-0.81	-(0.14-0.19)		
†Bluhm *et al.* [22]	0.67	-0.17	0.12	0.54
‡Zhang *et al.* [1]	0.4	-0.15		
†Mean field theory (current)	0.77	-0.18	-0.051	0.864
†Hong *et al.* [21]	$l \propto Z_C^{\gamma}$, $\gamma = 0.68$			
†Halperin [25] $Z_{CB} \ll Z_{CA}$	$l \propto Z_{CB}^{\alpha} Z_{CA}^{\beta}$, $\alpha = 4/25$ and $\beta = 3/5$			
†Halperin [25] $Z_{CB} \gg Z_{CA}$	$l \approx l_B \propto Z_{CB}^{\alpha}$, $\alpha = 2/3$			
‡Munk *et al.* [120]	$R_H \propto Z_{CB}^{\alpha} Z_{CA}^{\beta}$, $\alpha = 0.71$ and $\beta = -0.09$			
‡Hurtrez [121]	$R_H \propto Z_C^{\gamma}$, $\gamma = 0.36$			
‡Hurtrez [121]	$R_H \propto Z_{CB}^{\alpha} Z_{CA}^{\beta}$, $\alpha = 0.09$, $\beta = 0.31$			
‡Hurtrez [121]	$R_H = 1.01 Z_{CB}^{\alpha} Z_{CA}^{\beta} + 0.78 Z_{CB}^{\mu} Z_{CA}^{\nu}$ $\alpha = 0.75$, $\beta = -0.17$, $\mu = -0.53$, $\nu = 0.74$			
†Bluhm *et al.* [22]	$R_M \propto Z_C^{\gamma}$, $\gamma = 0.44$			

Table 4.1: Scaling laws for various theories (†) and experiments (‡): l_B is the core radius, l_A is the thickness of the corona, $l = l_B + l_A$, R_H is the hydrodynamic radius and R_M is the radius of gyration of the micelle.

with $0.75 \leq \alpha \leq 0.81$ and $-0.19 \leq \beta \leq -0.14$. These results are consistent with the results and assumptions of the theory of Whitmore and Noolandi. Liu *et al.* [132] performed experiments on polystyrene-*b*-poly(2-cinnamoylethyl methacrylate) block copolymer micelles in cycloheptane. They observed that the core radius could be well represented by the scaling laws predicted from existing theories. Similar results were obtained by Kinning *et al.* [133] for poly(styrene-butadiene) block copolymer micelles in a polystyrene homopolymer. Other experimental results were obtained by Munk *et al.* [120]. They found that the hydrodynamic radius of polystyrene-*b*-poly(methacrylic acid) block copolymer micelles in dioxane and water scaled as $Z_{CB}^{\alpha} Z_{CA}^{\beta}$ with $\alpha = 0.71$ and $\beta = -0.09$.

In all cases reported above, the core radius is proportional to Z_{CB}^{α} with $\alpha \geq 0.6$. However, recent experiments give results which are quite different. Hurtrez [121] has performed experiments on poly(styrene-*b*-ethylene oxide) copolymers in water with short PS blocks and long PEO blocks forming the core and corona of the micelles, respectively. The author measured the hydrodynamic radius R_H of the micelles and fitted powers to the scaling functions predicted by the theory of Hong and Noolandi, Halperin, and Nagarajan and Ganesh and found $R_H \propto Z_C^{0.36}$, $R_H \propto Z_{CB}^{0.09} Z_{CA}^{0.31}$ and $R_H = 1.01 Z_{CB}^{0.75} Z_{CA}^{-0.17} + 0.78 Z_{CB}^{-0.53} Z_{CA}^{0.74}$, respectively. The comparison between experimental and theoretical results can be seen in Table 4.1. The important point is that all these scaling laws show weak dependence on the degree of polymerization of the copolymer. Superficially, this resembles the results of Bluhm and Whitmore [22] who

found a similar scaling relation for the radius of gyration R_M of the micelles with $R_M \propto Z_C^{\gamma}$ with $\gamma = 0.44$. However, that result is a consequence of the variable chemical composition of the molecules used in the experiments, and is fully accounted for by the theory. The third scaling law obtained by Hurtrez can be interpreted as the sum of two scaling laws: one for the core radius and one for the corona thickness. From such an analysis the strong dependence of the core radius on the B block is recovered. This result suggests that the hydrodynamic radius is better described as a function of the sum of the radius of the core and the thickness of the corona. Nonetheless, it is striking from this analysis that the thickness of the corona is strongly inversely dependent on the degree of polymerization of the B block, in disagreement with theory. We note that in these systems the measured radius of a micelle was, in some cases, comparable to the radius of gyration of a single molecule and the radius of the core is expected to be small compared to the thickness of the corona. It is therefore difficult to extract an accurate power law for the core radius from a measurement of the hydrodynamic radius.

Zhang *et al.* studied "crew-cut" micelles composed of polystyrene-*b*-poly(acrylic acid) block copolymers in water. They measured the core radii by transmission electron microscopy (TEM) and found that they scaled as $l_B \propto Z_{CB}^{\alpha} Z_{CA}^{\beta}$ where $\alpha = 0.4$ and $\beta = -0.15$. The weak dependence of the core radii on the core block once again contradicts the theoretical predictions. As noted by the authors, this difference may be due to non-equilibrium effects. If this is the case, the same effect might apply to

the similar systems studied by Hurtrez. Nonetheless, from this discrepancy in scaling, questions arise about the theoretical picture of the micelles, and further theoretical studies of micelles, and in particular crew-cut micelles, are warranted.

In this chapter, crew-cut micelles are studied with the use of MC simulations and simple mean field theory. The MC simulations are performed to probe the assumptions made in the mean field approach regarding the structure and size distributions of the micelles. The simulations are performed to study micelles in weakly segregated systems, and how the mechanisms involved in micelle formation might affect the final non-equilibrium structures found experimentally in strongly segregated systems. Scaling relations for the radius of the core with the composition of the block copolymer are investigated by simulating the equilibrium conditions under which the micelles form and determining the equilibrium conditions under which the polymers begin to be "frozen" in the micelles. In this way, the MC simulations are used to complement mean field theory.

The following section reviews the theoretical and experimental studies related to block copolymer micelles. Other sections include mean field results and discussion, a description of the MC simulation technique with results and discussion, and a summary.

4.2 Mean Field Study

The simple mean field theory of Bluhm and Whitmore [22] has been extended in Section 3.2 of Chapter 3 to systems of diblock copolymer in selective solvent. The solvent is now a different species than either block of the copolymer, as in the recent experiments (Hurtrez, Zhang *et al.*). We perform a direct comparison with the experimental results of Zhang *et al.* [1]. We calculate the scaling of the core radius of the micelle and the number of copolymers per aggregate N_M with the degree of polymerization of the copolymer.

In the expression for the free energy derived in Section 3.2, the statistical segment lengths for the A and B components of the copolymer are set to $b_A = 0.56$ nm and $b_B = 0.71$ nm, respectively. We did not find accurate values for the Flory interaction parameters in the literature so we estimated them. The solvent is a good solvent for the A block, so we chose $\chi_{AS} = 0.2$. Similarly, we set $\chi_{AB} = 0.2$. We found that the results in the strong segregation limit were relatively insensitive to changes in χ_{AS} and χ_{AB} compared to the dependence on χ_{BS}. For PS in water, χ_{BS} was found to be equal to 4.4 [134] for a temperature of 263.13°C. As the solvent quality worsens, χ_{BS} increases. The effect of this is to increase the size of the micelles. The mean field results will show micelles much larger than observed in experiments, but we found that the scaling laws are insensitive to the choice of Flory parameters. Our estimates are therefore adequate for our purposes. The densities for A and B components of the copolymer are $\rho_{0A} = 8.749$ nm^{-3} [134] and $\rho_{0B} = 6.204$ nm^{-3} [22], respectively, and

Composition		Experiment		Theory $\chi_{BS} = 4.4$			Theory $\chi_{BS} = 1.26$		
Z_{CB}	Z_{CA}	l_B	N_M	l_B	l_A	N_M	l_B	l_A	N_M
170	33	13	268	26.2	5.52	2735	16.8	4.82	581
180	28	12	217	27.7	4.67	3061	17.9	4.18	663
390	40	16	246	46.8	6.15	6783	30.4	5.44	1488
390	80	14	175	43.4	12.0	5416	27.4	9.90	1094
410	46	15	190	47.9	7.02	6934	31.0	6.13	1505
500	60	14	139	53.9	8.93	8103	34.7	7.64	1730
740	55	20	268	72.0	7.90	13032	46.8	6.90	2876
740	180	16	125	61.7	24.1	8216	38.1	19.3	1551
1140	170	20	188	86.8	22.4	14817	54.4	18.2	2925
1400	120	21	159	106	15.9	21960	67.9	13.2	4635
1400	310	18	87	90.7	37.9	13806	55.4	29.9	2523

Table 4.2: Radius of core, thickness of corona and number of copolymers per micelle from experiment [1] and theory.

$\rho_{0S} = 33.44\ \text{nm}^{-3}$ for the solvent density. The reference density is chosen as $\rho_0 = \rho_{0S}$. The molecular weights of the A and B monomers and solvent are $M_{CA} = 72.06\ u$, $M_{CB} = 104.15\ u$ and $M_S = 18.016\ u$, respectively.

Table 4.2 displays the experimental results of Zhang *et al.* and the mean field theoretical results. The core radii for the experimental and mean field theoretical data are plotted as a function of the degree of polymerization of the B block in Figure 4.1. In all cases, for $\chi_{BS} = 4.4$, the core radii from the theoretical results are much larger than the corresponding ones obtained experimentally. As discussed in Section 3.2.2, in strongly segregated systems such as the case here, it has been shown that the size of the core is determined mainly by the interplay between the stretching of the B block in the core of the micelle and the interfacial tension [21]. In these experiments the cores are too small for the B block to be significantly stretched.

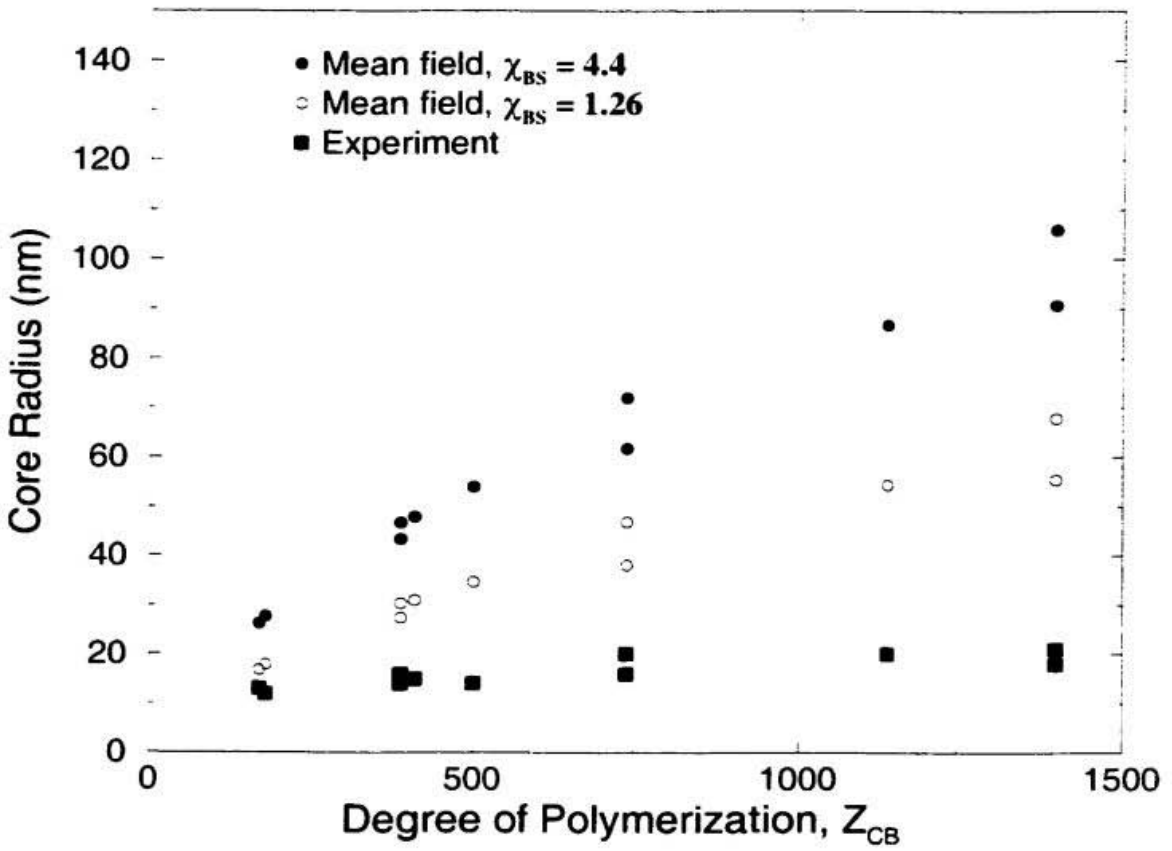

Figure 4.1: Core radius of micelle (l_B) as a function of the degree of polymerization of the B block (Z_{CB}).

There must therefore be a different mechanism that stabilizes the size of the micelles.

The explanation may lie in the process of micellization. In the experiments of Zhang *et al.*, the micelles are prepared by slowly decreasing the solvent quality. They describe two methods of preparation. In both cases the copolymers are dissolved in N,N-dimethylformamide (DMF). In the first method, 100 ml of water was added slowly from a burette. The solution was then dialyzed against water for 1 week until the DMF was removed. In the second method, the same process was used except

that methanol was slowly added to the solution of copolymer and DMF before any water was added. The effect of adding methanol was to ensure a gradual change in the solvent property. The two methods produced quite different results in the average size of the micelle cores. Method 2 produced micelles with cores much larger than those from method 1, clearly indicating that the method does affect the size distribution of the micelles which, in turn, indicates that these are non-equilibrium structures. It appears that micelles form relatively suddenly as the solvent quality decreases with increasing concentrations of water: A further decrease in the solvent quality causes the relaxation times for polymer exchange between micelles to become extremely long and the systems become trapped in a non-equilibrium state.

In light of this we have performed a second mean field calculation intended to simulate conditions of weaker segregation at which micelles might form. For these calculations, the Flory interaction parameter, χ_{BS}, was chosen such that $\phi_{CB} \simeq 0.8$ in the core, which resulted in $\chi_{BS} = 1.26$. The results are shown in Table 4.2 and Figure 4.1. For all systems the results are closer to the experimental data. For lower degree of polymerization of the B block the results are comparable to the experimental data. However, for higher degree of polymerization, the predicted core radii are still much larger than in the experiments, by as much as a factor of three.

The calculated core radius and corona thickness are shown in Figures 4.2(a) and 4.2(b). The results are well described by power laws, with $l_B \propto Z_{CB}^{\alpha} Z_{CA}^{\beta}$ with $\alpha = 0.77 \pm 0.01$ and $\beta = -0.18 \pm 0.01$, and for the corona $l_A \propto Z_{CB}^{\mu} Z_{CA}^{\nu}$ where

$\mu = -0.051 \pm 0.004$ and $\nu = 0.864 \pm 0.004$. In both cases the plots show good fits

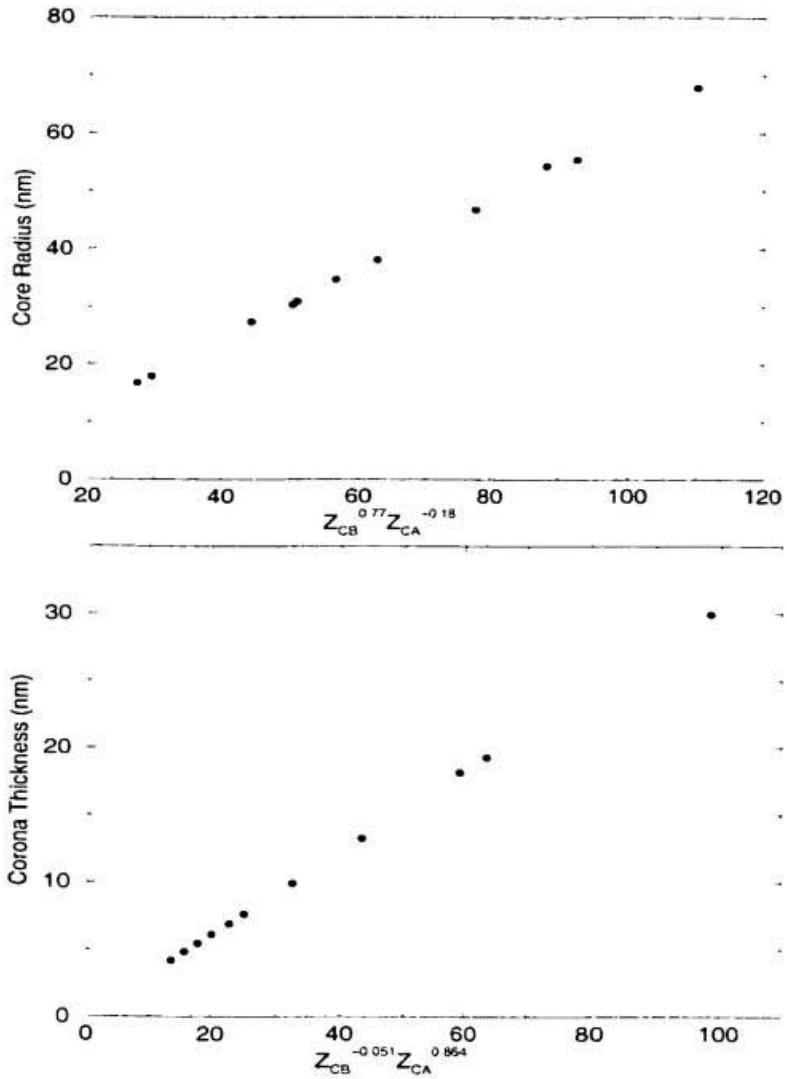

Figure 4.2: a) Core radius of micelle (l_B) as a function of the degree of polymerization of the A and B blocks. b) Thickness of corona (l_A) as a function of the degree of polymerization of the A and B blocks. ($\chi_{BS} = 1.26$)

and the fitted results are consistent with previous theoretical results but not with the experimental results of Zhang *et al.*

The theoretical results give a power law dependence on Z_{CB} for l_B which is close to 2/3, as seen in earlier theoretical predictions and experiments, for both choices of χ_{BS}. We note that in the experiments the sizes were measured using transmission electron microscopy (TEM). The samples of micelles were transferred to copper EM grids with thin film coatings of Formvar and carbon, and the water was then evaporated from the grid. The water in the core of the micelles was effectively removed which would result in a decreased radius. We investigated whether or not this effect explains the weaker scaling observed, by calculating, from the mean field results, what the radius of the micelles would be if all the solvent were removed from the core. The core radius with no solvent is then given by

$$R_{core} = \left(\frac{3 N_M Z_{CB}}{4\pi \rho_{0B}} \right)^{1/3} . \tag{4.1}$$

For this calculation, we took the results using $\chi_{BS} = 1.26$ for which the volume fraction in the core is $o_{CB} \simeq 0.8$ for all systems. Removing the solvent would cause the radii of the micelles to decrease by approximately 7%. The most important point is that all the radii are reduced proportionately, and this would have occurred for any choice of χ_{BS}. Hence, this effect cannot account for the discrepancy between experiment and theory in the scaling results.

Mean field theory predicts that the critical micelle concentration is mainly driven by the product $\chi_{BS} Z_{CB}$ as shown in Equation (3.24). As a result, for higher degree of polymerization Z_{CB} micelles should begin to form in systems with relatively better solvent quality (lower χ_{BS}). In addition, the enthalpic energy penalty in removing a

polymer from a micelle at a given χ_{BS} increases with increasing Z_{CB}. The relaxation time of a system is therefore expected to increase with increasing Z_{CB} for constant χ_{BS}. As a result non-equilibrium effects should begin to appear at a lower χ_{BS} for systems with higher Z_{CB}. In the following sections we performs MC simulations to study this effect and how it affects the power laws. This is done by identifying the solvent quality along with the properties of the micelles at the point where the polymers begin to be "frozen" in the micelles.

4.3 Monte Carlo Study

4.3.1 Monte Carlo Simulations

The general procedure describing the MC algorithm has been outlined in Chapter 2. Here we summarize the method. The simulations are performed on a cubic lattice of volume $V = L \times L \times L$. Periodic boundary conditions are applied in all directions. The systems contain A-b-B copolymer and solvent. The linear dimensions are chosen to accommodate all the polymers with the condition that $L > Z_C$ where Z_C is the chain length of the copolymer.

The effective monomers are subject to reduced nearest neighbor interaction energies, ϵ_{ij}, with $(i, j = A, B, S)$. In this instance the solvent is the same species as the A block of the copolymer, and only one effective reduced interaction energy remains where $\epsilon = \epsilon_{AB} = \epsilon_{BS}$. All remaining polymer-polymer and solvent-solvent

interactions are equal to zero. A new configuration is generated via all four types of motions: reptation, kink-jump, crankshaft and Brownian motion [79-82]. A new configuration is accepted or rejected on the basis of the *Metropolis* rule (described by Equation (2.6) and following paragraphs) and excluded volume constraints.

The number of iterations required to reach equilibrium is determined from the autocorrelation times which are calculated from the autocorrelation functions defined in Equations (2.11) and (2.12). The end-to-end vector autocorrelation function is defined to describe the relaxation of the end-to-end vectors of the polymers. When aggregates are present, it is imperative that polymers be allowed to escape from aggregates and migrate to other aggregates. The chain extraction [23, 83], chain exchange [23, 83], weighted chain extraction and weighted chain exchange autocorrelation times are therefore used to monitor these two processes. We also calculate the time required for all polymers to migrate a distance corresponding to the average nearest neighbor distance of free polymers as given in Equation (2.16). The relaxation time of the system is taken as the maximum of all time scales.

At the beginning of each simulation, the polymers are allowed to move freely for 10,000 N-bead cycles where $N = N_C Z_C$. The interaction energy is then increased in small increments. For each interaction energy the system is allowed to equilibrate for a period of 100 relaxation times, after which ensemble averages are taken over a period of 200 relaxation times.

As the interaction energy increases, small aggregates begin to form and, at lower

solvent quality, micellization occurs. Once micelles have formed, the density in the micelle cores is generally high and the enthalpic penalty in removing a polymer from a micelle is high due to the large number of energetic contacts. The result is a long system relaxation time. Therefore, there exists a lowest solvent quality (or maximum interaction energy ϵ) for which the simulations are feasible. The simulations are therefore performed by slowly increasing the interaction energy until the required solvent quality is reached or the central processor unit (CPU) time required to perform the simulations is too large. This method allows us to monitor structural properties and time scales as a function of solvent quality. This approach can therefore be used to identify the behavior at the point at which the polymers begin to be "frozen" in the micelles. As a practical matter, the simulations are restricted to relatively short polymers and weakly segregated systems.

4.3.2 MC Simulations of a Typical System

In the first simulation, we discuss the micelle characteristics and the behavior of a typical system as a function of the interaction energy. There are 1,000 copolymers in the system with $Z_{CB} = 50$ and $Z_{CA} = 10$. The overall volume fraction of copolymer is $\phi_C^0 = 0.02$.

In Figure 4.3(a), the various autocorrelation times and the time associated with the diffusion of the copolymers are plotted as functions of the interaction energy ϵ on a semi-log plot. During the simulation, ϵ was increased to 0.248 and subsequently

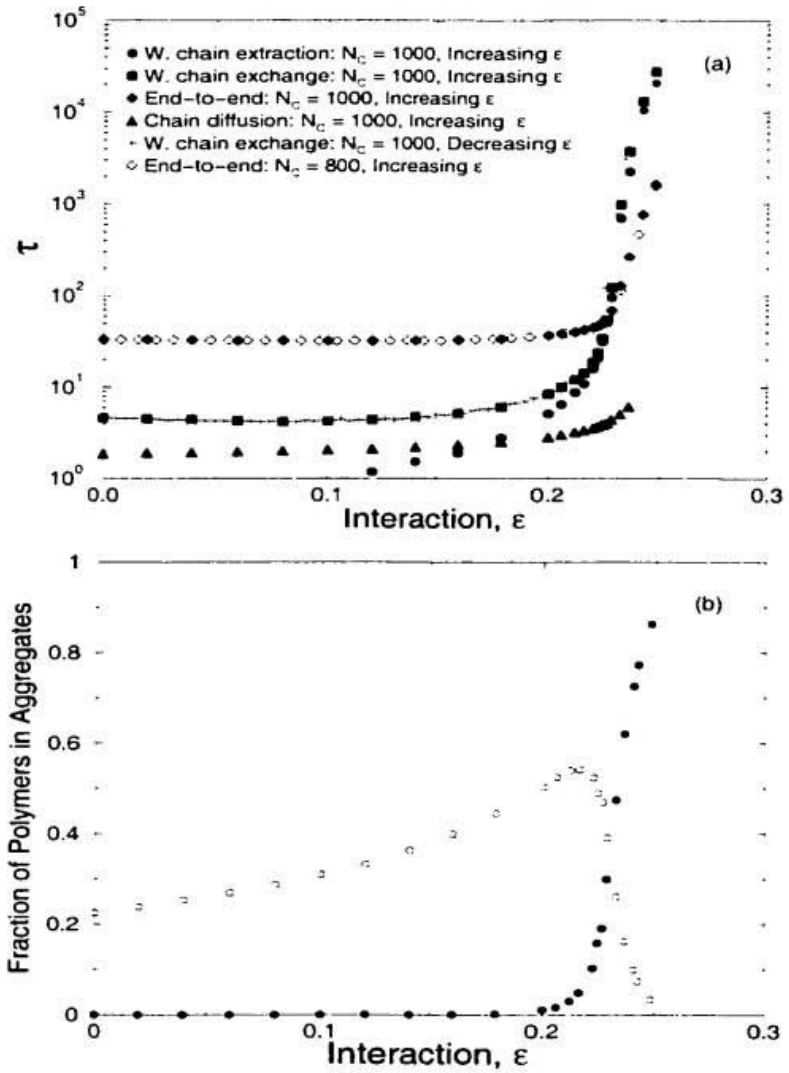

Figure 4.3: (a) Semi-log plot of the relevant autocorrelation times as functions of the interaction energy: Copolymer extraction (•), copolymer exchange (■), copolymer end-to-end (♦), copolymer diffusion (▲), copolymer exchange with decreasing ϵ (□) and copolymer end-to-end (◇) with $N_C = 800$. (b) Fraction of polymers in micelles (•) and small aggregates (○) vs ϵ.

reduced to zero. The results show that the weighted chain exchange autocorrelation time is independent of the annealing process. A second simulation with $N_C = 800$

was done to assure that finite size effects are negligible. As shown in Figure 4.3(a), the end-to-end vector autocorrelation times from both simulations agree.

For $\epsilon = 0$, there can be small, short lived aggregates with as few as 2 polymers in each one. Hence, the weighted chain extraction autocorrelation time is very small. However, the weighted chain exchange time is long compared to the weighted chain extraction time. As shown in Figure 4.3(b), when $\epsilon = 0$, a small fraction of polymers is in aggregates which results in few aggregates. In addition, the volume fraction of free chains in solution is small ($\phi_C \simeq 0.017$). The time required for a polymer to come in contact with another polymer or aggregate can therefore be long compared to the extraction time. As shown in Figure 4.3(b), the fraction of polymers in small aggregates increases slowly with ϵ while the fraction of polymers in micelles remains essentially zero for $\epsilon \lesssim 0.21$. When $\epsilon \simeq 0.23$, the weighted extraction and exchange times suddenly increase by two orders of magnitude over a small range of ϵ. At this point, the fraction of polymers in micelles increases sharply while the fraction of polymers in small aggregates decreases considerably. The changes in fractions of polymers in micelles and small aggregates are accompanied by an increase in the average size of micelles.

The copolymer end-to-end vector autocorrelation time and the time associated with the diffusion of polymers, which are quantities averaged over *all* polymers in the system, also increase with decreasing solvent quality. However, the increase in the end-to-end vector time is modest compared to the weighted extraction and exchange

times.

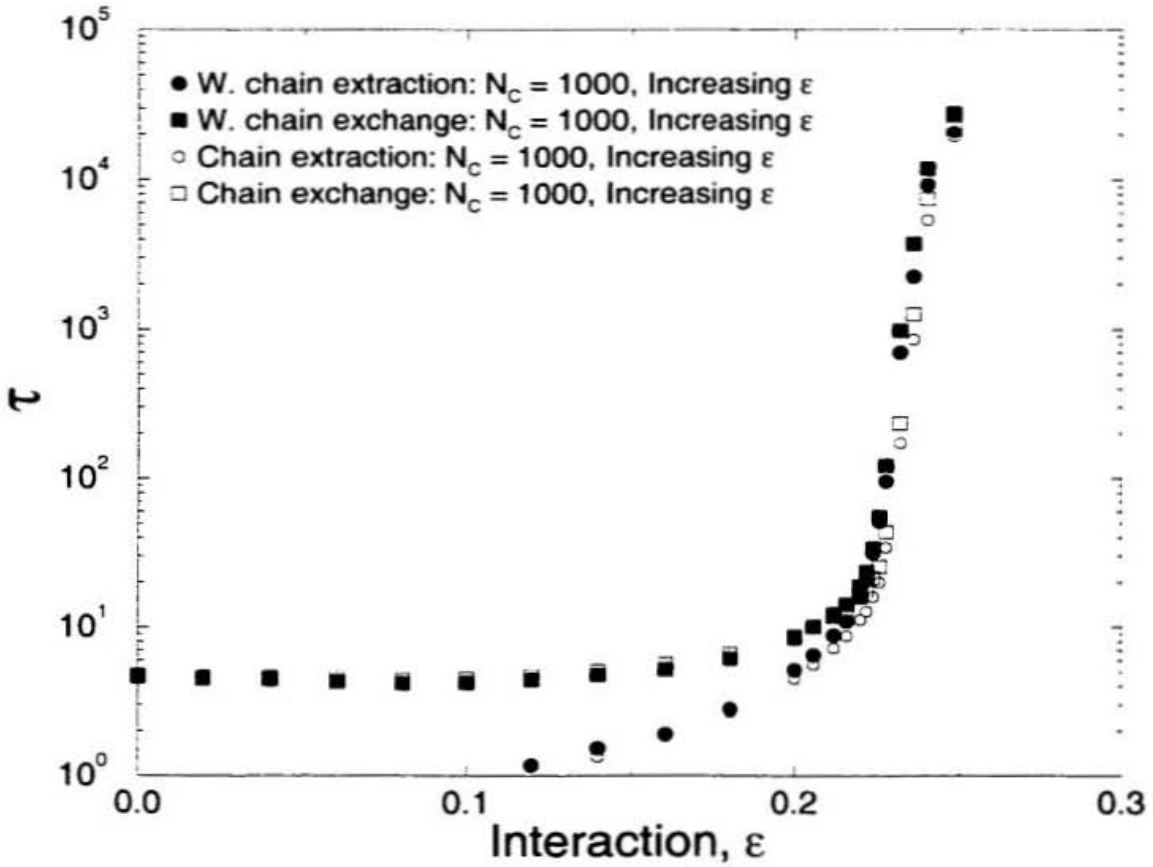

Figure 4.4: Semi-log plot of the weighted and non-weighted chain extraction and exchange autocorrelation times vs ϵ.

Figure 4.4 shows a comparison between the chain extraction and weighted chain extraction times, and the exchange and weighted exchange times. When $\epsilon > 0.2$ the weighted extraction time begins to deviate considerably from the extraction time. Differences between the two exchange times are qualitatively similar. As shown in Figure 4.3(b), the differences coincide with a sharp increase in the fraction of polymers in micelles. When the polymers are approximately equally distributed in micelles

and small aggregates ($\epsilon \simeq 0.23$), the relative differences between the two extraction and the two exchange times are maximum. The relative differences decrease with increasing ϵ as the fraction of polymers in micelles reaches unity. Nonetheless, when $\epsilon \gtrsim 0.21$ the weighted functions are always greater than their non-weighted counterpart. The polymers therefore have long residence times in the micelles compared to their residence times in small aggregates.

We now turn to the micelle characteristics. In the theory of Whitmore and Noolandi [21] a single size of micelles was assumed. This assumption was consistent with experiments [116] in the case of micelles with relatively small cores compared to the size of the corona, for which the experiments showed a narrow size distribution of micelles. This assumption is also reasonable in view of the experiments [1] on crew-cut micelles, which indicated a polydispersity index of 1.08. Figure 4.5 displays the frequency distribution of aggregates as a function of the number of polymers in the aggregates. The distribution shows the presence of small aggregates and micelles. The distribution of the micelles is narrow except for a rather long tail region. The long tail is due to micelles which have come in contact and are being counted as a single large aggregate. This is because, in the simulations, two micelles are counted as one aggregate if any B monomer from the core of one micelle is in contact with a B monomer in the core of the other one. Micelles coming in contact with each other can also be observed in a visual representation of a series of snap-shots of the polymer configurations. In our MC simulations of diblock copolymer micelles, the long tails in

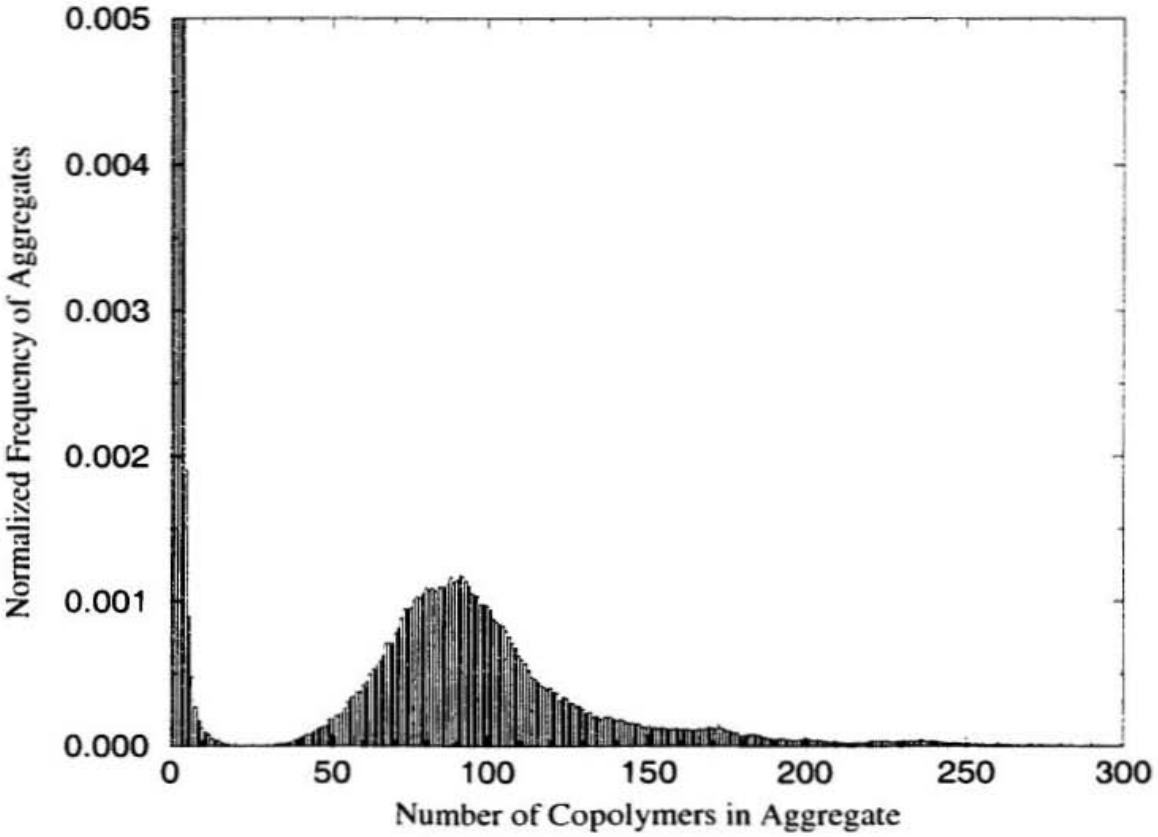

Figure 4.5: Normalized distribution of aggregates as a function of the number of copolymers in the aggregates. ($\epsilon = 0.248$. $Z_{CA} = 10$. $Z_{CB} = 50$)

the size distributions are seen only in cases where micelles consist of relatively short corona blocks. In the case of crew-cut micelles, the long tails diminish with increasing Z_C for constant Z_{CB}/Z_{CA}. The relatively thin coronas in crew-cut micelles therefore seem to enhance the frequency of micelles coming in contact with each other and forming larger micelles and aggregates. To quantify the size distribution of micelles,

we calculate the polydispersity index.

$$\frac{\tilde{N}_w}{\tilde{N}_n} = \frac{\left(\sum_{N=10}^{\tilde{N}} M_N N^2\right)\left(\sum_{N=10}^{\tilde{N}} M_N\right)}{\left(\sum_{N=10}^{\tilde{N}} M_N N\right)^2} . \tag{4.2}$$

The summation is over micelles and large aggregates with 10 or more polymers. N is the number of copolymers in a micelle. $\tilde{N}$ is the total number of copolymers in the system and M_N is the average number of micelles with N polymers. For the distribution in Figure 4.5, the polydispersity index is 1.14.

Figure 4.6(a) shows volume fraction profiles for both components of the copolymer averaged over micelles with 86 to 100 copolymers. The maximum in the distribution of micelles shown in Figure 4.5 lies in this interval. In general, averaging over all micelles tends to broaden the interface and the size specific averaging is therefore done to more accurately specify the volume fraction profiles.

In the core of these micelles at $\epsilon = 0.248$, the polymer volume fraction is as high as 0.82 and $10.5 \pm 0.9\%$ of copolymers remain in solution. The facts that the maximum volume fraction of the copolymer in the core is well below unity and the fraction of polymers in solution is moderately high indicate that the system is weakly segregated. As noted earlier, most experiments are in the limit of strong segregation. Nonetheless, we can extract information about the structure of the micelles and other characteristics of the system. As assumed in most mean field theories, the volume fraction profile in the core is relatively uniform, with the exception of the volume fraction of the A-block in the corona, $o_{CA}(r)$, as suggested by Halperin [25]. What is most striking in Figure 4.6(a) is the poorly defined core-corona interface: the corona

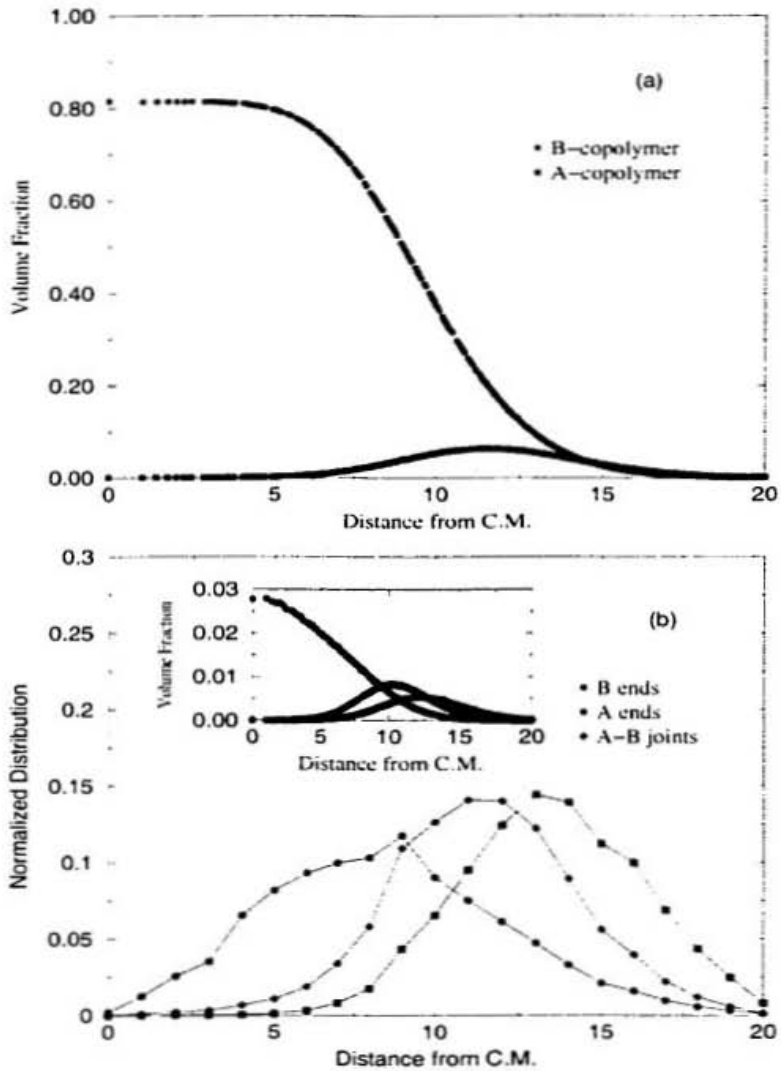

Figure 4.6: (a) Volume fraction profiles of A and B blocks and, (b), normalized distributions of A and B ends and A-B joints as functions of the distance from the center of mass (C.M.) of the micelles ($\epsilon = 0.248$, $Z_{CA} = 10$, $Z_{CB} = 50$): The inset in (b) shows the volume fraction profiles of A and B ends and A-B joints. The lines are shown as a guide to the eye only. Averages are taken over micelles with 86 to 100 copolymers.

region is not even well defined with $\phi_{CB}(r) \gtrsim \phi_{CA}(r)$ throughout most of the corona.

We attribute this to the fact that the corona block is relatively short, the host matrix

is solvent as opposed to homopolymer, and the system is weakly segregated. Entropic effects due to the solvent tend to produce a larger interface whereas enthalpic effects tend to produce the opposite effect. Therefore, for lower solvent quality, *i.e.* stronger segregation, the core and corona regions are expected to become better defined.

The similarity between the results of Halperin and other models with constant density profiles (see Table 4.1) implies that the approximation of uniform profiles does not affect the scaling relations significantly. Therefore, the fact that $o_{C,A}(r)$ is not constant cannot account for the discrepancy with the recent experimental results.

Figure 4.6(b) displays normalized distributions of the free A and B ends and the A-B joints of the copolymer. Normally, the distributions would be calculated from the number of ends or joints present in each shell of radius r about the center of mass the micelle. In this way, there can be large fluctuations in the number of sites per shell between two adjacent concentric shells. To reduce the effects of these variations, the data are collected in bins of unit width. A single bin can therefore include data from several shells, and this results in a smoother distribution of available sites per bin as a function of r. To a first approximation, the distribution of sites is well represented by the quadratic function Ar^2 where A is a constant.

The B ends do indeed penetrate to the center of the micelle core as assumed in the mean field picture, but they are distributed throughout the core. This result is consistent with previous MC simulations [124] and experiments [135]. For the A copolymer ends, the peak in the distribution is shifted slightly to the outer portion

System			$\tau_c = 8.000$			$\tau_c = 12.000$		
$Z_{C,B}$	$Z_{C,A}$	N_C	ϵ_c	N_M	R_{core}	ϵ_c	N_M	R_{core}
20	4	1000	0.320	91	7.58	0.325	111	8.09
30	6	1000	0.279	78	8.23	0.283	88	8.59
40	8	1000	0.254	68	8.64	0.256	73	8.88
50	10	1000	0.240	64	9.13	0.242	69	9.38
60	12	1000	0.228	54	9.17	0.230	64	9.71
20	10	1000	0.332	40	5.76	0.339	47	6.07

Table 4.3: Results for the radius of aggregate cores (R_{core}), the number of copolymers per aggregate (N_M) and the reduced interaction energy (ϵ_c) for $\tau_c = 8.000$ and $\tau_c = 12.000$ from MC simulations at different molecular weights.

of the corona as compared with Figure 4.6(a). This indicates that the A copolymer ends tend to reside on the outer edges of the corona, but a considerable fraction of the A ends is dispersed throughout the corona. The distribution of joints shows a maximum at the interface, and the wide distribution is consistent with a poorly defined interface. The distribution of B ends decreases to zero with decreasing r near the center of mass of the micelle, since the number of sites decreases to unity. However, the volume fraction of B ends is maximum at $r = 0$ as shown in the inset of Figure 4.6(b).

4.3.3 Systematic Monte Carlo Study

In this section, a series of MC simulations is performed to investigate if non-equilibrium effects can account for the discrepancy in power laws found in experiment and theory. The molecular weights of the copolymers are different in each simulation but the composition is kept constant in most cases (see Table 4.3). In each case the

solvent quality is decreased until the system relaxation time reaches a value well up in the range of relaxation times where micelles have formed. The properties of the system are determined for an interaction ϵ_c which corresponds to a system relaxation time of $\tau_c = 12.000$. This method of choosing ϵ provides a criterion for capturing the solvent quality at which non-equilibrium effects become significant. The choice of τ_c is arbitrary but the important point is that it is the same for all systems. The radius of the micelle cores, the number of copolymers per micelle, and the reduced interaction energy at which the system relaxation time is 12.000 N-bead cycles are shown in Table 4.3. We calculated the core radii from Equation (4.1) with $\rho_{0B} = 1$ to simulate "dried" micelles. Data are also given in Table 4.3 for values of ϵ which give $\tau_c = 8.000$. This is done to investigate the effect of the system relaxation time τ_c.

As shown in Figure 4.3, there can be a large change in the system relaxation time for a relatively small increment in ϵ. It is therefore difficult to determine, *a priori*, the interaction for which $\tau = \tau_c$. To determine ϵ_c, we performed an interpolation of the weighted chain exchange autocorrelation time as a function of ϵ. From our interpolation we determined the values of ϵ at which the weighted chain exchange autocorrelation time is equal to 8.000 and 12.000 N-bead cycles. At each value of ϵ we performed a Gaussian fit to the distribution of micelles as a function of the number of copolymers per micelle. The average number of polymers in micelles, N_M, was determined from the maximum of the Gaussian fits. An interpolation of N_M as a function of ϵ was also performed to determine N_M at ϵ_c. This method of determining

the average number of polymers per micelle is adequate since the relative change in N_M is small compared to the change in τ with increasing ϵ. Uncertainties in N_M due to the interpolation are only a few percent.

The system with $Z_{CB} = 20$ and $Z_{CA} = 4$ behaves differently than the rest. When the system relaxation time exceeds about 10,000 N-bead cycles very large non-spherical aggregates begin to form showing signs of macrophase separation. To illustrate the effect of the corona block, we performed a MC simulation for $Z_{CB} = 20$ and $Z_{CA} = 10$. The results are included in Table 4.3. In this case there is a narrow distribution of micelles with no large aggregates. Our simulations with Z_{CA}/Z_{CB} kept constant also show that the width of size distribution of micelles decreases with increasing Z_C. Nonetheless, as shown earlier from the MC simulation with $Z_{CB} = 50$ and $Z_{CA} = 10$, even when $Z_C = 60$ there remains a long tail in the distribution of micelles. The presence of large aggregates in the simulation with $Z_{CB} = 20$ and $Z_{CA} = 4$ is therefore attributed to the relatively short corona block compared to the core block augmented by the fact that Z_C is small.

The reduced interaction energy at which the copolymers begin to be trapped in the aggregates decreases with increasing molecular weight of the copolymer, as expected from the mean field predictions. Figure 4.7(a) shows a plot of the product $\epsilon_c Z_{CB}$ as a function of the chain length Z_{CB} for both $\tau_c = 8.000$ and $\tau_c = 12.000$. The plot shows a linear increase with Z_{CB} which can be expressed as

$$\epsilon_c Z_{CB} = m Z_{CB} + b \tag{4.3}$$

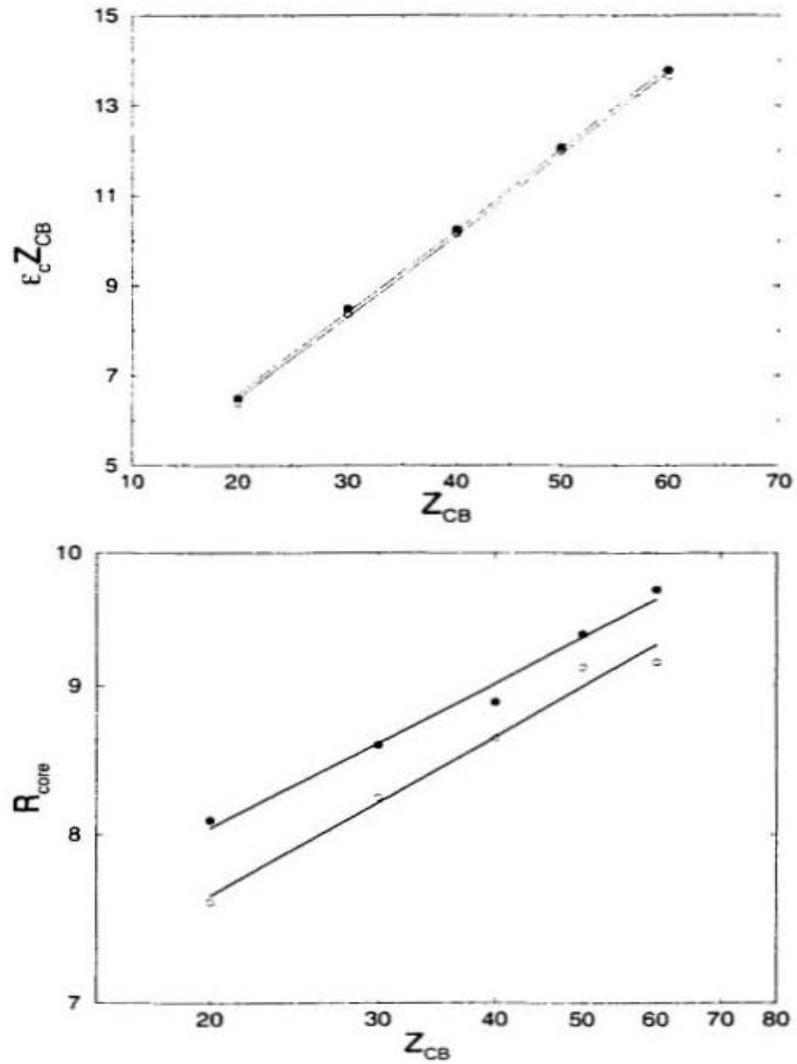

Figure 4.7: a) Product of the reduced interaction energy and the chain length of the B block versus the chain length of the B block. b) Radius of gyration of the core of the micelles versus the chain length of the B block (semi-log plot). The open and closed symbols correspond to $\tau_c = 8.000$ and $\tau_c = 12.000$, respectively. The straight lines correspond to the lines of best fit.

with $m = 0.182 \pm 0.003$ and $b = 2.85 \pm 0.14$ for $\tau_c = 8.000$ and, $m = 0.182 \pm 0.002$ and $b = 2.95 \pm 0.12$ for $\tau_c = 12.000$.

In Figure 4.7(b) the radius of the micelle core, with the solvent expelled from the core, is plotted on a log-log graph as a function of $Z_{C\text{-}B}$ for both choices of τ_c. Although N_M decreases with increasing molecular weight of the copolymer, as seen in Table 4.3, the core radii increase. The slope of the curve gives $\alpha = 0.181 \pm 0.014$ where $R_{core} \propto Z_{C\text{-}B}^{\alpha}$ for $\tau_c = 8.000$ and $\alpha = 0.165 \pm 0.012$ for $\tau_c = 12.000$. The power law therefore does not seem to be affected significantly by the choice of τ_c. The value of α is lower than the experimental results which give $\alpha \simeq 0.4$, and much less than equilibrium mean field results for which $\alpha \geq 0.6$.

The interpretation of these results requires care. It appears that setting the system relaxation time as a criterion for the solvent quality at which the micelle characteristics are calculated can explain a weak power law, as observed experimentally. There are other factors that may contribute to the observed scaling behavior. The choice of τ_c is judicious but, in each simulation, the combination of different types of moves was held fixed. In addition, the unit of time defined in the MC simulations is not necessarily proportional to the physical time. Therefore the criteria used to identify the conditions under which non-equilibrium effects become significant may not be optimal. Nonetheless, we note that for systems with well defined micelles, the radius of the micelle cores varies relatively slowly with increasing ϵ, or increasing system relaxation time. A relatively small change in the scaling law for the core radius would therefore be expected for a more realistic correspondence with the real physical time. The chosen criteria for τ_c are therefore believed to be reasonable and it is reasonable

to interpret the observed lower power as mainly an effect of the time scales.

4.4 Summary

We have performed mean field calculations and Monte Carlo simulations of block copolymer micelles. The mean field calculations were used to make direct comparisons with experiments and to investigate the scaling behavior of the micelles' cores and coronas. The MC simulations were used to probe the micelle structure, the polydispersity of micelles, the scaling of the core radius with the degree of polymerization of the core block of copolymer, and the effects of solvent quality in weakly segregated systems.

In recent experiments on crew-cut micelles, it was found that the core radii had a relatively weak power law dependence on the molecular weight of the B block. The mean field results showed micelles with core radii and number of polymers per micelle much larger than those found in these experiments. The calculations also showed that the crew-cut micelles observed in experiments are too small to have significantly stretched core blocks. The calculated core radii obeyed a stronger power law dependence, similar to those predicted by previous mean field calculations. This discrepancy between experiment and theory may be attributable to non-equilibrium effects. An attempt to investigate the non-equilibrium effects on the micelle size and scaling laws was made by varying the compatibility between the B block and the solvent. These calculations showed that improving the solvent quality produced

micelles with smaller cores, but they could not account for the discrepancy in the scaling laws between experiment and theory. In addition, mean field theory predicts that the critical micelle concentration and the solvent quality at which the polymer begin to be "frozen" in micelles is expected to be highly dependent on the product $\chi_{BS}Z_{CB}$. Together, these two effects suggest that the solvent quality at which the micelle systems cease to be at equilibrium depends on the molecular weight of the B block.

This was investigated with the use of Monte Carlo simulations. Other systems characteristics were also investigated using MC simulations. Autocorrelation functions were monitored to obtain system relaxation times. In all cases, the system relaxation time increases dramatically with an increase in the interaction energy as micelles form. The sharp increase in the system relaxation time is consistent with the idea that the strongly segregated systems found in experiments are non-equilibrium structures.

The MC simulations showed micelle cores comprised of the B block of the copolymer and solvent with relatively uniform density profiles, as assumed in mean field theory. However, the A block, which normally forms the corona, showed a non-uniform density profile. This is inconsistent with the structure of the corona region assumed in most mean field theories, but the work of Halperin [25] suggests that this assumption does not significantly affect any scaling behavior. The distributions of copolymer ends and the A-B copolymer joints were also investigated. The B ends

penetrate to the center of the micelles and the A ends extend to the edge of the corona. However, the A and B ends are also present throughout corona and core regions, respectively. The A-B joints are distributed across a relatively broad interface which is not well defined. This is attributed to a low molecular weight corona block, a low molecular weight host and weak segregation. The presence of a significant amount of copolymer in solution, along with a considerable amount of solvent in the cores of the micelles, also indicate that the systems are weakly segregated.

The micelle sizes were distributed with a relatively narrow distribution except for a long tail region. This is attributed to the fact that the core-corona interface is not well defined and the A block is relatively short, allowing the cores of micelles to come in contact with each other. The calculated polydispersity in the distribution of micelles was 1.14, which is slightly higher than the polydispersity of 1.08 observed in experiments [1].

The non-equilibrium effects on the scaling behavior of the micelle cores was investigated by identifying the equilibrium conditions under which the micelles form and the solvent quality at which they start to become non-equilibrium structures. Results from the MC simulations show that the system relaxation times do depend on the molecular weight of the B block and this effect can account for a large discrepancy in the scaling of the core radii between experiment and theory.

Chapter 5

Swollen Micelles

5.1 Introduction and Review

As discussed in Chapter 1, the swollen micelle systems consist of a ternary blend of A-b-B diblock copolymer micelles in an A homopolymer, or solvent, matrix with small amounts of added B homopolymer. The simple mean field theory of micelles has been extended to swollen micelles as reviewed in Section 3.3. The theory predicts that the threshold volume fraction of homopolymer (ϕ_{HB}^{macr}), at which the homopolymer macrophase separates, is given by Equation (3.38). The predicted phase behavior is in qualitative agreement with experiments which were reported by Whitmore and Smith [32]. However, questions arise about the assumed structure and size distributions of the micelles. These assumptions, along with the predicted phase behavior, can be investigated with the use of MC simulations.

Several MC studies [136,137] of block copolymer micelles have been done to study the structure of the micelles. Mattice *et al.* [83,123-130] have performed several MC

studies and developed techniques to study these systems. Further MC [138,139], mean field [52–54,140] and experimental [141,142] studies of micelles were done to study the effects of added solvent which was compatible with the core forming block of a triblock-copolymer. A MC study [143] was done with shorter surfactant molecules composed of a head group and a short tail in a solvent-solvent mixture. The studies were done to investigate the effects of added surfactants on stabilizing the domain sizes of the minority solvent component. Although these simulations have been restricted to relatively short polymers, the insights obtained on the behavior of these systems have been important.

In this chapter, we perform MC simulations of block copolymer in solvent with added homopolymer which is compatible with the core-forming block of the micelle. The main focus is on the investigation of the theoretical and experimental results obtained by Whitmore and Smith [32] which was discussed in Chapters 1 and 3. We revisit the phase behavior predicted by the mean field calculations by investigating the threshold volume fractions of homopolymer and its dependence on the volume fraction and degree of polymerization of the B homopolymer. The techniques developed by Mattice *et al.* to perform the simulations are used as described in Section 2.2.1 and have also been extended to suit this particular type of simulation and gain some understanding of these types of systems. The MC simulations have been restricted to relatively low molecular weight polymers. Nonetheless, they are used to address questions about some of the assumptions in the mean field approach, including the

structure and size distribution of micelles, for weakly segregated systems.

5.2 Monte Carlo Simulations

The general Monte Carlo algorithm is given in Chapter 2. Here we describe the simulations specific to swollen micelles. The systems contain A-b-B copolymer (C), homopolymer (HB) and solvent (S). As usual, each effective monomer occupies a site of a simple cubic lattice and the empty sites correspond to solvent. Periodic boundary conditions are applied in all directions.

The monomers are subject to an excluded volume interaction and nearest neighbor reduced interaction energies ϵ_{ij} $(i, j = A, B, HB, S)$. The homopolymer is the same species as the B block of copolymer and the solvent is the same species as the A block of copolymer. All interactions between like species of polymer-polymer and solvent-solvent are set to zero ($\epsilon_{ii} = 0$). Therefore, only one effective reduced interaction energy parameter remains, which is $\epsilon = \epsilon_{AB} = \epsilon_{BS}$. New configurations are generated by reptation, kink-jump, crankshaft and Brownian motion [79–82]. For Brownian motion the polymers are allowed to move anywhere within a sphere of radius corresponding to 30 lattice sites.

After a new configuration is chosen, if the new site is occupied the move is rejected; otherwise the change in energy is calculated and transitions are accepted or rejected according to the *Metropolis* rule.

Autocorrelation functions are calculated using Equation (2.11) for the polymer

end-to-end vectors $\vec{R}_C$, $\vec{R}_{CB}$, $\vec{R}_{CA}$ and $\vec{R}_{HB}$, corresponding to the copolymer, B block of copolymer, A block of copolymer and B homopolymer, respectively.

To monitor relevant relaxation times associated with the polymers in aggregates we make use of the weighted chain extraction and exchange autocorrelation functions defined in Equation (2.13). The autocorrelation functions are calculated for the copolymer and the homopolymer separately. Each autocorrelation function is monitored, and its related autocorrelation time is calculated in Equation (2.14).

The motion of the copolymers and homopolymers is also monitored by calculating diffusion constants D_C and D_{HB}, respectively, as defined in Equation (2.15), and the related times defined by Equation (2.16).

As in the MC simulations of crew-cut micelles, there are limits on the degree of polymerization of the polymers and the solvent quality where the simulations are feasible. As a consequence, the simulations are done with relatively low molecular weight polymers and weak segregation.

At the beginning of each simulation the interaction energy ϵ is set to zero and the simulation is run for a period of 10,000 N-bead cycles, where $N = N_C Z_C + N_{HB} Z_{HB}$. Once the polymers have reached a random configuration the interaction energy ϵ is slowly increased in small increments. At each value of ϵ the system is allowed to reach equilibrium by iterating for a period of time. For every value of ϵ, ensemble averages are taken over a period of 100-200 relaxation times. Once the ensemble averages are done, the interaction energy is increased and this process is repeated until the

maximum interaction energy is reached.

5.3 Results and Discussion

5.3.1 Swollen Micelle System

For relatively low homopolymer molecular weight and volume fraction, the homopolymer is expected to be solubilized within the micelle cores. In this section we study a typical system in which solubilization is expected, to probe the assumptions of the mean field model. The system consists of copolymers with $Z_{CB} = 30$ and $Z_{CA} = 42$ and homopolymers with $Z_{HB} = 4$. The composition of the copolymer was chosen to correspond with the experiments of Whitmore and Smith [32]. The overall volume fractions of copolymer and homopolymer are $\phi_C^0 = 0.025$ and $\phi_{HB}^0 = 0.0125$, respectively. The maximum interaction parameter was $\epsilon = 0.31$.

Figure 5.1 shows the autocorrelation functions for $\epsilon = 0.31$. They are plotted on different time scales, for convenience. When $\epsilon = 0.31$, micelles have formed and the copolymer weighted chain extraction and exchange autocorrelation functions exhibit the slowest decay. At constant ϵ, the enthalpic penalty in removing a polymer from an aggregate increases with increasing number of B units in the molecules. Therefore, the weighted chain extraction and exchange functions for the low molecular weight homopolymers decay much more rapidly than the corresponding copolymer functions.

Previous simulations by Haliloğlu *et al.* [84] suggest that the decays of these func-

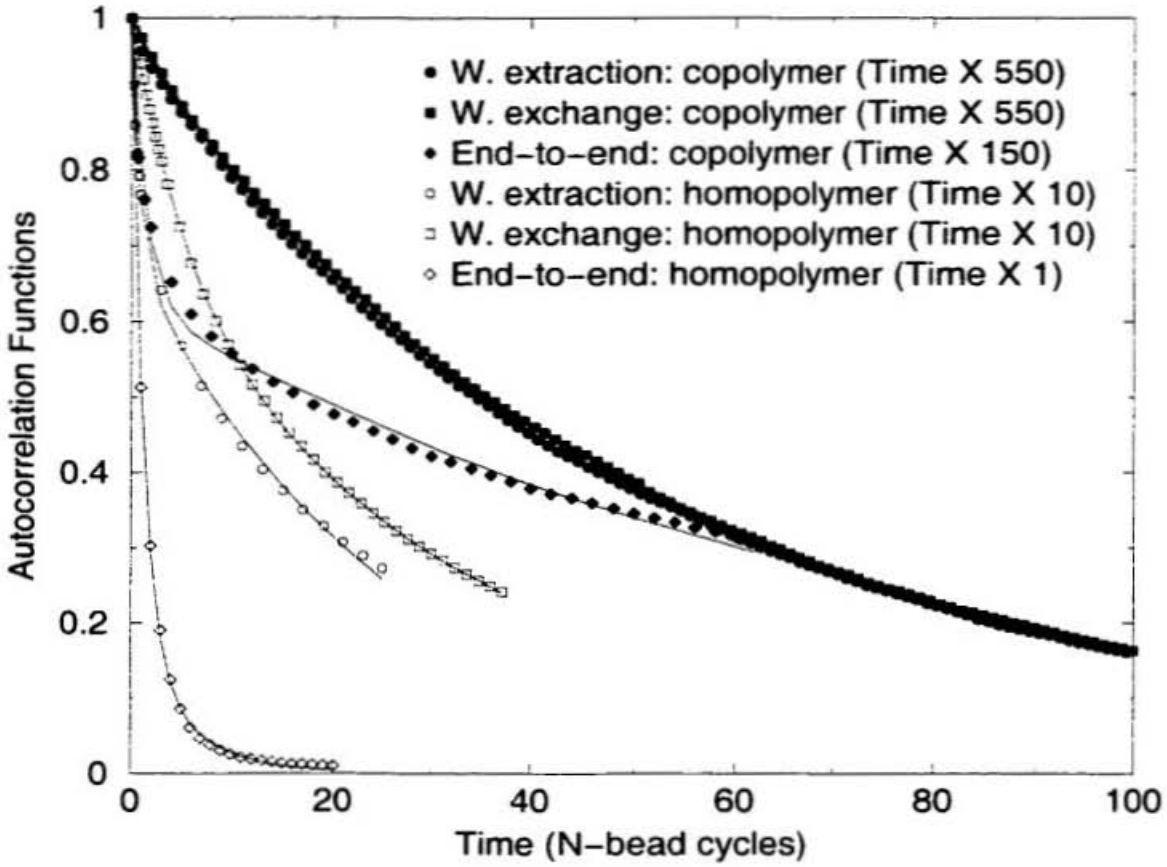

Figure 5.1: Autocorrelation functions: Homopolymer extraction (○), homopolymer exchange (□) and homopolymer end-to-end (◇). The filled symbols correspond to the copolymer autocorrelation functions. $\epsilon = 0.31$, $Z_{CA} = 42$, $Z_{CB} = 30$, $Z_H = 4$, $o_C = 0.025$ and $o_{HB} = 0.0125$. The lines are fits to a function of the sum of two exponentials. The functions are plotted on different time scales which are given in the legend.

tions are not necessarily simple exponentials. Therefore, we fitted the data for each function to a sum two exponential functions, *i.e.*,

$$C_s(t) = Ae^{-t/\tau_s} + (1 - A)e^{-t/\tau_l} \tag{5.1}$$

where A, τ_s and τ_l are the fitted parameters. The results are shown in Table 5.1. The

Function	A	τ_s	τ_l
Copolymer weighted extraction	0.074	5.4×550	56×550
Copolymer weighted exchange	0.056	6.2×550	56×550
Copolymer end-to-end	0.38	1.5×150	82×150
Homopolymer weighted extraction	0.31	0.84×10	26×10
Homopolymer weighted exchange	0.36	6.2×10	38×10
Homopolymer end-to-end	0.81	1.3×1	5.3×1

Table 5.1: Results from the fit of the autocorrelation functions to a sum of two exponential functions. The times τ_s and τ_l are given in N-bead cycles. $\epsilon = 0.31$. $Z_{CA} = 42$. $Z_{CB} = 30$. $Z_{HB} = 4$. $\phi_C = 0.025$ and $\phi_{HB} = 0.0125$.

fitted curves show reasonably good agreement with the data for all curves. Stretched exponential relaxation has also been studied [85,86] in polymer dynamics. We did fits to Kohlrausch-William-Watts stretched exponential functions [87] of the form $e^{-(t/\tau)^\beta}$. These fits also resulted in good agreement with the data, with values of β varying from 0.39 to 0.93. In contrast, fits to single exponential functions did not result in a good agreement. We note that the fits are done over a short time interval and a full analysis would require monitoring the functions over a longer time.

The values of A in Equation (5.1) which are shown in Table 5.1 are higher for the functions averaged over homopolymer than their counterparts involving the copolymers. When $\epsilon = 0.31$, about 68% of homopolymers are in solution while only 11% of copolymers are in solution. Qualitatively, the mechanisms responsible the short time scales are therefore expected to dominate for functions related to the homopolymer. On the other hand, the long time processes in the relaxation of copolymer are expected to be more important. The values of A for the end-to-end vector functions

are higher than those from the weighted chain extraction and exchange functions. In this system there are micelles, small aggregates and free molecules. The end-to-end vector autocorrelation functions are averaged over all polymers in the system, while the weighted chain extraction and exchange functions do not include the free polymers. The fact that the weighted functions include only those polymers in aggregates is consistent with lower values of A. Our results are in qualitative agreement with the physical picture that the short time processes are associated with relaxation of the free polymers and perhaps the polymers in small aggregates. We note that a quantitative analysis would require a detailed analysis of all mechanisms in each function. In conclusion, the non-exponential decay of the autocorrelation functions is due to heterogeneity in the systems and the fact that there can be more than one mechanism responsible for relaxation, as suggested in Section 2.2.1.

Figure 5.2 shows the various autocorrelation times and the times associated with diffusion of the copolymer and homopolymer as functions of the interaction ϵ. As discussed above, the autocorrelation times increase with increasing interaction energy. The onset of the rapid increase occurs at $\epsilon \simeq 0.28$ where small aggregates and micelles have formed. As the solvent quality decreases more micelles form and consequently the relaxation times, and more specifically the copolymer weighted exchange autocorrelation time, increase dramatically. The relatively low molecular weight homopolymer can more easily migrate from aggregates to other aggregates, and more remain in solution. This effect is seen from the homopolymer weighted exchange auto-

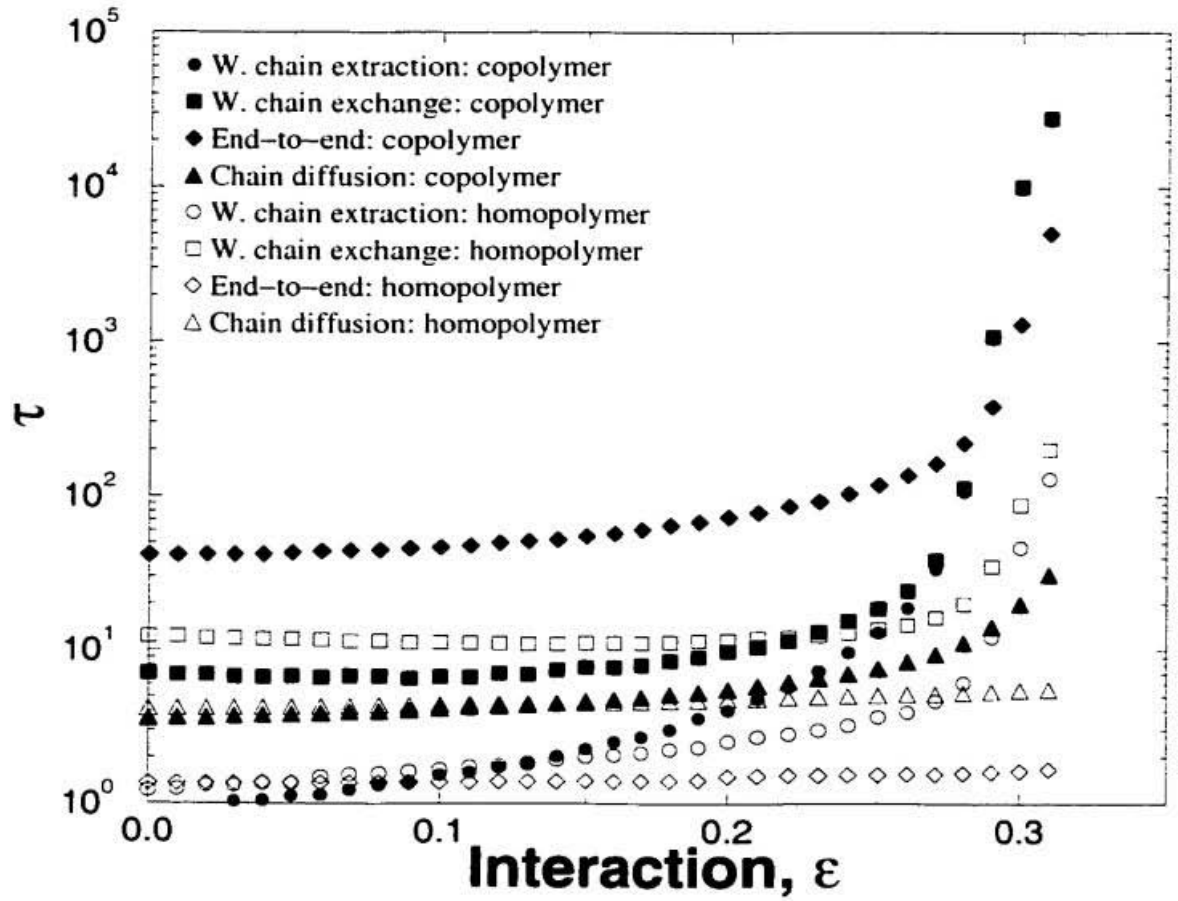

Figure 5.2: Semi-log plot of the relevant autocorrelation times as a function of the interaction energy: Homopolymer extraction (○), homopolymer exchange (□), homopolymer end-to-end (◇) and homopolymer diffusion (△). The closed symbols correspond to the data for the copolymer. $Z_{CA} = 42$, $Z_{CB} = 30$, $Z_{HB} = 4$, $o_C = 0.025$ and $o_{HB} = 0.0125$.

correlation time which shows a relatively modest increase with increasing interaction ϵ.

At low values of ϵ, there is a considerable difference between the weighted chain exchange and extraction autocorrelation times for both copolymer and homopolymer. As discussed in Chapter 4, the time required for a polymer to come into contact with

another polymer or aggregate may be large compared to the time required to escape the aggregate. At lower solvent quality, the opposite is true and time required to escape a micelle is much larger than the time needed to migrate freely to another micelle which results in nearly equal chain exchange and extraction times for the copolymer. Also, as aggregates form, the copolymers present in the aggregates become elongated and they can remain oriented for long periods of time. In the core of the aggregates, the polymer volume fraction can be high and both copolymers and homopolymers may remain in the aggregates for extended periods of time. The mobility of the polymers in the aggregates is reduced, which results in an increase in the end-to-end vector autocorrelation times and the time associated with the diffusion of polymers. At high solvent quality, the time associated with the diffusion of polymers is smaller than the end-to-end vector autocorrelation times. As discussed in Section 5.2, the polymers are allowed to move a large distance during a Brownian motion type move which accounts for the relatively high diffusion constants.

Figures 5.3(a) and 5.3(b) show the normalized frequency of aggregates as a function of the number of copolymers and homopolymers, respectively, in the aggregates. The distributions in both figures show the presence of free polymers in solution, small aggregates and micelles. Generally, as the solvent quality decreases, small aggregates first begin to form as shown in Figure 5.4. With decreasing solvent quality the number of small aggregates increases and micelles begin to form (see inset of Figure 5.4). A further decrease in the solvent quality, *i.e.* beyond $\epsilon \simeq 0.27$, results in fewer small

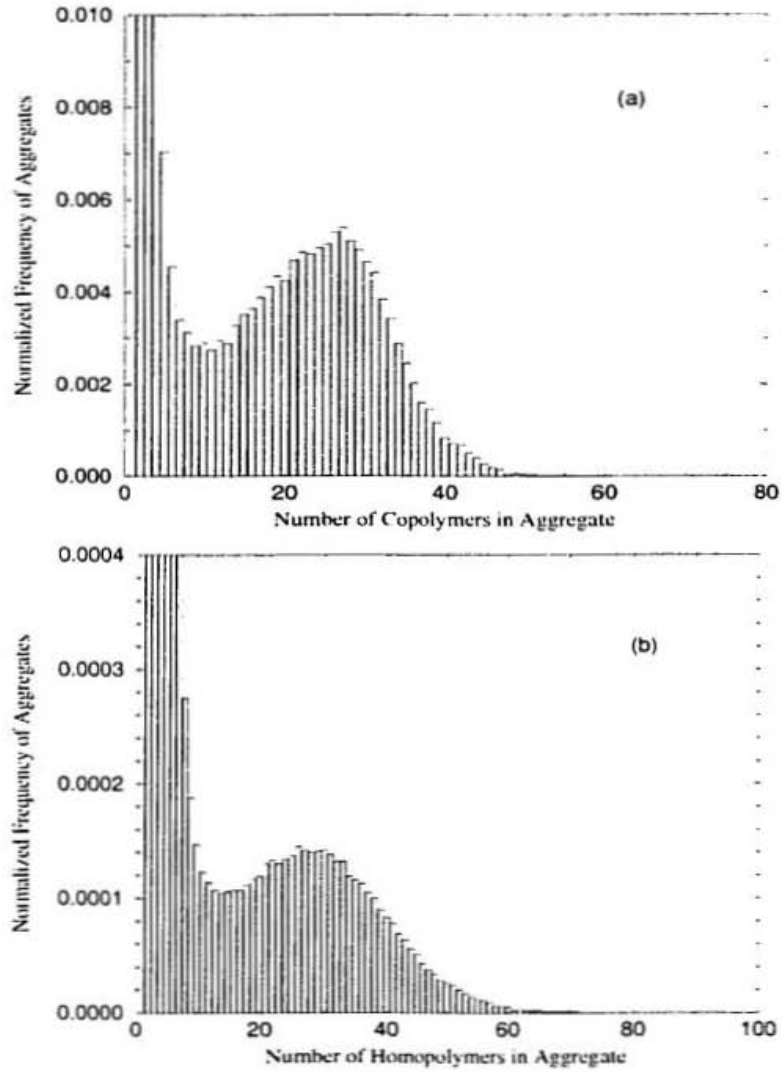

Figure 5.3: Normalized distribution of aggregates as a function of the number of copolymers (a) or homopolymers (b) in aggregates ($\epsilon = 0.31$).

aggregates and an increase in the number and size of the micelles. As this process continues, the micelles continue to grow in size but the number of micelles decreases.

In addition, as ϵ increases, the fraction of polymers in aggregates also increases, as shown in Figure 5.5. When micelles have formed, the fraction of homopolymer

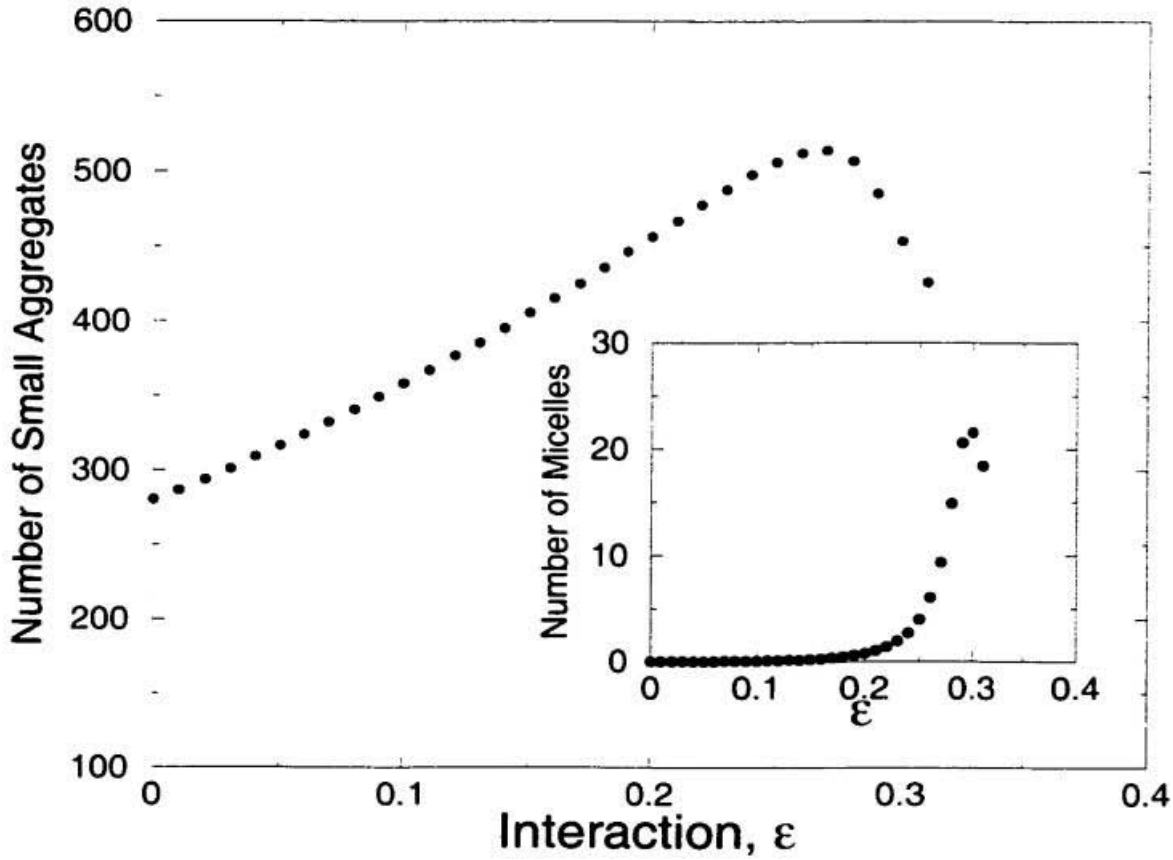

Figure 5.4: Number of small aggregates in the system as a function of the interaction energy, ϵ. The inset shows the number of micelles in the system as a function of ϵ. A small aggregate is defined as having more than two but less than ten polymers. A micelle has ten or more polymers and a well defined core-corona interface.

in aggregates is much lower than that of the copolymer, due to the lower molecular weight of the homopolymer.

Figure 5.6(a) shows the volume fraction profiles averaged over micelles with approximately $1135 \pm 7\%$* effective monomers which corresponds to approximately the

*Actually the volume fraction profiles are averaged over micelles with 1135 ± 85 effective monomers. The entire range of micelle sizes is discretized into 10 intervals and this defines the number of monomers and the width of the interval. The interval which matches the maximum in the distribution of micelles is then chosen.

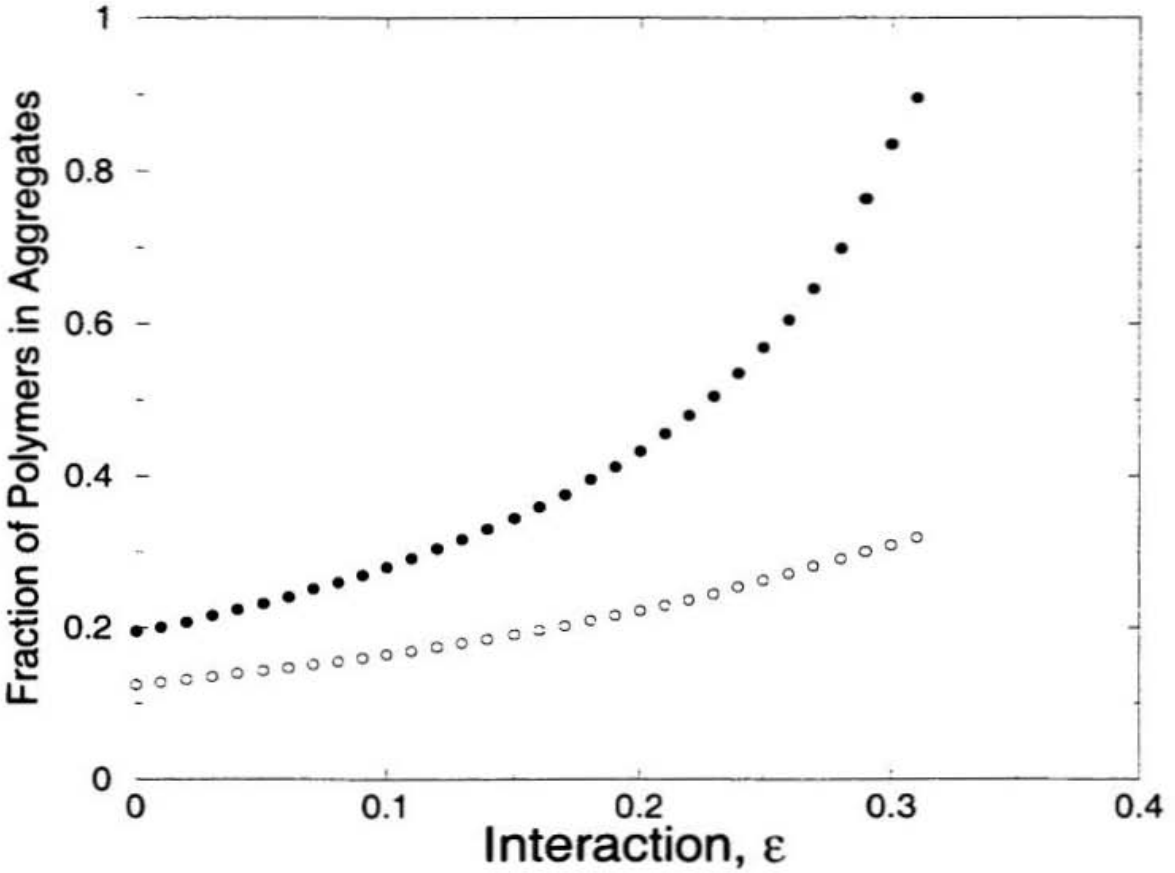

Figure 5.5: Fraction of polymer in aggregates as a function of the interaction ϵ: copolymer (•) and homopolymer (○).

average size of the micelles. The volume fraction of the copolymer plus that of the homopolymer is as high as 90%. In the core region the volume fraction profiles for the B copolymer and B homopolymer are quite uniform. This result supports previous experiments [92–95] and theories [96, 97] in showing solubilized low molecular weight homopolymer throughout the subdomains. On the other hand, the volume fraction profile in the corona region is non-uniform.

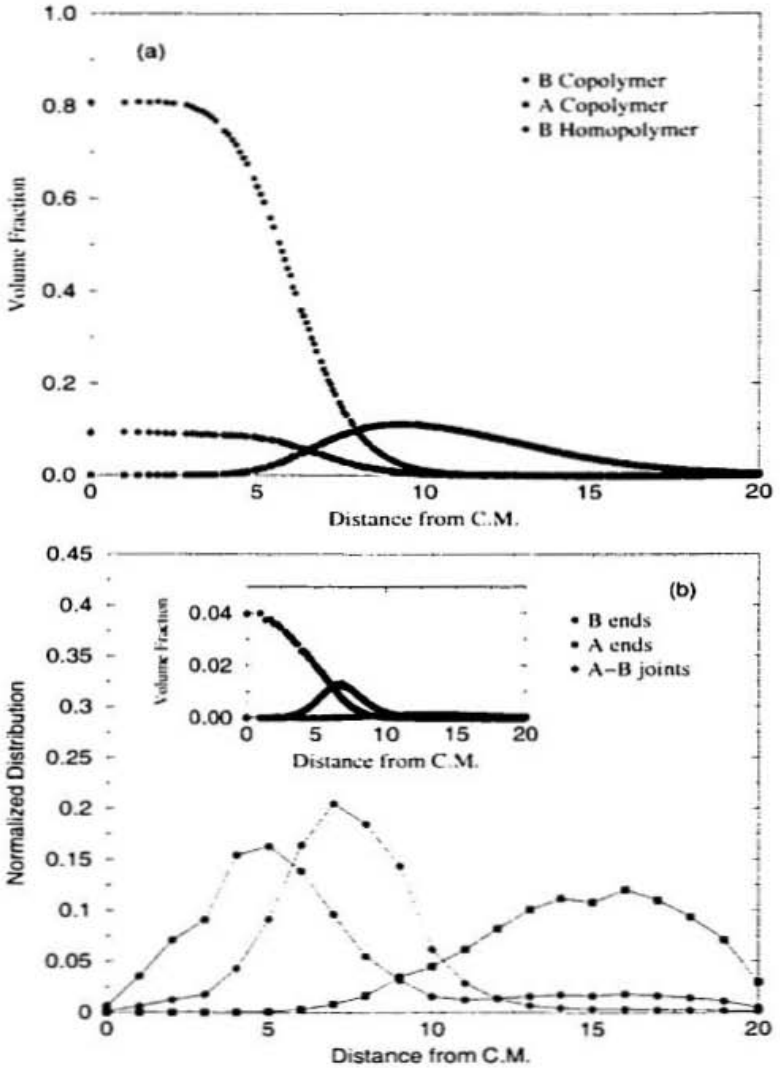

Figure 5.6: (a) Volume fraction profiles of A and B blocks of copolymer and, (b), normalized distributions of A and B copolymer ends and A-B copolymer joints as functions of the distance from the center of mass (C.M.) of the micelles: B copolymer (•), A copolymer (■) and B homopolymer (♦). The inset in (b) shows the volume fraction profiles of A and B ends and A-B joints. The lines are shown as a guide to the eye only. $\epsilon = 0.31$.

Figure 5.6(b) shows normalized distributions of copolymer ends and A-B copolymer joints throughout the micelles. For this Figure, the data were binned in the same

way as described for Figure 4.6(b). The B copolymer ends penetrate to the center of the micelles as assumed in the mean field approach but, again, they are distributed throughout the core. The maximum in the distribution of the B ends occurs at $r = 5$. This is consistent with an increase in the number of sites available with increasing r. The inset of Figure 5.6(b) indicates a decrease, with increasing r, in the volume fraction of B ends, beyond $r \simeq 5$. However, a local maximum in this distribution occurs at $r \simeq 16$ in a region of the corona beyond the core-corona interface. This is obviously due to the increased number of available sites, but is nonetheless surprising. The A copolymer ends are distributed throughout the corona, and the A-B copolymer joints are at the core-corona interface. The interface is not sharp, as expected for a weakly segregated system. This relatively weak segregation is also consistent with the fraction of copolymer and homopolymer remaining in solution, 11% and 68%, respectively, as shown in Figure 5.5.

To summarize, this system shows a reasonably narrow distribution of micelle sizes. The homopolymers are solubilized within the micelle cores resulting in a microphase consisting of micelles swollen by the homopolymer. The volume fractions are uniform within the core, as assumed in the mean field approach, but not in the corona. A considerable fraction of the polymers remain in solution which indicates that for interaction energies up to $\epsilon = 0.31$ the system is not strongly segregated.

5.3.2 Microphase vs. Macrophase Separation

As discussed earlier, mean field calculations predict a threshold volume fraction of homopolymer below which the homopolymer is solubilized within the micelle cores, and above which, the system will separate into a macrophase. We are interested in the solubilization limits imposed on the homopolymer. Furthermore, the mean field theory predicts that the solubilization limit depends on the product χZ_{CB}. ϕ^0_{CB} and the ratios Z_{HB}/Z_{CB}. In this section, a series of simulations has been done for various ratios of volume fractions and degrees of polymerization. As seen in the previous section, the system relaxation time imposes limits on the solvent quality at which the simulations are feasible. In order to perform a series of simulations at constant interaction energy a lower molecular weight copolymer with $Z_{CA} = 14$ and $Z_{CB} = 10$ has been chosen for all subsequent simulations. The linear dimensions are chosen such that $L_i = 80$ $(i = x, y, z)$.

Two simulations are of particular interest. In both simulations the copolymer volume fraction has been set to $\phi^0_C = 0.02$ and $Z_{HB} = 6$. In the first one, the homopolymer volume fraction is chosen such that $\phi^0_{HB}/\phi^0_{CB} = 0.1$. In the second one, the homopolymer volume fraction is increased to $\phi^0_{HB}/\phi^0_{CB} = 0.5$ with Z_{HB} kept constant. Systems with a narrow distribution of micelles and homopolymer uniformly distributed throughout the micelle cores are identified as microphase separated. System showing the presence of very large aggregates with the homopolymer accumulated at the center and copolymer at the edges are identified as macrophase separated.

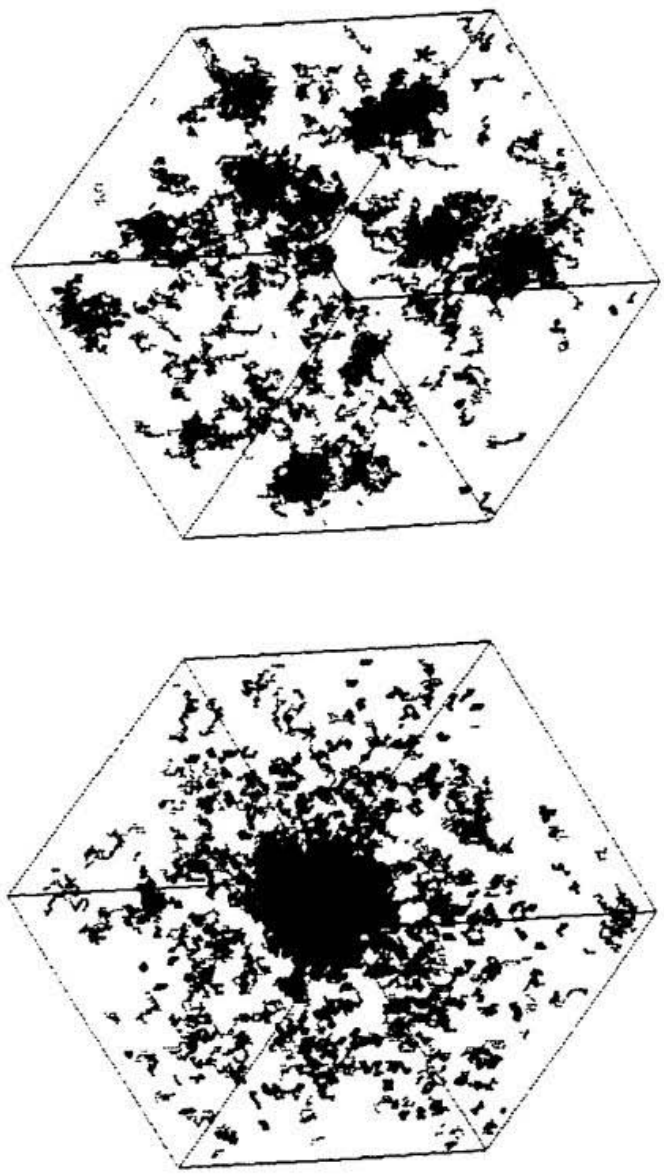

Figure 5.7: Snap-shot of the polymer configuration: a) $\phi^0_{HB}/\phi^0_{CB} = 0.1$, $Z_{HB} = 6$. b) $\phi^0_{HB}/\phi^0_{CB} = 0.5$, $Z_{HB} = 6$.

Figures 5.7(a) and 5.7(b) display snap-shots of the systems for the first and second simulations, respectively. Figure 5.7(a) shows micelles with the homopolymer solubilized in the cores, whereas in Figure 5.7(b), we see a single large domain comprised mostly of homopolymer with copolymers at the interface. This indicates a macrophase separated system. In both cases, there is a significant number of polymers in solution and in small aggregates, which indicates a weakly segregated regime.

Figure 5.8(a) shows a semi-log plot of the autocorrelation times and the time associated with the diffusion of polymers for the first simulation. We also did a simulation with $L_i = 100$ and decreasing ϵ. Results for the copolymer weighted chain exchange autocorrelation time show that finite sizes effects are negligible and independent of the annealing process.

The general trends shown in Figure 5.8(a) for the first simulation are similar to the results shown in Figure 5.2 from the previous section. In this case, micelles and small aggregates first form at a higher interaction energy than the system corresponding to Figure 5.2, since these are lower molecular weight polymers. This is consistent with mean field theory [21], which predicts that the critical micelle concentration is strongly dependent on the product χZ_{CB}. A second difference with respect to Figure 5.2 is in the homopolymer weighted extraction and weighted exchange autocorrelation times. In the present case, these relaxation times increase with ϵ in concert with the corresponding times for the copolymer. This is due to higher molecular weight homopolymer which is now closer to the degree of polymerization of the B block

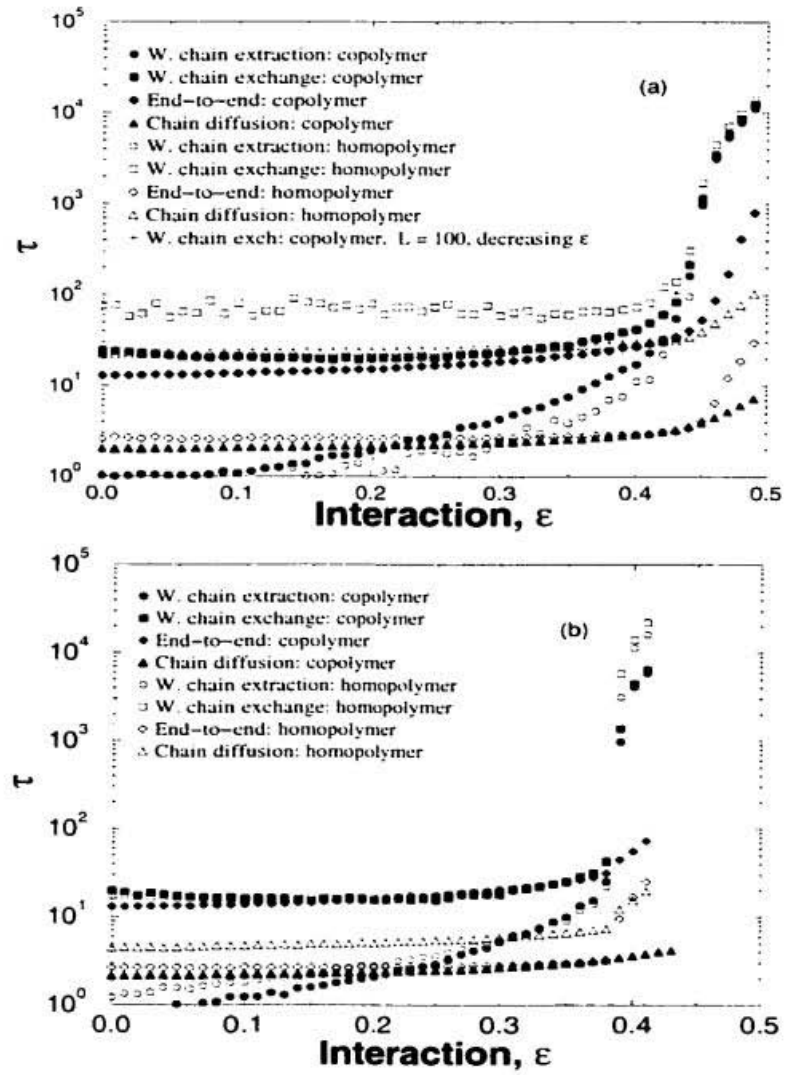

Figure 5.8: Semi-log plot of the relevant autocorrelation times as functions of the interaction energy: Homopolymer extraction (○), homopolymer exchange (□), homopolymer end-to-end (◇) and homopolymer diffusion (△). The closed symbols correspond to the data for the copolymer. a) $o^0_{HB}/o^0_{CB} = 0.1$. $Z_{HB} = 6$. b) $o^0_{HB}/o^0_{CB} = 0.5$. $Z_{HB} = 6$

of copolymer. In Figure 5.8(b), where $o^0_{HB}/o^0_{CB} = 0.5$, the homopolymer weighted extraction and exchange times actually surpass those of the copolymer. In this case,

the homopolymers present in large aggregates are concentrated in the center of the cores and the copolymers tend to be located at the surface of the large domains as shown in Figure 5.7(b). The homopolymers therefore remain in the dense cores of the large domains for extended periods of time. For the macrophase separated system, the interaction could only be increased up to $\epsilon = 0.42$ due to the large system relaxation time.

The volume fraction profiles for the first system are shown in Figure 5.9(a). Once again, the homopolymer is solubilized within the core of the micelle although the volume fraction profiles in the core are no longer uniform. The profile for the B component of copolymer actually decreases slightly near the center. The copolymer joints tend to be localized at the core-corona interface due to enthalpic effects, and entropic effects prevent the ends of the B block from stretching to the center of the cores. Nonetheless, the micelles have a smooth size distribution with a well defined peak at about 36 polymers per aggregate, as shown in Figure 5.10(a). This distribution is once again a signature of a microphase separated system.

In contrast, the domain size distribution shown in Figure 5.10(b) for the second simulation shows a single large aggregate with up to about 850 polymers. A large aggregate with 850 polymers contains about 66% of all polymers in the system. The volume fraction profiles shown in Figure 5.9(b) are for aggregates with approximately 800 polymers, and clearly show that the homopolymer accumulates in a large aggregate, with copolymers at the surface. These features imply a macrophase separated

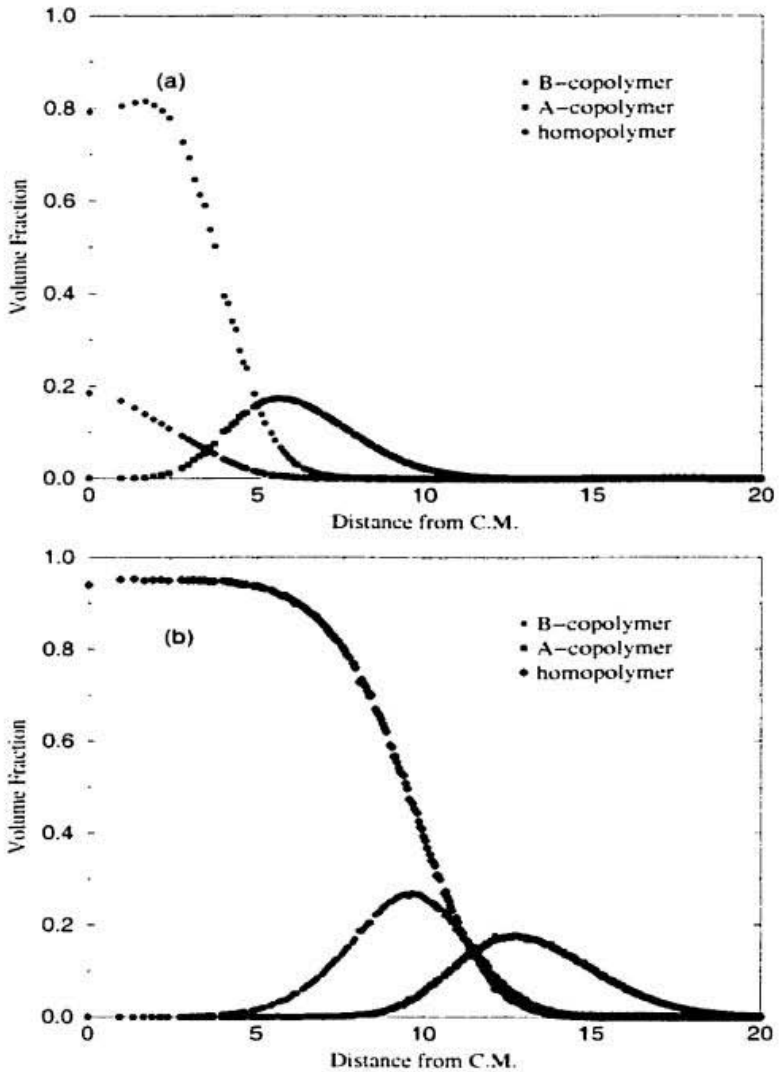

Figure 5.9: Volume fraction profiles as functions of the distance from the center of mass (C.M.) of the micelles: B-copolymer (•), A-copolymer (■) and homopolymer (♦). a) $o^0_{HB}/o^0_{CB} = 0.1$, $Z_{HB} = 6$ and b) $o^0_{HB}/o^0_{CB} = 0.5$, $Z_{HB} = 6$.

system. The results from these two simulations therefore suggest that a threshold homopolymer volume fraction does exist as predicted by mean field theory.

Further simulations were performed to obtain the solubilization limit as a function

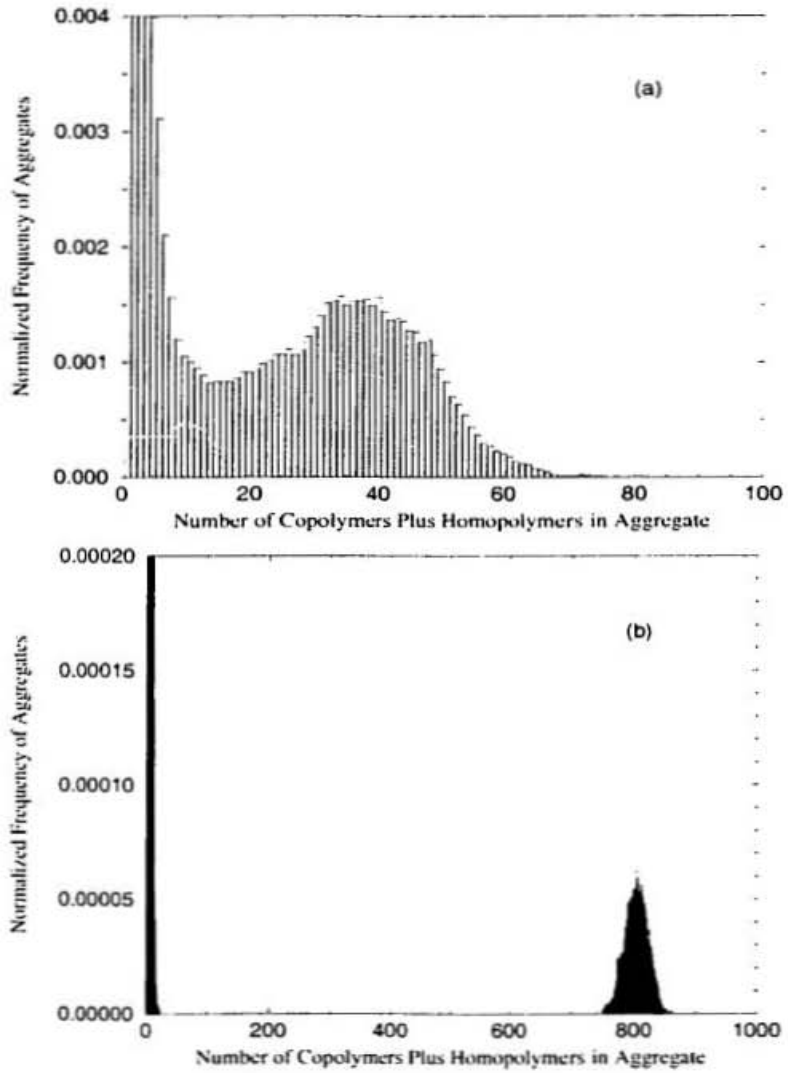

Figure 5.10: Normalized distribution of aggregates as a function of the number of homopolymers plus copolymers in the aggregates: a) $o^0_{HB}/o^0_{CB} = 0.1$, $Z_{HB} = 6$, $\epsilon = 0.49$ b) $o^0_{HB}/o^0_{CB} = 0.5$, $Z_{HB} = 6$, $\epsilon = 0.42$.

of the relative volume fractions o^0_{HB}/o^0_{CB} and the ratio Z_{HB}/Z_{CB} by varying the homopolymer volume fraction and degree of polymerization. Figure 5.11 shows a phase diagram displaying both microphase and macrophase separated regions. The

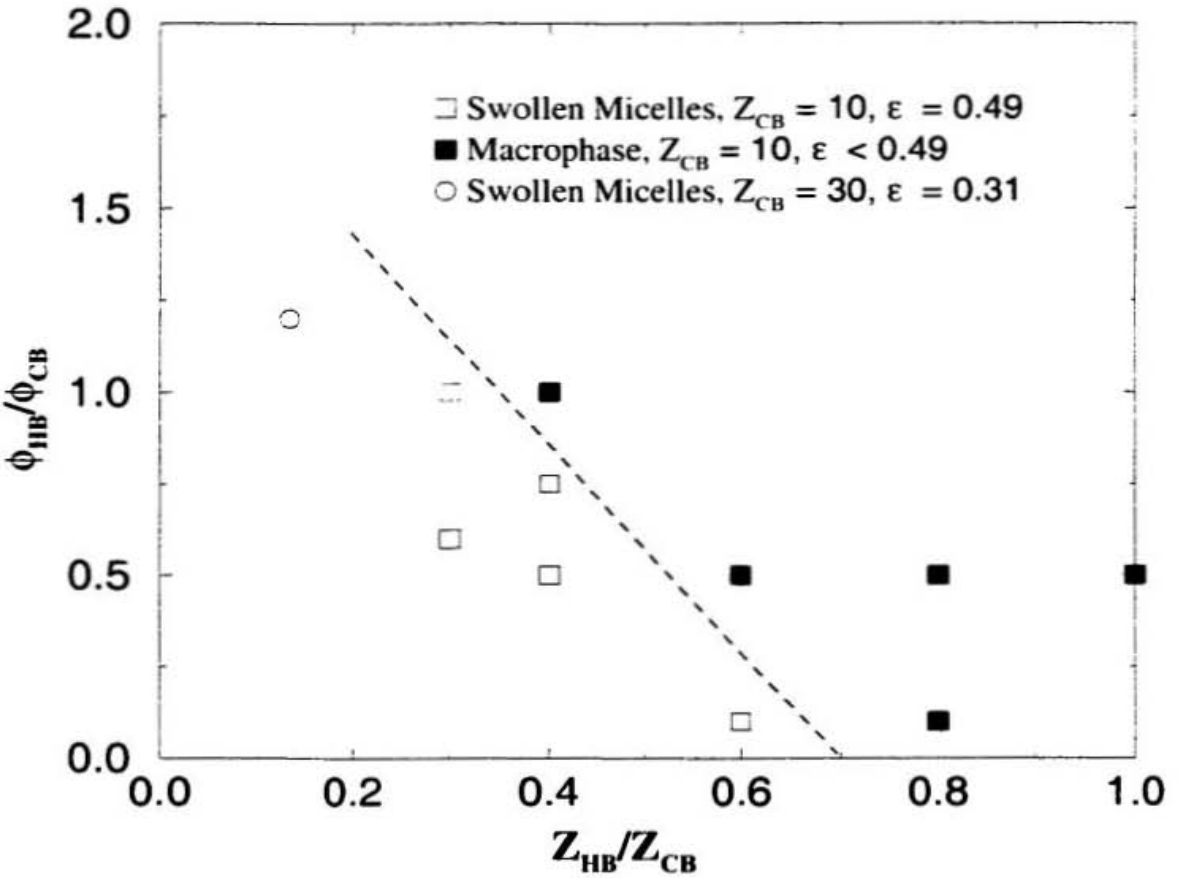

Figure 5.11: Phase diagram indicating the macro/microphase regions as functions of the ratios ϕ^0_{HB}/ϕ^0_{CB} and Z_{HB}/Z_{CB}: Microphase (□), macrophase (■). The dashed line corresponds to the phase boundary.

open symbols refer to microphase separated systems, whereas the filled symbols refer to a macrophase. The datum from the simulation in Section 5.3.1 with $Z_{CA} = 42$, $Z_{CB} = 30$ and $Z_{HB} = 4$ is also shown in Figure 5.11 (open circle), even though the interaction ϵ could not be increased up to 0.49 as in other microphase separated systems with $Z_{CB} = 10$. For this simulation the interaction could only be increased up to $\epsilon = 0.31$ because of the longer system relaxation time. Nonetheless, the results are

consistent with an increase in the threshold volume fraction of added homopolymer with a decrease in Z_{HB}/Z_{CB}. For the macrophase separated systems, ϵ was increased until the system relaxation time was too large to continue the simulations. In all cases this occurs when $\epsilon < 0.49$. Nonetheless, since the threshold volume fraction is expected to decrease with increasing ϵ, the macrophase separated systems are expected to remain macrophase separated for $\epsilon = 0.49$.

The boundary between the two phases is approximated by the dashed line in Figure 5.11. This boundary shows that the threshold volume fraction decreases with increasing ratio Z_{HB}/Z_{CB} until only very small amounts of added homopolymer are required to produce a macrophase separated system. This result is once again consistent with the mean field approach, which not only predicts a threshold volume fraction, but that the threshold decreases with increasing Z_{HB}/Z_{CB} as shown in Figure 5.11.

5.4 Summary

We have performed MC simulations of block copolymer micelles swollen by added homopolymer. The simulations were performed by slowly lowering the solvent quality of the system in order to carefully monitor the system characteristics. More specifically, autocorrelation functions and their respective autocorrelation times were calculated to obtain information on the required duration of the simulations and to extract information on the dynamic behavior of the systems. This turns out to be

important since the system relaxation time is strongly dependent on the solvent quality and limits the simulations to low ϵ. These limitations restrict the MC simulations to a weak segregation regime. The MC simulations therefore serve as a complement to a mean field theory which was developed for strongly segregated systems. In addition, information about the micelle characteristics and other quantities is extracted to investigate approximations made in the mean field approach and the predictions of the theory on the interplay between the macrophase and microphase.

We probed the micelle structure for a system in which the degree of polymerization of the homopolymer is much smaller than that of the core forming block of the copolymer. The homopolymer is solubilized within the micelle cores. The volume fraction profiles in the cores are relatively uniform as assumed in the mean field approach, but in the coronas the profiles show a definite maximum with no uniform regions. The A and B copolymer ends are distributed throughout the coronas and cores of the micelles, respectively, and the joints are localized to a relatively broad interface.

Further MC simulations were used to study the phase behavior which was characterized as being microphase or macrophase separated. The phase behavior was determined from criteria based on the volume fraction profiles in the cores of the micelles, and the average size and the size distribution of the aggregates. A threshold volume fraction of homopolymer as a function of Z_{HB}/Z_{CB} was identified. Above the threshold volume fraction a system is macrophase separated otherwise microphase

separation occurs. As a result, a phase diagram was obtained showing a decrease in the threshold volume fraction with increasing ratio Z_{HB}/Z_{CB}. This phase behavior is in qualitative agreement with the theory and experiments of Whitmore and Smith [32].

In the case of microphase separation, micelles form, the homopolymer is solubilized within the cores, and the aggregates correspond to micelles with a reasonably narrow size distribution. In the case of macrophase separated systems, there is a single large aggregate, consisting of homopolymer with copolymer at the surface. The decrease in the threshold volume fraction with increasing Z_{HB}/Z_{CB} is attributed to entropic effects. For higher molecular weight homopolymer, the entropic penalty, in segregating the homopolymer to a separate macrophase of smaller volume, is reduced. The result is a decrease in the threshold.

Chapter 6

End-tethered Polymers

6.1 Introduction and Review

In this Chapter, we are concerned with end-tethered layers of polymers in good solvent. The molecular weights and coverages range from the *mushroom* regime where polymers act as isolated chains to high surface coverages where they strongly interact with each other and stretch away from the surface. We are also interested in obtaining information on the regimes where each of the theoretical approaches discussed in this thesis is valid and comparing it with the behavior observed in experiments.

Historically, analytical scaling and mean field theories marked important contributions to the study of end-tethered layers and supplied the framework for further study. In this section, we first review the important analytical theories in detail to obtain some physical insights into the structure of the end-tethered layers. We then review the experimental and theoretical work pertaining to this thesis.

To begin, we define various regimes which can be expressed in terms of the re-

duced surface coverage, σ^*, as described in Section 1.5. In the *mushroom* regime the thickness of the layer is independent of the reduced surface coverage. The radius of gyration, R_g, is a characteristic length scale, and $h \sim Z_A^{3/5}$ for end-tethered polymers in good solvent, where h is the layer height and Z_A is the degree of polymerization of the end-tethered polymer. The limiting case of $\sigma \to 0$ has recently been studied by Adamuti-Trache *et al.* [144] using renormalization group (RG) theory.

When the polymers strongly interact with each other, the picture is quite different. The chains can be highly stretched, the layer thickness depends on the reduced surface concentration, and the average distance, d, between anchoring sites becomes a characteristic length scale. The concept of "blobs" of linear size d, as shown in Figure 1.4, was introduced in the theory of AdG [12, 13]. In the work of AdG, the surface coverage is high enough that the chains are highly stretched. Furthermore, the chains are assumed to be uniformly stretched so that the free ends are located in the tail region of the brush. The introduction of this characteristic length scale, d, along with the assumption that the ends are in the tail region leads to a step-like density profile except for a small depletion zone and a tail region. Within the layer, the polymer volume fraction is $\phi \sim Z_A b_A^3/d^2 h$ where b_A is the statistical segment length. On the scale of the blob size d, the polymer chains are considered as ideal Gaussian chains. The chains are envisioned as strings of Z_A/g blobs with g monomers per blob. The size of each blob is d as shown in Figure 1.4 with $g^{3/5} b_A = d$. This gives a thickness $h \sim Z_A \sigma^{1/3}$ as shown in Equation (1.6).

Mean field arguments have also been used to determine the scaling law shown in Equation (1.6). In this regime of strong overlap between chains, the number of monomer-monomer contacts increases and effectively results in an increase in the interaction energy for polymers in good solvent. This effect is reduced by stretching the chains perpendicular to the surface but at the cost of a loss in entropy, or increase in the elastic energy, due to the increased layer thickness. The interplay between the interaction and elastic energies can be used to determine the equilibrium layer thickness. The free energy per chain (in units of k_BT) is

$$F \sim v\phi_A^2 \frac{d^2 h}{b_A^3} + \frac{h^2}{Z_A b_A^2} \tag{6.1}$$

where v is a dimensionless excluded volume parameter which is a measure of the effective binary monomer-monomer contacts. The first term in Equation (6.1) represents the interaction energy and the second term is the elastic free energy relative to an ideal unperturbed chain with $R_0 = Z_A^{1/2} b_A$ where R_0 is the *rms* end-to-end distance. We can write Equation (6.1) in terms of the surface coverage $\sigma \sim 1/d^2$. Neglecting the numerical prefactors, it is

$$F \sim v\frac{Z_A^2 \sigma}{h} + \frac{h^2}{Z_A b_A^2}. \tag{6.2}$$

Minimizing Equation (6.2) with respect to the thickness h gives $h \propto Z_A \sigma^{1/3}$ as in Equation (1.6).

Other analytical theories have been developed. In particular, as discussed in Chapter 1, Milner, Witten and Cates (MWC) developed an analytic SCF theory.

This approach is suitable for high surface coverage in the asymptotic limit of infinite molecular weight ($Z_A \to \infty$). In this limit the solution gave a parabolic density profile for the end-tethered layer and a layer thickness $h \propto Z_A\sigma^{1/3}$, in agreement with the above results. Later, finite molecular weight corrections were included [40, 61] which produced a smooth tail.

Monte Carlo [58, 65] and molecular dynamics [62] studies have been done to investigate results obtained from scaling theory and SCF theory. Murat and Grest [62] performed MD studies of end-tethered layers in good solvent and compared their results with the SCF results of Milner *et al.* [14, 40] for reduced surface coverage $1 \lesssim \sigma^* \lesssim 11$ and $10 \lesssim Z_A \lesssim 150$. Results for the density profiles and the thickness of the layer were in agreement for higher surface concentration and molecular weight ($Z_A^{3/5}\sigma^{*1/3} \gtrsim 12$). Chakrabarti and Toral [65] performed MC simulations on similar systems of grafted polymers. For $Z_A = 50$, the range of reduced surface coverage was $2 \lesssim \sigma^* \lesssim 7$ and, for $Z_A = 100$, the range was $5 \lesssim \sigma^* \lesssim 15$. The density profiles consisted of a parabolic profile but augmented by a depletion region next to the grafting surface and a smooth tail. They were compared directly with the parabolic density profiles obtained from the asymptotic SCF theory of MWC. The quality of the fit to the parabolic profile increased with increasing molecular weight.

The SCF theory implies that the unperturbed radius of gyration of the molecules, R_g, is not a relevant length scale for these systems in the asymptotic limit. Instead, the appropriate scaled distance from the wall is $z/(Z_A\sigma^{1/3})$. As well, the volume

fraction profiles scale as $o(z) \propto \sigma^{2/3}$. Lai and Binder [58] followed earlier work [65] by performing Monte Carlo simulations using the bond fluctuation algorithm for $10 \leq Z_A \leq 80$ and plotting $o(z)/\sigma^{2/3}$ vs. $z/(Z_A\sigma^{1/3})$ for $20 \leq Z_A \leq 40$. For $Z_A = 20$ the range of reduced surface coverage was given by $0.5 \lesssim \sigma^* \lesssim 4$ whereas for $Z_A = 80$ the range was $2 \lesssim \sigma^* \lesssim 20$. A rough collapse onto a master curve was observed, and the authors remarked that systematic deviations from scaling occurred due to the short chain lengths.

End-tethered layers have also been studied experimentally. As noted in Section 1.5, the reduced surface coverage is limited to $\sigma^* \lesssim 15$ in many cases. This raises the question of whether these many experimental systems fall in the asymptotic brush limit.

Kent *et al.* [69] carried out an extensive and systematic study of end-tethered polymers in good solvent. For the root mean squared (*rms*) layer thicknesses, h_{rms}, they found that the best fit scaling relation was

$$h_{rms} \propto Z_A^{0.86}\sigma^{0.22} . \tag{6.3}$$

The *rms* layer thickness is defined by

$$h_{rms} = \sqrt{\frac{\int_0^\infty dz o_A(z) z^2}{\int_0^\infty dz \phi_A(z)}} \tag{6.4}$$

where o_A is the volume fraction of end-tethered polymer. Kent *et al.* also found that the observed layer thicknesses were well represented by a simple linear function

$$\frac{h_{rms}}{R_g} = A + B\sigma^* \tag{6.5}$$

where A and B are constants, independent of molecular weight. The values of h_{rms}/R_g ranged from about 1.5 to 2.2. These results indicate that the stretching is modest, that the layer thickness scales more weakly with Z_A than linearly, and that R_g remains a relevant length scale in the end-tethered systems. The experiments also indicated that the density profiles contained both a depletion region and a smooth tail.

Baranowski and Whitmore [46] made a direct comparison of numerical self-consistent field (NSCF) theory with the experiments of Kent *et al.* Results for the density profiles and layer thicknesses were in good agreement for $\sigma^* \gtrsim 2$, expressed either as scaling relations as in Equation (6.3) or as a linear relation as in Equation (6.5). They support the conclusion that these systems do not correspond to the asymptotic limit for $\sigma^* \lesssim 15$, and that R_g remains a relevant length scale. They also hint at a quantitative discrepancy between the NSCF theory and experiment at coverages $\sigma^* \lesssim 2$. Similar results for end-tethered polymers in Θ solvent have been obtained in experiments [113] and NSCF calculations. [145]

Our primary interests in this Chapter are in detailed comparisons of the results of the analytic SCF theories, NSCF calculations, MC simulations, and experiment. For the MC simulations, we use an athermal solvent. We first simulate isolated polymer in solution, and extract from these calculations an expression for R_g and an effective statistical segment length which we label b_{MC}. We then perform a series of MC simulations of the layered systems, and use our results for R_g in the analysis of our results for the layers.

For the NSCF calculations, we discuss three sets of results. In the first, we choose the Flory parameter $\chi = 0$ and statistical segment length $b = b_{MC}$. In the second set, we choose $\chi = 0$ but fit the statistical segment length. The fitting is done by finding the value of b which gives the best agreement of the NSCF profile with the corresponding MC profile. The MC profile chosen for the fit corresponds to the system for which the mean field approximations of the NSCF approach should be best. This is the one with the combination of the highest molecular weight polymers and surface coverages for which we calculated MC profiles. In the third set of calculations, we fit both χ and b in this way. It turns out that the value obtained for b when $\chi = 0$ is the same as b_{MC} to within the statistical error. Hence, the first and second set of calculations are virtually identical and we have only two distinct sets of results to consider. We then carry out comparisons of the MC and NSCF results using these two sets of parameters. In particular, we examine how differences between the MC and NSCF results appear at low coverages where density fluctuations and inhomogeneities parallel to the surface can become important. We are able to identify where, in terms of σ^*, these differences occur. We can also examine the low coverage regime with our MC calculations, and compare the results with experiment. We include in this discussion the possibility of a mushroom limit where the layer thickness would be independent of coverage.

Z_A	SCF	Monte Carlo			
	σ^*	σ^*	$L_x = L_y$	L_z	N_A
80	0.5–15	0–10	86–141	80	1: 100–800
100	0.5–15	0–10	102–161	100	1: 100–800
150	0.5–15	0–4.0	153–206	150	1: 100–880
200	0.5–15	0–3.5	201–245	200	1: 100–1.080
800	0.5–15				

Table 6.1: General specifications of systems modeled in the NSCF calculations and Monte Carlo simulations. The variable N_A is the number of polymers in the system. For each molecular weight there was one set of MC simulations performed with one chain, $N_A = 1$, corresponding to the limiting case of $\sigma^* \to 0$. No MC simulations were done for $Z_A = 800$.

6.2 Monte Carlo Simulations

The general algorithm used in the MC simulations of end-tethered polymers is discussed in Section 2.2.2. In this section, more detail is given. The simulations are carried out on a simple cubic lattice. One end of each polymer is confined to the $z = 1$ plane, but it is allowed to move in this plane. Periodic boundary conditions are used in the x and y directions and impermeable walls are chosen at $z = 1$ and $z = L_z$. The systems contain a minimum of 100 and up to 1,080 polymers (see Table 6.1). For a given reduced surface concentration σ^*, the linear dimensions L_x and L_y are chosen to accommodate the polymers and in all cases $L_x = L_y \geq Z_A$ and $L_z = Z_A$. The only exceptions are cases with only one polymer, which correspond to $\sigma = 0$. Other simulations with free polymer in solution are also carried out to investigate the end-to-end distance and radius of gyration of free chains in solvent. In this instance, the periodic boundary conditions are applied in all directions, the polymer ends are

not constrained to any surface, and the systems contain only a single chain.

All interactions, with the exception of an excluded volume interaction, have been set to zero ($\epsilon_{AS} = \epsilon_{SS} = \epsilon_{AA} = 0$).

The usual Monte Carlo algorithm discussed in Section 2.2 is used to generate random configurations of the polymer chains except that only three types of motions are used: reptation, kink-jump and crankshaft [79–82]. In principle, if the site is unoccupied, then we calculate the change in energy and the probability of the transition occurring by the usual *Metropolis* rule. However, since all interaction energies are set to zero there is no change in energy in going from one configuration to another. Hence, the probability of the transition to an unoccupied site occurring is unity.

The number of end-tethered polymers in the system is N_A. There are therefore $N_A Z_A$ attempted MC moves per N-bead cycle. The time required to reach equilibrium is determined by monitoring the four different autocorrelation times, extracted from their respective autocorrelation functions, as defined in Equation (2.18). The autocorrelation functions are calculated for the quantities R_z, R_g, $R_{g\perp}$ and R_{gz}, which were defined in Section 2.2.2. The autocorrelation times are evaluated using Equation (2.14) and the relaxation time of the system is taken as the maximum of the four autocorrelation times, which always turns out to be $\tau_{R_{gz}}$. In order to let the system come to equilibrium the simulations are run for 10,000 N-bead cycles plus a minimum period of 20 relaxation times. Ensemble averages are then taken over a period of at least 40 relaxation times.

6.3 Numerical Self-consistent Field Theory

The general formalism for the NSCF theory of thin films was described in Section 3.4. In this section, the theory is applied to end-tethered polymers by simply excluding the free polymer from the system. The problem reduces to solving self-consistently for the propagators of end-tethered chains only.

The density profiles for the polymer and solvent are described by the local volume fractions $\phi_\kappa(z)$ which are defined in Equation (3.94), for $\kappa = A, S$. The incompressibility condition in Equation (3.4) reduces to

$$\phi_A(z) + \phi_S(z) = 1 \ . \tag{6.6}$$

The polymer density profile can be obtained from the convolution of two propagators, $q_A(z,\tau)$ and $\tilde{q}_A(z,\tau)$. Using Equations (3.94) and (3.108), $\phi_A(z)$ is given by

$$\phi_A(z) = \frac{\sigma}{\rho_{0A}\mathcal{Q}_A'} \int_0^{Z_A} d\tau \ \tilde{q}_A(z,\tau)\, q_A(z, Z_A - \tau) \ . \tag{6.7}$$

where $\mathcal{Q}_A'$ is given in Equation (3.106). Both propagators satisfy the modified diffusion equation with initial and boundary conditions defined in Equations (3.109) to (3.113) with b_A as the statistical segment length. The self-consistent potential, Equation (3.98), reduces to

$$\omega_A(z) = \frac{\rho_{0S}}{\rho_{0A}} \ln\left(\frac{\bar{\phi}_S}{\phi_S(z)}\right) - 2\frac{\rho_{0S}}{\rho_{0A}}\chi_{AS}\left[\phi_A(z) - \bar{\phi}_A\right] \ . \tag{6.8}$$

A specific system is characterized by the parameters Z_A, σ, ρ_{0A}, ρ_{0S} and χ_{AS}. The propagators $\tilde{q}_A$ and q_A are determined by solving the modified diffusion Equa-

tion (3.109). The polymer volume fraction profile, $\phi_A(z)$, is calculated from Equation (6.7), and $\phi_S(z)$ is then determined from the incompressibility condition. However, solving the diffusion equation requires the potential $\omega_A(z)$, and so the problem is solved via a self-consistent algorithm which is described in detail elsewhere [46]. In the first iteration $\omega_A(z) = 0$, but in subsequent iterations the potential $\omega_A(z)$ is constructed using Equation (6.8) and from the volume fraction profiles calculated from the previous iteration. This iterative procedure is continued until a self-consistent solution is achieved.

6.4 Results and Discussion

6.4.1 Free Polymers in Good Solvent

We begin with the MC simulations of single polymer in good solvent. This provides us with R_g for our lattice-based calculations which will be used in the next section, as well as a minimal test of the simulations.

A series of calculations is performed with Z ranging from 80 to 200, for which we calculate the mean squared end-to-end distance, $< R^2 >^{1/2}$, and the radius of gyration. The results are plotted in Figure 6.1 as functions of the number of effective bonds and units, $Z - 1$ and Z, respectively. On the log-log scales, both sets of results fall very close to straight lines. The best fit lines imply power law relations

$$< R^2 >^{1/2} \;=\; b_{MC}(Z-1)^{\beta_1}$$

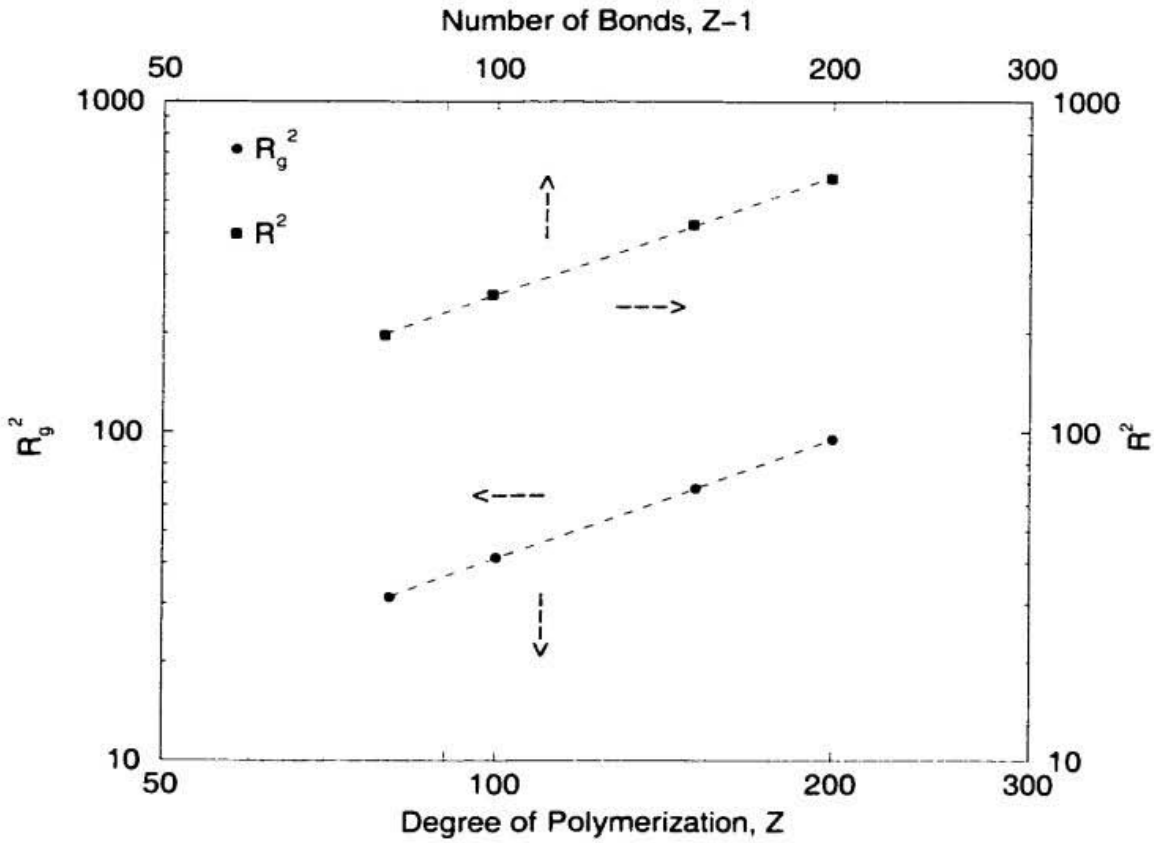

Figure 6.1: Log-log plot of the average radius of gyration squared, R_g^2, and end-to-end distance squared, R^2, as functions of Z and $Z-1$, respectively, for free polymers in athermal solution calculated in the Monte Carlo simulations. The dashed lines are the lines of best fit.

$$R_g = a_{MC} Z^{\beta_2} \tag{6.9}$$

with values

$$b_{MC} = 1.06 \pm 0.04 \qquad \beta_1 = 0.592 \pm 0.009$$

$$a_{MC} = 0.403 \pm 0.008 \qquad \beta_2 = 0.602 \pm 0.003 \tag{6.10}$$

where the uncertainty is the statistical noise.

We performed a similar analysis on the results of Gurler *et al.* [82] who modeled chains on a simple cubic lattice with $12 \leq Z_A \leq 60$. The fits to their data for $< R^2 >^{1/2}$ give $b_{MC} = 1.028 \pm 0.003$ and $\beta_2 = 0.601 \pm 0.002$. The two sets of results agree within the statistical uncertainty. The scaling exponents β_1 and β_2 are also consistent with the simple Flory type approach where they would have a value of about 3/5.

We also compared with the results of renormalization group theory, which predicts a correction to scaling due to finite molecular weight corrections with [146]

$$R_g^2 = A_{R_g} Z^{2\beta}(1 + b_{R_g} Z^{-\Delta_1} + ...) \tag{6.11}$$

with

$$\beta = 0.5880 \pm 0.0015 \, . \tag{6.12}$$

We first fitted our MC results used in Figure 6.1 to Equation (6.11). We then extended our simulations to lower Z, using the four degrees of polymerization used by Gurler *et al.* [82], and fitted this extended set to Equation (6.11). In both cases, we obtained $\beta = 0.600$, which agrees with our value of β_2 to within the small statistical uncertainty of ± 0.003. We conclude that our results for the scaling exponents lie just at the edge of agreement with renormalization group theory. As noted earlier, [147] simulations with degrees of polymerization up to $Z = 80,000$ are required to obtain full agreement.

In this Chapter, we need to know R_g in our lattice-based MC model so that we

can analyze our results for the end-tethered polymers in terms of σ^* and R_g. The result in Equation (6.9) and (6.10) is more than adequate for this purpose. The value of $b_{MC} = 1.06$ obtained from this analysis also provides a starting point in choosing a statistical segment length b_A in the NSCF calculations which are to be compared with MC simulations.

6.4.2 End-tethered Polymers

Autocorrelation Functions

Figure 6.2 shows a typical set of calculated autocorrelation functions, which are for a system with $\sigma^* = 1.5$ and $Z = 80$. At short times, the one that monitors the z-component of the end-to-end vector, R_z, decays the most rapidly. This reflects the relatively high mobility of the free end. At later times, however, this rapid decay is suppressed due to effects from the confined end. Overall, the slowest decaying autocorrelation function is the one associated with the component of the radius of gyration perpendicular to the surface, R_{gz}, which is again attributable to the confinement of one end to the surface. The decay associated with $R_{g\perp}$ is faster because both ends of each polymer can move freely in the x and y directions. In all cases the autocorrelation times increase with increasing Z and σ^*, and this imposes a practical restriction of the simulations to relatively low Z and σ^*.

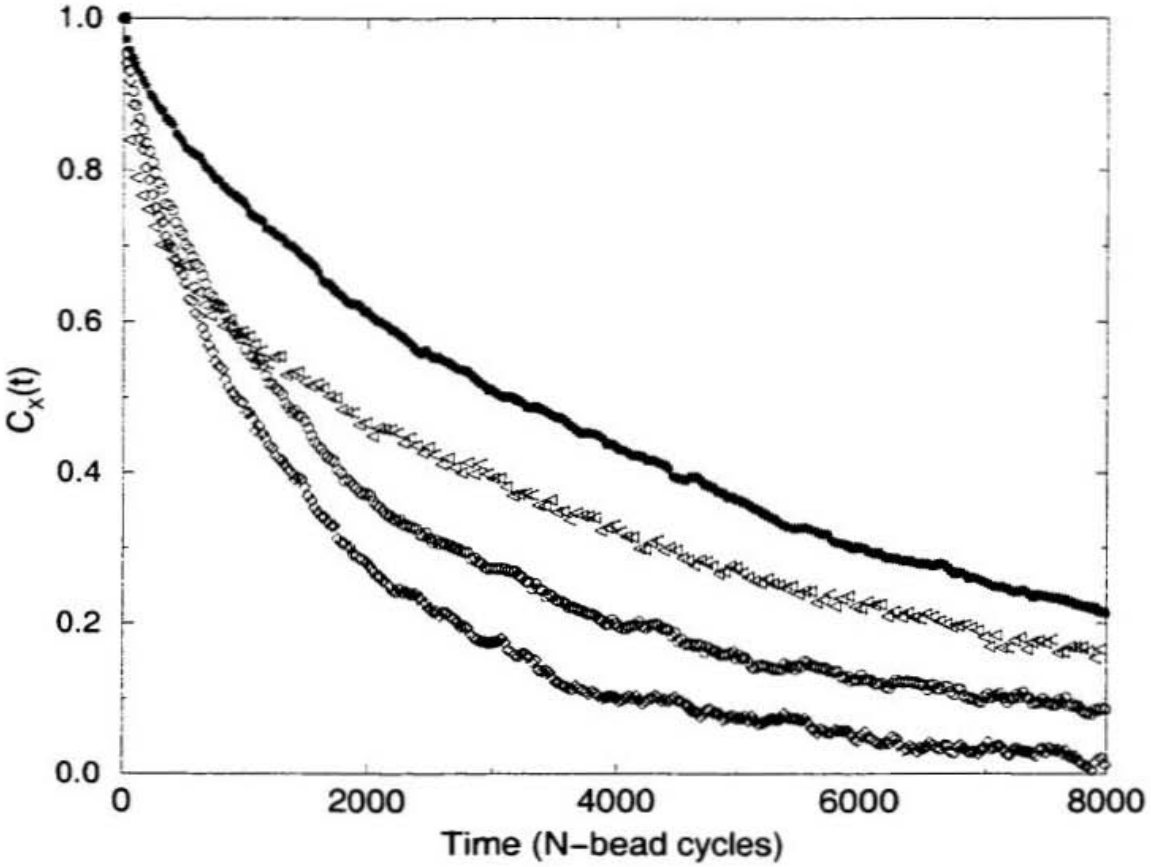

Figure 6.2: Autocorrelation functions for end-tethered polymer layers as functions of time (N-bead cycles) for a system with $\sigma^* = 1.5$ and $Z_A = 80$: $(\triangleleft) R_z$. $(\circ) R_g$. $(\star) R_{gz}$. $(\diamond) R_{g_\perp}$.

6.4.3 Density Profiles

As detailed in Table 6.1, we have performed a systematic study using MC simulations and NSCF theory. The ranges of surface coverage and degree of polymerization covered by the MC simulations is $\sigma^* \in [0, 10]$ and $Z_A \in [80, 200]$. For the NSCF calculations, $\sigma^* \in [0.5, 15]$ and $Z_A \in [80, 800]$ were used. Typical density profiles are shown in Figures 6.3 and 6.4.

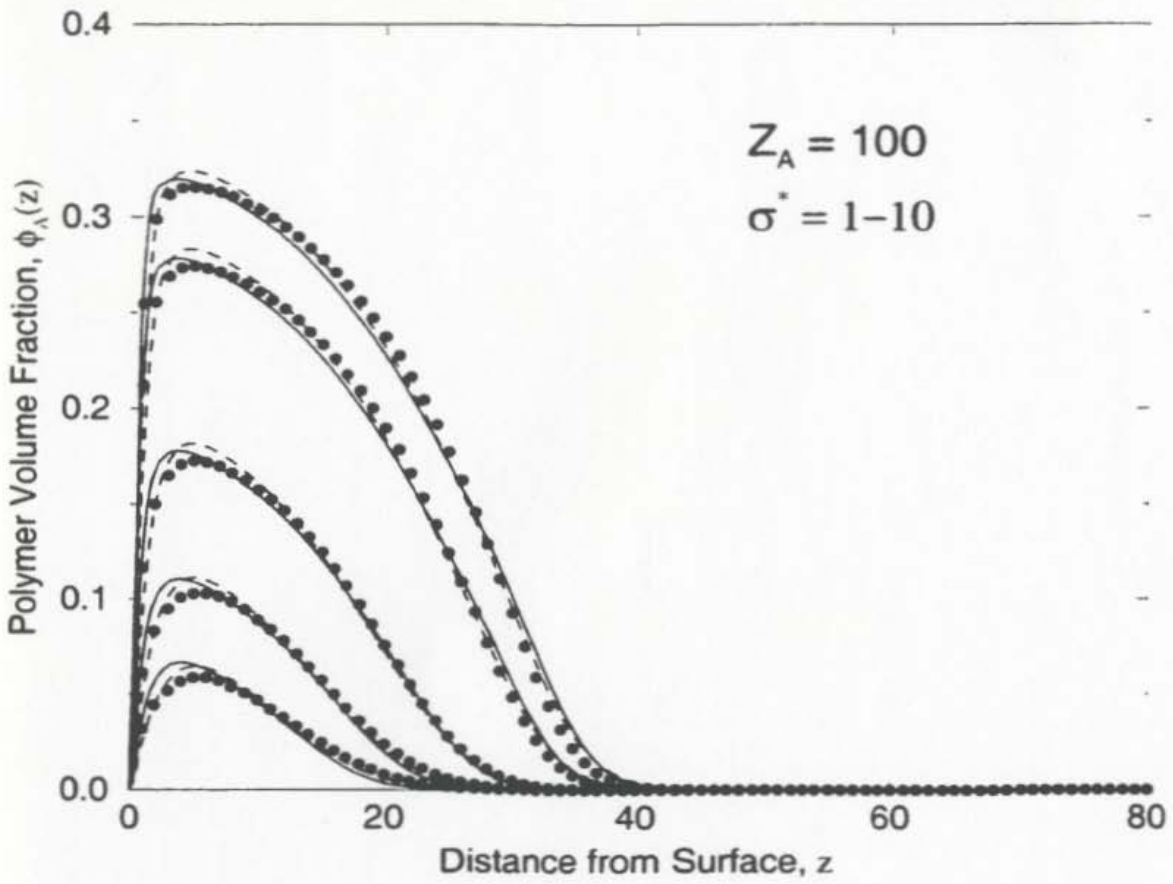

Figure 6.3: Polymer volume fraction profiles for $Z_A = 100$ and $\sigma^* = 1$ (lowest curves), 2, 4, 8 and 10 (highest curves). The circles are the MC results and the lines are the NSCF results. The solid lines correspond to $b_A = 1.06$ and $\chi = 0$, and the dashed lines to $b_A = 1.32$, $\chi = 0.26$.

In order to compare the MC and NSCF calculations quantitatively and, in particular, to probe differences at low Z and σ^*, it is necessary to use appropriate values of the effective χ parameter, the statistical segment length, and $\rho_{0\kappa}$. We investigated three choices, all using $\rho_{0\kappa} = 1$. The first is $\chi = 0$ and $b_A = b_{MC}$, i.e., the parameters were taken directly from the MC results of the previous section. The other two

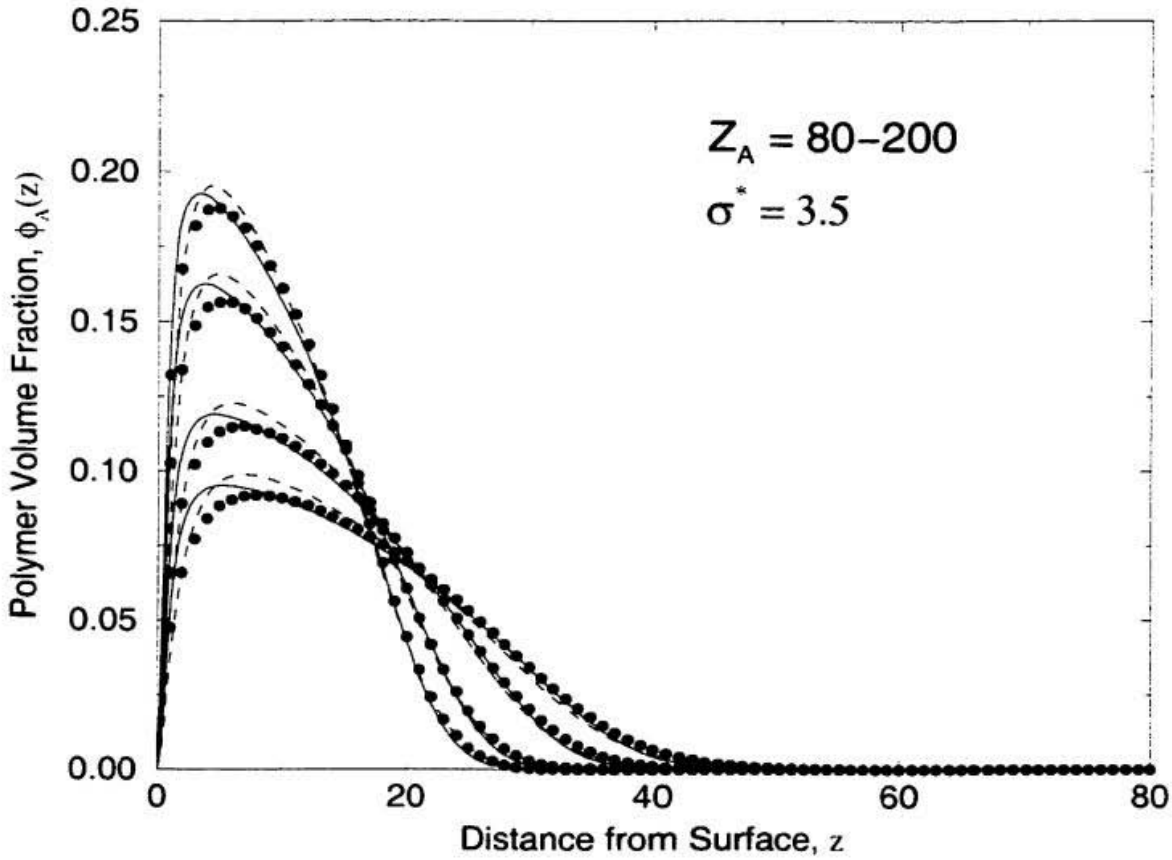

Figure 6.4: Polymer volume fraction profiles for $\sigma^* = 3.5$ and $Z_A = 80$ (highest peak), 100, 150 and 200 (lowest peak). The circles are the MC results and the lines are the NSCF results. The solid lines correspond to $b_A = 1.06$ and $\chi = 0$, and the dashed lines to $b_A = 1.32$ and $\chi = 0.26$.

choices were obtained by fitting NSCF profiles to MC profiles. For this fitting, we used the highest possible combination of Z_A and σ^* for which we have MC profiles, $Z_A = 100$ and $\sigma^* = 10$, which corresponds to the uppermost curves on Figure 6.3. The fits were done by minimizing the average of the square of the differences:

$$\Delta = \frac{1}{Z_A} \sum_{i=2}^{Z_A} (o_{MC}(i) - o_{NSCF}(i))^2. \tag{6.13}$$

where $o_{MC}(i)$ and $o_{NSCF}(i)$ are the volume fractions at a distance i from the surface in the MC simulation and NSCF calculation, respectively.

The result of the first fit, i.e., with fixed $\chi = 0$, was $b_A = 1.04$. This is in full agreement with the MC results for the single polymer, $b_{MC} = 1.06 \pm 0.04$. The result of the second fit was $\chi = 0.26$ and $b_A = 1.32$. Of itself, the increased value of χ would produce thinner layers with higher peak densities; this is countered by the increase in b_A. Since the b_A obtained from the MC simulation is virtually the same as that obtained from the NSCF fit with $\chi = 0$, there are essentially only two independent sets of parameters: $\chi = 0$ and $b_A = b_{MC}$, and $\chi = 0.26$ and $b_A = 1.32$.

Figures 6.3 and 6.4 provide a visual comparison of the MC results and the two sets of NSCF results. In Figure 6.3, the degree of polymerization is held constant and the coverage is varied, while in Figure 6.4, σ^* is constant and Z_A is varied. All profiles show an increase from zero at the surface to a maximum, followed by a smooth decrease and an extended tail. In each set of calculations, the location of the maximum relative to the surface is essentially independent of σ^*, but increases slowly with increasing Z_A. The dependence on Z_A is slightly stronger in the MC results than in the NSCF ones. These dependences are in overall agreement with previous numerical [46] and experimental [69] work, but in contrast with the ideas of scaling theory.

The agreement of both sets of NSCF calculations with the MC ones is rather good, with neither NSCF set dramatically better than the other. The main difference is

that, in the set with both χ and b_A fitted, the location of the peak is farther from the surface, in better agreement with the MC results. The value at the maximum, o_m, is increased modestly for $\sigma^* \gtrsim 3.5$, slightly worsening the agreement with the MC in this way, except for lower reduced surface coverage where o_m actually decreases. As either Z_A or σ^* decreases, the overall agreement worsens only slightly, even as low as $\sigma^* = 1$.

For our quantitative analysis, we will primarily use the NSCF results obtained with $\chi = 0.26$ and $b_A = 1.32$, which we interpret as mean field renormalized parameters. This choice of parameters provides the best agreement with the MC results, and so will best allow us to focus on the effects of the lateral inhomogeneities in the densities with decreasing σ^*.

Returning to o_m, the asymptotic theories predict that it scales as $o_m \propto \sigma^{2/3} Z_A^0$. Using $R_g \propto Z_A^{3/5}$, this implies $o_m \propto \sigma^{*2/3} Z_A^{-4/5}$. The fits to the current MC and NSCF data for $\sigma^* \geq 2$ give $o_m \propto \sigma^{*0.69} Z_A^{-0.76}$ and $o_m \propto \sigma^{*0.66} Z_A^{-0.75}$, respectively. These powers are all in good agreement with each other, and with the earlier NSCF results [46] which gave $o_m \propto \sigma^{*0.68} Z_A^{-0.71}$.

6.4.4 Layer Thickness

Figure 6.5 shows the MC and NSCF results for the *rms* layer thicknesses as functions of σ^*. The nearly perfect agreement of the MC and NSCF results near $\sigma^* = 10$ is consistent with the fact that the fitting was done there. As σ^* decreases, the

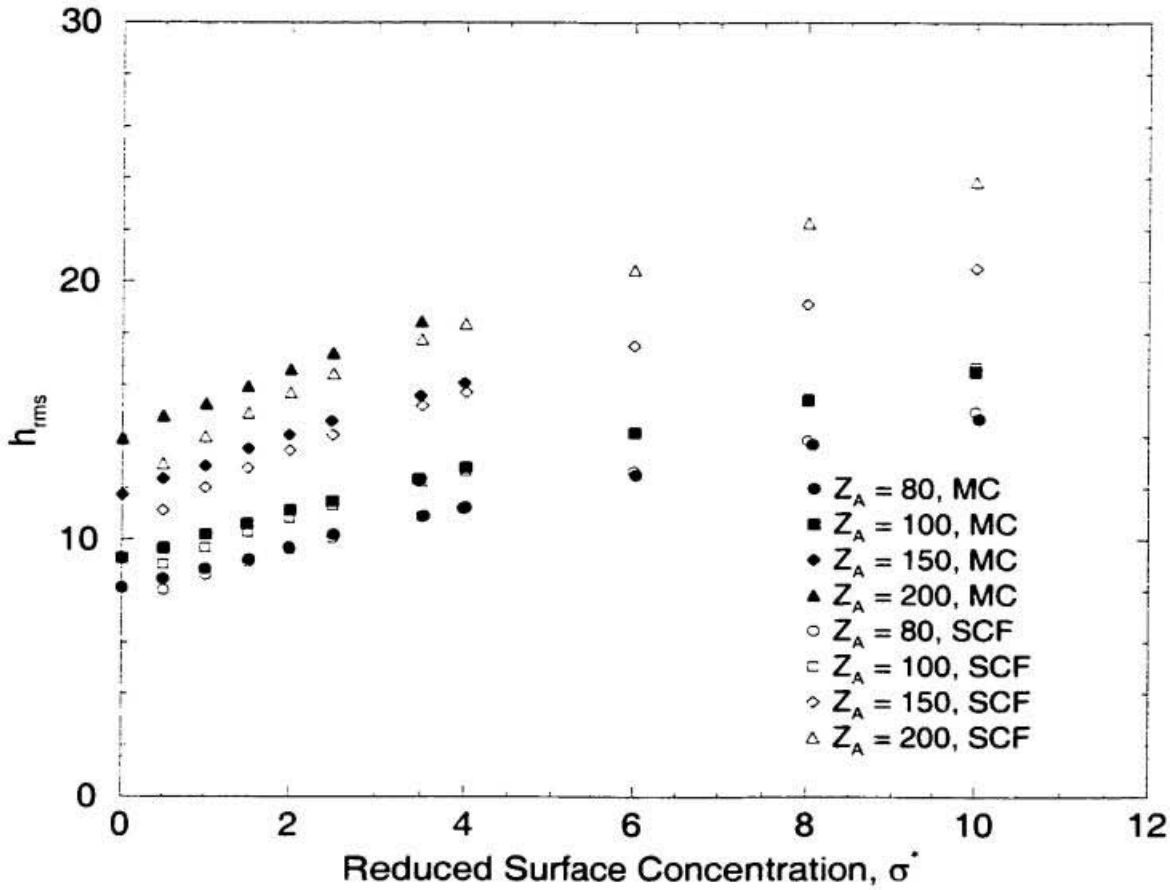

Figure 6.5: The *rms* layer thicknesses, h_{rms}, as functions of the reduced surface concentration σ^*. The filled symbols are from MC simulations and the open symbols are from NSCF calculations using $b_A = 1.32$ and $\chi = 0.26$.

thicknesses decrease. The NSCF values decrease slightly more quickly and, below $\sigma^* = 4$, the MC thicknesses are always greater than the NSCF thicknesses. However, the differences are less than 6% for $\sigma^* \geq 2$. (For the NSCF calculations with $\chi = 0$ and $b_A = b_{MC}$ the discrepancy is a bit larger but remains less than 12% for $\sigma^* \geq 2$.) Below $\sigma^* \simeq 2$, the differences grow. This is expected at these lower coverages where inhomogeneities in the planes parallel to the surface are more important. The

lateral averaging of the polymer densities inherent in the NSCF approach therefore underestimates the local polymer density within each chain. As a result, the effective monomer-monomer interactions are underestimated, which results in less stretching of the polymers.

What is perhaps most surprising is that, like the NSCF results, the MC results show an essentially linear decrease in h_{rms} with decreasing coverage, which continues down to zero concentration. There is no evidence of plateau regions at low σ^* through which h_{rms} would be constant. These results contrast with the suggestion of Kent *et al.* that the mushroom regime develops around $\sigma^* \lesssim 2$. However, our results do not actually contradict the experiments because the error bars in the measurements become large at low coverage. The absence of plateaus implies that there is some stretching of the polymers due to interactions between polymers for reduced surface concentrations even below $\sigma^* \simeq 0.5$. This is not unreasonable since an analysis of the overlap between neighboring chains in terms of the average polymer end-to-end distance, rather than R_g, suggests some overlap of neighboring chains for $\sigma^* \simeq 0.5$. The fact that the MC thicknesses continue to decrease, but more slowly than the NSCF ones, indicates that both lateral inhomogeneities and the overlap of neighboring chains play roles in this regime.

As noted in Section 6.1, the experiments of Kent *et al.* indicate that, when divided by R_g, the layer thicknesses can be reasonably represented as a linear function of σ^*, at least for $\sigma^* \geq 2$, i.e., Equation (6.5). The earlier NSCF calculations obeyed

similar linear relationships. [46] although with slightly different coefficients. A and B. for polymers of different degrees of polymerization. Our NSCF results here behave similarly so. for brevity. we discuss only our MC results. For R_g in this analysis. we use the results from the MC simulations of the free polymers. Equation (6.9). Figure 6.6 shows the MC thicknesses. presented in this manner. Like the experimental and NSCF results. they are nearly linear in σ^*. Also like the experimental results. but unlike the NSCF ones. they all obey essentially the *same* linear relationship. At very low coverage. the *rms* thicknesses reach a limiting value of $1.44R_g$. This is consistent with the experimental value of about $1.5R_g$ obtained by Kent *et al.*. about $1.43R_g$ obtained from MC simulations by Sorensen and Kovac. [148] and about $1.47R_g$ obtained by Adamuti-Trache *et al.* [144] in the absorbing chain limit.

As in earlier work. and in the analysis of many experiments. the fitting of power law relationships for the layer thicknesses. covering the range $2 \leq \sigma^* \leq 15$ and $80 \leq Z_A \leq 800$ was also investigated. We did separate fits to the NSCF and MC results. but they gave essentially the same results. Fitting to *both* sets of results throughout this range gives

$$h_{rms} \propto Z_A^{\nu} \sigma^{\mu}, \tag{6.14}$$

where $\nu = 0.86 \pm 0.02$ and $\mu = 0.27 \pm 0.02$. These values are consistent with previous [46] NSCF values of $\nu = 0.81$ and $\mu = 0.24$ and with the experimental values of $\nu = 0.86$ and $\mu = 0.22$ obtained by Kent *et al.* [69]. As noted earlier. the extracted exponents depend on the range σ^* used because of the continuous evolution from the

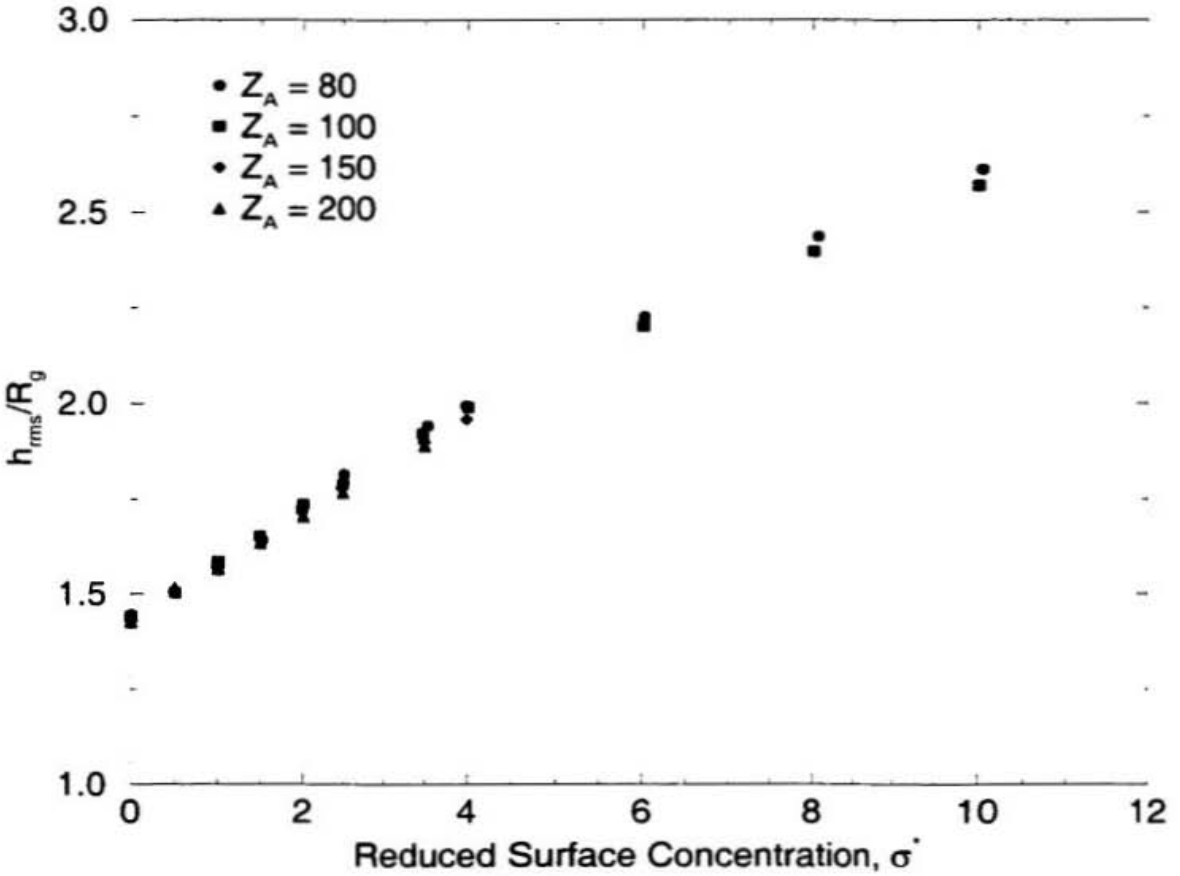

Figure 6.6: The *rms* layer thicknesses divided by the unperturbed radius of gyration, h_{rms}/R_g, as functions of the reduced surface concentration σ^*. Only the MC results are shown.

mushroom regime towards the high stretching regime, so these values should not be interpreted as applying to any sub-interval of this range of σ^*. However, the most interesting point is that the experiments and both kinds of calculations indicate that the scaling with Z is significantly weaker than linear.

With $R_g = 0.403 Z_A^{0.602}$, as given in Section 6.4.1, and Equation (1.4), the *rms*

thickness of the layer can be expressed as

$$\begin{aligned} h_{rms} &\propto Z_A^{0.86}\sigma^{0.27} \\ &\propto R_g^{0.90}\sigma^{*0.27} \end{aligned} \tag{6.15}$$

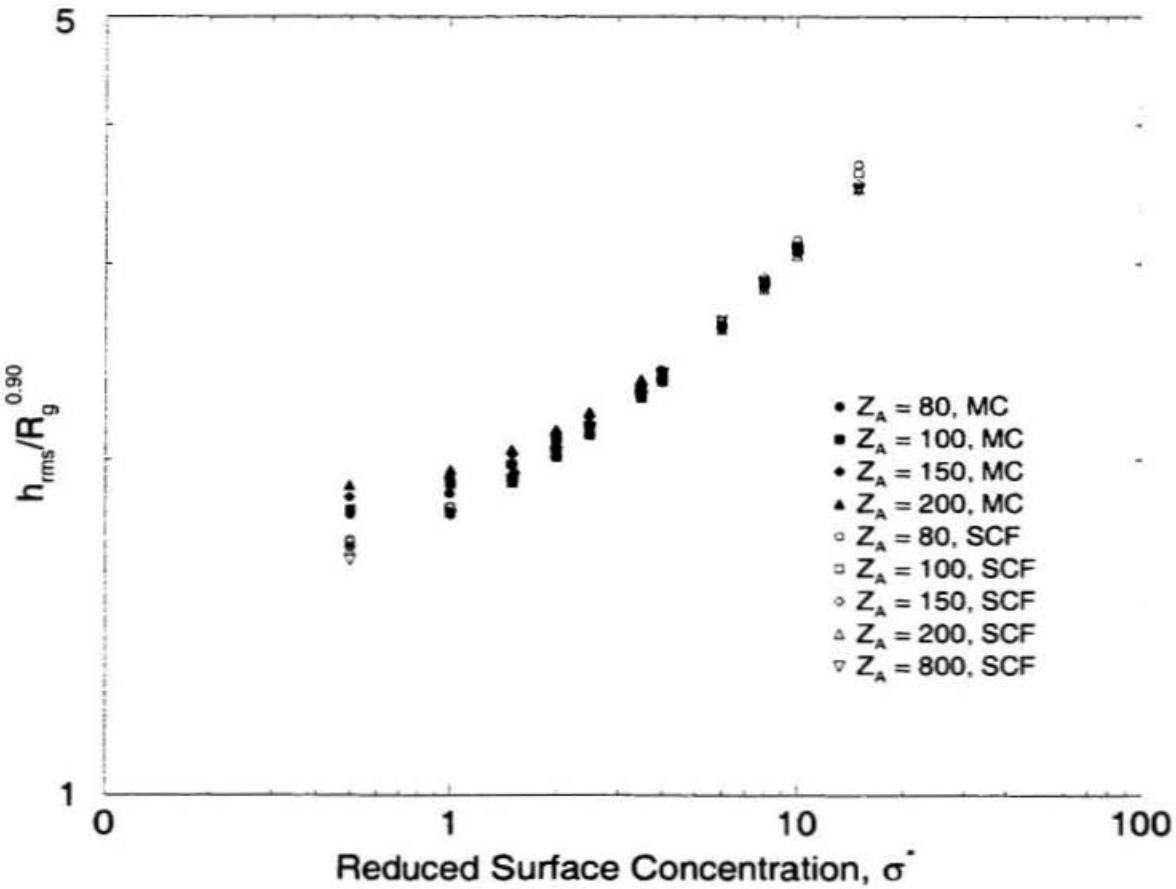

Figure 6.7: Monte Carlo (filled symbols) and NSCF (open symbols) layer thicknesses, plotted on a log-log scale as functions of the fitted power law.

Figure 6.7 provides a clear picture of the quantitative comparison between the MC and NSCF approaches by showing a log-log plot of $h_{rms}/R_g^{0.90}$ vs. σ^* for $\sigma^* \in [0.5, 15]$.

This range of σ^* varies from a regime in which the chains overlap weakly to one in which the polymers are strongly stretched. At lower concentrations ($\sigma^* \lesssim 2$) the NSCF calculations begin to deviate considerably from the Monte Carlo simulation results. As noted before, this difference is attributed to lateral inhomogeneities which are expected to be more prominent at lower concentrations. For $\sigma^* \gtrsim 2$ the lateral concentration fluctuations decrease and the two approaches agree well.

6.5 Summary

There is a growing body of evidence that most end-tethered polymer systems are in a regime of reduced surface concentrations which does not correspond to the brush limit of highly stretched chains. In this chapter, a systematic theoretical study of end-tethered polymers in good solvent was carried out, using numerical self-consistent field calculations and Monte Carlo simulations. Interests in this study include detailed comparisons of the results of the two methods with each other and with experiment. The comparisons include the limitations in the mean field NSCF approach at low surface coverage, where fluctuation effects and lateral inhomogeneities may be important. As in other Chapters, our MC approach incorporates the calculation of various autocorrelation functions and related time scales.

In our first set of MC simulations, we modeled free polymer in athermal solvent. From our results, we extracted an effective statistical segment length, b_{MC}. For the end-tethered systems, we did MC simulations and NSCF calculations. For the latter,

we needed to choose appropriate values for χ and b_A, which we did by fitting NSCF profiles to the MC profile for high molecular weight and coverage. We did two fits. In the first, we set $\chi = 0$ and varied b_A: the resulting value for b_A agreed with b_{MC} to within 2%, which is within statistical error in the fit. In the second fitting, we varied both χ and b_A: the result was $\chi = 0.26$ and $b_A = 1.32$.

All the MC and NSCF calculations produced similar polymer density profiles. There is a depletion layer at the surface, through which the polymer density increases smoothly to a maximum. Beyond that, the profile decreases monotonically and ends smoothly in an extended tail. The location of the maximum is nearly independent of coverage, in agreement with the experiments of Kent *et al.* [68, 69] The dependence of ϕ_m on σ^* and Z_A is consistent with the analytical SCF predictions.

The NSCF calculations for which both χ and b_A were fitted were in somewhat better agreement with the MC results, and we used these for the systematic comparisons. This choice better isolates the effects of lateral inhomogeneities at low surface coverages, but it does not have qualitative effects.

Earlier calculations have suggested that the NSCF gives quantitative agreement with experiment for $\sigma^* \geq 2$. This is corroborated here with the good agreement between the MC and NSCF results for the *rms* layer thicknesses in this regime. They also agree well with experiment in this range of σ^*. Below $\sigma^* \simeq 2$, NSCF layer thicknesses are less than the MC thicknesses, implying that the lateral inhomogeneity is playing a role here. The limiting values of the rms thickness at $\sigma^* \to 0$, calculated

using the MC simulations, are in quantitative agreement with experiments. [68, 69] other MC studies [148] and renormalization group calculations. [144]

However, a surprising result occurred at low σ^*: Both the MC and NSCF *rms* thicknesses decreased monotonically as $\sigma^* \to 0$, with no evidence of a plateau region. This is expected for the NSCF formalism, in which the density is approximated by its laterally averaged value which decreases to zero at zero coverage. However, this approximation is not made in the MC calculations, and the layer thicknesses were expected to level off at small σ^*, i.e., in the mushroom regime. Our results imply that chains are still perturbed by their neighbors, even for $\sigma^* \leq 0.5$. This is perhaps not as surprising when one considers that the average *end-to-end distance* is greater than the average distance between anchoring points even at $\sigma^* \simeq 0.5$. The absence of a plateau region is not inconsistent with the experimental results in this region, since the experimental uncertainties were large.

When normalized by the corresponding R_g, the MC layer thicknesses for all molecular weights reduce to a single function of σ^*, which is nearly linear. This agrees with experiments, with slightly better agreement than the NSCF results give. [46] This representation is much better than a power law fit. This implies the general result that R_g remains a relevant length scale in these systems.

Together, our results imply that the MC and NSCF calculations agree well with each other for $\sigma^* \gtrsim 2$. For $\sigma^* \lesssim 2$, the lateral inhomogeneities begin to play a role, but chains are perturbed by their neighbors at coverages at least as low as $\sigma^* \simeq 0.5$.

The radius of gyration of unperturbed molecules, R_g, remains a relevant length scale throughout this regime, and a simple linear relationship, Equation (6.5), describes the layer thicknesses much better than a power law relationship in this experimentally interesting range of coverage.

Chapter 7

Thin Films

7.1 Introduction and Review

The study in this chapter is used to provide information on equilibrium statistics of thin films. It is motivated by previous theoretical work and the results from two separate experimental studies. The work of Yerushalmy-Rozen *et al.* [5, 6, 149, 150] implies that a thin film with both an end-tethered layer and free polymers in solution can be stabilized for periods of up to years. It is believed that the coupling between the two polymers is responsible for the stability of the film. Whether stability is obtained via a thermodynamic or a dynamic mechanism is not clear, and requires further investigations of the structure and properties of thin films. In other experiments, Lee and Kent [2] presented an experimental study of the penetration of the free chains into the end-tethered layer. It was investigated for a series of molecular weights of both polymers, various surface coverages, and various volume fractions of free chains.

de Gennes [13] used a scaling approach to study these systems. The analysis was

restricted to $Z_F \lesssim Z_A$. de Gennes' work was followed by detailed analytical SCF calculations [16, 74] for $Z_F \ll Z_A$. Both approaches identify three major regimes in terms of the surface coverage and the bulk volume fraction of free chains. The scaling

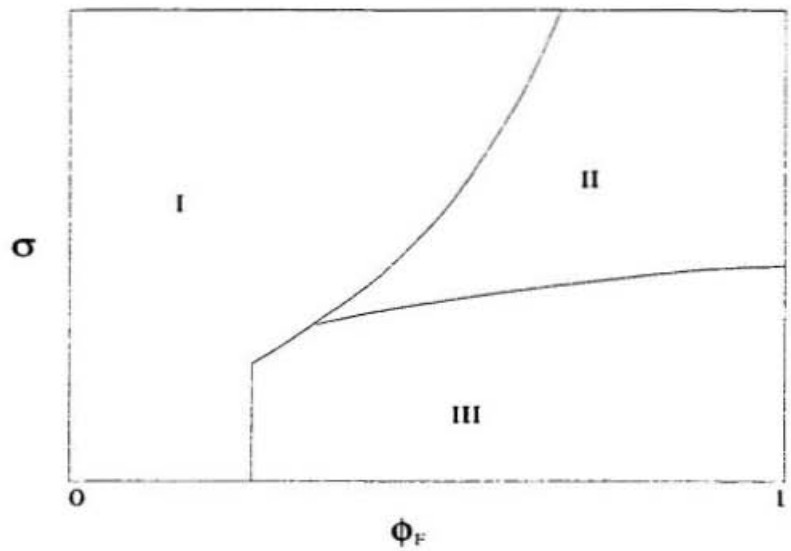

Figure 7.1: Sketch of the boundaries for different regimes predicted by scaling theory for $Z_F \lesssim Z_A$. SCF theory predicts similar behavior.

of the layer height for each regime and the equations for boundaries between regimes are given in Table 7.1 for the analytical SCF and scaling theories.

In discussing the de Gennes theory, it is useful to use σ_A and σ_A^0 to denote the volume fraction of end-tethered polymer in the presence and absence of free polymer, respectively. For the free chains, $\bar{\phi}_F$, ϕ_F and ${}_L\phi_F$ denote the overall volume fraction, the volume fraction in the bulk, and the volume fraction in the end-tethered layer.

Regime I corresponds to relatively low density of free chains. In this regime, there is very little penetration of the free chains, and the structure of the end-tethered layer

Power dependences of layer height		
Regime	SCF	Scaling
I	$Z_A\sigma^{1/3}$	$Z_A\sigma^{1/3}$
II	$Z_A\sigma o_F^{-1}$	$Z_A\sigma o_F^{-1}$
III	$Z_A\sigma^{1/3}Z_F^{-1/3}o_F^{-1/3}$	$Z_A\sigma^{1/3}Z_F^{-1/3}o_F^{-5/12}$
Equations of Boundaries between Regimes		
Boundary	SCF	Scaling
I-II	$b_A^2\sigma \simeq o_F^{3/2}$	$b_A^2\sigma \simeq o_F^{3/2}$
II-III	$b_A^2\sigma \simeq o_F Z_F^{-1/2}$	$b_A^2\sigma \simeq o_F^{7/8}Z_F^{-1/2}$
I-III	$o_F \simeq Z_F^{-1}$	$o_F \simeq Z_F^{-4/5}$

Table 7.1: Power law dependences for the layer height h from scaling and SCF theories for different regimes and equations for boundaries between regimes. These are all for the case $Z_F < Z_A$.

is controlled by the end-tethered chains as described in Chapter 6. The layer height is therefore given by Equation (1.6). Assuming a step-like profile in the end-tethered layer, the volume fraction o_A is equal to o_A^0, and is determined from Equation (1.6). As o_F is increased, there is a transition from regime I to regime II or III when σ is high or low, respectively. The boundary between regimes I and II occurs when $o_F = o_A^0$. Given o_A^0 from Equation (1.6), the boundary is then given by

$$b_A^2\sigma \simeq o_F^{3/2} \,. \tag{7.1}$$

In regimes II and III, the bulk volume fraction of free chains is large enough so they influence the properties of the end-tethered layer. In regime II, there is still negligible penetration of free chains into the end-tethered layer and the layer is said to be "dominated" by the end-tethered chains. In the scaling theory of de Gennes [13], the following argument is used to determine the equilibrium layer height. In the

bulk solution. each free chain sees a repulsive potential $\mu_{rep}(o_F)$ which is due to the other free chains. In the end-tethered layer. each free chain sees a repulsive potential which has the same functional form as the potential in the bulk. but arises from the end-tethered chains. *i.e.* $\mu_{rep}(o_A)$. The equilibrium condition for the free chains requires

$$\mu_{rep}(o_F) = \mu_{rep}(o_A) \ . \tag{7.2}$$

The end-tethered layer responds to the free chains by decreasing its thickness so that $o_A = o_F$. Assuming a step-like profile. $ho_A = \sigma b_A^3 Z_A$. and this results in

$$h = b_A^3 Z_A \sigma o_F^{-1} . \tag{7.3}$$

In regime III. the free chains penetrate into the end-tethered layer and $o_A \ll {}_L o_F$ where ${}_L o_F$ is the volume fraction of free chains in the end-tethered layer. The free chains therefore screen out the interactions between the end-tethered chains. and the end-tethered layer is dominated by the free polymer. This results in a reduction in the layer height. so [13]

$$h \simeq Z_A \sigma^{1/3} Z_F^{-1/3} o_F^{-5/12} \ . \tag{7.4}$$

Regime III includes a sub-regime corresponding to unstretched end-tethered polymer. and one might expect some corrections to scaling in this limit of low surface coverage. de Gennes [13] defined the boundary where the chains begin to stretch as

$$b_A^2 \sigma \simeq Z_F Z_A^{-3/2} \ . \tag{7.5}$$

The condition ${}_L o_F = o_A$ defines the boundary between regimes II and III. Equation (7.4) with a step-like profile for the end-tethered layer, results in

$$b_A^2 \sigma \simeq o_F^{7/8} Z_F^{-1/2} \tag{7.6}$$

at the boundary. We note that although Equation (7.3) assumes no penetration of free chains into the end-tethered layer, we expect considerable penetration of free chains near the boundary between regimes II and III.

In regime III, screening of volume interactions between end-tethered chains decreases with decreasing ${}_L o_F$. For $o_F \simeq {}_L o_F \simeq Z_F^{-4/5}$, a transition to a semi-dilute solution occurs and the screening of the end-tethered chains disappears. This defines the boundary between regimes I and III. These results for the boundaries and scaling of the layer height are summarized in Table 7.1.

The scaling laws and boundaries predicted by the SCF theory of Zhulina *et al.* [16] are also presented in Table 7.1. The scaling results are the same except for slight differences in the layer height and boundaries for regime III. This SCF theory was restricted to $Z_F \ll Z_A$ and extremely high surface coverage. The authors noted that the expressions derived for each regime are approximate and corrections to scaling of the layer height due to non-power dependencies were investigated.

Wijmans, Zhulina and Fleer [17] extended the SCF theory of Zhulina *et al.* [16]. Their study provided details of the power laws for the layer height and the degree of penetration of the end-tethered chains into the polymer solution, and of the free chains into the end-tethered layer. Results were obtained for a wide range of sur-

face coverages and homopolymer volume fractions. For non-overlapping or slightly overlapping end-tethered chains, *i.e.* low σ^*, three other regimes were identified with their corresponding scaling laws for the height of the end-tethered layer. For very low densities, $o_F < Z_F^{-1}$ and $\sigma < Z_A^{-6/5}$, the free polymer has a negligible effect on the layer height, the end-tethered chains behave as isolated chains and

$$h \sim Z_A^{3/5} . \tag{7.7}$$

With an increase in o_F, the effect of the free polymer is accounted for by introducing an effective virial coefficient, $\nu_{eff} = (Z_F o_F)^{-1}$, and the layer height scales as

$$h \sim Z_A^{3/5} (Z_F o_F)^{-1/5} \tag{7.8}$$

when $Z_F^{-1} < o_F < Z_F^{-1} Z_A^{1/2}$ and $\sigma < (Z_F o_F)^{2/5} Z_A^{-6/5}$. A further increase in the volume fraction of free polymer results in end-tethered polymers which can be described as Gaussian coils and

$$h \sim Z_A^{1/2} \tag{7.9}$$

which applies if $o_F > Z_A^{1/2} Z_F^{-1}$, $b_A^2 \sigma < Z_F o_F Z_A^{-3/2}$ and $b_A^2 \sigma < o_F Z_F^{-1/2}$ are satisfied.

These analytic theories are applied to systems with $Z_F \ll Z_A$. In the case that $Z_F \gg Z_A$, regime III is expected to disappear since, in the work of Zhulina and Semenov *et al.* [29], the authors concluded that partial penetration of long free chains is negligible.

Wijmans, Zhulina and Fleer [17] also performed a direct comparison of volume fraction profiles between their SCF theory and lattice based NSCF calculations. In all

cases, the profiles for the end-tethered layer were well represented by the SCF theory due to the strongly stretched high molecular weight end-tethered chains ($Z_A = 600$). For the interpenetration of free and end-tethered chains, there was good agreement for $Z_F \ll Z_A$ ($Z_F = 30$) and $\sigma^* \gtrsim 5$, but $\sigma^* \gtrsim 25$ was required for good agreement when $Z_F \sim Z_A/2$ ($Z_F = 300$). At all surface coverages, the SCF theory predicted lower interpenetration of chains compared to the NSCF calculations. However, the difference became negligible at extremely high surface coverages ($\sigma^* \simeq 110$) where the free chains were practically completely expelled from the end-tethered layer.

Lee and Kent [2] performed experiments and measured the volume fraction profiles of both, end-tethered and free chains. Penetration of relatively high molecular weight free polymer into the end-tethered layer was observed. They concluded that finite molecular weight effects are important, and regime III may be relevant for relatively high molecular weight free chains and coverage.

In the experiments of Yerushalmy-Rozen *et al.* [5, 6, 149, 150] the authors noted that end-tethered and free polystyrene (PS) in good solvent can form stable films on surfaces when the concentration of free chains exceeds some critical value. The end-tethered layers were composed of chains with degree of polymerization $Z_A \simeq 3,600$ and reduced surface coverage $\sigma^* \simeq 6$. The degree of polymerization of the free chains was relatively high, with $Z_F \simeq 3,200$ to 68,000. They found the critical concentration to be approximately $5C^*$, where C^* is the overlap concentration of the free chains. The ability of these high molecular weight chains to stabilize the films is interesting

since the analytic SCF theories [16, 29] suggest that there is no penetration of free chains into the end-tethered layer for $Z_F \gg Z_A$. In fact, these experiments show that the critical concentration of the free polymer decreases with increasing Z_F.

Wijmans and Factor [47] performed lattice based NSCF calculations to compare with the experimental results of Lee *et al.* [151] for free and end-tethered PS in ethyl benzoate (EB). Volume fraction profiles were obtained for the end-tethered polymer and compared with the neutron reflectivity data of Lee *et al.* [151] with and without free polymer. The profiles were in reasonable agreement with experiment. No comparison of the profiles of the free polymer was done. Further NSCF calculations were performed and showed that, with an increase in the molecular weight of the free chains, the profiles became more step-like in the region of interpenetrating chains.

The recent studies by Lee and Kent [2] suggest that the penetration of the free chains should be investigated for surface coverages which are more closely related to experiment. This is the subject of the rest of this study. As in Chapter 6, a NSCF approach is appropriate, except at low concentrations, where lateral inhomogeneities develop. As discussed in previous chapters, Monte Carlo simulations are well suited for studying systems at low concentrations but are restricted to low molecular weight polymers. A Monte Carlo study is therefore to obtain information on the structure and properties of the films and to provide a quantitative measure of the accuracy of the NSCF approach. A NSCF study is also done to make direct comparisons with the experimental work of Lee and Kent, and predictions from analytical SCF and scaling

theories. In both studies we investigate the layer thickness and the penetration of the free polymers into the end-tethered layer as functions of the molecular weights of both polymers, the surface coverage and the volume fraction of free polymer in solution.

7.2 Monte Carlo Simulations

The general description of the MC simulations for thin films has been given elsewhere [32, 152] and in Chapter 2. Here, we provide a brief description of the simulations. As in Chapter 6, we use a simple cubic lattice, with periodic boundary conditions in the x and y directions and impermeable walls at $z = 1$ and $z = L_z$. The systems contain free (F) and end-tethered (A) polymers, and the empty sites correspond to solvent (S). The free polymers are allowed to move anywhere in the system whereas the end-tethered polymers have one end of each chain confined to, but free to move within, the $z = 1$ plane. The number of polymers N_i ($i = A, F$) and number of effective monomers Z_i vary in each simulation with $N_F = 100 - 5,625$, $Z_F = 25 - 100$, $N_A = 100 - 1,707$ and $Z_A = 60 - 100$. Details are shown in Table 7.2. The linear dimensions are chosen to accommodate all the polymers with the restriction that $L_x = L_y \geq Z_i$ and $L_z \gg Z_i$ with $i = A, F$.

As in Chapter 6, all nearest neighbor interactions have been set to zero ($\epsilon_{ij} = 0$). All four types of motions are used: reptation, kink-jump, crankshaft and Brownian motion [79–82], and all MC transitions that satisfy excluded volume constraints are

MC & NSCF					Monte Carlo		
Z_F	Z_A	σ^*	L_z	$\bar{\phi}_F$	$L_x = L_y$	N_F	N_A
25	100	1–12	200	0.54	100–114	4.320–5.625	100–923
80	80	1–12	200	0.54	100	1.353	101–1.207
100	60	1–12	200	0.54	100	1.082	142–1.707

Table 7.2: Description of MC simulations and NSCF calculations for thin films.

accepted. End-to-end vector autocorrelation functions, which are defined in Equation (2.11), are used to monitor the relaxation of the end-to-end vectors of the free polymers. The motion of the free polymers is also monitored by calculating a diffusion constant D_F which is approximated in Equation (2.15). The average time required for a free polymer to travel the average distance between nearest neighbor free polymers is given in Equation (2.16). For the end-tethered polymers, we calculate and monitor the same autocorrelation functions as in Chapter 6.

The relaxation time of the system is taken as the maximum of all the autocorrelation times. The time is measured in terms of N-bead cycles where $N = N_F Z_F + N_A Z_A$ Monte Carlo attempts. The simulations are run for 10,000 N-bead cycles plus a minimum of 20 relaxation times. Ensemble averages are then taken over a minimum of 40 relaxation times.

7.3 Numerical Self-consistent Field Theory

The general NSCF theory for this system is described in Chapter 3. A specific system is characterized by the parameters Z_i $(i = A, F)$, b, σ, $\bar{\phi}_F$, $\rho_{0\kappa}$ $(\kappa = A, F, S)$

and the Flory parameter χ_{lm} $(l, m = A, F, S)$. In this study, the free and end-tethered polymers are the same species, therefore, $b = b_A = b_F$, $\chi_{AF} = 0$, and we set $\chi = \chi_{AS} = \chi_{FS}$ and $\rho_{0\kappa} = 1$ $(\kappa = A, F, S)$. The local volume fraction of free polymer, $\phi_F(z)$, can be determined from the convolution of the propagator $q_F(z, \tau)$ with itself, and from Equations (3.94), (3.105) and (3.107). It is given by

$$\phi_F(z) = \frac{\bar{\phi}_F L}{Z_F \mathcal{Q}'_F} \int_0^{Z_F} d\tau q_F(z, \tau) q_F(z, Z_F - \tau) \ . \tag{7.10}$$

The volume fraction of end-tethered polymer is calculated from $q_A(z, \tau)$ and $\tilde{q}_A(z, \tau)$, through Equation (6.7).

All three propagators satisfy the modified diffusion equation, Equation (3.109), and are subject to the initial and boundary conditions given by Equations (3.112), (3.113), and (3.114).

The incompressibility condition implies that

$$\phi_A(z) + \phi_F(z) + \phi_S(z) = 1 \tag{7.11}$$

everywhere.

From Equation (3.98), the potentials acting on both polymers can be written as

$$\omega_j(z) = \ln\left(\frac{\bar{\phi}_S}{\phi_S(z)}\right) - 2\chi(\phi_P(z) - \bar{\phi}_P) \tag{7.12}$$

where $j = A, F$, $\phi_P(z) = \phi_A(z) + \phi_F(z)$ and $\bar{\phi}_P = \bar{\phi}_A + \bar{\phi}_F$, and an additive constant has been chosen such that $\omega_j(z) \to 0$ as $\phi_S \to \bar{\phi}_S$.

As usual, the problem is solved self-consistently, via the iterative procedure described in Reference [46].

7.4 Results and Discussion

This Section is divided into four subsections. In Section 7.4.1, a quantitative comparison between MC simulations and NSCF theory is done for various surface coverages, and molecular weights of both end-tethered and free chains. The extent of penetration of the free chains in the end-tethered layer is investigated, and a qualitative comparison with predictions from analytical theories is also performed. In Section 7.4.2, a direct comparison between the experiments of Lee and Kent [2] and NSCF theory is done for relatively high surface coverage and for both relatively high and low molecular weight free chains. The results for the penetration of the free chains into the end-tethered layer are compared with predictions from analytical theories. Section 7.4.3 is devoted to a systematic study of the effects of the free polymer on the end-tethered layer profiles, the interpenetration of the free and end-tethered polymers, and comparisons with predictions from analytical theories for the three regimes discussed in the Introduction. Because of the high molecular weight polymers included in this study, the NSCF approach is used. In Section 7.4.4, the scaling of the layer height is investigated for the three regimes defined by the analytical theories using the NSCF approach. A supplementary series of NSCF calculations is also done to investigate the change in physical behavior from one regime to another.

7.4.1 MC Simulations and NSCF Theory

A series of NSCF calculations and MC simulations with degrees of polymerization ranging from $Z_F > Z_A$ to $Z_F \ll Z_A$, $\sigma^* = 1$ to 12, and $\bar{o}_F = 0.054$ has been done to investigate the behavior of these systems and compare results between the MC and NSCF approaches. The simulations and calculations are listed in Table 7.2. As in Chapter 6, two sets of NSCF calculations were done. In the first set, $\chi = 0$ and $b = b_{MC} = 1.06$. In the second set, $\chi = 0.26$ and $b = 1.32$, the renormalized mean field parameters.

In Figure 7.2(a), the volume fraction profiles of the free and end-tethered chains are plotted as functions of the distance from the end-tethering surface for a system with $\sigma^* = 12$, $Z_A = 100$ and $Z_F = 25$. The filled circles are the results from the MC simulations; the solid lines are the NSCF calculations with $b = 1.06$ and $\chi = 0$, and the dashed lines are the NSCF calculations with the renormalized parameters. The MC results agree very well with both sets of NSCF results, except for slight differences in the vicinity of the peak and tail of the end-tethered layers. The NSCF results from the renormalized parameters agree best with the MC simulations. The overall agreement between MC simulations and NSCF calculations is not surprising considering that the system is in the upper limit of experimental surface coverages. What is surprising is the agreement in regions of low concentrations of free and end-tethered polymers, *i.e.* the overlap region.

Figure 7.2(b) displays the profiles for a system which is the same as the previous

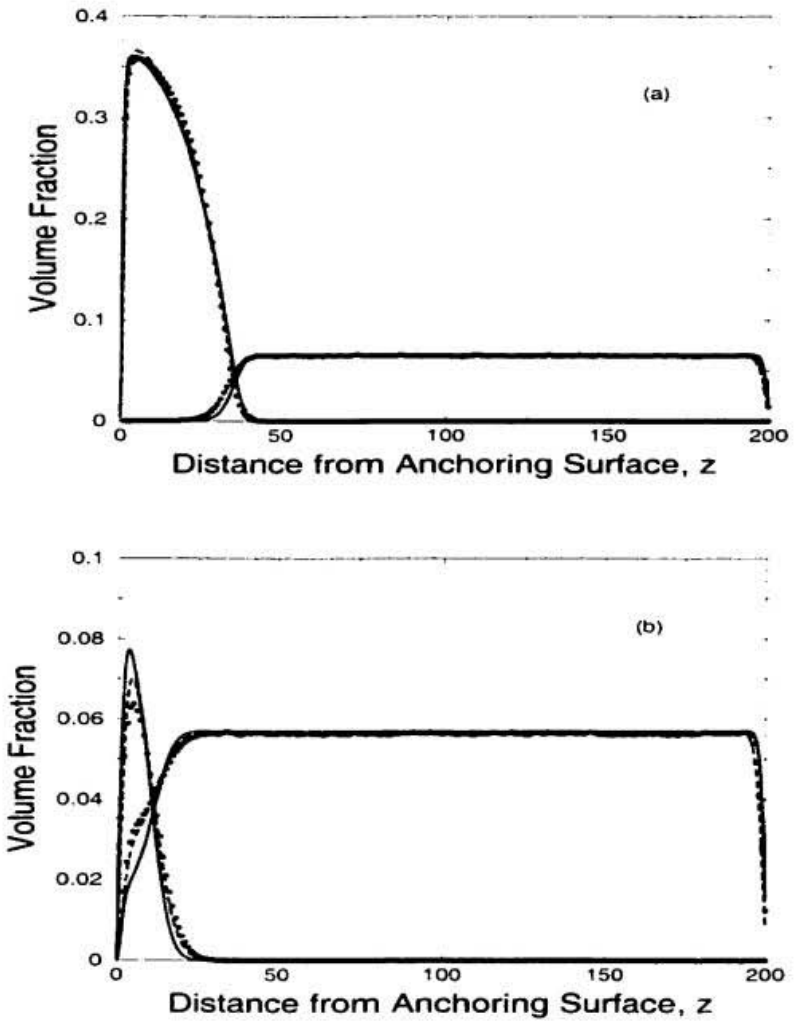

Figure 7.2: Volume fraction profiles of end-tethered and free polymers: $Z_F = 25$, $Z_A = 100$. $\bar{\phi}_F = 0.054$ and $\sigma^* = 12$ (a) and $\sigma^* = 1$ (b). MC simulation (•). NSCF calculation with $\chi = 0$ and $b = 1.06$ (solid lines) and NSCF calculation with $\chi = 0.26$ and $b = 1.32$ (dashed lines).

one except that the surface density is lowered to $\sigma^* = 1$. The results are plotted on a different scale, for convenience. In this instance, both sets of NSCF results agree reasonably well with the MC simulations. In particular, the ones using the

renormalized parameters show remarkable agreement, especially considering that the system is now in a regime of low coverage. The NSCF calculation reproduces the detailed structure of the profiles of both polymers. What is striking is the shape of the volume fraction profile for the free polymer within the end-tethered layer: A kink in the profile appears at the position corresponding to the maximum of the volume fraction of end-tethered polymer. Beyond the position of the maximum, the volume fraction of free polymer increases at a slower rate and reaches a constant value when $\phi_A(z)$ reaches zero. These details are in remarkable agreement in the two calculations.

Since the second set of NSCF calculations, with $\chi = 0.26$ and $b = 1.32$, agrees better with the MC results, as with end-tethered layers alone, the calculations with the renormalized parameters are used for the quantitative analysis. This is the same procedure as in Chapter 6.

For a quantitative measure of the range of validity of the NSCF theory, the *rms* layer thickness, h_{rms}, is plotted, in Figure 7.3(a), as a function of σ^* for all MC simulations and NSCF calculations described in Table 7.2. Three systems are shown, with $Z_F = Z_A/4$, $Z_F = Z_A$ and $Z_F = Z_A/0.6$. For a given Z_A, h_{rms} increases with increasing σ^*, as expected, for both MC simulations and NSCF calculations. When $Z_A = 100$, the discrepancy between the two approaches decreases with increasing σ^*. This result is consistent with the fact that the parameters were fitted to $Z_A = 100$ and $\sigma^* = 10$. It is also consistent with the fact that, as σ^* decreases, inhomogeneities begin to develop and the lateral averaging in the NSCF calculations underestimates the

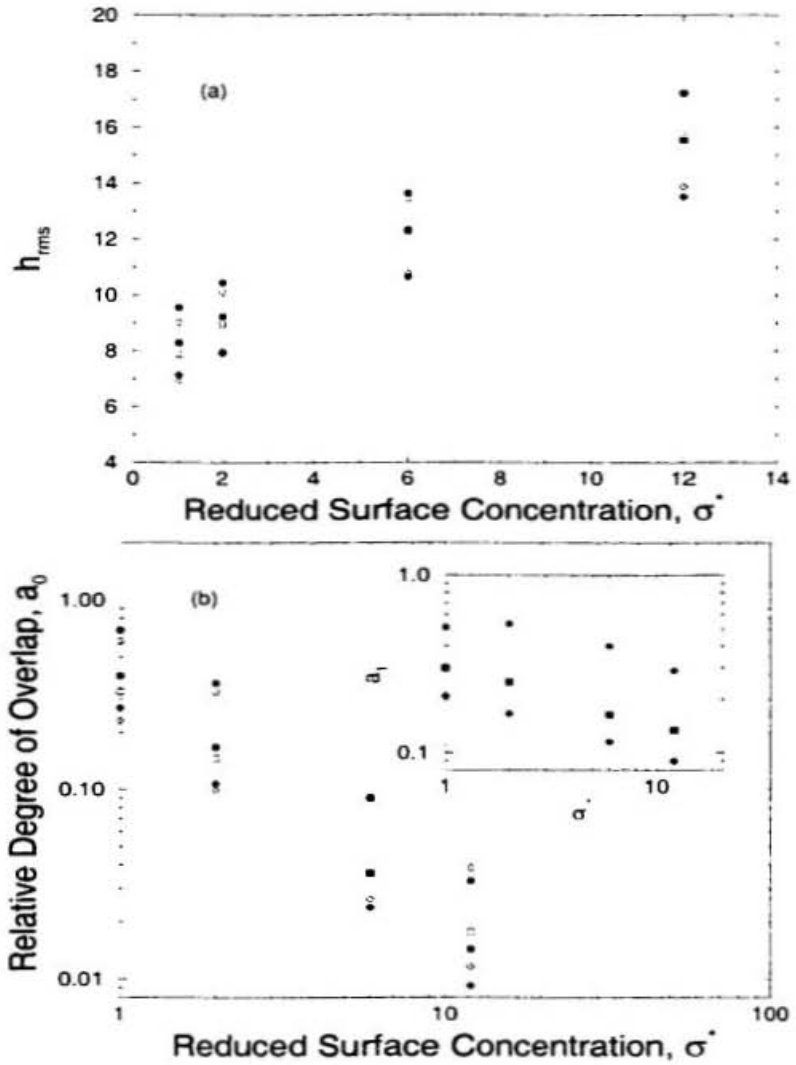

Figure 7.3: a) *rms* thickness of the end-tethered layer versus the reduced surface concentration. b) Log-log plot of the relative degree of overlap versus the reduced surface concentration. The inset shows a log-log plot of the area of overlap versus the reduced surface coverage: MC simulations (filled symbols), NSCF calculations (open symbols), $Z_F = 25$ and $Z_A = 100$ ($\circ$), $Z_F = 80$ and $Z_A = 80$ ($\square$), $Z_F = 100$ and $Z_A = 60$ ($\diamond$). $\chi = 0.26$ and $b = 1.32$.

local polymer volume fraction. When $Z_A \leq 80$ and $\sigma^* \geq 6$, the relative discrepancy between the two approaches actually increases slightly with increasing σ^*.

As seen in Figure 7.2(b), the penetration of the free chains into the end-tethered layer can be considerable. In fact, the free polymers can completely envelop the end-tethered layer. We introduce the *relative degree of overlap* of the free and end-tethered polymers to quantify the interpenetration. We define it as the fraction of the end-tethered layer profile which intersects the free polymer profile. It is given by

$$a_o = \frac{\int_0^L \min(\phi_F, \phi_A) dx}{\int_0^L \phi_A dx} \quad . \tag{7.13}$$

where L is the film thickness.

As discussed above, the analytical theories predict that, for systems in regimes I and II, there is no penetration of free chains, and therefore a_0 should be close to zero. The boundary between regimes II and III occurs when the volume fractions of free and end-tethered chains in the layer are equal, ${}_L\phi_F = \phi_A$. Qualitatively, this happens at the free polymer volume fraction at which $a_0 \simeq 1$. The boundary between regions I and III separates a regime where there is no penetration of free chains and a regime where the free chains completely envelop the end-tethered layer. In practice, the evolution from zero penetration to complete enveloping may not be sharp, resulting in $0 \lesssim a_0 < 1$ in either regime I, II or III. Whether the system is in regime I or II, the presence of free polymer in the end-tethered layer would indicate a continuous evolution towards regime III with increasing ϕ_F or decreasing σ^*. As shown in Figure 7.1, the cross-over can occur either from regime I or regime II, with an increase in ϕ_F or a decrease in σ.

Figure 7.3(b) shows a log-log plot of a_0 as a function of σ^* for the same calculations

and simulations shown in Figure 7.3(a). Overall in these systems, a_0 ranges from about 0.7 when σ^* is low and $Z_F = Z_A/4$ down to about 0.01 when σ^* is high and $Z_F = Z_A/0.6$. For constant Z_A, as σ^* increases from unity to $\sigma^* = 12$, a_0 decreases by a factor of about 20. At constant σ^*, a_0 decreases by a factor of about 3 in going from $Z_F = Z_A/4$ to $Z_F = Z_A/0.6$. The largest relative discrepancy between the MC and NSCF results occurs at $\sigma^* = 12$. For high surface coverage, the free chains are expelled from most of the end-tethered layer and a_0 is sensitive to the volume fraction profiles in the tail region of the end-tethered layer. In this case, the NSCF results show a longer tail region for the end-tethered polymer profile (see Figure 7.2(a)) and this results in a larger a_0. At lower surface coverage, the opposite is true and the NSCF results show a smaller a_0 compared to the Monte Carlo results. In this case, there is more penetration of the free chains and a_0 depends on the volume fraction profiles throughout the end-tethered layer.

When $Z_F = Z_A/4$ (circles), a_0 varies from about 0.7 down to about 0.03 with increasing σ^*. For $Z_F = Z_A/0.6$ (diamonds), $a_0 \lesssim 0.18$ for $\sigma^* \geq 2$, reaching as low as $a_0 \sim 0.01$ for $\sigma^* = 12$. These results are consistent with the predictions of the analytical theories that higher molecular weight free polymers penetrate the end-tethered layers to a lesser extent than lower molecular weight ones.

The decrease in a_0 with increasing surface coverage can be attributed to a decrease in the overlap region and/or expulsion of the free polymers from the end-tethered

layer. To further investigate this effect, we define the overlap integral, a_1, by

$$a_1 = \int_0^L \min(\phi_F, \phi_A) dx. \tag{7.14}$$

which is just the numerator of Equation (7.13). Results for a_1 are presented in the inset of Figure 7.3(b).

For $Z_F = Z_A/4$, the overlap a_1 initially increases with increasing σ^*. This is due to the extensive penetration of the free chains ($a_0 \simeq 1$). When the free polymer still completely envelops the end-tethered layer ($a_0 = 1$), as σ^* increases, the area under the curve $\phi_A(x)$ increases, *i.e.* there is more end-tethered polymer. In the limiting case where the end-tethered layer remains completely enveloped by the free polymer, a_1 must increase with σ^*. When further increase in the surface coverage begins to cause expulsion of the free chains from the end-tethered layer, the overlap begins to decrease. When $Z_F > Z_A$, the system begins in a regime of weak relative degree of overlap, and both a_0 and a_1 decrease monotonically with increasing surface coverage.

What is interesting to note is the relatively small change in the overlap compared to the relative degree of overlap. An increase in the reduced surface coverage from $\sigma^* = 1$ to $\sigma^* = 12$ causes a decrease of approximately 50% in the overlap whereas the relative degree of overlap decreases by a factor of at least 25. Increasing the surface coverage therefore effectively expels the free chains from the main part of the end-tethered layer while keeping the overlap relatively constant compared to the relative degree of overlap.

We note that these results are for relatively low molecular weight polymers. We

investigate these effects for real systems in the following sections.

7.4.2 Comparison with Experiments

In this section we make a comparison with the profiles measured experimentally by Lee and Kent [2]. The systems they studied consisted of free and end-tethered PS in EB. They used two combinations of molecular weights of the free and end-tethered polymers. In the first case, $Z_F \ll Z_A$ with $Z_F = 413$ and $Z_A = 1.625$, and in the second case, $Z_F \simeq 2Z_A$ with $Z_A = 3.846$ and $Z_F = 1.625$. We note that the molecular weights for the free and end-tethered chains obtained from the experiments of Lee and Kent were precise to two significant figures. As shown in Figures 7.4(a) and 7.4(b), with $\sigma^* = 12$ and $\phi_F \simeq 0.06$, they observed considerable penetration of the free chains when $Z_F \ll Z_A$. When $Z_F \simeq 2Z_A$, the experiments showed a surprisingly large degree of penetration of the free polymer, with a plateau region reaching relatively deep into the end-tethered layer. In contrast, analytic SCF theories predict no interpenetration of the polymers for these parameters.

The volume fraction profiles from the NSCF calculations are also presented in Figures 7.4(a) and 7.4(b). For these comparisons we used experimental system characteristics. For PS free and end-tethered polymers the statistical segment length was $b = 0.71$ nm and the Flory interaction parameter for PS polymer in EB was $\chi = 0.44$ [46]. The reduced surface-coverage σ^* is determined from Equation (1.4)

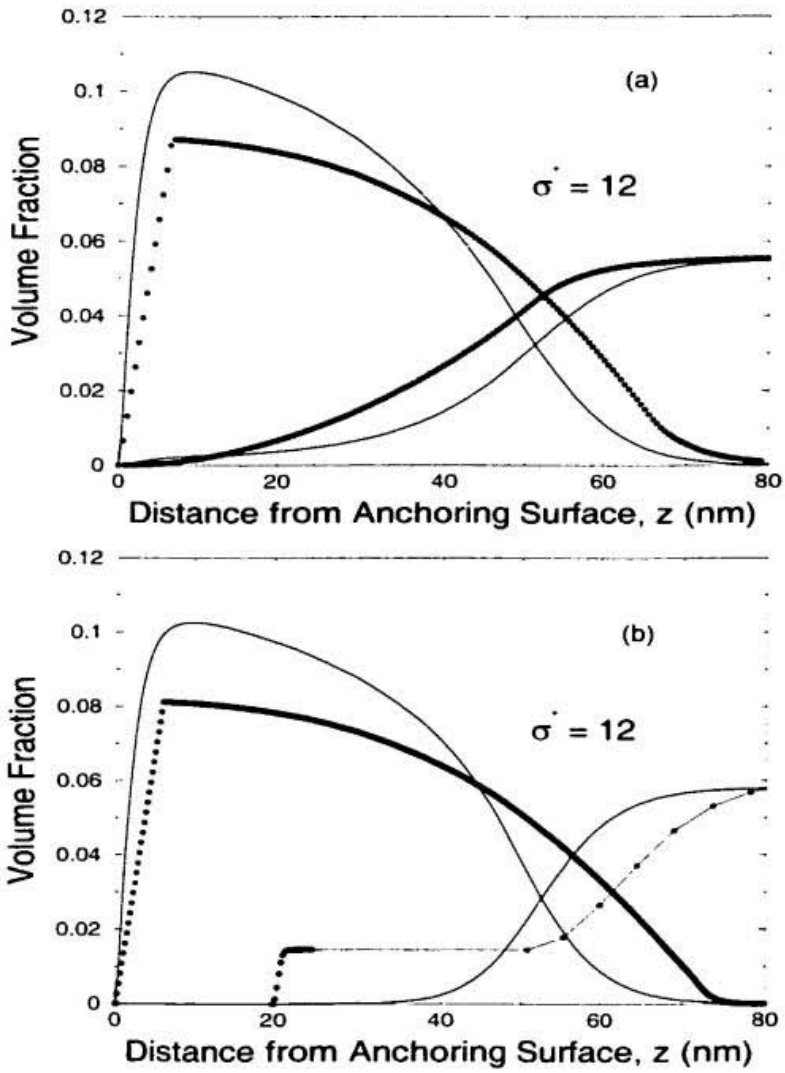

Figure 7.4: Volume fraction profiles of end-tethered and free polymers: a direct comparison with experiments of Lee and Kent [2]. a) $Z_F = 413$, $Z_A = 1,625$, $\phi_F \simeq 0.06$ and $\sigma^* = 12$. b) $Z_F = 3,846$, $Z_A = 1,625$, $\phi_F \simeq 0.06$ and $\sigma^* = 12$: Experiments (•) and NSCF calculations (lines). The solid curve for the experimental volume fraction profile of free chains in (b) serves as a guide to the eye.

with the radius of gyration given by [46, 68, 69, 153]

$$R_g = 0.0117 M_w^{0.595} . \tag{7.15}$$

where M_w is the molecular weight of the polymer amd R_g is in nanometers. For $Z_F \ll Z_A$, the free polymer does indeed show some penetration of the free chains deep into the end-tethered layer for σ^* as high as 12. The volume fraction $o_F(z)$ reaches the surface, and the tip of the end-tethered layer extends to about 75 to 80 nm. The condition $o_F \sim o_A$ occurs at $z \simeq 52 - 55$ nm. In the case of $Z_F > Z_A$, neither the experimental or theoretical profile for the free polymer reaches the surface, but they both end at $z \sim 20 - 30$ nm. The end-tethered layer extends to about 75 nm and $o_F \sim o_A$ occurs at $z \simeq 55$ nm. In the theoretical result, the free polymer again penetrates into the end-tethered layer, but there is no plateau region. In both cases, the maximum volume fraction is greater in the theoretical profile than in the experiments, and this results in smaller layer thicknesses. There is also less penetration than found experimentally, but it is still greater than predicted by analytical SCF theory. The experimental, NSCF and analytical SCF results give $a_0 = 0.30, 0.16$ and < 0.04 for $Z_F \ll Z_A$, and $a_0 = 0.21, 0.077$ and $\lesssim 0.005$ for $Z_F > Z_A$, respectively.

7.4.3 Systematic Study: Volume Fraction Profiles, Overlap and Layer Height

To complement the experimental studies of Lee and Kent we have performed a systematic series of NSCF calculations on free and end-tethered PS polymers in EB. We investigated the height and shape of the end-tethered layer, and the relative degree

of overlap as functions of the molecular weight of both polymers, the overall volume fraction $\bar{\phi}_F$ of free polymer and σ^*. Our series included 256 NSCF calculations in which the degree of polymerization of both polymers was varied from 400 to 4,000, $\bar{\phi}_F$ from 0.005 to 0.06, and σ^* from 2 to 12. The maximum overall volume fraction, $\bar{\phi}_F = 0.06$, was chosen to correspond to the experiments of Lee and Kent [2].

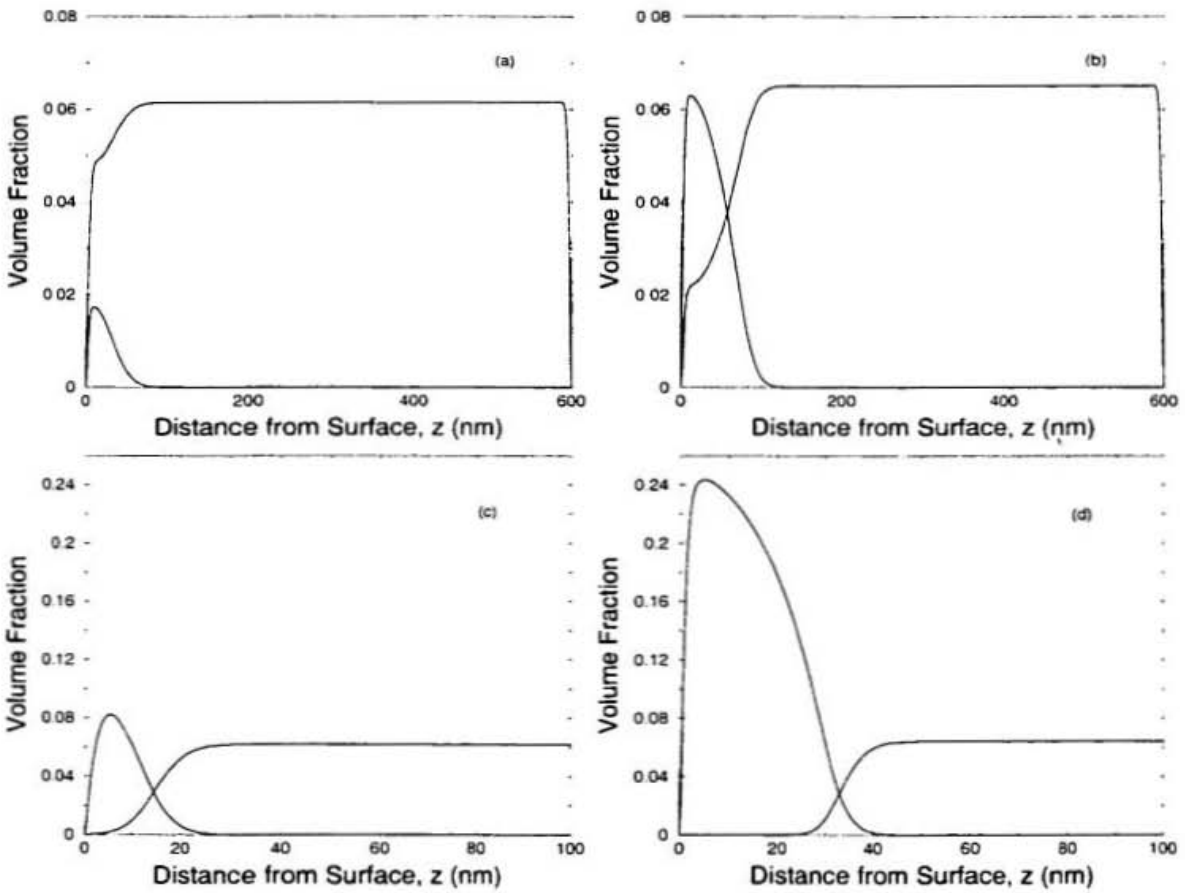

Figure 7.5: Volume fraction profiles of end-tethered and free polymers: a) $Z_F = 400$, $Z_A = 4,000$, $\bar{\phi}_F = 0.06$ and $\sigma^* = 2$. b) $Z_F = 400$, $Z_A = 4,000$, $\bar{\phi}_F = 0.06$ and $\sigma^* = 12$. c) $Z_F = 4,000$, $Z_A = 400$, $\bar{\phi}_F = 0.06$ and $\sigma^* = 2$. d) $Z_F = 4,000$, $Z_A = 400$, $\bar{\phi}_F = 0.06$ and $\sigma^* = 12$.

Figures 7.5(a) and 7.5(b) show volume fraction profiles from calculations with $Z_F = 400$, $Z_A = 4.000$ and $\bar{o}_F = 0.06$ for $\sigma^* = 2$ and $\sigma^* = 12$, respectively. The shapes of the profiles show some interesting features, as seen in results from the MC simulations, with a kink in $o_F(z)$ at the position corresponding to the maximum in $o_A(z)$.

In Figure 7.5(a), the low molecular weight free chains completely envelop the end-tethered layer due to the relatively low surface coverage. In Figure 7.5(b) the tethered polymer coverage is increased to $\sigma^* = 12$ and yet the free polymers still penetrate into the end-tethered layer, with $a_0 = 0.58$. This implies that systems with $Z_F \ll Z_A$ and volume fractions of free chains as low as $\bar{o}_F \simeq 0.06$ are restricted to regimes where there is considerable penetration, by the practical upper limit of $\sigma^* \simeq 12$.

At the other extreme, $Z_F \gg Z_A$. Figures 7.5(c) and 7.5(d) show volume fraction profiles for $Z_F = 4.000$, $Z_A = 400$ and $\bar{o}_F = 0.06$. For convenience, the data in Figures 7.5(c) and 7.5(d) are plotted on a different scale than those in Figures 7.5(a) and 7.5(b). At low reduced surface coverage where $\sigma^* = 2$, the free polymers still penetrate the end-tethered layer, as shown in Figure 7.5(c). However, they are expelled from the end-tethered layer in comparison with Figures 7.5(a) and 7.5(b). In Figure 7.5(d) the surface density is increased to $\sigma^* = 12$ and now the free chains are expelled from most of the layer with the exception of some partial penetration in the tail region. What is interesting in this case is that, although there is little to no penetration deep in the layer, the overlap between the two polymers is similar to

the case shown in Figure 7.5(c). When Figures 7.5(c) and 7.5(d) are superimposed, the profiles in the overlap regions are almost identical for both $o_F(z)$ and $o_A(z)$. The major effect of increasing σ^* is thus to move the free chains farther from the surface. To a first approximation, the overlap is independent of σ^*. The most important point is that there is still penetration of the free chains for reduced surface densities up to $\sigma^* = 12$, more than predicted by analytical SCF theories.

To discuss the shape of the profiles, we begin with Figure 7.5(d) where there is little relative degree of overlap. The end-tethered layer has a depletion region near the surface, a parabolic region, and a short tail at the tip, reminiscent of the end-tethered layers found in Chapter 6. Figures 7.5(c) and 7.5(d) show that the parabolic region shortens and the tail region lengthens, with decreasing σ^*. This trend was also observed in systems of end-tethered polymers in solvent in Chapter 6 and Reference [46]. The density of the free chains also affects the shape of the end-tethered layer. At constant σ^*, the length of the tail and the relative degree of overlap, a_0, both increase with increasing $\bar{o}_F$. These same effects are also observed for $Z_F \ll Z_A$, as shown in Figures 7.5(a) and Figures 7.5(b), except that the case involving a long tail region occurs at higher relative degrees of overlap.

In Figure 7.6(a) the relative degree of overlap, a_0, is plotted as a function of σ^* for three sets of molecular weights of the free and end-tethered chains: $Z_F \ll Z_A$ (filled symbols), $Z_F = Z_A$ (open symbols) and $Z_F \gg Z_A$ (grey symbols). In each set, $\bar{o}_F$ is varied from 0.005 to 0.06. In all cases, a_0 decreases with increasing σ^*

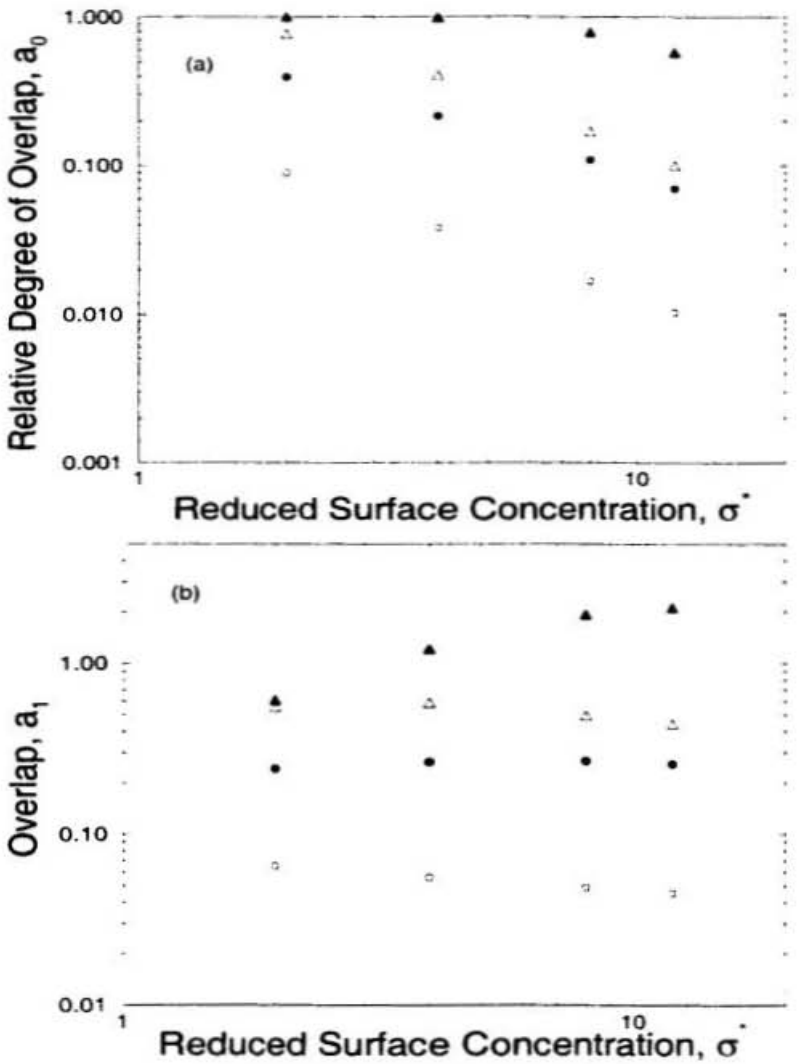

Figure 7.6: Log-log plots of the relative degree of overlap, a_0, (a) and overlap, a_1, (b) versus the reduced surface concentration: $Z_F = 400$ and $Z_A = 4.000$ (filled symbols), $Z_F = 1.600$ and $Z_A = 1.600$ (open symbols), $Z_F = 4.000$ and $Z_A = 400$ (grey symbols). $\bar{\phi}_F = 0.005$ (○), $\bar{\phi}_F = 0.06$ (△).

and decreasing overall volume fraction of free polymer. This general trend is seen in all other calculations and is consistent with previous results shown in Figures 7.5(a)-(d). In general, there is a modest decrease in the overlap a_1 with increasing surface

coverage, as shown in Figure 7.6(b), except in those cases where the free polymers completely, or almost completely, envelop the end-tethered layer. In all cases, a_1 decreases with increasing molecular weight of the free polymer. These observations are consistent with MC results observed in Section 7.4.1.

For $Z_F \ll Z_A$ and $\bar{o}_F = 0.06$ in Figure 7.6(a) (filled triangles), $a_0 \simeq 1$ when $\sigma^* \lesssim 6$ and, beginning at $\sigma^* \simeq 6$, decreases down to about 0.6 with increasing σ^*. When $\bar{o}_F = 0.005$ (filled circles), $a_0 \simeq 0.4$ when $\sigma^* = 2$ and decreases down to $a_0 \simeq 0.07$ when $\sigma^* = 12$. For $Z_F \gg Z_A$ (grey symbols), in all cases $a_0 \lesssim 0.2$ which suggests a regime corresponding to weaker penetration (see also Figures 7.5(c)-(d)). We also note that, although a_0 decreases with increasing surface coverage, Figure 7.6(b) shows that a_1 remains relatively constant. This is also shown qualitatively in Figures 7.5(c)-(d). The intermediate case with $Z_F = Z_A$ follows the same general trends: more interpenetration of polymers than with relatively high molecular weight free polymers, and less than with relatively low molecular weight free chains.

Figure 7.7 shows the *rms* layer thickness as a function of the reduced surface coverage. The data are labeled in the same manner as in Figure 7.6. In all cases, h_{rms} increases with increasing σ^* and the variation is almost linear in σ^*. The latter result is consistent with previous experimental [69] and NSCF [46] studies, and with our results in Chapter 6 on end-tethered layers. A second general trend is the fact that h_{rms} decreases with increasing overall volume fraction of free polymer. Quantitatively, h_{rms} increases by approximately 62% with σ^* increasing from 1 to 12, and decreases

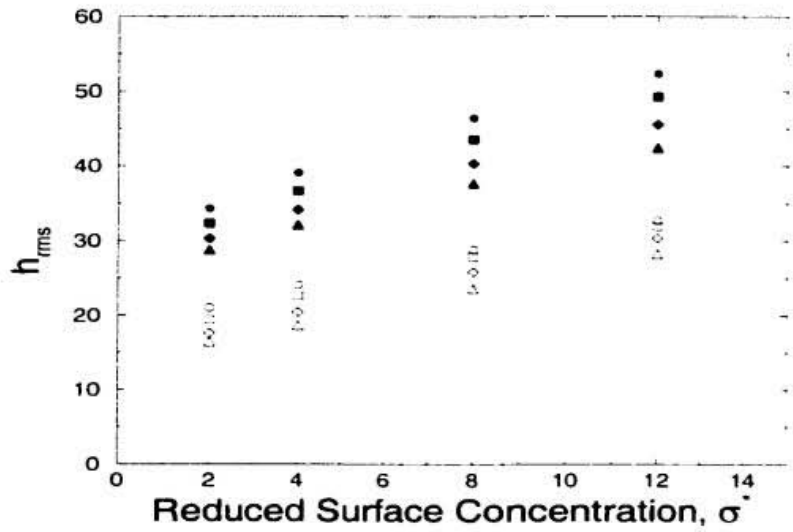

Figure 7.7: *rms* height of the end-tethered layer versus the reduced surface concentration: $Z_F = 400$ and $Z_A = 4,000$ (filled symbols), $Z_F = 1,600$ and $Z_A = 1,600$ (open symbols), $Z_F = 4,000$ and $Z_A = 400$ (grey symbols). $\bar{\phi}_F = 0.005$ (○), $\bar{\phi}_F = 0.02$ (◇), $\bar{\phi}_F = 0.04$ (□), $\bar{\phi}_F = 0.06$ (△).

by approximately 14% with $\bar{\phi}_F$ increasing from 0.005 to 0.06.

7.4.4 Systematic Study: Scaling of the Layer Height

In this section, layer heights are analyzed in terms of the three major regimes predicted by the analytical SCF and scaling theories. The data include the set of 256 NSCF calculations described in the previous section, augmented by a supplementary series of NSCF calculations for reasons which will become clear.

Scaling relations were calculated for both $Z_F \ll Z_A$ and $Z_F \gg Z_A$ for ranges of surface coverages and overall volume fractions similar to those found in the experiments of Lee and Kent [2]. For $Z_F \ll Z_A$, the following three combinations of

degrees of polymerization were used for the analysis: $Z_F = 400$ and $Z_A = 4000$. $Z_F = 800$ and $Z_A = 4000$. and $Z_F = 400$ and $Z_A = 1600$. Similarly, for $Z_F \gg Z_A$ we used $Z_F = 4000$ and $Z_A = 400$. $Z_F = 4000$ and $Z_A = 800$. and $Z_F = 1600$ and $Z_A = 400$. Although the analytical theories were not intended to apply when $Z_F \gg Z_A$. a comparison between the NSCF results with $Z_F \gg Z_A$ and the SCF predictions for $Z_F < Z_A$ is of interest.

We used the boundaries predicted by the asymptotic theories to determine the corresponding regime for each of the 256 systems in the systematic study. In our systematic study, the values of σ^* are 2, 4, 8 and 12. We sorted these into two categories: a low range ($\sigma^* = 2, 4$) and a high range ($\sigma^* = 8, 12$). Similarly, the values of $\bar{\phi}_F = 0.005$, 0.02, 0.04 and 0.06 were sorted in the following categories: the low range ($\bar{\phi}_F = 0.005, 0.02$) and the high range ($\bar{\phi}_F = 0.04, 0.06$). In regime I of the analytical theories, the end-tethered chains are assumed to be highly stretched (high σ^*) and there is no penetration of free chains (low $\bar{\phi}_F$). Therefore, to a first approximation, systems in the high and low ranges in σ^* and $\bar{\phi}_F$, respectively, should fall in regime I. In regime III, the analytical theories predict that the free chains completely envelop the end-tethered layer ($_L\phi_F \gg \phi_A$). Again to a first approximation, systems in the low and high ranges in σ^* and $\bar{\phi}_F$, respectively, should fall in regime III.

For our analysis in regimes I and III, we first screened the set of 256 calculations by specifying a high or low range in σ^* and $\bar{\phi}_F$, as described above. The selected systems were then verified against the boundaries predicted by analytical theories

and systems which were outside the regime of interest were excluded. The analysis in regime III was done for $Z_F \ll Z_A$ only, because none of the NSCF calculations with $Z_F \gg Z_A$ fell within this regime.

For $Z_F \ll Z_A$, regime II may not be well defined due the close proximity of the boundaries between regimes I and II, and regimes II and III (see Figure 7.1). In this case, all systems with $Z_F \ll Z_A$ which fell within regime II were included in the analysis. The limits were therefore the same as those from the set of 256 NSCF calculations which correspond to $2 \leq \sigma^* \leq 12$ and $0.005 \leq \bar{\phi}_F \leq 0.06$. For $Z_F \gg Z_A$, all systems in the high and low ranges of σ^* and $\bar{\phi}_F$, respectively, were in regime I whereas systems in the low and high ranges of σ^* and $\bar{\phi}_F$, respectively, were in regime II.

We note that, the limits on the ranges of σ^* and $\bar{\phi}_F$ are too short for a proper scaling analysis and our results are only *semi-quantitative*.

The scaling analysis of the *rms* height of the layer was done by fitting h_{rms} to the following function

$$h_{rms} = A Z_A^{\alpha} \sigma^{\beta} Z_F^{\gamma} \phi_F^{\nu} \tag{7.16}$$

where A, α, β, γ and ν are the fitted parameters.

We begin our analysis with the case of $Z_F \ll Z_A$. We note that ϕ_F is defined as the bulk volume fraction of free chains. In our NSCF calculations, the thickness of the films is finite. In our calculations ϕ_F therefore corresponds to the volume fraction of free polymer in the region away from both surfaces where the $\phi_F(z)$ is constant. The

$Z_F \ll Z_A$			$h_{rms} \propto Z_A^{\alpha}\sigma^{\beta}Z_F^{\gamma}\bar{\phi}_F^{\nu}$					Overlap
Regime	σ^*	$\bar{\phi}_F(\%)$	α	β	γ	ν		
I			1	1/3	0	0	Scaling & SCF	No
I	≥ 8	≤ 2	0.87	0.30	-0.01	-0.04	NSCF	Yes
II			1	1	0	-1	Scaling & SCF	No
II	≥ 2	0.5 - 6	0.81	0.30	-0.08	-0.16	NSCF	Yes
III			1	1/3	-1/3	-5/12	Scaling	Yes
III			1	1/3	-1/3	-1/3	SCF	Yes
III	≤ 4	4 - 6	0.70	0.16	-0.12	-0.07	NSCF	Yes
$Z_F \gg Z_A$			$h_{rms} \propto Z_A^{\alpha}\sigma^{\beta}Z_F^{\gamma}\bar{\phi}_F^{\nu}$					
Regime	σ^*	$\bar{\phi}_F(\%)$	α	β	γ	ν		
I	≥ 8	≤ 2	0.89	0.34	0.001	-0.003	NSCF	Partial
I-II	≤ 4	4 - 6	0.69	0.25	0.004	-0.14	NSCF	Yes

Table 7.3: Power law dependences for the layer height h from scaling and SCF theories, and calculated power laws from the NSCF calculations of h_{rms} for different regimes. The regimes are determined by the scaling and analytical theories.

scaling analysis is performed in terms of $\bar{\phi}_F$ for consistency with analytical theories.

In Table 7.3, the exponents γ and ν are close to zero for systems in regime I. These results are in agreement with analytical theories. On the other hand, they remain small compared to most of the corresponding exponents predicted by the analytical theories for systems in regimes II and III. Our results therefore suggest that, for $\sigma^* \leq 12$ and $\bar{\phi}_F \leq 0.06$, the end-tethered layer remains largely unaffected by the presence of the free chains.

For each regime, there is a range of σ^* and the average σ^* in each regime increases in going from regime III to regime I (see column 2 of Table 7.3). Our results show that the exponents α and β increase in going from regime III to regime I. Baranowski and Whitmore [46] performed a scaling analysis of the *rms* layer height for a similar

system of end-tethered polymers in solvent with no free polymer. For $2 \leq \sigma^* \leq 4$, they obtained $h_{rms} \propto Z^{0.76}\sigma^{0.21}$ and, for $10 \leq \sigma^* \leq 12$, $h_{rms} \propto Z^{0.87}\sigma^{0.29}$, showing an increase in the exponents with increasing σ^*. These results are in agreement with ours for regimes III and I and provide further evidence that the end-tethered layers are not significantly affected by the presence of the free polymer. Baranowski and Whitmore interpreted the increase in the values of the exponents as a continuous evolution towards the asymptotic brush limit. This behavior is also seen in our MC and NSCF results for end-tethered layers in good solvent discussed in Chapter 6. Since the free chains do not appear to affect the end-tethered layers in our systems, the increase in the exponents α and β with increasing σ^* can also be attributed to a continuous evolution towards the limit of highly stretched chains.

When $Z_F \gg Z_A$, the features are similar. The exponents α and β increase with increasing σ^* while the exponents γ and ν remain close to zero in regimes I and II.

The fact that the free chains do not significantly affect the end-tethered layer thickness even when there is considerable penetration of free chains disagrees with the analytic theories for regimes II and III. We therefore performed a further series of NSCF calculations and increased the volume fraction of free chains up to $\bar{\phi}_F = 0.5$. This was done to probe the behavior in systems where there is little to no penetration of free chains to cases where the free chains dominate the end-tethered layer. The physical behavior of the systems was compared with the behavior predicted by analytical theories. According to Figure 7.1, there are two possible scenarios when

ϕ_F increases. When the surface coverage is high there is an evolution from regime I to regime II. A further increase in ϕ_F may result in a cross-over to regime III. The second scenario happens when the surface coverage is low. In this case the systems move from regime I directly to regime III with increasing ϕ_F.

Four sets of calculations were done. In the first set $Z_F = 400$, $Z_A = 4,000$ and $\sigma^* = 12$. The results correspond to the filled squares in Figure 7.8. Figure 7.8(a) shows a log-log plot of h_{rms} as a function of ϕ_F. When $\phi_F \lesssim 0.01$, h_{rms} does not change significantly. Beyond $\phi_F \simeq 0.01$, h_{rms} decreases with increasing ϕ_F until the slope reaches about -0.51 at $\phi_F \simeq 0.5$. Although the analytical theories predict a transition to regime II, with a slope reaching -1, there is no evidence here of behavior typical of this regime. The slope might reach -1 if ϕ_F is increased beyond 0.5, but we note that when $\phi_F = 0.5$ the system is actually predicted by analytical theories to be past regime II and well in regime III. The fact that the slope is -0.51 when $\phi_F \simeq 0.5$ and the dependence of h_{rms} on ϕ_F continues to increase for ϕ_F as high as 0.5 suggest that the dependence on ϕ_F might continue to decrease well beyond the power law of $-5/12$ predicted for regime III, for $\phi_F > 0.5$. These results show a different physical picture than expected from the analytical theories. When $\phi_F \simeq 0.5$, the free chains completely envelop the end-tethered layer and the profiles of the end-tethered layers are peaked very close to the surface with a long exponential tail. This type of profile is quite different from the uniform or parabolic profiles of the analytical theories. Hence, predictions from analytical theories are not expected to apply in this

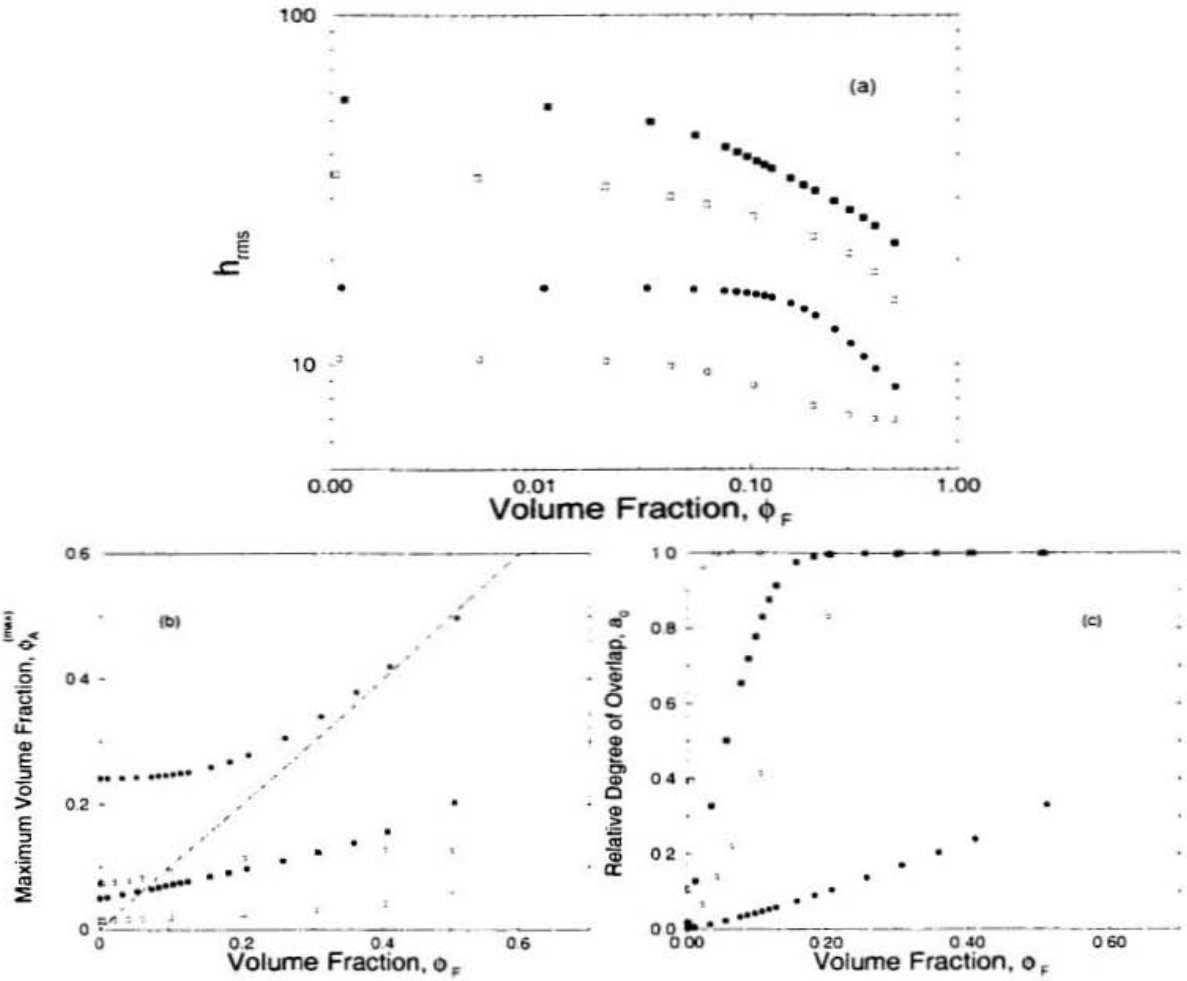

Figure 7.8: a) Log-log plot of the *rms* height of the end-tethered layer as a function of the volume fraction of free polymer ϕ_F. b) Maximum volume fraction of the polymer in the end-tethered layer as a function of the volume fraction of free polymer ϕ_F. The line corresponds to $\phi_A^{(max)} = \phi_F$. c) Relative degree of overlap (a_0) versus the volume fraction ϕ_F. $Z_F = 4,000$. $Z_A = 400$ (circles) and $Z_F = 400$. $Z_A = 4,000$ (squares). $\sigma^* = 12$ (filled symbols) and $\sigma^* = 2$ (open symbols). The symbols $*$ and $\times$ represent the volume fractions at which $\phi_A^{(max)} = \phi_F$ and $a_0 = 1$, respectively.

case.

Figure 7.8(b) shows the maximum in the volume fraction profile of end-tethered polymer, $\phi_A^{(max)}$, as a function of ϕ_F. Behavior typical of regime II should show

an interval in o_F where $o_A^{(max)} \simeq o_F$, which is indicated by the solid line. There is no evidence of such interval in Figure 7.8(b) for this first set of calculations. In contrast, $o_A^{(max)}$ increases slowly with increasing o_F and simply crosses the solid line. Figure 7.8(c) shows a_0 as a function of o_F. For this set of calculations a_0 quickly increases to unity and there is no significant sub-interval in o_F where a_3 is relatively constant and close to zero. Again this result contrasts with the behavior predicted by analytical theories for regime II. In summary, although the analytical theories predict that regime II is relevant in these systems, Figures 7.8(a), (b) and (c) show no evidence of physical behavior typical of this regime. Instead, the physical behavior is consistent with a continuous evolution towards regime III.

In the second set of NSCF calculations, the degrees of polymerization are the same but the surface coverage is reduced to $\sigma^* = 2$. The results correspond to the open squares in Figure 7.8. The results are qualitatively similar to the previous set of calculations. When $\sigma^* = 2$, h_{rms} is always lower than when $\sigma^* = 12$ for the same value of o_F, as expected because of the decrease in stretching. The slope in Figure 7.8(a) reaches about -0.86 at $o_F \simeq 0.5$. This result is close to the predicted value for regime II. However, we do not identify this as regime II because, as in the previous case, the end-tethered layer is completely enveloped by the free chains and the profile is no longer parabolic. In Figure 7.8(b), $o_A^{(max)}$ is relatively small compared to the results from the previous calculations due to the lower surface coverage. In Figure 7.8(c), a_0 quickly reaches unity with increasing o_F as in the previous set of

calculations. Again, this system is much different than any other system considered in the analytical theories.

In the third set of NSCF calculations, the degrees of polymerization are interchanged to $Z_F = 4.000$ and $Z_A = 400$, and $\sigma^* = 12$. The results are shown by the closed circles in Figure 7.8. In Figure 7.8(b), when $0.25 \lesssim \phi_F \lesssim 0.45$, $\phi_A^{(max)}$ shows an asymptotic-like behavior with $\phi_A^{(max)} \simeq \phi_F$. There is, therefore, evidence of behavior which corresponds to regime II. In Figure 7.8(a), the *rms* height decreases considerably at higher volume fractions and a minimum slope of $\nu \approx -0.65$, occurs at $\phi_F \simeq 0.35$. If the condition $\phi_A^{(max)} = \phi_F$ holds, one would expect a stronger power giving a slope closer to -1 but, in this case, a log-log plot of $\phi_A^{(max)}$ versus ϕ_F showed a power law with $\phi_A^{(max)} \propto \phi_F^{0.77}$, for $\phi_F \geq 0.2$. From this result, a weaker power law for the *rms* layer height is expected, namely $h_{rms} \propto \phi_F^{-0.77}$, which is closer to the result obtained. Further evidence of physical behavior consistent with regime II is shown in Figure 7.8(c) where a_0 remains low ($a_0 \lesssim 0.3$) for $\phi_F \lesssim 0.45$.

When $\phi_F \simeq 0.5$, Figure 7.8(a) indicates a slight increase in the slope of the curve, and Figures 7.8(b) and 7.8(c) show that $\phi_A^{(max)} \lesssim \phi_F$ and a_0 becomes significant. These results indicate that, when $\phi_F \gtrsim 0.5$, behavior corresponding to regime III may be observed. This suggestion contrasts with the predictions of analytical theories where relatively high molecular weight free chains are not expected penetrate the end-tethered layer.

In the fourth and final set of NSCF calculations, $Z_F = 4.000$ and $Z_A = 400$

again, but the surface coverage is decreased to $\sigma^* = 2$. The results are shown by the open circles in Figure 7.8. The free chains can now penetrate the end-tethered layer considerably, as seen in Figure 7.8(c). At low o_F, Figure 7.8(a) shows that the end-tethered layer height is largely unaffected by the free chains when $o_F \lesssim 0.04$. A further increase in o_F causes a decrease in the layer height and a minimum slope ≈ -0.20 for $o_F \simeq 0.15$ is obtained. This is consistent with the prediction of Equation (7.8), which includes corrections to scaling of the layer height to account for screening effects. A continued increase in o_F results in a leveling of the *rms* layer height. This is consistent with a regime in which the end-tethered chains behave as Gaussian coils, as seen in Equation (7.9).

To summarize, the physical behavior of systems at commonly observed surface coverages and $Z_F \ll Z_A$ suggests that regime II is not observed and a continuous evolution from regime I to regime III occurs with increasing o_F. When $Z_F \gg Z_A$ and $\sigma^* = 12$, the physical behavior suggests a continuous evolution from regime I to regime II. When $Z_F \gg Z_A$ and $\sigma^* = 2$ the systems move directly from regime I to regime III with increasing o_F. Interestingly, the behavior observed for $Z_F \gg Z_A$, is consistent with analytical predictions for $Z_F \ll Z_A$ but, for $Z_F \ll Z_A$, the NSCF results show quite different behavior.

7.5 Summary

In this chapter, we have carried out a detailed comparison among analytic scaling and SCF theories, NSCF calculations, MC simulations and experiments. The volume fraction profiles, the *rms* layer height and the relative degree of overlap between the end-tethered and free chains provide a means for a comparison. For a comparison with MC simulations, two sets of NSCF calculations were done, as in Chapter 6. The NSCF calculations with the renormalized mean field parameters provided better agreement with MC simulations.

In all cases the agreement between the two approaches is remarkable, and extends to reduced surface concentrations as low as $\sigma^* = 1$. The MC simulations were also used to investigate the *rms* layer height and the relative degree of overlap between free and end-tethered polymers for a series of degrees of polymerization ranging from $Z_F \ll Z_A$ to $Z_F > Z_A$. The *rms* height of the end-tethered layer increased with increasing reduced surface concentration and Z_A as seen in analytical SCF theory, NSCF calculations and experiments. The extent of interpenetration of the free and end-tethered polymers was characterized by defining the relative degree of overlap a_0. Extensive penetration of free chains was shown for $\sigma^* \lesssim 6$ and $Z_F \ll Z_A$ whereas for $Z_F > Z_A$ the penetration of free chains is considerably reduced with $a_0 \lesssim 0.1$ for surface coverage as low as $\sigma^* = 2$ and overall volume fraction of free chains as high as $\bar{o}_F = 0.06$. This result is in qualitative agreement with analytical scaling and SCF theories where relatively high molecular weight free polymers are expected to

be expelled from the end-tethered layer. However, in this case there remains partial penetration of the free chains. In all cases the free chains were progressively expelled from the end-tethered layer with an increase in the surface coverage.

The comparison between MC simulations and NSCF theory provides a means to test the validity of the NSCF theory at lower concentrations while the general trends investigated in the *rms* height and the relative degree of overlap provide a test against the predictions of the analytic SCF theories. Together, they supply a basis for further NSCF calculations which were used for comparisons with experiments of Lee and Kent [2]. In their study, the authors argued that, because most experiments are limited to $\sigma^* \lesssim 12$, the density of end-tethered polymers is relatively low and the free polymers can penetrate into the end-tethered layer even when $Z_F \gg Z_A$. This disagrees with analytical SCF theories where the penetration of relatively high molecular weight free chains is negligible.

The NSCF results show qualitative agreement with experiment for $Z_F \ll Z_A$ with the penetration of free chains in the end-tethered layer for $\sigma^* = 12$. In the case $Z_F > Z_A$, the NSCF results are in partial agreement with the experiments of Lee and Kent [2] showing no plateau region in the volume fraction profile of the free chains in the end-tethered layer and with the free chains expelled from most of the layer.

A systematic study was performed to investigate the behavior of the volume fraction profile of the end-tethered layer, the *rms* layer height, and the extent of interpenetration of end-tethered and free chains. NSCF calculations were done for systems in

the three regimes which were predicted by analytical theories, for various molecular weights, surface coverages and overall volume fractions of free chains. The general results show that the free chains are progressively expelled from the end-tethered layer with increasing surface coverage and decreasing overall volume fraction of free polymers. Relatively low molecular weight free chains penetrate the end-tethered layer considerably for reduced surface coverage as high as $\sigma^* = 12$. On the other hand, when $\sigma^* = 12$ the extent of the penetration of high molecular weight free chains is reduced considerably showing no physical evidence of regime III for reduced surface coverages as low as $\sigma^* = 2$ for $\bar{\phi}_F \leq 0.06$. This result does not support the arguments of Lee and Kent [2], who suggest that regime III is relevant due to limits on the maximum surface coverage observed in most experiments and accounts for the observed high degree of penetration of free chains for $Z_F > Z_A$.

The *rms* layer height increases with increasing surface coverage and decreasing overall volume fraction of free chains. This is consistent with the MC results. A semi-quantitative scaling analysis of the *rms* layer height was also done for the three major regimes predicted by analytical theories. In all three regimes the exponents related to the dependences on Z_A and σ are largely independent of the presence of free chain for $\phi_F \lesssim 0.06$, regardless of the degree of polymerization of the free chains. Furthermore, an increase in the scaling exponents with respect to Z_A and σ suggest a continuous evolution from the weakly stretched limit towards the limit of highly stretched chain. This is consistent with corrections to scaling observed

for end-tethered layers in Chapter 6. Further evidence that the free chains do not significantly affect the end-tethered layer is found in the small exponents describing the dependence of the layer thickness on Z_F and o_F. The weak dependences persist even in regimes where there is considerable overlap.

The results from the scaling analysis of the layer height suggest a physical picture which is quite different than predicted by analytical theories. Therefore, further NSCF calculations were done for volume fraction of free chains as high as $o_F \simeq 0.5$ to probe the behavior in systems over a broad range of volume fractions of free chains. The results show that for $Z_F \ll Z_A$ there is no evidence of behavior typical of regime II for reduced coverage as high as $\sigma^* = 12$. In contrast, for $Z_F \gg Z_A$ and $\sigma^* = 12$, behavior typical of regime II is observed when monitoring the relative degree of penetration of free chains, a_0, the maximum volume fraction of end-tethered chains, $o_A^{(max)}$, and the the *rms* layer height. Furthermore, when $Z_F \gg Z_A$ there is no physical evidence of behavior typical of regime III for overall volume fractions as high as $\bar{o}_F = 0.5$ except for lower reduced surface coverage where $\sigma^* = 2$.

Chapter 8

Conclusions

8.1 Introductory Remarks

For a number of years, mean field theories have been used extensively in the study of polymers and polymers in solution. They include analytical scaling and self-consistent field, numerical SCF and other simple mean field theories. The success of the mean field approach is attributed to its ability to deal with systems corresponding to polymers with realistic molecular weights, and its relatively low computer requirements. The analytical theories provide useful information with respect to scaling laws and may provide detailed information on the structure of the systems in limiting cases. The numerical mean field theories have also been successful in providing detailed information on realistic systems of polymers in solution while providing more detailed information, but they are restricted to certain conditions where fluctuation effects can be neglected, and they sometimes require *a priori* knowledge of the structure of the system. In this thesis we have primarily used Monte Carlo simulations and numer-

ical self-consistent field calculations to study polymers in solution and end-tethered layers.

Although MC simulations cannot model realistic molecular weights, they can be used to investigate assumptions made in the mean field approach and they can be useful in identifying regimes in which the mean field theories are valid. Furthermore, MC, scaling and mean field approaches deal with the physical properties of equilibrium systems. In physical systems, non-equilibrium effects can lead to very different physical properties in a system. Although the MC approach does not deal with such systems, studies under equilibrium conditions up to the point where non-equilibrium effects become significant, are feasible. The point at which non-equilibrium effects occur has been determined by monitoring various autocorrelation times and the diffusion of polymers, and identifying the conditions where the maximum autocorrelation time, which we define as the system relaxation time, reaches a critical value. MC simulations can therefore be used to identify the physical properties of a system under equilibrium conditions at the point where non-equilibrium becomes significant.

In this thesis, MC simulations have been used as a complement to mean field theories to study the following four systems of polymers in solution: crew-cut micelles, swollen micelles, end-tethered polymers and thin films. These systems have important applications in industry, and several experimental studies have been done on them. The MC and mean field studies in this thesis are therefore compared to existing experimental results. In the following section we provide a summary of the major

results obtained for all four systems studied.

8.2 Summary of Results

The first system consists of low concentrations of A-b-B diblock copolymers in selective solvent. A simple mean field theory predicts that the core radii of the micelles scale primarily with the degree of polymerization of the core block, Z_{CB}. The predicted scaling law is in general agreement with experiment. Recent experiments on crew-cut micelles, where the copolymers are comprised of relatively long core forming blocks, show a much weaker dependence of the radius of the core on Z_{CB}. The discrepancy between experiment and theory is believed to be due to non-equilibrium effects. Mean field theory suggests that the micelles observed in experiments might reflect equilibrium structures formed at different solvent quality and that the solvent quality at which non-equilibrium becomes important depends on Z_{CB}. Our analysis of the system relaxation time in MC simulations, for weakly segregated systems, suggests that a small change in the solvent quality can dramatically change the time scales involved in the equilibrium processes. This effect supports the argument that the strongly segregated systems of micelles, observed in experiments, are non-equilibrium structures. Furthermore, the non-equilibrium effects on the scaling of the core radius with Z_{CB} were investigated with the use of MC simulations by identifying the solvent quality at which the polymers begin to be trapped in the micelles. Results from the MC simulations show a scaling which is weaker than predicted by mean field theory

and comparable to the scaling law obtained in experiments.

In the second system studied in this thesis, small amounts of B homopolymer are added to a system of A-b-B diblock copolymer micelles in A solvent or homopolymer. An extension to the simple mean field theory of diblock copolymer micelles predicts that, for $Z_{HB}/Z_{CB} \ll 1$, there is a threshold volume fraction of added B homopolymer, below which the homopolymer is solubilized within the micelle cores, and above which the homopolymer macrophase separates. Furthermore, the theory predicts that the threshold volume fraction depends on Z_{HB}/Z_{CB}, ϕ^0_{CB} and the product χZ_{CB}. These predictions are consistent with experiments [32]. In this simple mean field theory, volume fraction profiles of each component in the core and corona of the micelles are assumed uniform. The assumptions about the structure, and the prediction of the phase behavior, were investigated with the use of MC simulations. The MC results show homopolymer solubilized within the micelle core for $Z_{HB}/Z_{CB} \ll 1$ with an approximately uniform volume fraction profile of B homopolymer and B block of copolymer in the core of the micelles. The volume fraction of the A block in the corona shows a non-uniform profile, but this does not appear to affect the phase behavior significantly. The MC results qualitatively reproduce the phase behavior predicted by mean field theory, showing a decrease in the threshold volume fraction with an increase in the molecular weight of the B homopolymer.

End-tethered polymers in good solvent are the third system studied in this thesis for which analytical SCF and scaling theories have been developed. According to these

theories, at low surface coverage, the end-tethered polymers act as isolated chains and the radius of gyration, R_g, is a relevant length scale. At high surface coverage, the end-tethered polymers strongly overlap. R_g is no longer a relevant length scale, and the layer height is predicted to scale linearly with the polymer degree of polymerization. This prediction is strictly intended for the limit of infinite molecular weight and high stretching. Recent experiments [68,69] have shown that finite molecular weight effects are important for commonly observed surface coverages ($\sigma^* \lesssim 15$). In particular, for $\sigma^* \lesssim 15$, corrections to the scaling of the height of the end-tethered layer were observed. The authors concluded that these corrections were due to the lower limit on the surface coverages observed in most experiments, and that R_g remains a relevant length scale. Numerical SCF calculations [46] corroborate this conclusion and the experimental results. The results from the NSCF calculations are in good agreement with the experimental results for $\sigma^* \gtrsim 2$, showing a similar scaling law with respect to the *rms* layer height.

In this thesis, a comparison between MC simulations and NSCF theory was done for various surface coverages and molecular weights to investigate the corrections to scaling of the *rms* layer height, and quantitatively determine the range of surface coverages where the NSCF theory is accurate. For $\sigma^* \gtrsim 2$, the MC simulations and NSCF theory agree well whereas, for $\sigma^* \lesssim 2$, lateral inhomogeneities in the planes parallel to the end-tethering surface become significant and the two approaches no longer agree. An analysis of the *rms* layer height also shows corrections to scaling

in the range of experimentally interesting surface coverages. This result is consistent with observations in the experiments of Kent [68, 69] and the NSCF calculations of Baranowski and Whitmore [46]. Furthermore, the MC results also indicate that the layer height, normalized by R_g, is nearly linear in σ^*. This implies that R_g remains a relevant length scale and that this linear relationship is a better representation of the data than any scaling relation.

In the fourth and final system studied in this thesis, the structure and properties of thin films with both end-tethered and free polymers in solution were investigated. Experiments imply that the coupling between the end-tethered and free chains can affect the stability of the films. Analytical SCF and scaling theories have been developed to study thin films. These analytical theories predict various regimes for the penetration of free chains into the end-tethered layers, which depend on the molecular weights, surface coverage and volume fraction of free chains. Generally, for high surface coverage, there is very little penetration of free chains, particularly for relatively high molecular weight free chains. In recent experiments [2], penetration of free polymers was observed for both low and high molecular weight free polymers, for surface coverages as high as $\sigma^* = 12$. The authors argued that the significant degree of penetration of free chains, even in the case of high molecular weight free polymer, is due to the lower limit imposed on the surface coverage in experiment. In this thesis, the shape and height of the end-tethered layer and the degree of overlap were therefore investigated for various surface coverages, volume fractions of free chains

and molecular weights of end-tethered and free chains.

A comparison between MC simulations and NSCF theory shows good agreement for reduced surface coverages as low as $\sigma^* = 1$. The MC and NSCF results are also compared to analytical scaling and SCF theories. For relatively low molecular weight free chains, the free polymers can penetrate the end-tethered layer considerably. This is consistent with analytical scaling and SCF theories. For relatively high molecular weight free chains, partial penetration of free chains occurs, and complete penetration of free chains is expected to occur only at very low surface coverages. The expulsion of the high molecular weight free chains from the end-tethered layer is in qualitative agreement with analytical theories except that there remains partial penetration of free chains even at relatively high surface coverage.

These results are for relatively low molecular weight polymers. NSCF calculations were also performed for polymers with realistic molecular weights and compared with the experiments of Lee and Kent [2]. The NSCF calculations show good agreement with these experiments for low molecular weight free polymers but, for higher molecular weights, the NSCF results show less penetration of the chains. Nonetheless, the degree of overlap between the end-tethered and free chains is considerably more than predicted by analytical theories. Finite molecular weight corrections can therefore explain a larger degree of penetration of free polymers in the end-tethered layer, but not to the extent observed in the experiments of Lee and Kent [2].

A further analysis of the *rms* layer thickness was done to investigate scaling rela-

tions predicted by the analytical theories for three different regimes predicted by the analytical theories. In particular, the exponents related to the degree of polymerization of the end-tethered polymer, Z_A, and the surface coverage, σ, show corrections to scaling for $\sigma^* \leq 12$. The scaling exponents related to the degree of polymerization, Z_F, and volume fraction, ϕ_F, of the free polymers show a much weaker dependence than predicted by analytical theories. For the ranges of surface coverage and volume fraction of free chains used in the experiments of Lee and Kent [2], a description of the behavior of the systems in terms the three predicted regimes was not adequate. An increase in the volume fraction showed an increase in the exponents related to Z_F and ϕ_F as the systems progressed further into a regime where the free chains strongly overlap the end-tethered layer but, nonetheless, the results were not completely accounted for by the analytical theories.

8.3 Final Remarks

In this thesis, the MC approach has served as a powerful tool to complement mean field theories in studying four systems of polymers in solution. Monte Carlo simulations were used to investigate limitations to analytical SCF, scaling, simple mean field and numerical SCF theories. The analytical theories are restricted to limiting cases, and MC simulations were used to study systems more closely related to experiments. Results showed that some limiting cases proposed in analytical theories do not necessarily correspond to conditions usually observed in experiments.

At low polymer concentration, the mean field approach is not valid due to inhomogeneities in the polymer concentrations. In layered systems, MC simulations were used to determine the point at which the mean field approximation fails. Physical properties such as the physical structure, non-equilibrium effects, phase behavior and scaling laws which were either predicted by or assumed in these theories were also investigated. The physical structure of a system, assumed in some mean field models, was probed by observing the self-assembled structures in the MC simulations. Non-equilibrium effects were investigated by simulating equilibrium conditions under which the structures form, and identifying the point at which non-equilibrium effects become significant. Criteria for this condition were based on the system relaxation time.

In this way, physical properties of polymers in solution and end-tethered layers were investigated for systems closely related to experiments and allowed for a comprehensive comparison between simulation, experiment and theory. As a result, this particular study shows how the MC approach can be a powerful tool in studying polymers in solution. With increasing computing power, simulation techniques such as MC simulations and molecular dynamics are becoming more widely used and offer an important means of investigating systems of polymers in general.

Bibliography

[1] L. Zhang, R. Barlow, and A. Eisenberg, Macromolecules **28**, 6055 (1995).

[2] L. Lee and M. S. Kent, Phys. Rev. Lett. **79**, 2899 (1997).

[3] W. M. Moreau, *Semiconductor Lithography* (Plenum, New York, 1988).

[4] H. Yamakawa, *Modern Theory of Polymer Solutions* (Harper & Row, New York, 1971).

[5] R. Yerushalmi-Rozen and J. Klein, Langmuir **11**, 2806 (1995).

[6] R. Yerushalmi-Rozen and J. Klein, Physics World **August**, 30 (1995).

[7] B. Vincent, Adv. Colloid Interface Sci. **4**, 193 (1974).

[8] D. H. Napper, *Polymeric Stabilization of Colloidal Dispersions* (Academic, New York, 1983).

[9] S. Wu, *Polymer Interfaces and Adhesion* (Decker, New York, 1982).

[10] P.-G. de Gennes. *Scaling Concepts in Polymer Physics* (Cornell University Press, Ithaca, NY, 1979).

[11] P. G. de Gennes. Advances in Colloid and Interface Science **27**, 189 (1987).

[12] S. Alexander. J. Physics (Paris) **38**, 983 (1977).

[13] P. G. de Gennes. Macromolecules **13**, 1069 (1980).

[14] S. T. Milner, T. A. Witten, and M. E. Cates. Macromolecules **21**, 2610 (1988).

[15] V. A. Pryamitsyn, O. V. Borisov, E. B. Zhulina, and T. M. Birshtein. *Modern Problems in Physical Chemistry of Solutions* (Donish and Leningrad University, Dunshabe and Leningrad (USSR), 1987).

[16] E. B. Zhulina, O. V. Borisov, and L. Brombacher. Macromolecules **24**, 4679 (1991).

[17] C. M. Wijmans, E. B. Zhulina, and G. J. Fleer. Macromolecules **27**, 3238 (1994).

[18] A. N. Semenov, Sov. Phys JETP. **61**, 733 (1985).

[19] L. Leibler, H. Orland, and J. C. Wheeler. J. Chem. Phys. **79**, 3550 (1983).

[20] J. Noolandi and K. M. Hong. Macromolecules **16**, 1443 (1983).

[21] M. Whitmore and J. Noolandi. Macromolecules **18**, 657 (1985).

[22] T. Bluhm and M. Whitmore. Can. J. of Chem. **63**, 249 (1985).

[23] M. Pépin and M. Whitmore. Homopolymer Solubilization Limits in Copolymer Micelles: A Monte Carlo Study. in preperation.

[24] R. Nagarajan and K. Ganesh. J. Chem. Phys. **90**. 5843 (1989).

[25] A. Halperin. Macromolecules **20**. 2943 (1987).

[26] M. Daoud and J. Cotton. J. Phys. (Les Ulis. Fr.) **43**. 531 (1982).

[27] D. Izzo and C. M. Marques. Macromolecules **26**. 7189 (1993).

[28] M. R. M. A. Gast. Macromolecules **21**. 1360 (1988).

[29] E. B. Zhulina and A. N. Semenov. Polym. Sci. USSR **31**. 196 (1989).

[30] A. N. Semenov. Macromolecules **26**. 2273 (1993).

[31] R. Xu *et al.*. Macromolecules **25**. 644 (1992).

[32] M. Whitmore and T. Smith. Macromolecules **27**. 4673 (1994).

[33] P. J. Flory. *Principles of Polymer Chemistry* (Cornell Univ. Press. Ithaca. NY. 1953). p. 509.

[34] M. A. Carignano and I. Szleifer. J. Phys. Chem. **98**. 5006 (1993).

[35] M. A. Carignano and I. Szleifer. Macromolecules **28**. 3197 (1995).

[36] M. A. Carignano and I. Szleifer. J. Phys. Chem. **102**. 8662 (1995).

[37] M. A. Carignano and I. Szleifer. Macromolecules **27**. 702 (1994).

[38] M. A. Carignano and I. Szleifer. J. Phys. Chem. **100**. 3210 (1994).

[39] M. A. Carignano and I. Szleifer. Europhys. Lett. **30**. 525 (1995).

[40] S. T. Milner. J. Chem. Soc. Faraday Trans. **86**. 1349 (1990).

[41] G. Fleer and J. Lyklema. in *Adsorption from Solution at the Solid/Liquid Interface*, edited by G. D. Prafitt and C. H. Rochester (Academic Press. London. 1983), pp. 156–219.

[42] J. Scheutjens and G. Fleer. J. Phys. Chem. **83**. 1619 (1979).

[43] J. Scheutjens and G. Fleer. J. Phys. Chem. **84**. 178 (1980).

[44] J. Scheutjens and G. Fleer. Macromolecules **18**. 1882 (1985).

[45] T. Cosgrove *et al.*. Macromolecules **20**. 1692 (1987).

[46] R. Baranowski and M. D. Whitmore. J. Chem. Phys. **103**. 2343 (1995).

[47] C. M. Wijmans and B. J. Factor. Macromolecules **29**. 4406 (1996).

[48] P. Linse. Macromolecules **27**. 2685 (1994).

[49] F. A. M. Leermakers. C. M. Wijmans. and G. J. Fleer. Macromolecules **28**. 3434 (1995).

[50] B. van Lent and J. Scheutjens. Macromolecules **22**. 1931 (1989).

[51] P. Linse and M. Malmsten. Macromolecules **25**. 5434 (1992).

[52] P. N. Hurter, J. M. H. M. Scheutjens, and T. A. Hatton, Macromolecules **26**, 5592 (1993).

[53] P. N. Hurter, J. M. H. M. Scheutjens, and T. A. Hatton, Macromolecules **26**, 5030 (1993).

[54] R. Nagarajan and K. Ganesh, Macromolecules **22**, 4312 (1989).

[55] O. A. Evers, J. Scheutjens, and G. J. Fleer, Macromolecules **23**, 5221 (1990).

[56] O. A. Evers, J. M. Scheutjens, and G. J. Fleer, J. Chem. Soc. Faraday Trans. **86**, 1333 (1990).

[57] O. A. Evers, J. Scheutjens, and G. J. Fleer, Macromolecules **24**, 5558 (1990).

[58] P. Lai and K. Binder, J. Chem. Phys. **95**, 9288 (1991).

[59] P. Doruker and W. L. Mattice, Macromolecules **31**, 1418 (1998).

[60] Z. Gao, S. Varshney, S. Wong, and A. Eisenberg, Macromolecules **27**, 7923 (1994).

[61] T. Witten, L. Leibler, and P. Pincus, Macromolecules **23**, 824 (1990).

[62] M. Murat and G. S. Grest, Macromolecules **22**, 4054 (1989).

[63] G. S. Grest and M. Murat, Macromolecules **26**, 3108 (1990).

[64] G. S. Grest, Macromolecules **27**, 418 (1994).

[65] A. Chakrabarti and R. Toral, Macromolecules **23**, 2016 (1990).

[66] L. A. P. Auroy and L. Leger, Macromolecules **24**, 2523 (1991).

[67] L. A. P. Auroy and L. Leger, Phys. Rev. Lett. **66**, 719 (1991).

[68] M. S. Kent, L. T. Lee, B. Farnoux, and F. Rondelez, Macromolecules **25**, 6240 (1992).

[69] M. S. Kent *et al.*, J. Chem. Phys. **103**, 2320 (1995).

[70] T. Cosgrove, T. G. Heath, J. S. Phipps, and R. M. Richardson, Macromolecules **24**, 94 (1991).

[71] J. B. Field *et al.*, Macromolecules **25**, 434 (1992).

[72] C. M. Wijmans, J. M. H. M. Scheutjens, and E. B. Zhulina, Macromolecules **25**, 2657 (1992).

[73] A. W. Adamson, *Physical Chemistry of Surfaces* (Wiley, New York, 1990).

[74] A. Gast and L. Leibler, Macromolecules **19**, 686 (1986).

[75] M. N. Barber, in *Phase Transitions and Critical Phenomena*, edited by C. Domb and J. L. Lebowitz (Academic Press, New York, 1983), Vol. 8.

[76] V. Privman, *Finite Size Scaling and Numerical Simulation of Statistical Systems*, 1st ed. (World Scientific Publishing Co. Pte. Ltd., Signapore, 1990).

[77] N. Metropolis *et al.*, J. Chem. Phys. **21**, 1087 (1953).

[78] K. Binder and D. W. Heermann, *Monte Carlo Simulation in Statistical Physics* (Springer-Verlag, Berlin Heidelberg, 1979), Vol. **80**.

[79] P. Verdier and W. Stockmayer, J. Chem. Phys. **36**, 227 (1962).

[80] C. Domb, Adv. Chem. Phys. **15**, 229 (1962).

[81] J. M. D. H. J. Hilhorst, J. Chem. Phys. **63**, 5153 (1975).

[82] D. M. D. M. T. Gurler, C. C. Crabb and J. Kovak, Macromolecules **16**, 398 (1983).

[83] T. Haliloğlu and W. Mattice, Polymer Preprints **34**, 460 (1993).

[84] T. Haliloğlu, I. Bahar, B. Erman, and W. Mattice, Macromolecules **29**, 4764 (1996).

[85] B. J. Cherayil, J. Chem. Phys. **97**, 2090 (1992).

[86] C. M. Roland and C. A. Bero, Macromolecules **29**, 7521 (1996).

[87] G. Williams and D. C. Watts, Trans. Faraday Soc. **66**, 80 (1970).

[88] M. D. Whitmore and J. Noolandi, Macromolecules **23**, 3321 (1990).

[89] M. D. Whitmore and J. Noolandi, Macromolecules **21**, 1482 (1988).

[90] K. M. Hong and J. Noolandi, Macromolecules **14**, 727 (1981).

[91] E. Helfand and T. Y.. J. Chem. Phys. **56**. 3592 (1972).

[92] T. Hashimoto. T. Tanaka. and H. Hasegawa. Macromolecules **23**. 4378 (1990).

[93] H. Tanaka and H. H. T. Hashimoto. Macromolecules **24**. 240 (1991).

[94] H. Tanaka and T. Hashimoto. Macromolecules **24**. 5712 (1991).

[95] K. Winey. E. L. Thomas. and L. J. Fetters. Macromolecules **24**. 6182 (1991).

[96] K. Schull and K. Winey. Macromolecules **25**. 2673 (1992).

[97] M. Banaszak and M. D. Whitmore. Macromolecules **25**. 2757 (1992).

[98] S. Edwards. Proc. Phys. Soc. **85**. 613 (1966).

[99] A. Dolan and S. Edwards. Proc. R. Soc. Lond. **A 343**. 427 (1975).

[100] S. Edwards. Proc. Phys. Soc. **88**. 265 (1966).

[101] E. Helfand. J. Chem. Phys. **62**. 999 (1975).

[102] E. Helfand. Macromolecules **8**. 552 (1975).

[103] E. Helfand. in *Recent Advances in Polymer Blends. Grafts and Blocks*. edited by L. Sperling (Plenum. New York. 1974).

[104] K. M. Hong and J. Noolandi. Macromolecules **16**. 1083 (1983).

[105] J. Noolandi and K. Hong. Macromolecules **17**. 1531 (1984).

[106] T. Ohta and K. Kawasaki. Macromolecules **19**. 2621 (1986).

[107] M. Banaszak. Ph.D. thesis. Memorial University of Newoundland. 1991.

[108] M. Banaszak and M. D. Whitmore. Macromolecules **25**. 3406 (1992).

[109] R. Baranowski. Ph.D. thesis. Memorial University of Newoundland. 1997.

[110] K. F. Freed. *Renormalization Group Theory of Macromolecules* (John Wiley & Sons. New York. 1987).

[111] M. Doi and S. Edwards. *The Theory of Polymer Dynamics* (Calderon Press. Oxford. 1986).

[112] L. Schulman. *Techniques and Applications of Path Integration* (John Wiley & Sons. New York. 1981).

[113] M. S. Kent *et al.*, J. Chem. Phys. **108**. 5635 (1998).

[114] J. Jensen. *Saddlepoint Approximation* (Oxford University Press. Oxford. 1995).

[115] H. Kleinert. *Path-Integrals in Quantum Mechanics Statistics and Polymer Physics* (World Scientific. Singapore. 1990).

[116] J. Selb *et al.*, Polymer Bulletin **10**. 444 (1983).

[117] P. G. de Gennes. in *Solid State Physics*. edited by J. Liebert (Academic. New York. 1978). p. 1. supplement 14.

[118] J. Noolandi and K. Hong. Macromolecules **16**. 1443 (1983).

[119] K. A. Cogan. A. Gast, and M. Capel. Macromolecules **24**. 6512 (1991).

[120] A. Qin *et al.*. Macromolecules **27**. 120 (1994).

[121] G. Hurtrez. Ph.D. thesis. Université de Haute Alsace. 1992.

[122] B. Smit *et al.*. Langmuir **9**. 9 (1993).

[123] K. Rodrigues and W. Mattice. Polymer Bulletin **25**. 239 (1991).

[124] K. Rodrigues and W. Mattice, J. Chem. Phys. **95**. 5341 (1991).

[125] K. Rodrigues and W. Mattice. J. Chem. Phys. **95**. 5341 (1991).

[126] K. Rodrigues and W. Mattice. Langmuir **8**. 456 (1992).

[127] Y. Wang. W. Mattice. and D. Napper. Langmuir **9**. 66 (1993).

[128] Y. Zhang and W. Mattice. Macromolecules **27**. 677 (1994).

[129] Y. Zhang and W. Mattice. Macromolecules **27**. 683 (1994).

[130] K. Rodrigues and W. Mattice. J. Chem. Phys. **94**. 761 (1991).

[131] M. Nguyen-Misra and W. Mattice, Macromolecules **28**. 1444 (1995).

[132] J. Tao. S. Stewart. G. Liu, and M. Yang, Macromolecules **30**. 2738 (1997).

[133] D. J. Kinning. E. L. Thomas, and L. J. Fetters. J. Chem. Phys. **90**. 5806 (1989).

[134] J.Brandup and E. Immergut. *Polymer Handbook. 3rd Edition* (John Wiley and Sons Inc., New York, 1989).

[135] K. Rodrigues *et al.*, Polymer Bulletin **26**, 695 (1991).

[136] A. Bernandes, V. Henriques, and P. Bish, J. Chem. Phys. **101**, 645 (1994).

[137] L. Molina and J. Freire, Macromolecules **28**, 2705 (1995).

[138] L. Xing and W. Mattice, Macromolecules **30**, 1711 (1997).

[139] L. Xing and W. Mattice, Langmuir **14**, 4074 (1998).

[140] K. A. Cogan, F. A. M. Leermakers, and A. Gast, Langmuir **8**, 429 (1992).

[141] K. A. Cogan and A. Gast, Macromolecules **23**, 745 (1990).

[142] L. J. M. Vagberg, K. A. Cogan, and A. Gast, Macromolecules **24**, 1670 (1991).

[143] S. Talsania, Y. Wang, R. Rajagopalan, and K. Mohanty, J. Coll. Int. Sci. **190**, 92 (1997).

[144] M. Adamuti-Trache, W. E. McMullen, and J. F. Douglas, J. Chem. Phys. **105**, 4798 (1996).

[145] R. Baranowski and M. D. Whitmore, J. Chem. Phys. **108**, 9885 (1998).

[146] B. G. Nickel, Macromolecules **24**, 1358 (1991).

[147] M. E. Fisher, Rep. Prog. Phys. **30**, 615 (1967).

[148] Reported as a private communication in Ref. 66.

[149] R. Yerushalmi-Rozen, J. Klein, and L. Fetters, Science **263**, 793 (1994).

[150] R. Yerushalmi-Rozen and N. Dan, TRIP **5**, 46 (1997).

[151] L. T. Lee, B. J. Factor, and F. Rondelez, J. Chem. Soc. Faraday Discuss. **98**, 139 (1994).

[152] M. P. Pépin and M. D. Whitmore, in preparation.

[153] Y. Higi, N. Ueno, and I. Noda, Polym. J. **15**, 367 (1983).

Appendix A

Monte Carlo Algorithm

In this appendix, a brief description of the most important details of the MC algorithm are presented. The purpose is to highlight some important technical details of the simulations which are used to produce an efficient algorithm. This section is divided into three parts. The first part describes the basic algorithm used to generate new states, the second part discusses the calculation of the autocorrelation functions, and the last section describes the evaluation of the averaged quantities.

A.1 Generating New States

The general algorithm for generating new states is described in Chapter 2. In this section we describe the algorithm in more detail.

A.1.1 Choosing New Configurations

The first step in generating a new state involves choosing a transition. Transitions are chosen randomly by choosing a polymer, the type of move (reptation, kink-jump, crankshaft or Brownian motion), the monomer or end that moves, and if required, the direction of motion. In principle, one can determine a new state from only one random number by evaluating the number of possible transitions (N), choosing a random number in the range $[1, N]$ and using look-up tables to specify the transition. In practice, this causes problems because the number of possible transitions becomes very large and the look-up tables are too big. Therefore, three random numbers are used to determine a new state. The first random number is used to determine the polymer, the second to determine the type of move, and the third to determine the monomer and/or the direction of motion.

Polymers are chosen with a weight Z_i where Z_i is the number of effective monomers for polymer i. This is done to produce an efficient algorithm where polymers with higher degree of polymerization are chosen for a transition more often. For a system with P polymers, a random number in the range $[1, N']$, where $N' = \sum_{i=1}^{P} Z_i$, is chosen and the polymer is determined from a look-up table. A type of move is then chosen with a certain weight. Typically the percentage of each type of move corresponds to 50%, 40%, 8% and 2%, for reptation, kink-jump, crankshaft and Brownian motion, respectively. This ratio of moves was chosen in order to allow an efficient algorithm. In particular, without crank-shaft motion certain configurations of parts of the polymer

can relax only by local motions propagating from the chain ends which makes the algorithm very inefficient in simulations with higher molecular weight polymers. A choice of 8% for crank-shaft motion is adequate for all molecular weights involved in this study. In terms of Brownian motion, the ratio must not be too large so that the polymer moves a large distance before it samples the configuration space on a local scale.

Once the type of move is chosen, the monomer and/or direction of motion is chosen. For each type of move there is a number of possibilities and a specific move is once again chosen randomly with the use of a look-up table.

A transition must be chosen for every new configuration but, in order to effectively choose the transitions, we produce a table of 100,000 transitions prior to actually attempting to generate new states. After 100,000 MC attempts at generating new states a new table of transitions is generated. In this way, efficient vectorizable and parallelizable loops can be used to generate transitions.

A.1.2 Illustrative Cases of the Change in Energy

Before a new state is accepted the new configuration must satisfy excluded volume constraints. If a polymer moves to unoccupied sites, then the change in energy must be calculated. In principle, this is done by calculating the difference in total energy of the system before and after the move. This approach is very inefficient and, in poor solvent (low temperatures), many transitions are rejected due to the *Metropolis*

rule. This makes the algorithm even more inefficient because of the low acceptance rate and the fact that, for every rejected move, all look-up tables associated with the configuration of the polymer must be updated twice: once to perform the move and once to return the polymer to its original configuration.

In all MC simulations described in this thesis, there are no more than two different species of polymer. This results in a maximum of one reduced interaction energy parameter between nearest neighbors, which simplifies the calculation of the change in energy. The change in energy is effectively calculated by determining the change in the number of energetic contacts during the transitions. Its calculation is therefore localized to the vicinity of the polymer whose configuration is being changed, and the need to calculate the total energy of the system is eliminated. For most moves, there are only two sites involved and it is possible to determine the change in energy without actually performing the move and updating all tables. For example, assume that a B homopolymer is in solvent. Calculation of the change in energy requires determining the change in the number of energetic contacts at sites where effective B monomers are replaced by solvent and sites where solvent is replaced by effective B monomers. For A-*b*-B copolymer the calculation is essentially the same since the A block is the same species as the solvent.

Figure A.1 shows examples of various MC moves of a homopolymer. For reptation, the change in energy is given by

$$\Delta E = 2\epsilon(n_i - n_i' + \delta_i) \qquad \text{(A.1)}$$

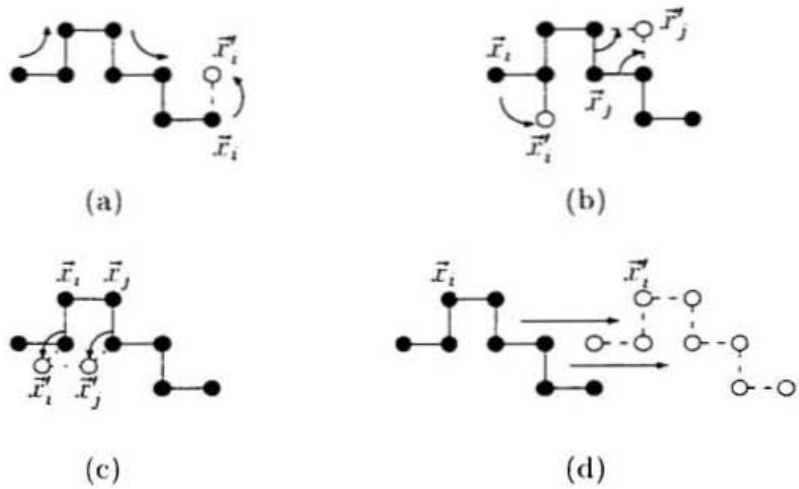

Figure A.1: Various elementary MC moves: a) reptation, b) kink-jump (and end-flip). c) crank-shaft. d) Brownian motion.

where n_i and n_i' are the number of nearest neighbors of type B at the lattice sites $\vec{r}_i$ and $\vec{r}_i'$, respectively, for $i = 1$ or Z. For copolymer, $i = 1$ or Z_{CB}. The variable δ_i is a correction term where

$$\delta_i = \begin{cases} 1, & \text{if } \vec{r}_i \text{ and } \vec{r}_i' \text{ are nearest neighbors} \\ 0, & \text{otherwise.} \end{cases} \tag{A.2}$$

It is due to a change in the number of nearest neighbors of type B at $\vec{r}_i$ and $\vec{r}_i'$ during the move. This occurs only when $\vec{r}_i$ and $\vec{r}_i'$ are nearest neighbors. We note that n_i, n_i' and δ_i are quantities which are known before the move is performed, and actually performing the move before calculating the change in energy is not required. With the change in energy known *a priori*, it is calculated with the use of a table consisting of the number of nearest neighbors of type B, for every site on the lattice.

For a kink-jump move, a similar expression is obtained, with

$$\Delta E = 2\epsilon(n_k - n'_k) \tag{A.3}$$

where, for an end monomer $k = i$ and for a monomer within the polymer $k = j$ (see Figure A.1(b)). If an A monomer of copolymer moves to another site, $\Delta E = 0$; otherwise the change in energy is calculated from Equation (A.3). For crankshaft motion there are two monomers that change location and the change in energy is given by

$$\Delta E = 2\epsilon(n_i - n'_i + n_j - n'_j) \ . \tag{A.4}$$

For copolymer, Equation (A.4) is valid only when the two effective monomers are of type B. If a monomer at position $\vec{x}_k$ ($k = i$ or j) is of type A, then term $n_k - n'_k$ in Equation (A.4) is set to zero.

For Brownian motion, an expression similar to Equation (A.1) can be obtained by summing over all effective monomers of the polymer except that the author of this thesis knows no effective method of calculating the correction terms, δ_i, for each monomer, as discussed in the case of reptation. The table representing nearest neighbors of type B must therefore be updated before the change in energy is calculated. The change in energy is therefore given by

$$\Delta E = \epsilon \sum_{i=1}^{Z} ({}_A n_i - {}_A n'_i + {}_B n_i - {}_B n'_i) \tag{A.5}$$

where Z is the number of effective B monomers and, ${}_k n_i$ and ${}_k n'_i$ are the number of nearest neighbors of type B at positions $\vec{x}_i$ and $\vec{x}'_i$, respectively, before the polymer

Function	% CPU
Choosing Transitions	19.4
Reptation	39.7
Kink-jump	20.7
Crankshaft	3.1
Brownian Motion	10.7
Averaged Quantities	5.1
Identify Polymers in Micelles	1.3

Table A.1: Profile of the CPU usage for a typical MC simulation: $o_C^0 = 0.02$, $Z_{CB} = 10$ and $Z_{CA} = 14$. The calculation of the autocorrelation functions is included under the category of averaged quantities.

is translated ($k = B$) and after the polymer is translated ($k = A$). In this case the table of nearest neighbors must be updated before the change in energy is calculated but this does not significantly affect the efficiency of the algorithm since only 2% of the moves correspond to Brownian motion. This is seen in Table A.1 where a profile of the CPU usage is shown for a typical simulation of copolymer micelles.

A.1.3 Autocorrelation Functions

In MC simulations of polymers, the system relaxation time depends on the degree of polymerization, the solvent quality which is determined by ϵ, and other parameters such as the volume fraction and surface coverage. A knowledge of the number of N-bead cycles required to reach equilibrium is therefore important in creating an efficient algorithm. Furthermore, the system relaxation time can also be used to determine the appropriate interval of time δt in data acquisition for the evaluation of averaged quantities. Data analysis of a system can take up most of the CPU time during a

simulation if the data are collected too often and, if the interval δt is too long, the total simulation time must be large in order to obtain statistically significant averaged quantities. In this section, the method used to effectively monitor the autocorrelation functions, which are used to determine various autocorrelation times of the systems, is discussed.

Generally, the autocorrelation functions $C_X(t)$ are monitored until a time t' at which $C_X(t') \simeq 1/e^2$. The time t' therefore corresponds to approximately twice the autocorrelation time τ_X, assuming that the function decays exponentially. In this time one might require an autocorrelation function to be monitored 100 times. Once $C_X(t)$ has reached the defined limit (e.g. $C_X(t') = 1/e^2$), the process is repeated so the functions can be averaged. There is therefore an interval $\delta t_X \simeq \tau_X/50$ between data points collected for the autocorrelation functions. It is therefore beneficial to have *a priori* knowledge of the autocorrelation times or, equivalently, the appropriate time interval δt_X. In general, this is not the case and the autocorrelation times must be approximated. At the beginning of each simulation all nearest neighbor interactions are set to zero. In the case of free polymers in solution the autocorrelation times are relatively short and $\delta t_X = 1$ to 10. For simulations with end-tethered polymer, the autocorrelation times can be long and the values for δt_X are determined on the basis of the degree of polymerization of the polymers and the surface coverage. At this point a rough estimate is adequate to produce efficient and accurate results during the process of reaching an equilibrium state. Once equilibrium is reached,

the autocorrelation times are estimated from the autocorrelation functions which were monitored during the process of equilibration. This provides better estimates of the equilibrium values of τ_X and δt_X. These new estimates are then used during the equilibrium process. Once all data have been collected and averaged quantities have been calculated, the times τ_X and δt_X are determined using Equation 2.14. In simulations of micelles and swollen micelles, once average quantities are evaluated, ϵ is increased slightly and the process is repeated. The calculated values for τ_X and δt_X from the previous ϵ are therefore used as estimates at the new solvent quality.

This method allows us to effectively approximate the relevant autocorrelation times which are required for an efficient algorithm which produces accurate results without *a priori* knowledge of the relaxation times involved in the simulations.

A.1.4 Averaged Quantities

In the previous section, we described how the autocorrelation functions and the relevant time scales are calculated to obtain the equilibration time, the time for equilibrium statistics and the intervals of time, δt_X, in collecting data for the averaged autocorrelation functions. For other averaged quantities, the interval of time δt for the collection of data is determined from the maximum of all δt_X. The calculation of the averaged quantities is relatively straightforward and we shall not delve into this any further except for quantities which require the identification of individual aggregates and each polymer within the aggregates. These quantities include some

of the autocorrelation functions such as the chain extraction and chain exchange autocorrelation functions.

The first step is identifying polymers which are nearest neighbors. This is essential for determining which molecules belong to particular aggregates, and the number of molecules in each aggregate. The method is discussed in more detail because an efficient algorithm is important in this case in order to perform a statistical analysis for all simulated solvent qualities.

To identify a polymer in an aggregate or in solution, a list of polymers which have not yet been identified as being part of an aggregate is kept. We begin with the first polymer in the list and look at the six nearest neighbors of each of its monomers, unless the polymer is a copolymer. In that case, we use only the core forming block (the B block) to identify aggregates. If any nearest neighbor is a B monomer of another polymer, then the new polymer is identified as being part of the same aggregate as the first polymer and it is eliminated from the list. The process is continued until all nearest neighbors of the first polymer have been identified. Now, the identified polymers may be in contact with other polymers so their nearest neighbors must also be identified. This process is repeated until all nearest neighbors from all polymers in the aggregate have been identified. Once this is done the first polymer is identified along with the other polymers as being part of the same aggregate. If the polymer in question is not in contact with any other polymer then it is said to be in solution and in either case it is eliminated from the list. This process is repeated until all polymers

in the list have been exhausted. At this point, all polymers have been identified with a certain aggregate or as being in solution.

This method is quite efficient, and with the properly estimated autocorrelation times, a statistical analysis at all simulated solvent qualities can be performed with less than 7% of the CPU time used for the analysis and identification of micelles (see Table A.1).

Appendix B

Interfacial Tension

In this appendix we derive an expression for the interfacial tension at an A-B homopolymer-homopolymer interface in the presence of selective solvent. The general expression from which it is derived was developed by Hong and Noolandi [90] who later [20] applied it to micelles.

For infinite molecular weight polymers, Hong and Noolandi obtained an expression for the interfacial tension given by

$$\frac{\gamma}{\rho_0 k_B T} = \int dx \left[\Delta f(x) + \frac{b^2}{24} \sum_P \frac{[o'_P(x)]^2}{o_P(x)} \right] \tag{B.1}$$

where $\Delta f(x)$ is the inhomogeneous free energy density which vanishes in the bulk, the sum is over both polymers in solution, $o_P(x)$ is the volume fraction of polymer P and $o'_P(x)$ is the spatial derivative of $o_P(x)$. The free energy density is

$$\Delta f(x) = f[o_A(x), o_B(x)] - \sum_\kappa o_\kappa(x)\mu_\kappa \tag{B.2}$$

where the sum is taken over all constituents in the system

$$f(o_A, o_B) = 1/2 \sum_{\kappa,\kappa'} \chi_{\kappa\kappa'} o_\kappa o_{\kappa'} + o_S \ln o_S \tag{B.3}$$

with o_S as the solvent volume fraction, and μ_κ is the chemical potential of component κ.

To calculate the interfacial tension, one must solve for the volume fractions $o_A(x)$ and $o_B(x)$ via a self-consistent algorithm which involves solutions to a modified diffusion equation for the volume fractions and related potentials. In the approximate expression for the interfacial tension derived by Hong and Noolandi [20], the authors assumed linear density profiles, as shown in Figure B.1, and were able to obtain an analytical expression for the interfacial tension.

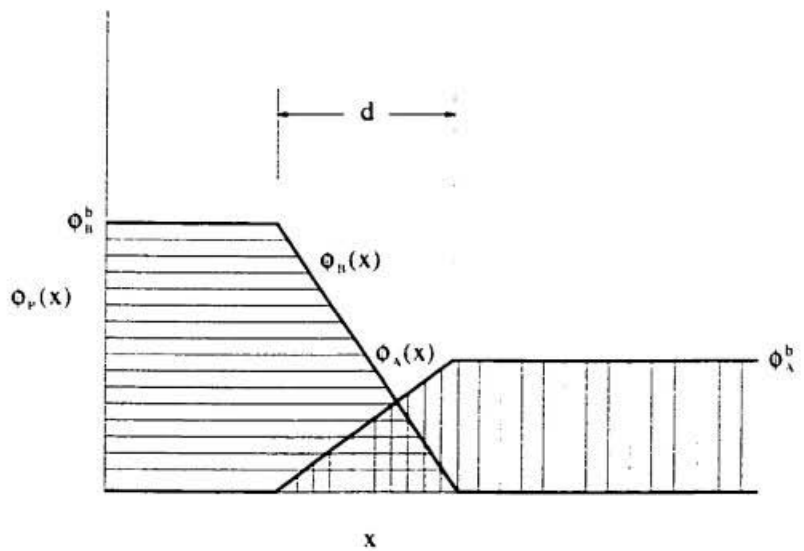

Figure B.1: Volume fraction profiles of the A and B homopolymer.

The integrand in Equation (B.1) vanishes except near the interface. We set

$$\phi_\kappa(0) \simeq 1/2[\phi_\kappa(\infty) + \phi_\kappa(-\infty)] \tag{B.4}$$

$$\phi'_A \simeq \frac{\phi_A(\infty)}{d} \equiv \frac{\phi^b_A}{d} \tag{B.5}$$

$$\phi'_B \simeq -\frac{\phi_B(-\infty)}{d} \equiv -\frac{\phi^b_B}{d} \tag{B.6}$$

where $x = 0$ is taken to be the midpoint of the interfacial region, d is the interfacial thickness, and ϕ^b_A and ϕ^b_B are the bulk volume fractions of the A and B homopolymer, respectively. From Equations (B.1)−(B.6), the interfacial tension is therefore approximated by

$$\frac{\gamma}{\rho_0 k_B T} = d\Delta f(0) + \frac{b^2}{12d}\sum_P \phi^b_P \,. \tag{B.7}$$

Minimizing γ with respect to d gives

$$d/b = \left[\sum_P \phi^b_P / 12\Delta f(0)\right]^{1/2} \tag{B.8}$$

and

$$\frac{\gamma}{\rho_0 k_B T} = b\sum_P \phi^b_P/6d. \tag{B.9}$$

It is convenient to express the chemical potential in terms of the asymptotic volume fractions ϕ^b_P. For a homogeneous system

$$f = \sum_\kappa \phi_\kappa \mu_\kappa \tag{B.10}$$

where the sum is over the polymers and solvent. Equation (B.2), with the use of Equation (B.4), therefore reduces to

$$\Delta f(0) = f|_{x=0} - 1/2(f|_{x=\infty} + f|_{x=-\infty})$$

$$= f\left(\frac{\phi_A^b}{2}, \frac{\phi_B^b}{2}\right) - \frac{1}{2}[f(\phi_A^b, 0) + f(0, \phi_B^b)]. \qquad \text{(B.11)}$$

The interfacial tension can therefore be expressed in terms of the Flory interaction parameters χ_{AB}, χ_{AS} and χ_{BS}, and the volume fractions of polymer in the bulk ϕ_A^b and ϕ_B^b.

B.1 Special Case

In Chapter 3, a simple expression for the interfacial tension is required to obtain an approximate scaling expression for the core radius of the micelles. In this case the analysis is restricted to strongly segregated systems in which the volume fraction of polymer in the core is very close to unity ($\phi_{CB}^{(1)} \simeq 1$), $\chi_{BS} = \chi_{AB} = \chi$ and $\chi_{AS} = 0$. We can therefore derive a simple expression for the interfacial tension by setting $\phi_B^b = 1$. Equations (B.8) and (B.11) give

$$d = d_0 \sqrt{\frac{2 - \phi_S(\infty)}{2(1 - 2\phi_S(\infty)(\ln 2)/\chi)}}, \qquad \text{(B.12)}$$

where d_0 is the width of an A-B homopolymer-homopolymer interface with no solvent present. It is given by

$$d_0 = b\sqrt{\frac{2}{3\chi}}. \qquad \text{(B.13)}$$

In the limit $\phi_S(\infty) \to 0$, $d \to d_0$ as expected. A relatively simple expression for the interfacial tension is also obtained from Equations (B.9) and (B.11) in this approximation, where

$$\frac{\gamma}{\rho_0 k_B T} = \gamma_0' \sqrt{\frac{1}{2}(2 - \phi_S(\infty))(1 - 2\phi_S(\infty)(\ln 2)/\chi)} \qquad \text{(B.14)}$$

and

$$\gamma_0' = b\sqrt{\frac{\lambda}{6}} \,. \tag{B.15}$$

Similarly, γ_0' is the the interfacial tension for a homopolymer-homopolymer interface and $\gamma/\rho_0 k_B T \to \gamma_0'$ as $o_S(\infty) \to 0$.